Development of Luminescent Transition Metal Complexes for Correlative Light and Electron Microscopy and Super Resolution Microscopy

Jonathan R. Shewring

A thesis submitted to the University of Sheffield in partial fulfilment of the requirements for the degree of Doctor of Philosophy.

August 2017

The University of Sheffield

Department of Chemistry

Abstract

Microscopy is an invaluable tool for life scientists to scrutinise the micro- and nanoscopic world and probe the processes, organisation and structure of the building blocks of life. Light microscopy and electron microscopy are two key techniques used to analyse cell on a subcellular level and correlative light and electron microscopy seeks to allow the collection of much greater depths of information than either technique alone. However, utilizing both techniques in tandem has proven difficult as the probes typically used for light microscopy lack the ability scatter electrons, a key attribute for electron microscopy. This leads to inference between samples instead of true correlation between different techniques. Thus the main challenge in this area is the development of probes that allow truly correlative imaging by using a single probe that providing luminescence in light microscopy and contrast in electron microscopy.

Herein we demonstrate the ability of small, mononuclear platinum(II) N^C^N and iridium(III) C^N complexes to act as probes for light and electron microscopy at concentrations close to or the same in both light and electron microscopy. Moreover, the first examples of transition metal complexes in the super resolution microscopy technique 3D SIM are explored, with these complexes displaying excellent photostability, essential for super resolution imaging. The use of super resolution microscopy helps facilitate the shrinking of the “resolution gap” between light and electron microscopy, leading to better correlation between data sets. The first fully correlative images using a luminescent transition metal complex are reported, illustrating their ability to provide both luminescence and contrast from metal complexes at the same concentration. Through this work we have also discovered that the Ir(III) complex used causes rupturing of lysosomes when irradiated with visible light, a key mechanistic step in its activity as a photodynamic therapy agent. This complex is also explored using two-photon time resolved emission microscopy, in which it was discovered to be pH sensitive *in vitro*, giving a subcellular map of the pH within the cell.

Acknowledgements

First of all, I would like to thank my supervisor, Professor Julia Weinstein for the opportunity to work in her group. Her enthusiasm and guidance throughout my PhD has been invaluable, and providing many opportunities, such as working in the Rutherford Appleton laboratories. Her advice has always helped me maintain focus and context for my project when I've felt lost or unsure how to proceed.

I would also like to thank the University of Sheffield and the Imagine: Imaging Life initiative for the funding to undertake my project and thank you to the Imagine cohort who have been excellent.

Next I'd like to make special mention of Dr Elizabeth Baggaley who has consistently help me throughout my PhD, teaching me many techniques and always being willing to discuss any results I have. Not only helping me through my research but inviting me to climb with you, Jonny, Jon, Jeni and Dave has be awesome and has definitely help me get stronger and become a better climber! Your contribution can not be overstated and my PhD would have been a very different experience without you and for that I can't thank you enough.

Special thanks must also go to my co-supervisor, Professor Per Bullough, as well as to Helen Bryant, Stanley Botchway, Christa Walther and Chris Hill whose contributions have helped me gain knowledge and expertise in a wide range of techniques and fields crucial to the furthering of my PhD. I thank you all for you fruitful discussions and patience teaching a chemist to become something more.

I'm also grateful to the Weinstein group for being so warm and welcoming, working with all of you has been a pleasure from the first to the last day. A special mention must go to Luke McKenzie for all your help with cell culture and hard work done at RAL. I'd also like to thank Stuart Archer, Lewis Cletheroe, Steven Spall and Andrew Sadler for help in the lab and generally providing a fun and interesting environment to be in. This is also extended to the rest of D floor, whose inhabitant's addiction to tea and coffee has allowed me to enjoy tea break on G floor with fun and often abstract conversation.

Thanks must also go to all my friends outside of work and family who have provide help and support throughout my studies. Your encouragement over the years has helped me get to where I am; literally this is all your fault guys…

Finally, I'd like to thank my girlfriend Katherine Hardy, your companionship and support have helped keep me sane!

Table of Content

Chapter 1. Bioimaging: Chasing Photons and Electrons 1
1.1 Introduction 1
1.2 Photophysics of Luminescent Dyes 2
1.3 Fluorescence Microscopy 4
1.3.1 Confocal Microscopy 6
1.3.2 Colocalisation 8
1.3.3 Two-Photon Microscopy 9
1.4 Super Resolution Microscopy 11
1.4.1 Stimulated Emission Depletion Microscopy 12
1.4.2 Localisation Microscopy 13
1.4.3 Structured Illumination Microscopy 14
1.4.4 Super Resolution Probes 15
1.5 Probes for luminescence microscopy 16
1.5 Electron Microscopy 16
1.5.1 Transmission Electron Microscopy 18
1.5.2 Scanning Electron Microscopy 18
1.6 Correlative Light and Electron Microscopy 18
1.7.1 Technical Considerations 20
1.7.2 Cryo-Electron Tomography and High Pressure Freezing 20
1.7 CLEM Probes 21
1.7.1 Gold Nanoparticles 22
1.7.2 Quantum Dots 23
1.7.3 Metal Complexes 23
1.8 Summary 26
1.9 References 27
Chapter 2: Transition Metal Complexes as Probes for Cell Imaging 32
2.1 Introduction 32
2.2 Luminescent Transition Metal Complexes as Probes 32
2.2.1 Toxicity of Metal Complexes 34
2.3 Localisation of Metal Complexes 35
2.3.1 Nucleus 35
2.3.2 Nucleoli 43
2.3.3 Endoplasmic Reticulum 46

2.3.4 Golgi Apparatus 49
2.3.5 Mitochondria 52
2.3.6 Lysosomes 58
2.4 Emission Lifetime Microscopy 62
2.4.1 Lifetime Imaging Methods 63
2.4.2 Oxygen Sensing *in Vivo* 65
2.4.3 Oxygen Sensing *in Vitro* 69
2.5 Summary 75
2.6 References 76
Research objectives 83
Chapter 3. Exploring Pt N^C^N as a Dual Probe 84
3.1 Introduction 84
3.2 Establishing Intracellular Localisation of Pt(N^C^N)Cl, Compound 85
3.3 TEM Imaging 86
3.4 Super Resolution Imaging 94
3.4.1. Co-Staining 100
3.5 Summary 104
3.6 References 104
Chapter 4. Investigation of an Iridium (III) Complex as Dual Probe 107
4.1 Introduction 107
4.2 Screening Potential Complexes 108
4.2.1 Platinum (II) Complexes 109
4.2.2 Iridium (III) Complexes 110
4.2.3 Time Resolved Emission Microscopy Studies 114
4.3 Uptake and Localisation of 4.6. 120
4.4.1 *In Vitro* Lifetime Mapping with 4.6. 123
4.4 3D SIM Imaging with 4.6 125
4.4.1 Co-staining 126
4.4.2 Further Cell Lines 132
4.5 TEM Imaging 133
4.6 Summary 139
4.7 References 140
Chapter 5. Mitochondrial Specific Iridium (III) Complex for CLEM 142
5.1 Introduction 142
5.2 Localisation of Complexes 143
5.2.1 Lysosomal Co-Staining 144

5.2.2 Endoplasmic Reticulum Co-Staining 144
5.2.3 Mitochondrial Co-Staining 145
5.2.4 Toxicity Studies 147
5.3 TEM Imaging 148
5.4 Super Resolution Imaging 152
5.5 Summary 156
5.6 References 157
Chapter 6. Correlative microscopy with luminescent metal complexes 158
6.1 Introduction 158
6.2 Correlative Light and Electron Microscopy on TEM Grids 160
6.2.1 Results 161
6.3 CLEM Using Gridded Culture Dishes 164
6.3.1 Protocol Refinement 165
6.4 CLEM of Complex 4.6 171
6.5 CLEM Using High Pressure Freezing 175
6.5.1 Preliminary HPF Studies 176
6.6 Summary 177
6.7 References 178
Chapter 7. Experimental methods 180
7.1 Cell Culture 180
7.1.1 Live Cell Staining 180
7.1.2 Fixed Cell Staining for 3D Structure Illumination Microscopy 180
7.1.3 Transmission electron microscopy Staining 181
7.1.4 MTT Assay 181
7.1.5 Correlative Light and Electron Microscopy 181
7.1.6 High Pressure Freezing 182
7.2 Imaging 182
7.2.1 Confocal Microscopy 182
7.2.2 Two-Photon Time-Resolved Mircoscopy 183
7.2.3 Emission Spectra 183
7.2.4 Two-Photon Microscopy 183
7.2.5 3D Structure Illumination Microscopy 183
7.2.6 Transmission Electron Microscopy 183
7.3 References 183
Summary and Future work 185

List of Abbreviations

3T3	Cell Line; Mouse Embryonic Fibroblasts
3D SIM	3D Structure Illumination Microscopy
AntA	Antimycin A
ATP	Adenine Triphosphate
Bipy	bipyridine
C^N	Phenylpyridine
C2C12	Cell Line; Mouse myoblast
CCD	Charged-Coupled Device
CHO	Cell Line; Chinese Hamster Ovary
CLEM	Correlative Light And Electron
CPP	Cell Penetrating Peptide
cryo-ET	Cryo-Electron Tomography
DAPI	4’,6-diamidino-2-phenylindole
DMEM	Dulbecco’s modified Eagle’s medium
DIC	Differential Interference Contrast
DIP	4,7-diphenyl-1,10- phenanthroline
DMSO	Dimethylsulphoxide
DNA	Deoxyribonucleic Acid
Dppz	Dipyridophenazine
Dpq	dipyrido[3,2-*f*:20,30-*h*]quinoxaline
EDTA	Ethylenediaminetetraacetic Acid
EM	Electron Microscopy
ER	Endoplasmic reticulum
FCCP	Carbonyl cyanide-4-(trifluoromethoxy)phenylhydrazone
FCS	Fetal Calf Serum
FLIM	Flouroescence Lifetime Imaging Microscopy
FNG	FluoroNanogold
GFP	Green Fluorescent Protein
GM	unit; Goeppert-Mayer
HCL	Hydrochloric acid

HCT116	Cell Line; Human Colorectal Caricinoma
HEK293T	Cell Line; Human embryonic kidney
HeLa	Cell Line; Human cervical carcinoma
Hep G2	Cell Line; human liver cancer
HOMO	Highest Occupied Molecular Orbital
HPF	High Pressure Freezing
IC_{50}	50 % Inhibition Concentration
IMS	Industrial Methylated Spirits
ISC	Intersystem Crossing
k_i	Nonradiative Decay Rate Constant
k_r	radiative decay rate constant
LM	Light Microscopy
LSCM	Laser Scanning Confocal Microscopy
LUMO	Lowest Unoccupied Molecular Orbital
MCF-7	Cell Line; Human Breast Carcinoma
MCNR	Modulation Contrast-to-Noise Ratio
MDCK	Cell Line; Canine kidney
MEF	Cell Line; Mouse embryonic fibroblast
MRI	Magnetic Resonance Imaging
mtDNA	Mitocondrial Deoxyribonucleic Acid
MTT	(3-(4,5-dimethylthiazol-2-yl)-2,5-diphenyltetrazolium bromide) tetrazolium
N^C^N	1,3-di(2-pyridyl)benzene
N^N^C	2-phenyl-6-(1H-pyrazol-3-yl)-pyridine
N^N^N	2, 2':6'2"-terpyridine
NA	Numerical Aperture
NHC	*N*-Heterocyclic Carbene
OD	Optical Density
OTF	Optical Transfer Function
PALM	Photoactivation Localisation Microscopy
PBS	Phosphate Buffer Solution
PC12	Cell line; Rat Adrenal Medulla
PDT	Photodynamic Therapy
PEG	Polyethylene Glycol
Phen	1, 10 phenanthroline

PLIM	Phosphorescence Lifetime Imaging Microscopy
PSF	Point Spread Function
QD	Quantum Dot
RC	Relative Contrast
RN22	Cell Line; Rat Schwann cell
RNA	ribonucleic acid
S_o	Singlet Ground State
S_1	Lowest Energy Singlet Excited State
S_n	Singlet Excited State
SHEP-1	Cell Line; Human Neuroblast
SH-SY5Y	Cell Line; Human neuroblastoma
STED	Stimulated Emission Depletion
STORM	Stochastic Optical Reconstruction Microscopy
T_1	lowest energy triplet excited state
TEM	Transmission Electron Microscopy
Tppz	tetrapyrido- [3,2-a:2’,3’-c:3’’,2’’-h:2’’’,3’’’-j]phenazine
TP-TREM	Two-Photon Time Resolved Emission Microscopy
TREM	Time Resolved Emission Microscopy
U-2 OS	Cell Line; Human bone osteosarcoma
UV	Ultraviolet
ε	Molar extinction coefficient
λ_{ex}	Excitation Wavelength
τ	Lifetime
Φ	Quantum Yield

Chapter 1. Bioimaging: Chasing Photons and Electrons

1.1 Introduction

Since the development of the first microscope in the 1620's,[1] microscopy has developed in to an indispensable tool for the life sciences.[2] As further improvements were made in the 19th Century with better optics and compound microscopes, the idea that life was made up of microscopic cells was still disputed. However, once systematic investigations of animal and plant cells were reported, cell theory became widely accepted.[3] As such microscopes have been used to study the organisation, structure and processes of cells and as new technologies and developments have improved microscopes, new discoveries have followed. Until the 20th century microscopes simply used reflected light to illuminate and view a sample and any contrast, and therefore detail, seen was due to the scattering of light from components within the sample. As optics improved and illumination techniques became more sophisticated, such as Köhler illumination and phase contrast, it became possible to scrutinise these structures more clearly but were still limited to what could be observed.[4] Ernst Abbe was a key player in microscopy during his time at the optical systems manufacturer, Ziess. Abbe developed many fundamental technologies we now take for granted, such as the apochromatic lens which eliminates colour distortions. During his time at Zeiss Abbe published an equation that laid out the resolution limit of light microscopes[5]:

$$d = \frac{\lambda}{2NA} \qquad (1)$$

Were d is the resolution limit in the xy plane, λ is the wavelength of light used and NA is the numerical aperture. Abbe put forward that the main limiting factor to resolution was the numerical aperture which is shown below in figure 1 that can simply be described as the angle at which light is still accepted by the objective lens.

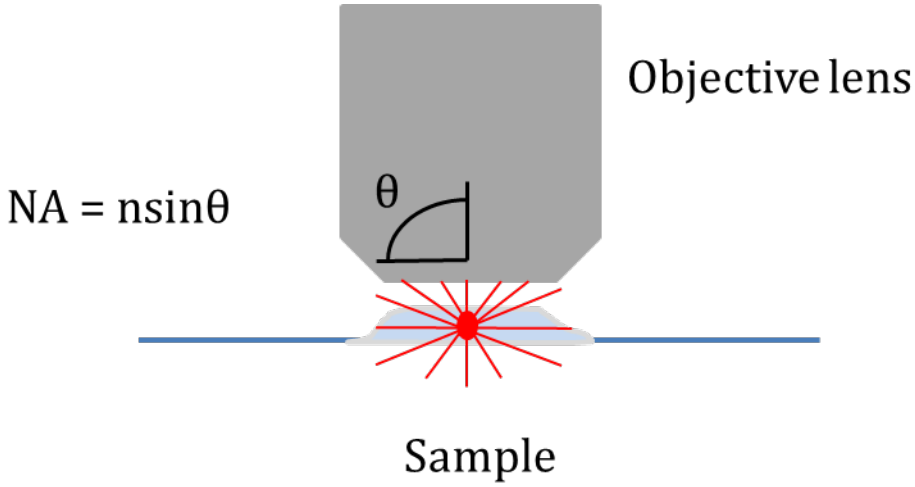

Figure 1. Diagram depicting the acceptance of light from a sample by an objective lense, showing the angle important to numerical aperture of the lense.

The equation describes the NA with n being the index of refraction of the medium and θ is the half-maximal angle of the light able enter and exit the objective lens. Typically objective lens' are designed to operate in air, water or oil and so have a constant value for n (1.00, 1.33 and 1.52 respectively), while θ is an intrinsic property of the objective lens being used. This equation set the minimum resolvable point in a light microscope to ~200 nm in the xy plane even with modern optics and the shortest wavelength visible light.[6]

The next major step forward in microscopy came from the development of the luminescence microscope, which made use of luminescent dyes to stain cells and specific wavelengths of light to illuminate the cell with the dye, creating a luminescence image.[4] This allowed new, previously unseen structures and processes of the cell to be examined. The photophysical properties of these luminescent dyes have serious implications for the utility and practical ease of use. Before luminescence microscopy is described further, the important photophysical properties of dyes will be discussed.

1.2 Photophysics of Luminescent Dyes

Luminescence is a general term used to describe the emission of light from a substance that is in an electronically excited state.[7] When a photon of light of a suitable energy is absorbed by a molecule, it is excited from the singlet ground state (S_0) into a higher energy single state (S_n, $n > 0$). From the excited state the electron can relax back down to the ground state via emission of a photon with the energy that corresponds to the energy gap between the excited state and ground state. This is known as fluorescence, a radiative transition between electronic states of the same multiplicity. Another possibility is for the excited state to undergo intersystem crossing (ISC), whereby there is a spin inversion for one of the unpaired electrons populating a triplet state (T_1). This formally spin-forbidden

transition is slow in most cases. From the triplet state (T_1) it is again possible for the excited state to relax back down to the single ground state (S_0) but this also requires a change of spin and is therefore a disallowed transition due to the spin selection rule and is slow. Emission from an electronically excited triplet state to a singlet state is known as phosphorescence, a radiative transition between states of different multiplicity. There are also non-radiative pathways that allow the molecule to lose energy as heat instead of emitting a photon to relax back to the ground state, which depends on coupling of vibrational modes to the electronic excited states and the environment of the molecule.

Compounds which emit via fluorescence pathways are known as fluorophores and via phosphorescence pathways are known as phosphores. In general, all emissive compounds can be termed luminophores and this is the term that shall be used throughout.

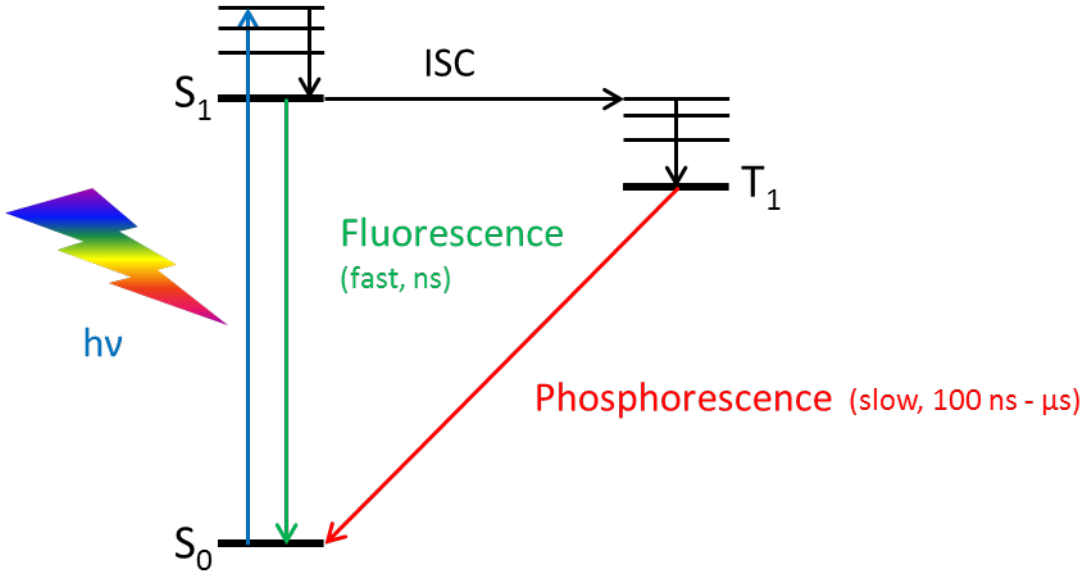

Figure 2. A simplified Jabloski diagram depicting a molecule absorbing a single photon and entering a electronically excited state. From here the molecule undergoes internal conversion to the lowest excited state before either emitting a photon of a lower wavelength called fluorescence or undergoing intersystem crossing in to a triplet excited state. The molecule then undergoes internal convertion again to the lowest excited triplet state before emitting a photon called phosphoresence. Molecules can also undergo nonradiative relaxation to the ground state from its' lowest excited single or triplet state, leading to no photons being emitted after excitation.[8]

The relevant photophysical parameters for a luminescent probe are extinction co-efficient (ε), which defines how strongly a molecule absorbs light of a particular wavelength, the quantum yield (Φ), which is directly linked to the brightness of the molecule and the emission lifetime (τ), which describes how long the molecule will emitting light for. The extinction co-efficient (ε) is a given by the following equation (2):

$$A = \varepsilon c l \qquad (2)$$

Where A is the absorbance of the material or solution, c is the amount concentration of the species and l is the path length. The greater the extinction co-efficient, the greater the amount of light absorbed by a molecule at a given wavelength and this increases the chance of a photon being re-emitted by the molecule.

The chance of a photon being emitted from an electronically excited state is expressed by the quantum yield (Φ) and is described by the following equations (3):

$$\Phi = \frac{k_r}{\Sigma k_i} = \frac{\text{number of photons absorbed}}{\text{number of photons emitted}} \quad (3)$$

Where k_r is the rate constant of spontaneous emission and Σk_i is the sum of all the rate constants of excited state decay. This can also be expressed as the second part of the equation, describing the efficiency of the radiative process as a ratio of the number of photons absorbed to the number of photons emitted. The maximum emission quantum yield attainable is 1.0 or 100 %; molecules with a quantum yields as low as 10 % are still considered reasonably emissive.

Another important property of luminescence compounds is their Stoke's shift. Stokes's shift is the difference between the energy of the absorption and emission, providing they involve the same electronic states (e.g., So-S_1 and S_1-S_0). For phosphorescence, Stokes shift is not strictly applicable, as two different excited states are involved; absorption corresponds to a S_0-S_1 transition, and emission to the T_1-S_0 transition. However, this term is still used in the literature, meaning "the difference in energy between the lowest absorption maximum and the highest energy emission maximum"[9]. It is an important parameter because of the necessity to separate the scattered excitation light from the true emission upon detection; and because of potential reabsorption of the emitted light.

Finally, photostability is a key attribute of luminescent molecules. As molecules are irradiated and enter electronically excited states, it is possible that these molecules will undergo photochemical reactions that can reduce their luminescent quantum yield and even completely deactivate these molecules by converting them to non-luminescent species. This is known as photobleaching and the degree of photobleaching is affected by the intrinsic stability of the molecule in its excited state and the environment the molecule experiences while in its excited state. Molecules that photobleach easily can be very difficult to image and often lead to substandard images being obtained, thus making photostability an extremely desirable property for luminescent probes.

1.3 Fluorescence Microscopy

The majority of fluorescence microscopes used today are epifluorecence microscopes, which use a broad excitation source, such as a xenon arc lamp, with an excitation filter to illuminate the sample

with more specific wavelengths of light. This light is then reflected by a dichroic mirror and focused on to the sample by the objective lens and illuminates the entirety of the sample. The luminophores present in the sample then begin emitting photons usually of a longer wavelength (lower energy), which is collected by the same objective lens and passes through the dichroic which reflects any excitation light. Before the emitted light arrives at the detector, which is typically a charge-coupled device (CCD) camera, the light passes through an emission filter to reject any other light which is not within the expected range of the luminophore.

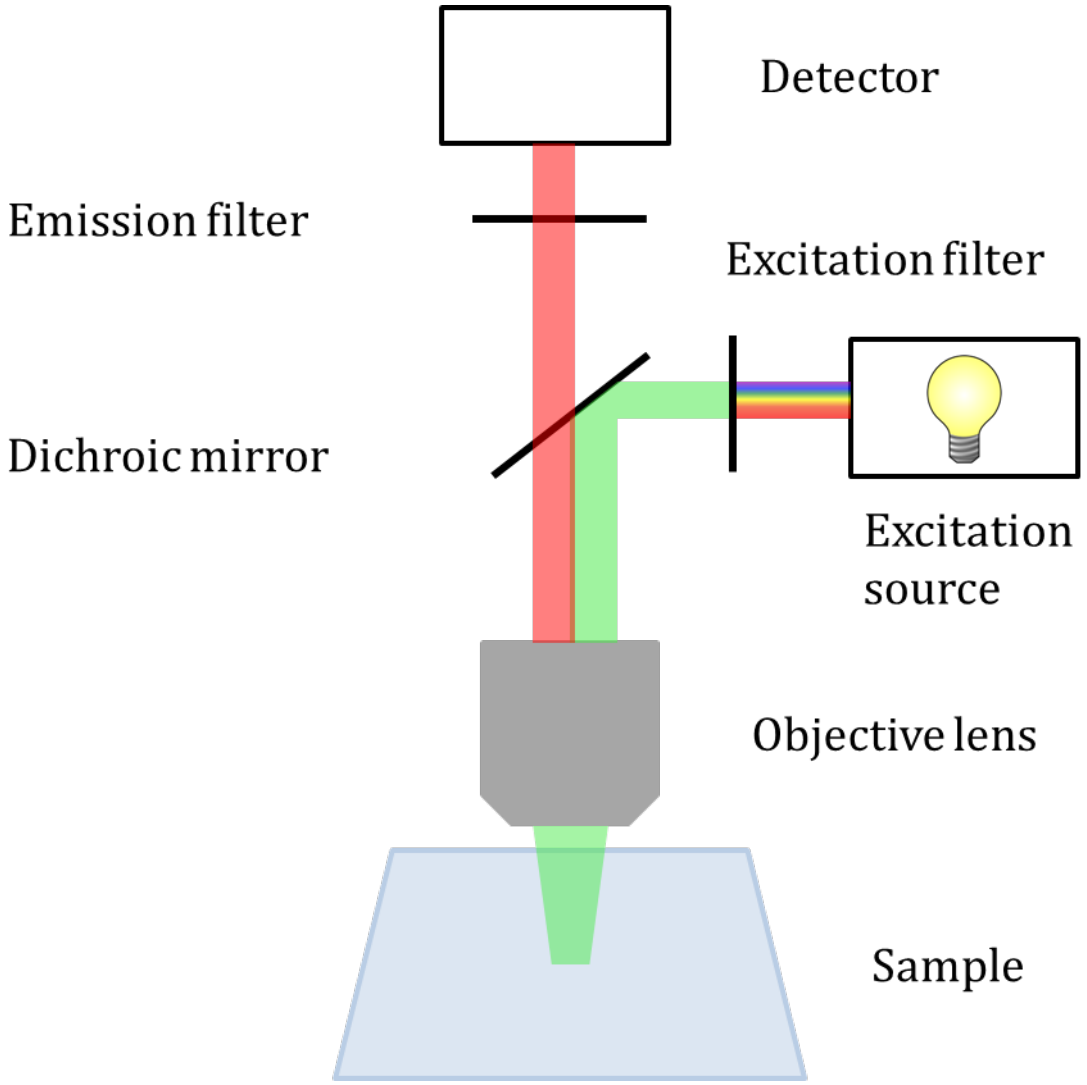

Figure 3. Schematic diagram of the basic light path of a widefield microscope.[4]

While this design has been in use for decades, enabling countless discoveries to be made, there are some drawbacks. Some of the major disadvantages arise from the whole sample being illuminated at once, consequently photobleaching across large areas of the sample simultaneously and any phototoxcity from the excitation wavelength used is seen to a greater degree. Furthermore, when the area of interest is being illuminated, areas of the sample above and below the focus are also being

illuminated, which leads to blurring of the image. This side effect can be mitigated through the use of deconvolution algorithms, which reassigns out of focus light back to where it was emitted from by using detailed models of the optical transfer functions (OTFs) for the wavelength range used.[10] However, this approach can become taxing in terms of computer power and time with large Z-stacks of high quality images.

1.3.1 Confocal Microscopy

Confocal laser scanning microscopy was developed to overcome some of the issues that affect conventional widefield microscopes; the principle was first patented in 1957.[11] As mentioned above, a key problem with conventional widefield microscopes is that they flood a large area of the sample with light, therefore emission is observed from luminophores above and below the plane of focus and photobleaching occurs across a large area. This is addressed in confocal microscopy as point illumination is used and the sample is raster scanned by the illumination, with the signal measured pixel by pixel. A pinhole is also placed in front of the detector to eliminate out of focus light (figure 4), thus only light very close to the plane of focus is detected, improving the z resolution of the image taken and allowing optical sectioning and 3D image reconstruction. There is also a small improvement in the xy resolution as the higher orders of the airy disc can rejected so only the first order of the diffraction pattern are collected.[12] However, the light cut out by the pinhole means the signal intensity is reduced, so to compensate for this longer dwell times are often employed and more sensitive detectors such as photomultipliers are used.

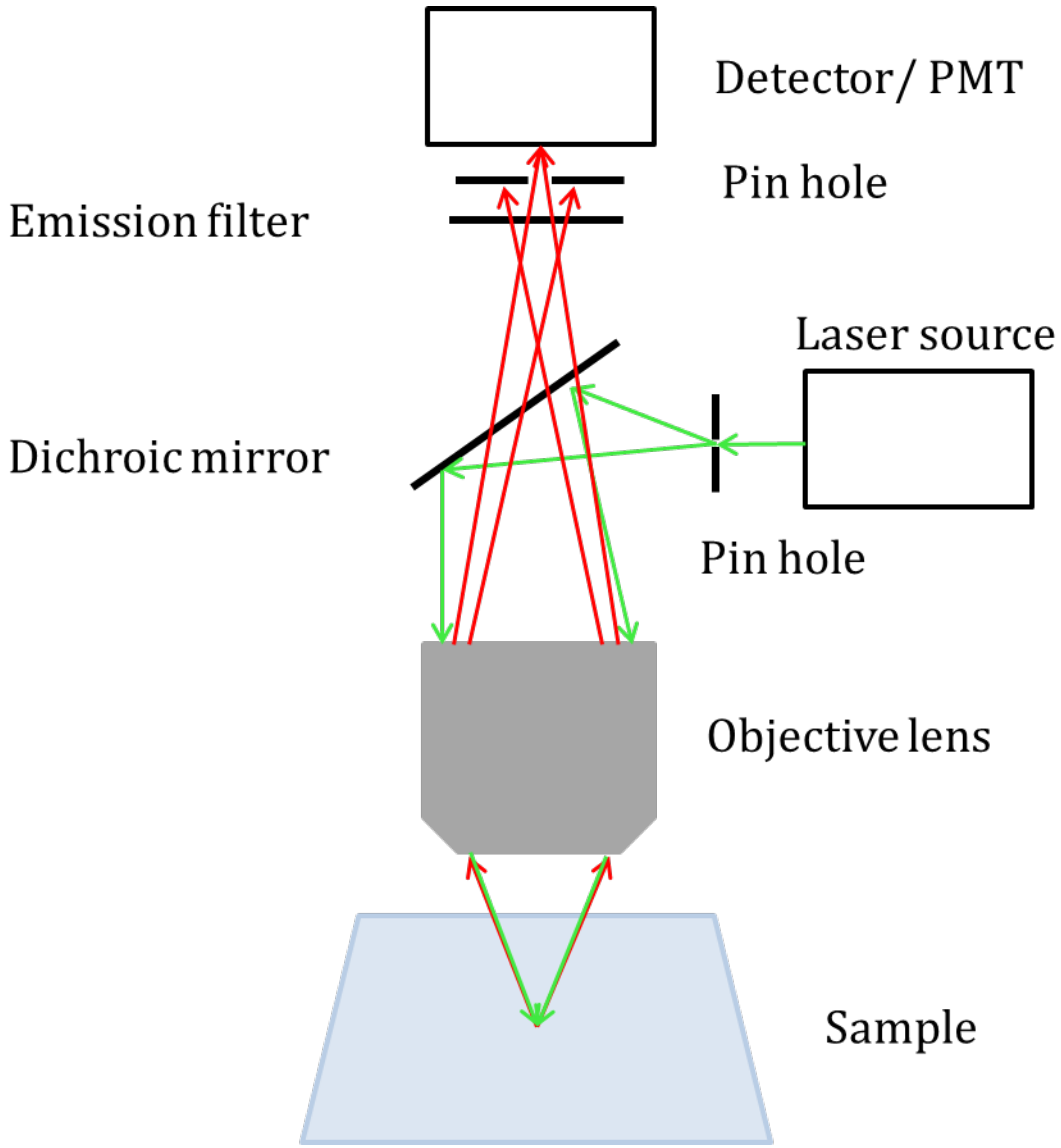

Figure 4. Schematic diagram of the light path of a confocal microscope.[4,11]

Photobleaching is still a problem with confocal microscopy as lasers are used as excitation sources and the beam passes through the sample in an hour glass shape, where the centre of the hour glass is the focal plane. This means that luminophores above and below the plane are still being excited (albeit at a smaller area than widefield), even though the signal is being rejected by the pinhole.

As with widefield microscopes, it is also possible to perform deconvolution on images to improve image quality using experimentally derived OTFs which accurately describe the point spread function.

1.3.2 Colocalisation

With the surging popularity of confocal microscopy as commercial systems became available and reports of the technical improvements allowing biological questions to be answered, colocalisation of dyes also gained favour as a way to analyse samples. Due to the optical sectioning of confocal vs widefield microscopy it became possible to perform co-localisation experiments with a good degree of confidence in the results that was not possible with normal widefield. However, it was realised that while overlapping different channels could depict colocalisation, this is fraught with potential errors. Due to the subjective nature of the analysis and inherent fallibility of human eyes and brains, misinterpretation of data is common due to potential optical illusions. Furthermore, if the colocalisation is being assessed by the degree of colour generated by combining the colours of either channel, then only when the two colours are of the correct intensity will the expected colour be visible, confusing data analysis. Thus, due to the intrinsic biases of humans, various analytical methods were designed to objectively quantify the degree of colocalisation using computers.

Of these methods, two stand out as the most popular and widely used; Pearson's coefficient and Mander's coefficient.[13] The Pearson's correlation coefficient is a common parameter used to quantify the correlation between two channels and has a range between -1 to 1, where -1 is perfect exclusion (the channels exclusively don't overlap). 0 represents no co-localisation and 1 is perfect correlation.[14] However, reality is not a perfect spectrum of co-localisation to no co-localisation, making interpretation of intermediate values difficult. Pearson's is not sensitive to differences in mean signal intensities but noise within the image causes the value to approach a value near 0. In summary, if a high Pearson's value is obtained in the analysis it can be said that there is a good degree of correlation between the two channels, but intermediate values can be difficult to analyse.

Mander's split coefficient is a variation on the Pearson's correlation coefficient which instead of estimating correlation, describes co-occurrence.[15] The range for Mander's split coefficient is 0-1 instead of -1-1 as in Pearson's, with 1 being perfect co-occurrence and 0 being the opposite. Mander's split co-efficient is usually displayed as M1 and M2 (possibly with a t in front denoting a threshold has been applied), M1 being the proportion of co-occurrence between the first channel and the second and M2 is simply the same thing but with the channels reversed. Mander's does not take into account the brightness of the pixels being co-localised and therefore might be better suited for samples where you do not expect to see the exact same amount of signal from then same area. This does however mean that the Mander's split co-efficient is very sensitive to poor background correction.

Due to the differences in model type of each method, it is important to consider the sample being imaged and the expected outcomes if the hypothesis is correct. As the Pearson's coefficient is an excellent measure of correlation and if the two dyes are expected to accumulate in exactly the sample compartments mirroring each other in localisation and intensity, then the Pearson's coefficient would

be a good measure of this. However, if percentage colocalisation of a specific channel against another to observe the association of one dye to a specific organelle dye for instance, then Mander's coefficient would be more informative and is better suited.

1.3.3 Two-Photon Microscopy

A further improvement of microscopy came from the discovery of a phenomenon known as two-photon absorption. Two-photon absorption was first theorised in 1931 by Maria Goeppert-Mayer but it wasn't until the development of lasers that two-photon absorption was first observed.[16] This was due to the nature of two-photon absorption, in which two photons of approximately half the energy of the excitation that is attempted to be excited are required to arrive simultaneously. This requires a large photon flux in a very small area for the likelihood of this event to excite a sufficient amount of molecules, thus lasers are a perfect excitation source for such experiments. While the flux requirement slowed the initial discovery, it is one of the main reasons why the property was picked up by microscopists as excitation only at the focal plane eliminates the problem of phototoxicity due to out of focus light(fig 5.).[17] This also improves the z resolution by only exciting molecules in a small area and without the use of pinhole to artificially exclude light. Furthermore, the wavelengths of light normally used to excite in the visible region become infrared in two-photon microscopy, which opportunistically lies in a region of the electromagnetic spectrum that biological tissue is much more transparent to than visible light, allowing imaging much deeper into samples than conventional microscopes.[18]

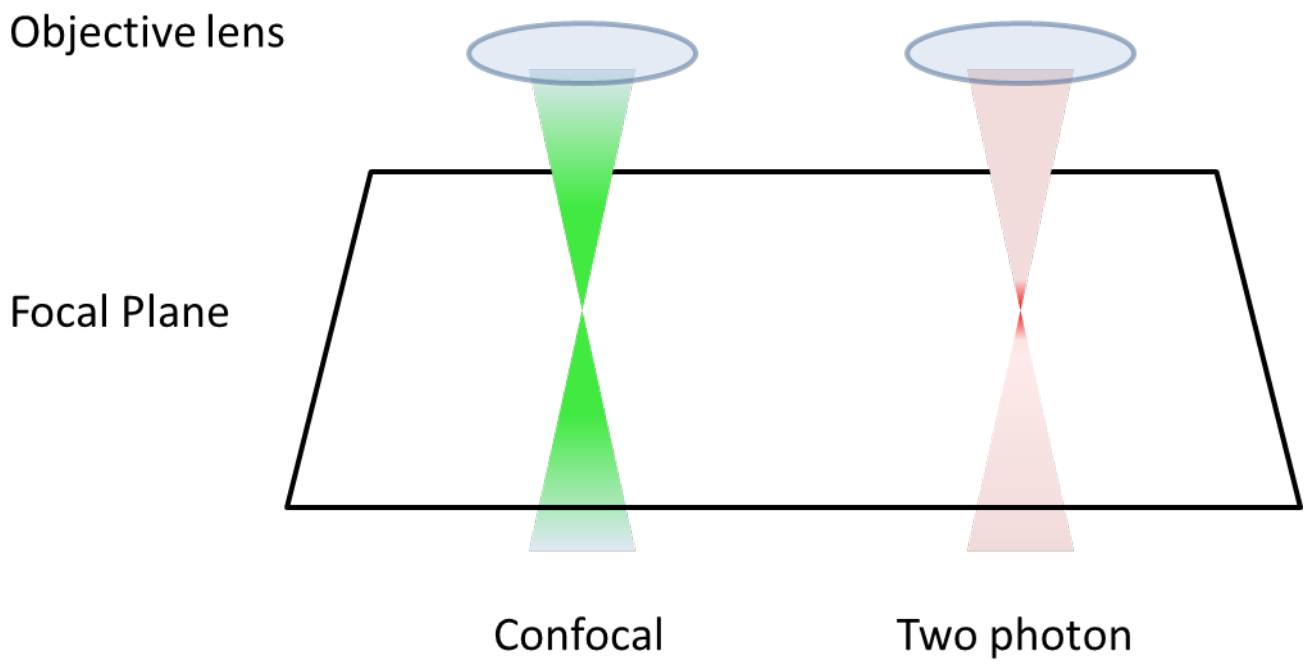

Figure 5. Diagram depicting the difference in confocal and multiphoton excitation.[19] Confocal focuses a beam of light through the sample exciting everything through the beam path. While multiphoton excitation does have a beam passing through the sample, only at the focal point is the photon flux high enough to cause excitation of luminophores.

However, dye are ideally required to have a good two-photon absorption cross section (>4 GM), which describes how likely a molecule is to absorb two photons at a given wavelength, and is similar to the extinction coefficient in one photon processes. Two-photon absorption is an intrinsic property of molecules, with a number of major factors contributing to the value of two-photon cross section. Large conjugated π systems are a key structural property for two-photon absorption and donor-acceptor systems have been shown to influence two-photon absorption.[19]

Dye	Two photon absorption (nm)	Two photon cross section (GM)
Fluorescein	750	57
Lucifer Yellow	850	2.6
Rhodamine 6G	750	55
Coumarin 485	750	35

Table 1. List of some common dyes with their two photon abosrptions wavelenghts and corresponding two photon cross sections.[20]

In vitro two-photon microscopy has benefited fields such as cancer research, where live 3D cancer models have been visualised, giving insight into how tumours organise and develop over time in 3D.[21] While two-photon microscopy offers useful advantages for *in vitro* imaging, the techniques greatest

strengths become apparent when it is utilized *in vivo*. Due to the lower scattering of the excitation beam and low phototoxicity, two-photon microscopy is ideal for imaging live animals and has been implemented in multiple fields.[22–24] Neuroscience has benifited greatly from the widespread implementation of two-photon microscopy, allowing real time observations into live animal brain circuitry at the cellular level.[25] While confocal microscopy can be useful for optical sectioning, the use of the pin hole reducing the signal from the sample, which coupled with scattering from imaging deep inside tissue diminishes the practical utility of confocal microscopy in these kinds of applications.

1.4 Super Resolution Microscopy

Over the past two decades there has been a revolution in light microscopy as the long standing diffraction limit has been subverted to yield new, far field super resolution microscopy techniques. With the advent of these new techniques, researches are able to explore the world at a scale that is set to improve and challenge our understanding of the most basic building blocks of life.[26]

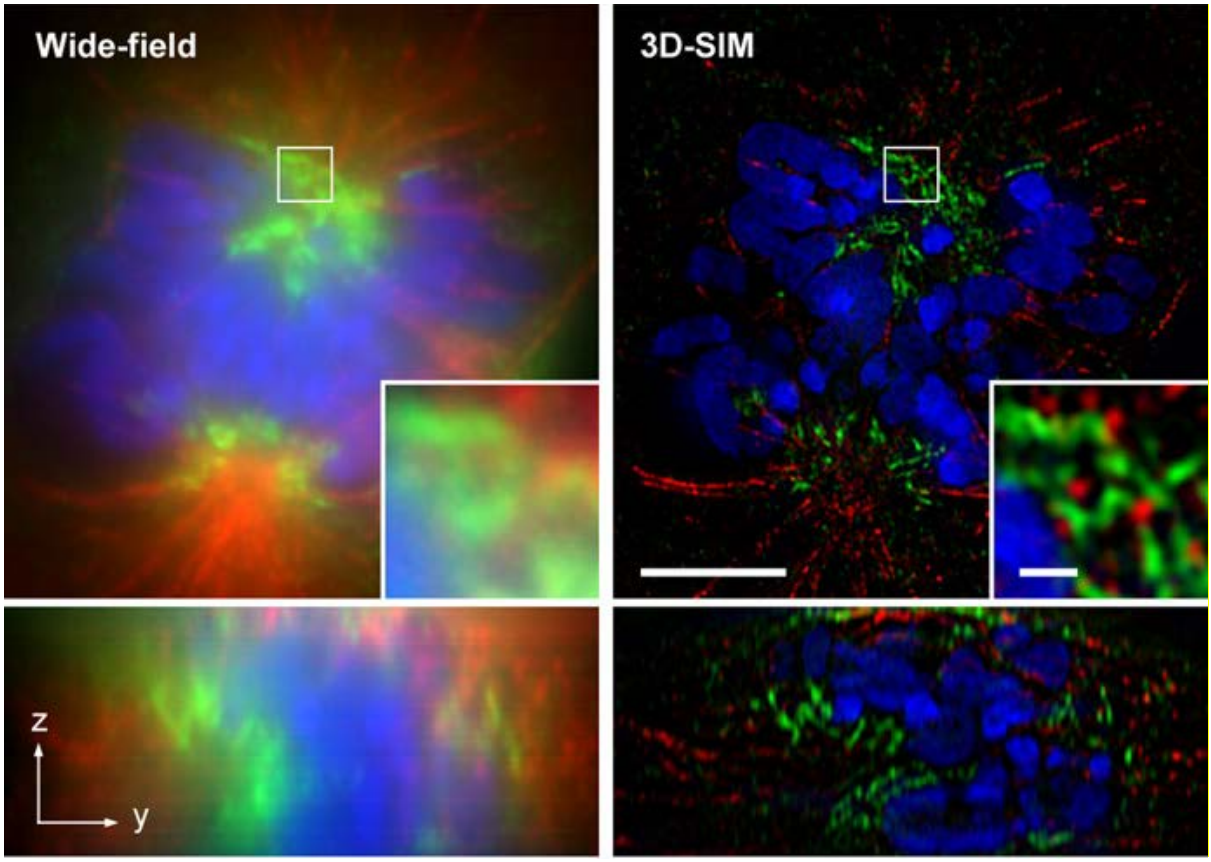

Figure 6. Conventional widefield image (left) and a 3D SIM image of C2C12 cells stained with immuno labelled Lamin B(green), tubulin (red) and stained with DAPI (blue). Adapted from ref.[27]

1.4.1 Stimulated Emission Depletion Microscopy

The first super resolution technique to be developed was based on a phenomenon known as STimulated Emission Depletion (STED), which centres on the ability to force an excited molecule to emit its energy as a lower energy photon by use of a specific wavelength depletion beam.[28] By aligning a depletion beam around an excitation beam, it is possible to scan the beams over a sample in a raster scan fashion akin to a confocal, and the tighter the depletion beam is around the excitation beam, the greater the resolution attainable. The resolution attainable with STED microscopy is now around 30 nm in the xy plane and 100 nm in the z plane using continuous wave lasers.[29] This technique is very laser intensive as the depletion beam is required to be at very high power to get the best improvements in resolution and therefore photobleaching can be a problem along with phototoxicity.

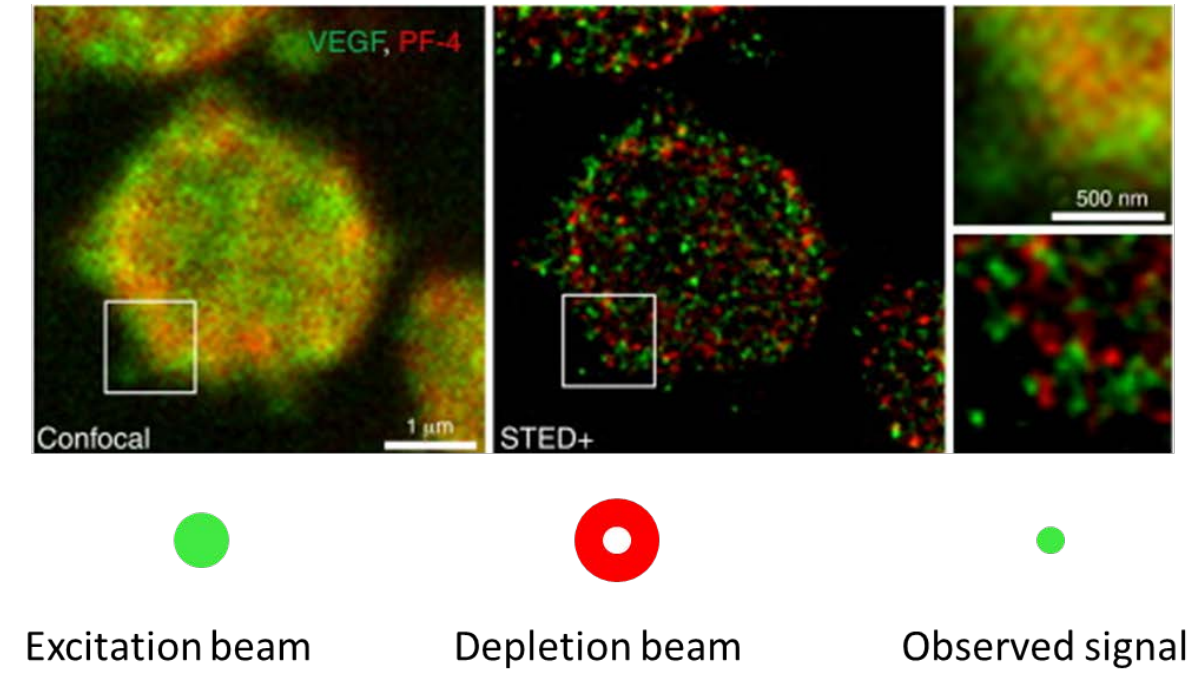

Figure 7. Confocal and STED micrographs of the same cell showing the resolution improvements in STED (top) (adapted from ref);[29] schematic diagram of a normal excitation beam at the focal plane and a donut shaped depletion beam used to yield improved resolution in the observed signal.

1.4.2 Localisation Microscopy

Two other closely related techniques that also utilise special photophysical phenomena are PhotoActivation Localisation Microscopy (PALM)[30,31] and STocastic Optical Reconstruction Microscopy (STORM).[32] These techniques are based on wide field microscopes and require luminophores that are either photoactivatable or that photoswitch between a dark and a light state, the purpose being that if a subset of all luminophores are on at once then these can be localised with precision and the point spread function (PSF) of these computationally reduced.[30,32] As multiple frames are collected and processed, a final image can be compiled from an amalgamation of all the frames, yielding a super resolution reconstruction. The blinking of luminophores is still under investigation with a number of proposed mechanisms but a number of buffer systems have been developed to yield desirable blinking characteristics.[33–36] Currently resolution of 10-40 nm in xy and 10-50 nm in the z axis are achievable with microscopes based on these techniques.[37] These techniques are also very laser intensive as they require the sample to be irradiated for long periods of time while thousands of frames are collected to fully reconstruct an image representative of the original sample.

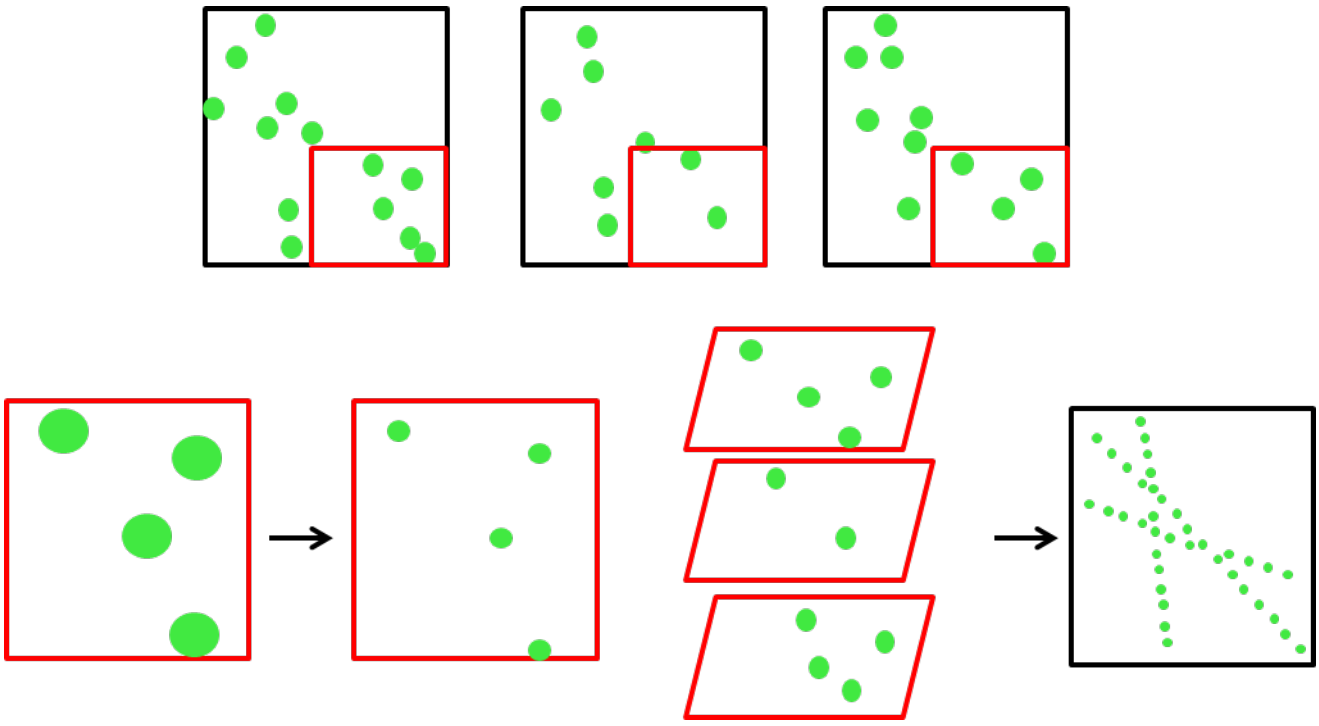

Figure 8. Schematic diagram of the principles of PALM/STORM, showing multiples frames being recorded from a sample with a subset of blinking fluorophores (top) and the PSF of the blinking fluorophores being artifically reduced (bottom left) and then compiled to yield a complete super resolution image (bottom right).

This is only a brief overview of STED and PALM/STORM as further information has been covered in other reviews.[29,38,39]

1.4.3 Structured Illumination Microscopy

The final super resolution microscopy techniques discussed will be Structure Illumination Microscopy (SIM). Unlike the other techniques, SIM does not require any kind of special photophysical properties to by-pass the diffraction limit. Instead SIM uses a sinusoidal striped pattern as an illumination beam with high spatial frequency, which when used on a sample with fine structure below the diffraction limit generates moiré fringes. Interference from the illumination beam and the moiré fringes allow high frequency information normally lost in widefield to be recovered, thus overcoming the diffraction limit.[40,41] SIM yields a doubling of the resolution achievable in conventional microscopes in x, y and z planes, yielding an approximately eight fold smaller volume.[42,43] Further work is also currently underway to further improve resolution by combining PALM and SIM.[44]

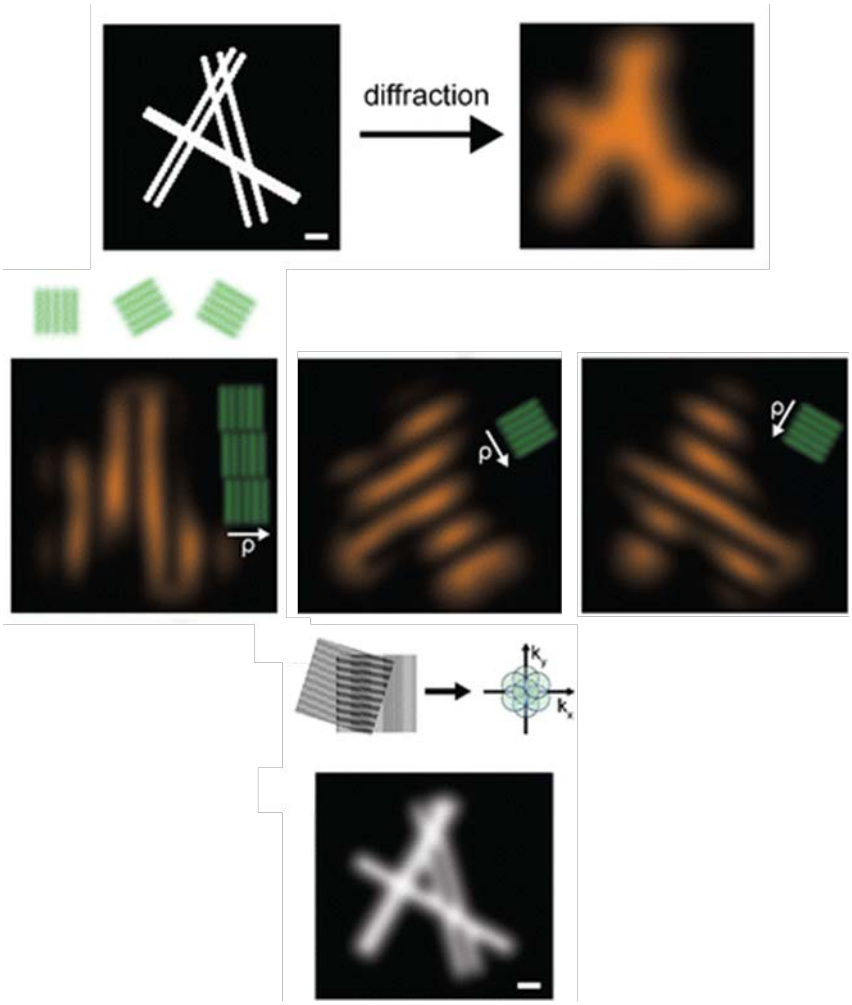

Figure 9. Depiction of SIM imaging of a structure showing the structured illumination using different angles and a visula depiction of moiré fringes.

SIM offers super resolution imaging without the need for specific probes, as there are no special requirements such as blinking fluorophores. SIM is moderately laser intense compared to the other super resolution techniques but photostable probes are still desirable otherwise artefacts can be introduced in the reconstruction due to the loss of signal.

1.4.4 Super Resolution Probes

As discussed previously, super resolution microscopy allows samples to be scrutinised at new levels of detail. However, there are no "free lunches", and while these techniques are extremely powerful they push the limits of the probes used, creating greater requirements for probes with better photophysical properties. All new super resolution techniques utilise higher laser powers than conventional widefield microscopes,[37] and as such photostability is extremely desirable for probes intended for use in these applications.

1.5 Probes for luminescence microscopy

One of the key considerations for all luminescence based microscopy is which luminescent probes to use. Many early probes were laser dyes that proved useful for microscopy, such as fluorescein and rhodamine (fig X) and dyes like these were the bed rock of the of experiments performed at the time. These dyes were typically used to study the areas of the cells they naturally accumulated in, with some being conjugated to biomolecules or antibodies.

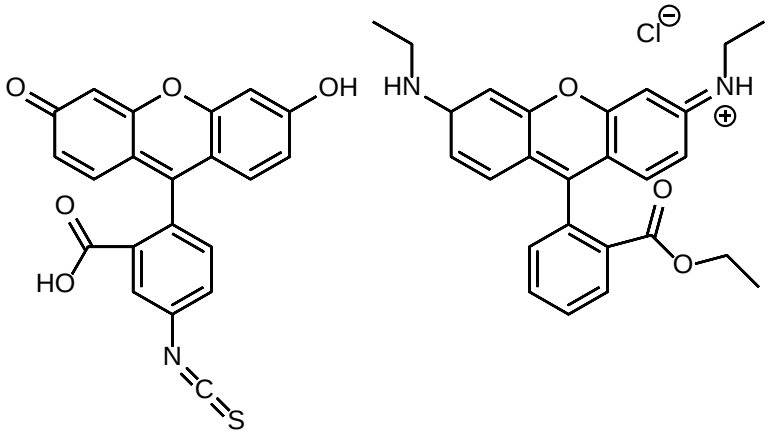

Figure 10. Molecular structures of Fluoroscein isocyanate and Rhodamine 6G

However, many of these dyes were found to be toxic and affect cells adversely, which defeats the idea of luminescence microscopy being unintrusive. As such, many of these dyes were developed in an attempt to reduce toxicity and improve other characteristics, such as solubility. There has been a number of developments since the early days of luminescent probes and one of the biggest has been the implementation of the Alexa dyes; these dyes are rhodamine derivatives with exceptional photostability and have been developed for a vast array of applications.[45]

Another big revolution for probes has been the development of green fluorescent protein,[46] which has allowed scientist to observe specific proteins of interest in live cells without fear of toxicity and safe in the knowledge that the structure illuminated are from specifically labelled proteins of interest.[47] This allowed the organisation and dynamic process of cells to be scrutinised in ways that were never before possible with coventional probes. However, these proteins are not perfect, they are not as bright as small organic dyes and often not as photostable.

1.5 Electron Microscopy

Electron microscopes (EM) use accelerated, focused beams of electrons as an illumination method.[48] Electron microscopes were first patented in the 1920's and were facilitated by the development of electromagnetic lenses which allow an electron beam to be usefully manipulated. One of the primary driving forces for the development of electron microscopes was the potential to surpass the diffraction limit set out by Abbe, as electrons have a considerably shorter wavelength. By 1933 electron

microscopes capable of surpassing the diffraction limit were constructed and the first commercial transmission electron microscope was available in 1939.

While electron microscopes have the theoretical potential to reach atomic levels of resolution, they are typically limited by the technical capabilities such as ability to focus a homogenous, coherent beam of electrons as an illumination source without spherical aberrations affecting imaging. Another limitation of electron microscopes is the need to operate in a strong vacuum to avoid scattering electrons in the illumination beam. Therefore, samples have to be fixed, dehydrated and embedded in resin before imaging, making live imaging impossible.[48]

Unlike luminescence microscopy, electron microscopy uses electron scattering to observe contrast differences in the sample. This is achieved by using heavy metal stains such as osmium tetroxide, uranyl acetate and lead citrate which effectively scatter elections due to the large nuclei present.[49–52] Osmium tetroxide is used as a fixative as well as a contrast agent for EM as the compound reacts with unsaturated lipids, stabilising the lipid membranes and depositing osmium metal, thus providing contrast in lipid rich membranes. Uranyl acetate is used as a negative stain in EM and should therefore not bind directly to the specimen but instead the uranyl ions bind to proteins, sialic acid groups, lipids and nucleic acid phosphate groups. Sialic acid groups are present in glycoproteins and gangliosides which are important components of all cellular plasma membranes, giving cellular context to the micrograph. Lead citrate on the other hand, binds to certain carbohydrates such as dextran, giving contrast to molecules that wouldn't normally be visible in the micrograph.[53] The latter two are often used in conjunction with one another as they complement each other well. Lead citrate can also react with the uranyl ions to intensify the staining giving a clearer micrograph. These compounds are all used as stains and not as specific probes, adding general cellular context to a micrograph by outlining membranes and certain common biomolecules, thus finding regions of interest requires searching through samples to find them, unlike luminescence microscopy where specific probes are used for easier identification.

Just as immunofluorescence techniques opened up the possibility of observing specific proteins within cells, immune techniques have been developed for EM with gold nanoparticles attached to antibodies, providing exquisite specificity.[54] These techniques provide information about protein expression, distribution and potentially co-localisation with other areas or proteins of interest, helping elucidate protein function.[47] These techniques do however require strong detergents to expose the antigens present within the section, potentially damaging the ultrastructure of the sample.[55]

1.5.1 Transmission Electron Microscopy

Transmission electron microscopes use a high voltage electron beam produced by an electron gun, which is typically a tungsten filament cathode. These electrons are then accelerated by an anode and then collimated and focused by a series of electromagnetic lenses before passing through the objective lens.[48] The beam then passes through the sample, interacting with the heavy elements within the sample to reveal structural information from the sample before being projected onto a detector. Without these heavy metal stains present it can be difficult to obtain suitable contrast in an image. Without the secondary fixing effect of osmium tetroxide, the sample can also be fragile and take damage from the electron beam during imaging.

1.5.2 Scanning Electron Microscopy

Scanning electron microscopy (SEM) is the other major electron microscopy configuration. As the name suggests, SEM is a scanning techniques, raster scanning across a sample in a similar fashion to a confocal microscope.[56] SEM also functions differently to TEM, instead of detecting electrons that have passed through the sample particles that are generated due to the interaction of the electron beam are detected. These particles range from secondary electrons, backscattered electrons, x-rays, Auger electrons and photons of various energies. This makes SEM a surface technique but allows for a wealth of information to be collected depending on the detection of the various types of particles collected. While SEM typically do not reach the same level of resolution achieved by the best TEM, improvements are such that the gap has been bridged substantially.

1.6 Correlative Light and Electron Microscopy

Correlative light and electron microscopy (CLEM) aims to combine both techniques and in doing so yield more information rich data than is achievable from either techniques individually. Optical microscopy is a non-invasive, high sensitivity technique which is ideal for real time observation of dynamic processes in live cells. A vast array of commercially available probes exist for optical microscopy with a myriad of applications.[45] However, as mentioned above, light microscopes are intrinsically limited by the wavelength of light used and are restricted to a resolution of ~200 nm in conventional microscopes. Super resolution techniques are steadily improving the potential resolution achievable using optical microscopy techniques, but these also add restrains on probes that are suitable for the techniques. Thus to be able to scrutinise biological samples at molecular resolution other techniques are required.

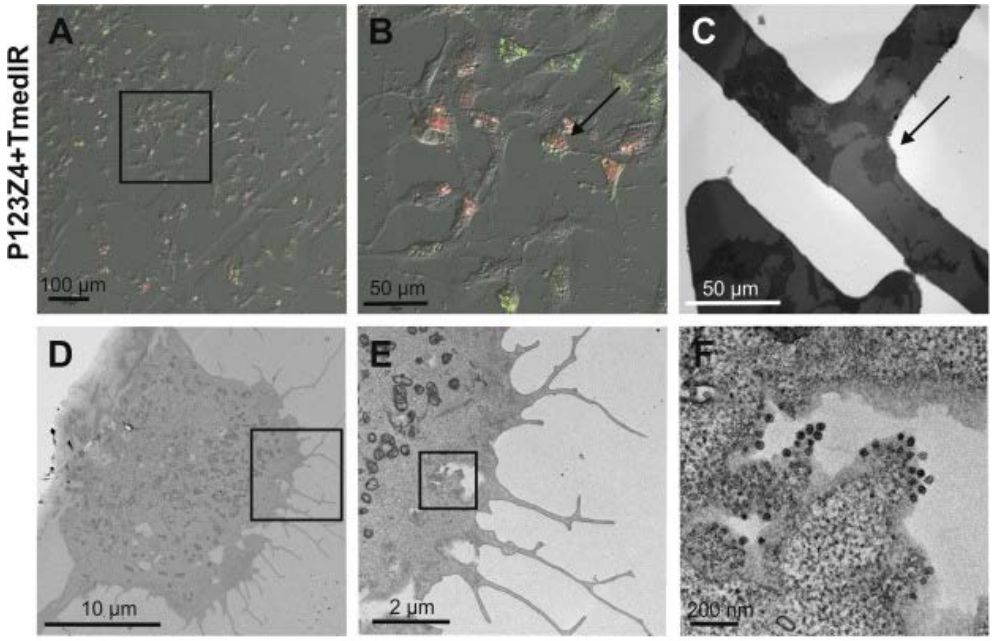

Figure 11. CLEM analysis of spherule formation. (A, B) Confocal micrographs of fixed cells being assessed for further analysis. (C-F) TEM micrographs of the same cells after preparing the sample for TEM providing ultrastuctural data. Adapted from ref.[57]

The typical method of choice for achieving better spatial resolution is electron microscopy, yielding nanometre resolution and ultrastructure data. In contrast to luminescence microscopy, electron microscopy produces ultrastructural data from the general staining used as well as potentially immunolabelling parts of the sample. However, EM also suffers disadvantages such as limited field of view and harsh fixing conditions. The former can make it difficult to find rare events or sites of interest, while the latter makes live cell imaging impossible and therefore cellular processes cannot be observed over time. Artefacts can also be introduced into the sample while fixation, dehydration and embedding take place.[55] Further problems arise from the use of a high power electron beam as it is damaging to the sample during use.

It becomes clear that no single imaging technique currently available is able to yield all the required information, but by combining these two modalities in a correlative approach, their strengths can be combined and their weaknesses mitigated. If the potential of correlative light and electron microscopy can be fully realised then it will be possible to probe areas of interest and/or processes using photon-based techniques before using EM to obtain greater resolution and ultrastructure data of the same area, thus providing a wealth of data not normally accessible. A number of challenges still remain before CLEM can be easily utilized in all applications. That being said, there have been many impressive discoveries that have been due to CLEM techniques being utilised; ranging from gaining greater understanding of the formation of clathrin coated pits, [58] to host pathogen interactions[59] and probing gap junctions in *Caernorhabditis* elegans.[60]

1.7.1 Technical Considerations

Due to the intrinsic differences of each microscopy technique, they generally require different sample preparations to yield the best results from imaging. This presents a problem for scientists attempting to utilize techniques in conjunction to study rare cellular events and wish to have truly correlative data of the same cell for LM and EM. Furthermore, being able to retrace the region of interest after preparing the sample for a second technique provides another obstacle to obtaining fully correlative data. This can be challenging if the sample is also being moved between microscopes as trying to find the same area of interest is not trivial on such small scales. Another problem also arises from the time taken to fix the cells for EM can allow the cells observed by LM to have changed if the cellular process being observed occurs over a period of minutes or less. There is also the chance that the fixing and dehydration of the cells for EM will cause artefacts in the sample.[55] These problems have led to some spectacular innovations, designed to address or mitigate these technical hurdles.

Probes are also a key consideration for researchers looking to utilises CLEM in their investigations which usually creates more restraints on the type of sample preparation that can be performed; leading to more complex pros and cons to be considered for each CLEM probe. Due to this, new cutting edge techniques are continuously being developed to improve sample preservation and biological accuracy.[61]

1.7.2 Cryo-Electron Tomography and High Pressure Freezing

Most EM is performed on dehydrated samples, which have been fixed and stained with osmium and uranium compounds. While these methods have allowed huge insight into the nanoscopic structure and organisation of cells, the cells are far removed from their original state. However, cryo-electron tomography (cryo-ET) and high-pressure freezing (HPF) have been developed as methods of preparing the sample so it is compatible for EM analysis while maintaining near native preservation of the cellular structure.[62,63] Both methods use flash freezing as a way to halt metabolic activity of cells while preserving the cellular structure. Rapid freezing is required so that samples form vitreous ice instead of a crystalline form of ice which damages cellular components and this requires samples to be plunged in liquid ethane for cryo-ET or subjected to high pressure and liquid nitrogen for HPF. These types of methods can have a double edged sword property, while being able to catch cells in a near native state, they are often imaged without further staining, maintaining excellent preservation but as a consequence the samples have a very low contrast under EM. This can be further exacerbated by the need to keep the electron dose low due to the fragility of the sample.

Cryo-ET has been utilized along with cryo-fluorescence microscopy to allow correlative light and electron microscopy to be performed on the sample with greater ease. A major development which facilitated this was the invention of a cryo-holder for the visualisation of the sample via fluorescence based microscopy while maintaining the lower temperature of the sample. One study employed a grid on the sample holder so that the same area of interest could be found and observed in both the cryo-fluoresence and cryo-electron microscopy.[64] While another study correlated the position of the EM with the LM by a piece of software, eliminating the need to visually identify the area of interest.[65]

A further improvement of high pressure freezing has come with the development of a rapid transfer system.[66] This system allows samples to be processed and fully frozen in five seconds. Thus, it makes it possible to capture specific cellular events occurring in live cells and then analyse the event at a higher resolution with EM afterwards. There have also been advances in combining the light microscopes with electron microscopes allowing imaging of a sample without the need for moving a sample between microscopes.[67–69]

1.7 CLEM Probes

A major consideration for correlative microscopy is the choice of the probe. Ideal probes would possess the characteristics to be observed by both LM and EM. This would allow for better correlation of both data sets. Another important trait for a CLEM probe would be the probe itself not perturbing the system while in use. If a separate luminophore is used for LM then it becomes difficult to correlate the same structures by EM. The main technique used to avoid this is immuno labelling[70] but this involves using detergents which disrupt the ultrastructure of the sample.[55] Further problems arise when the characteristic required for LM probes and EM probes are compared. LM probes require the use of a luminophore which either fluoresces or phosphoresces via excitation. In contrast, EM probes require probes which are more electron dense than their surroundings to provide contrast. These criteria are clearly not similar but efforts have been made to overcome these difficulties as described below.[71,72]

	Light microscopy	Electron microscopy
Probes/stains	Luminescent small molecules	Electron dense heavy metal salts
Resolution	Limited to ~200 nm*	~2 nm
Field of view	Wide	Limited
Sample preparation	Live cell imaging routine	Only fixed cells
Visible information	Limited to labelled structures	Ultrastructural data of cell

Table 2. Comparison of important criteria and imaging properties for light and electron microscopy. * apart from super resolution techniques which have achieved ~20 nm resolution.

1.7.1 Gold Nanoparticles

Gold nanoparticles have become an integral tool in ultrastructural immunocytochemistry. These tiny, electron dense particles of gold have found extensive use in immunoelectron microscopy[73,74]. It follows that if you could attach a luminophore to gold nanoparticles this would be a potentially ideal probe. However, there are few examples of such probes and this is in part due to the quenching of luminescence by Förster resonance energy transfer.[75] Further work has shown that nanoparticle with dyes attached through an antibody do manage to retain some luminescence[76] and nanoparticles with a coumarin dye attached via a polyethylene glycol linker can maintain fluorescence.[77] In light of this, there have been efforts to find an alternative form of gold labelling. This lead to the development of nanogold; 0.8 to 1.4 nm sized gold clusters which can be covalently bound to antibodies or used in other affinity labelling procedures[78,79]. Subsequently, nanogold was bound to fluorophores with no loss of fluorescence and became known as FluoroNanogold (FNG)[80,81]. A disadvantage of nanogold is the need for the clusters to be increased in size once labelling is performed so that they can be visualised clearly by EM. This is achievable using silver enhancement, which involves treating your sample with a silver salt solution in which the silver will be nucleated by gold nanoparticles and deposit silver on the surface making the nanoparticles larger and more visible.[82] Recent work has also cast doubt on the co-localisation of the fluorescent signal and scattering from the nanoparticle, suggesting that the fluorophores attached to the nanoparticles are almost completely quenched and

only untagged fluorophores are visible.[83] This raises questions on the ability of these nanoparticles to act as correlative probes.

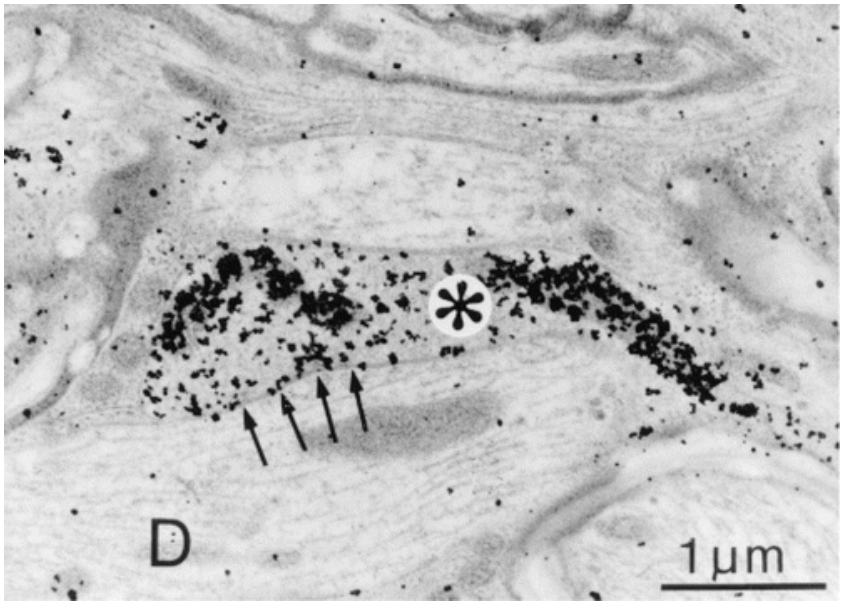

Figure 12. Electron micrograph of a rat spinal cord section imunnolabelled with nano gold which has been silver enhanced. D denoting dendrites in the thoracic spinal cord. Image reproduced from ref.[82]

1.7.2 Quantum Dots

Quantum dots (QDs) are nanocrystals of semiconductor which are small enough to exhibit quantum mechanical affects. They are generally made of cadmium/selenium or cadmium/ tellurium cores with a zinc sulphide shell and a polymer coating for attachment of biomolecules and to improve biocompatibility.[84] Due to the heavy metal cores of QDs and their intrinsic luminescence, QDs have received much attention for CLEM studies.[85] The size of the QDs is inversely related to the wavelength of the emission observed from the QDs which has a narrow emission spectra, allowing multicolour imaging with ease.[62] It would follow that multiple QDs of different sizes could be used as multiple labels using different sized QDs to give a range of colours and sizes when visualised. However, this is not necessarily the case as QDs do not offer enough contrast in EM to be easily distinguishable by size but three different QDs have been used to label distinct proteins simultaneously.[86] QDs do however tread a fine line in terms of their size and surface properties, having the potential to perturb the system they are intended to observe.[87,88]

1.7.3 Metal Complexes

Some of the major lines of inquiry for reliable CLEM probes have been highlighted above but there is one area that has largely been overlooked, transition metal complexes. It is well known that the

general preparation of samples for EM involves the use of electron dense metals which provide contrast to the biological sample. However, these methods have been tried and tested for decades and have not seen much development since their advent and acceptance into the wider scientific community. Typically osmium tetroxide, lead citrate and uranyl acetate are the compounds used to provide contrast in EM. While there are a few other examples of compounds used for contrast enhancement, there is no reason why other compounds containing heavy metals could not be used for enhancing contrast. One of the potential advantages of using luminescent transition metal complexes is the ease of use, as complexes have been shown to enter cells in a similar fashion to commercially available organic dyes and can stain organelles specifically.[89] This would allow a simplification of methods using them as contrasts agents as there is no special methodology that would be required to use them.

While there have been no studies to date reporting metal complexes as CLEM probes there have been a very small number of studies where luminescence metal complexes have been used to show contrast in EM. The early examples are that of two dinuclear ruthenium (II) complexes, used as nuclear stains when stained using media and mitochondrial staining when polymersomes were used as a delivery method.[90,91] In both the studies the localisation of the complexes in TEM was consistent with that seen in the optical microscopy, however very high concentrations of 500 μM were used to stain the cells. Following up this work, it was reported by Gill *et al.* that a mono nuclear ruthenium complex could also provide contrast in TEM. Curiously, it was observed that in contrast to the optical microscopy, in TEM the complex was found to stain the nucleus and the mitochondria, while no mitochondrial staining was noted in optical microscopy.[92]

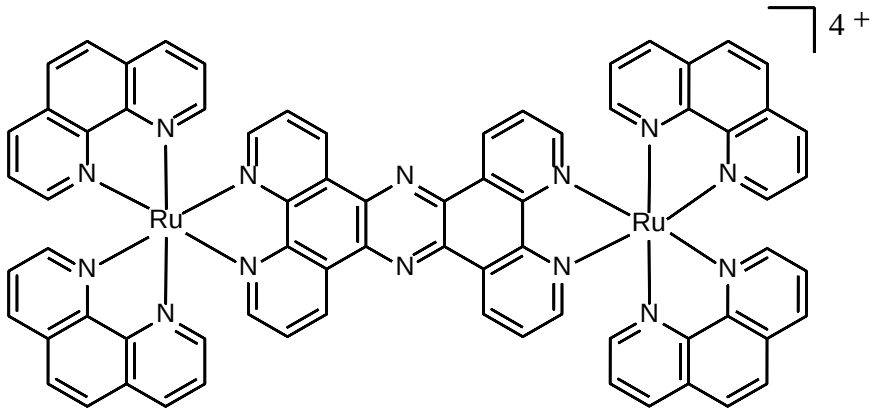

Figure 13. Molecular structure of an example ruthenium (II) complex, diruthenium, tetrakis(1,10-phenanthroline-κ*N*^{1},κ*N*^{10})[μ-(tetrapyrido[3,2-*a*:2',3'-*c*:3'',2''-*h*:2''',3'''-*j*]phenazine-κ*N*^{4},κ*N*^{5}:κ*N*^{13},κ*N*^{14})] used in TEM.[90]

Another dinulear ruthenium (II) complex, structurally very similar to the ones mentioned above, was reported recently that was observed to localise in the endoplasmic reticulum of MCF-7 cells by confocal microscopy.[93] Interestingly, the contrast enhancement in the TEM mircographs was found

not only to occur in the endoplasmic reticulum but also the nucleus and mitochondria of cells as seen in figure 12.

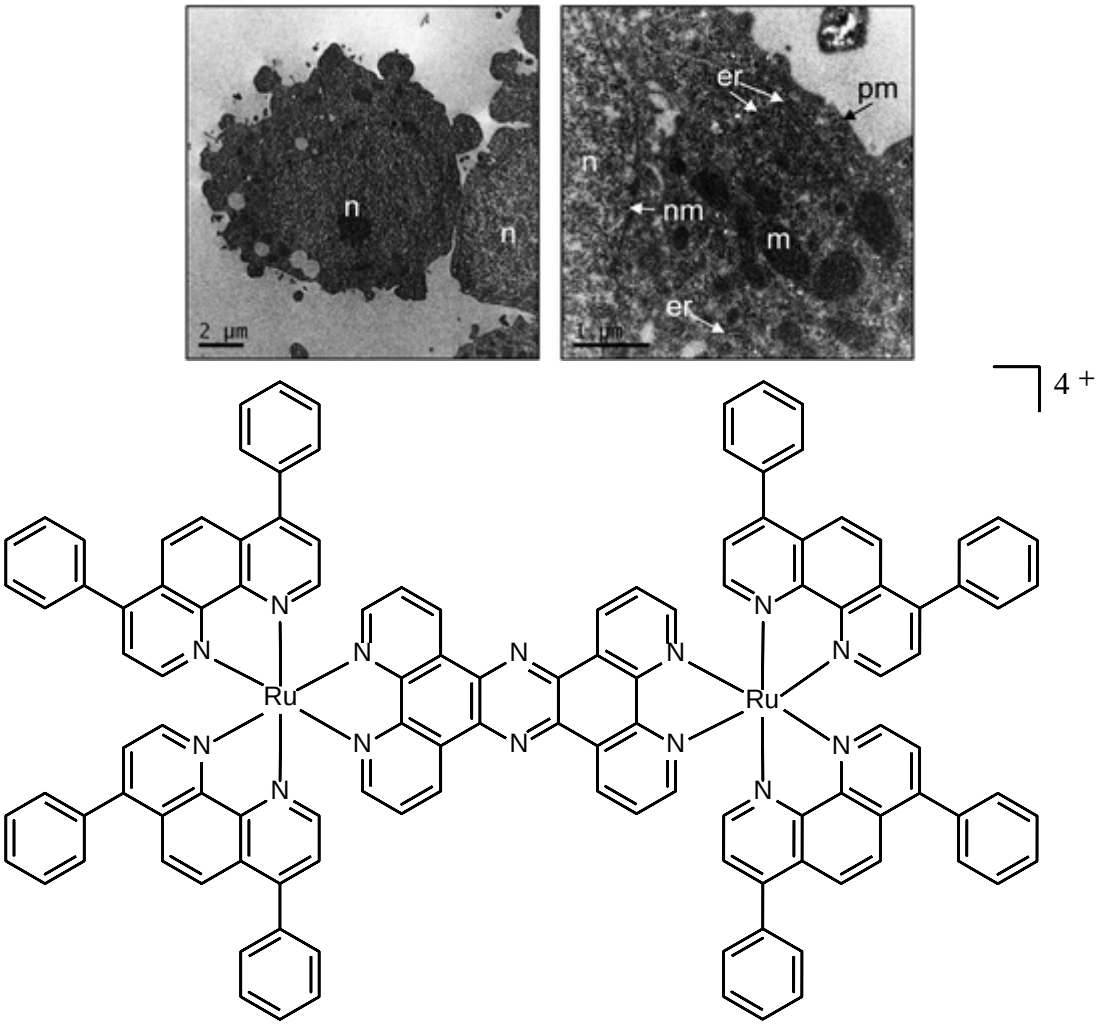

Figure 14. TEM micrograph of HeLa cells stained with a dinuclear ruthenium complex(top) and the molecular structure of the ruthenium (II) complex (bottom). Labeling: n = nucleus, nm = nuclear membrane, er = endoplasmic reticulum, m = mitochondria, pm = plasma membrane. Adapted from ref.[93]

A mononuclear platinum (II) complex which has been reported as a potential anti-cancer agent has also been observed to provide contrast in TEM.[94] The complex was suggested to predominately stain the lysosomes, however the Pearson's coefficient of 0.33 for co-staining against Lysotracker yellow does not provide a very high level of confidence in the assertion. TEM micrographs were reported showing some contrast enhancement in vesicles within cells identified as lysosomes.

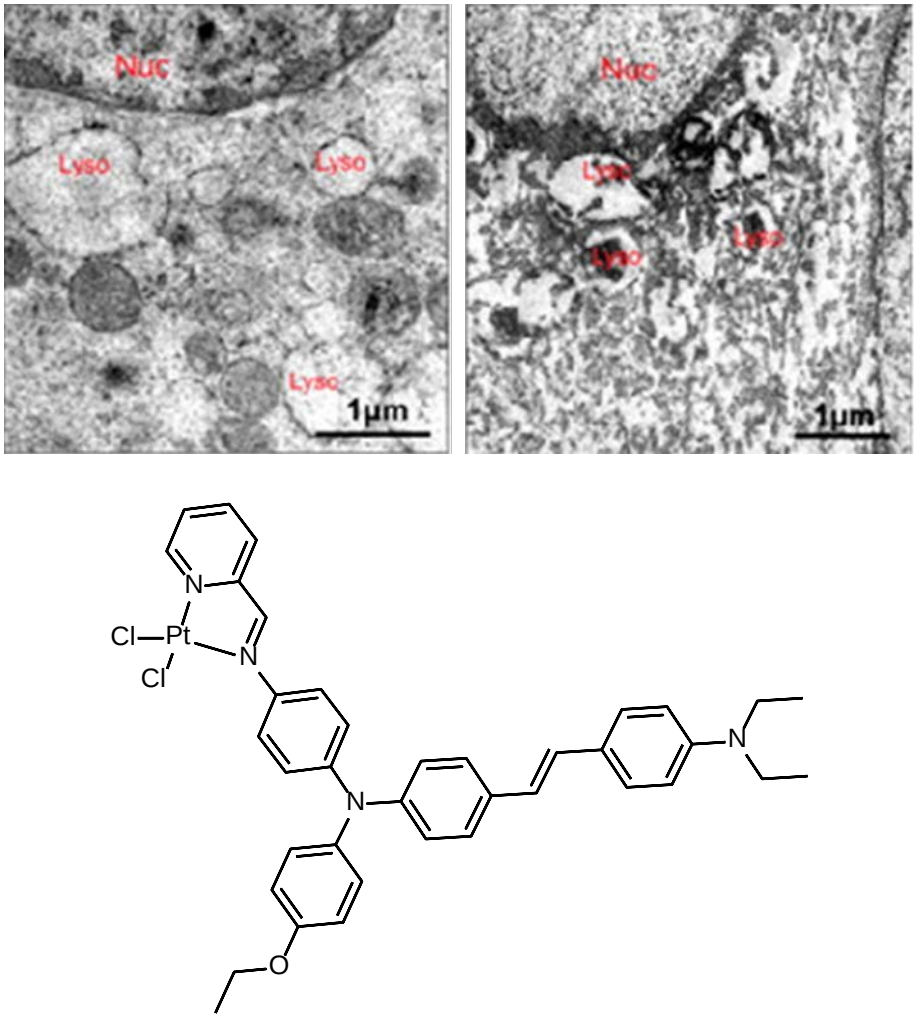

Figure 15. TEM micrographs of cells stained with typical and TEM contrast egents (top left) and platinum (II) complex (top right); Molecular structure of platinum (II) complex. Labels: Nuc = nucleus, Lyso = lysosomes. Adapted from ref.[94]

1.8 Summary

Microscopy has revolutionised our understanding of biology, with steady technical improvements allowing ever increasing scrutiny of biological systems on a microscopic scale and beyond. With further developments currently being explored the resolution limit of optical microscopes is quickly becoming a thing of the past as super resolution microscopes improve the limits of resolution attainable. However, with these new techniques comes a range of new requirements and many of these fall to the luminescence probes that allow researchers to follow single proteins or highlight specific compartments with cells. Development of new probes for super resolution microscopy is still ongoing and a diverse range of probes for different applications is still in dire need.

Electron microscopy has for over seventy years been providing biologists with some of the highest resolution information on samples and while also providing ultrastructural data. However, the main

drawback has been the inability to perform EM on live cells and therefore not having the ability to watch dynamic processes at the improved resolution. CLEM has developed one of the answers to this age old problem, with the utilisation of cutting edge technical developments and the development of probes for this specific application. However, as with advent of super resolution microscopy, CLEM probes have a number of specific requirements that must be met for a probe to be considered useful for application. Also the complex nature of CLEM methodologies, which endeavour to maintain biological relevance in samples while preparing them to be viewed across multiples microscope, means that single probes typically only perform well in certain applications. While a number of ingenious probes have been developed for CLEM the need for versatile and easy to use CLEM probes is a goal that has yet to be fully realised.

1.9 References

1 A. Van Helden, *The Origins of the Telescope. History of science and scholarship in the Netherlands*, KNAW Press, Amsterdam, 2010.

2 M. Fernández-Suárez and A. Ting, *Nat. Rev. Mol. Cell Biol.*, 2008, **9**, 929–943.

3 L. W. Sharp, *Introduction To Cytology*, McGraw Hill Book Company Inc, New York, 1921.

4 C. Guy, *Optical Imaging Techniques in Cell Biology*, CRC Press, Second Edi., 2012.

5 E. Abbe, *J. R. Microsc. Soc.*, 1883, **3**, 790–812.

6 M. Born and E. Wolf, *Principles of Optics : electromagnetic theory of propagation, interference and diffraction of light*, Cambridge University Press, Cambridge, 7th Editio., 1999.

7 P. W. Atkins, *Atkins' Phyiscal chemistry*, New York : Oxford University Press, Oxford, 10th Editi., 2014.

8 E. Baggaley, J. A. Weinstein and J. A. G. Williams, in *Luminescent and Photoactive Transition Metal Complexes as Biomolecular Probes and Cellular Reagents*, ed. K. K.-W. Lo, Heidelberg: Springer, Berlin, 165th edn., 2015, pp. 205–256.

9 M. P. Coogan and V. Fernández-Moreira, *Chem. Commun.*, 2014, **50**, 384–99.

10 J. S. Verdaasdonk, A. D. Stephens, J. Haase and K. Bloom, *J. Cell. Physiol.*, 2014, **229**, 132–138.

11 M. Minsky, *US Pat. 3013467*, 1957, **3013467**, 5.

12 M. Gu and C. J. R. Sheppard, *J. Opt. Soc. Am. A*, 1992, **153**, 1992.

13 K. W. Dunn, M. M. Kamocka and J. H. McDonald, *Am. J. Physiol. Cell Physiol.*, 2011, **300**, C723–C742.

14 E. M. M. Manders, J. Stap, G. J. Brakenhoff, R. Van Driel and A. Aten, *J. Cell Sci.*, 1992, **103**, 857–862.

15 E. M. M. Manders, F. J. Verbeek and J. A. Ate, *J. Microsc.*, 1993, 169, 375–382.

16 M. Pawlicki, H. A. Collins, R. G. Denning and H. L. Anderson, *Angew. Chemie - Int. Ed.*, 2009, **48**, 3244–3266.

17 W. Denk, J. H. Strickler and W. W. Webb, *Science*, 1990, **248**, 73–6.

18 T. G. Phan and A. Bullen, *Immunol. Cell Biol.*, 2010, **88**, 438–444.

19 G. S. He, L. S. Tan, Q. Zheng and P. N. Prasad, *Chem. Rev.*, 2008, **108**, 1245–1330.

20 N. S. Makarov, M. Drobizhev and A. Rebane, *Opt. Express*, 2008, **16**, 4029–4047.

21 S. Alexander, G. E. Koehl, M. Hirschberg, E. K. Geissler and P. Friedl, *Histochem. Cell Biol.*, 2008, **130**, 1147–1154.

22 T. Hato, S. Winfree and P. C. Dagher, *Methods*, 2017, **128**, 33–39.

23 M. B. Carneiro, L. S. Hohman, J. G. Egen and N. C. Peters, *Methods*, 2017, **127**, 45–52.

24 J. A. Coles, E. Myburgh, J. M. Brewer and P. G. McMenamin, *Prog. Neurobiol.*, 2017, **156**, 107–148.

25 K. Svoboda and R. Yasuda, *Neuron*, 2006, **50**, 823–839.

26 K. Bourzac, *Nature*, 2015, **526**, 50–54.

27 L. Schermelleh, R. Heintzmann and H. Leonhardt, *J. Cell Biol.*, 2010, **190**, 165–175.

28 S. W. Hell and J. Wichmann, *Opt. Lett.*, 1994, **19**, 780–2.

29 H. Blom and J. Widengren, *Curr. Opin. Chem. Biol.*, 2014, **20**, 127–133.

30 E. Betzig, G. H. Patterson, R. Sougrat, O. W. Lindwasser, S. Olenych, J. S. Bonifacino, M. W. Davidson, J. Lippincott-Schwartz and H. F. Hess, *Science*, 2006, **313**, 1642–1645.

31 S. T. Hess, T. P. K. Girirajan and M. D. Mason, *Biophys. J.*, 2006, **91**, 4258–4272.

32 M. Rust, M. Bates and X. Zhuang, *Nat. Methods*, 2006, **3**, 2006.

33 J. Vogelsang, R. Kasper, C. Steinhauer, B. Person, M. Heilemann, M. Sauer and P. Tinnefeld, *Angew. Chemie - Int. Ed.*, 2008, **47**, 5465–5469.

34 D. Baddeley, I. D. Jayasinghe, C. Cremer, M. B. Cannell and C. Soeller, *Biophysj*, 2009, **96**, L22–L24.

35 N. Olivier, D. Keller, V. S. Rajan, G. Pierre and S. Manley, *Biomed. Opt. Express*, 2013, **4**, 16840–16841.

36 S. Manley, N. Olivier, D. Keller and P. Go, *PLoS One*, 2013, **8**, 1–9.

37 B. Turkowyd, D. Virant and U. Endesfelder, *Anal. Bioanal. Chem.*, 2016, **408**, 6885–6911.

38 M. Sauer, *J. Cell Sci.*, 2013, **126**, 3505–13.

39 N. Durisic, L. L. Cuervo and M. Lakadamyali, *Curr. Opin. Chem. Biol.*, 2014, **20**, 22–28.

40 M. G. L. Gustafsson, *J. Microsc.*, 2000, **198(pt. 2)**, 82–87.

41 M. G. L. Gustafsson, *PNAS*, 2005, **102**, 13081–13086.

42 M. G. L. Gustafsson, L. Shao, P. M. Carlton, C. J. R. Wang, I. N. Golubovskaya, W. Z. Cande,

D. A. Agard and J. W. Sedat, *Biophys. J.*, 2008, **94**, 4957–4970.

43 L. Schermelleh, P. M. Carlton, S. Haase, L. Shao, L. Winoto, P. Kner, B. Burke, M. C. Cardoso, D. A. Agard, M. G. L. Gustafsson, H. Leonhardt and J. W. Sedat, *Science*, 2008, **320**, 1332–1336.

44 D. Li, L. Shao, B.-C. Chen, X. Zhang, M. Zhang, B. Moses, D. E. Milkie, J. R. Beach, J. A. Hammer, M. Pasham, T. Kirchhausen, M. A. Baird, M. W. Davidson, P. Xu and E. Betzig, *Science (80-.).*, 2015, **349**, 944.

45 I. Johnson and M. T. Z. Spence, Eds., *The Molecular Probes handbook. A guide to fluorescent probes and labeling technologies*, Life Technologies, 11th edn., 2010.

46 R. Y. Tsien, *Annu. Rev. Biochem.*, 1998, **67**, 509–544.

47 B. N. G. Giepmans, S. R. Adams, M. H. Ellisman and R. Y. Tsien, *Science (80-.).*, 2006, **312**, 217–224.

48 M. A. Hayat, *Principles and techniques of electron microscopy : biological applications*, Cambridge University Press, Cambridge, 4th editio., 2000.

49 M. L. Watson, *J. Cell Biol.*, 1958, **4**, 475–478.

50 J. H. VENABLE and R. COGGESHALL, *J. Cell Biol.*, 1965, **25**, 407–408.

51 B. Y. G. E. Palade, *J. Exp. Med.*, 1952, **95**, 285–298.

52 E. S. REYNOLDS, *J. Cell Biol.*, 1963, **17**, 208–212.

53 E. I. Christensen and a B. Maunsbach, *Kidney Int.*, 1979, **16**, 301–311.

54 C. E. Sarraf, in *Diagnostic and Therapeutic Antibodies.*, eds. A. J. T. George and C. E. Urch, Humana Press, Totowa, 2000, pp. 439–452.

55 U. Schnell, F. Dijk, K. A. Sjollema and B. N. G. Giepmans, *Nat. Methods*, 2012, **9**, 152–158.

56 R. Reichelt, in *Science of Microscopy*, eds. P. W. Hawkes and J. C. H. Spence, Springer, New York, 2007, pp. 133–272.

57 K. Hellström, H. Vihinen, K. Kallio, E. Jokitalo and T. Ahola, *Methods*, 2015, **90**, 49–56.

58 O. Avinoam, M. Schorb, C. J. Beese, J. A. G. Briggs and M. Kaksonen, *Science*, 2015, **348**, 1369–72.

59 V. Krieger, D. Liebl, Y. Zhang, R. Rajashekar, P. Chlanda, K. Giesker, D. Chikkaballi and M. Hensel, *PLoS Pathog.*, 2014, **10**, e1004374.

60 S. M. Markert, S. Britz, S. Proppert, M. Lang, D. Witvliet, B. Mulcahy, M. Sauer, M. Zhen, J.-L. Bessereau and C. Stigloher, *Neurophotonics*, 2016, **3**, 41802.

61 P. De Boer, J. P. Hoogenboom and B. N. G. Giepmans, *Nat. Methods*, 2015, **12**, 503–513.

62 B. N. G. Giepmans, T. J. Deerinck, B. L. Smarr, Y. Z. Jones and M. H. Ellisman, *Nat. Methods*, 2005, **2**, 743–9.

63 A. E. Weston, H. E. J. Armer and L. M. Collinson, *J. Chem. Biol.*, 2009, **3**, 101–12.

64 C. L. Schwartz, V. I. Sarbash, F. I. Ataullakhanov, J. R. McIntosh and D. Nicastro, *J. Microsc.*, 2007, **227**, 98–109.

65 A. Sartori, R. Gatz, F. Beck, A. Rigort, W. Baumeister and J. M. Plitzko, *J. Struct. Biol.*, 2007, **160**, 135–145.

66 P. Verkade, *J. Microsc.*, 2008, **230**, 317–28.

67 J. M. Plitzko, A. Rigort and A. Leis, *Curr. Opin. Biotechnol.*, 2009, **20**, 83–9.

68 A. C. Zonnevylle, R. F. C. Van Tol, N. Liv, A. C. Narvaez, A. P. J. Effting, P. Kruit and J. P. Hoogenboom, *J. Microsc.*, 2013, **252**, 58–70.

69 H. Iijima, Y. Fukuda, Y. Arai, S. Terakawa, N. Yamamoto and K. Nagayama, *J. Struct. Biol.*, 2014, **185**, 107–15.

70 R. S. Polishchuk, E. V Polishchuk, P. Marra, S. Alberti, R. Buccione, A. Luini and A. A. Mironov, *J. Cell Biol.*, 2000, **148**, 45–58.

71 B. N. G. Giepmans, *Histochem. Cell Biol.*, 2008, **130**, 211–7.

72 J. M. Robinson and T. Takizawa, *J. Microsc.*, 2009, **235**, 259–72.

73 M. R. Romano L Egidio, *Immunochemistry*, 1977, **14**, 711–715.

74 J. W. Slot and H. J. Geuze, *J. Cell Biol.*, 1981, **90**, 533–6.

75 I. Kandela, D. Meyer, P. Oshel, E. Rosa-Molinar and R. Albrecht, *Microsc. Microanal.*, 2003, **9**, 1194–1195.

76 I. K. Kandela and R. M. Albrecht, *Scanning*, 2007, **29**, 152–61.

77 D. Shenoy, W. Fu, J. Li, C. Crasto, G. Jones, C. DiMarzio, S. Sridhar and M. Amiji, *Int. J. Nanomedicine*, 2006, **1**, 51–7.

78 J. Hainfeld, *Science (80-.).*, 1987, **236**, 450–453.

79 J. F. Hainfeld and F. R. Furuya, *J. Histochem. Cytochem.*, 1992, **40**, 177–184.

80 R. D. Powell, C. M. R. Halsey, D. L. Spector, S. L. Kaurin, J. McCann and J. F. Hainfeld, *J. Histochem. Cytochem.*, 1997, **45**, 947–956.

81 R. D. Powell, C. M. Halsey and J. F. Hainfeld, *Microsc. Res. Tech.*, 1998, **42**, 2–12.

82 J. F. Hainfeld and R. D. Powell, *J. Histochem. Cytochem.*, 2000, **48**, 471–480.

83 B. T. Miles, A. B. Greenwood, D. Benito-Alifonso, H. Tanner, M. C. Galan, P. Verkade and H. Gersen, *Sci. Rep.*, 2017, **7**, 1–7.

84 A. P. Alivisatos, W. Gu and C. Larabell, *Annu. Rev. Biomed. Eng.*, 2005, **7**, 55–76.

85 E. Brown and P. Verkade, *Protoplasma*, 2010, **244**, 91–7.

86 T. J. Deerinck, B. N. G. Giepmans, B. L. Smarr, M. E. Martone and M. H. Ellisman, *Methods Mol. Biol.*, 2007, **374**, 43–53.

87 M. J. Saxton and K. Jacobson, *Annu. Rev. Biophys. Biomol. Struct.*, 2003, **26**, 373–399.

88 T. Q. Vu, W. Y. Lam, E. W. Hatch and D. S. Lidke, *Cell Tissue Res.*, 2015, 71–86.

89 E. Baggaley, J. A. Weinstein and J. A. G. Williams, *Coord. Chem. Rev.*, 2012, **256**, 1762–1785.

90 M. R. Gill, J. Garcia-Lara, S. J. Foster, C. Smythe, G. Battaglia and J. A. Thomas, *Nat. Chem.*, 2009, **1**, 662–7.

91 X. Tian, M. R. Gill, I. Cantón, J. A. Thomas and G. Battaglia, *Chembiochem*, 2011, **12**, 548–51.

92 M. R. Gill, H. Derrat, C. G. W. Smythe, G. Battaglia and J. A. Thomas, *ChemBioChem*, 2011, **12**, 877–880.

93 M. R. Gill, D. Cecchin, M. G. Walker, R. S. Mulla, G. Battaglia, C. Smythe and J. A. Thomas, *Chem. Sci.*, 2013, **4**, 4512–4519.

94 Q. Zhang, X. Tian, G. Hu, P. Shi, J. Wu, S. Li, H. Zhou, B. Jin, J. Yang, S. Zhang and Y. Tian, *Biochemistry*, 2015, **54**, 2177–2180.

Chapter 2: Transition Metal Complexes as Probes for Cell Imaging

2.1 Introduction

As described in Chapter 1, innovation in microscopy has driven discoveries for centuries but equally important to the development in microscopy is the progress in new and improved probes. Ideally these probes should allow the imaging of live systems with minimal perturbation. However, there are more criteria required of a molecule to be considered for a use as a bioimaging probe. Principally, High quantum yields are highly desirable as samples will not have to be irradiated as heavily, reducing phototoxicity and avoiding photobleaching. Probes should also be photostable under excitation and chemically stable under physiological conditions. The Stoke's shift of a probe should also be large enough to easily differentiate the excitation beam from the emission of the probe, otherwise crosstalk can become an issue. The final set of criteria concern the use of the probe in cells. The probe should exhibit good water solubility, as water is the solvent of life and any other solvents used to help with solubility can have adverse effect on cells. The probe should also display good cell penetration and low cytotoxicity.

These criteria reflect the properties an ideal luminescence molecule would possess but some of the requirements are more flexible depending on the intended use of the probe. For instance, some probes are designed as a "pro-probe" form which undergo chemical reactions within the cell to specifically label or accumulate in areas of interest. This would violate the chemical stability criteria but in an intended fashion. Further criteria can also come into play depending on the types of microscopy the probe is intended for. For example, photoactivation localisation microscopy (PALM) and stochastic optical reconstruction microscopy (STORM) require photo switchable and photoactivatable probes respectively, allowing them to achieve much higher levels of resolution by artificially reducing the point spread function of individual molecules that are localised frame by frame.

2.2 Luminescent Transition Metal Complexes as Probes

Metal complexes have many properties which make them stand out as potential bioimaging agents.[1–3] Transition Metal complex exhibit photophysical properties well suited to bioimaging, the most important of which is, in contrast to organic molecules, their emissive state is a triplet state, and consequently metal complexes phosphoresce and (usually) not fluoresce (Figure 2.). One of key differences for excited states in transition metal complexes arises from the heavy atom effect. This

effect is present in systems where the metal participates in the electronic transition, utilising the metals high spin-orbit coupling constant. This high spin orbit coupling accelerates intersystem crossing of the singlet excited state to the triplet state. The relaxation of the triplet state to the ground state, a formally forbidden transition, is also facilitated by this effect. This leads to long lifetimes of phosphorescence of tens of nanoseconds to microseconds compared to nanosecond for organic probes. It should be noted that, contrary to some statements in the literature, long lifetimes are not generally desirable for bio-imaging applications as this reduces the number of photons emitted per second and therefore the "brightness" of the probes. Longer lifetimes are predominately useful for either time gating (which only requires lifetimes > 50 ns) or molecules intended for time resolved applications where changes in lifetime are required to be accurately detected and longer lifetimes offer a larger range of change.

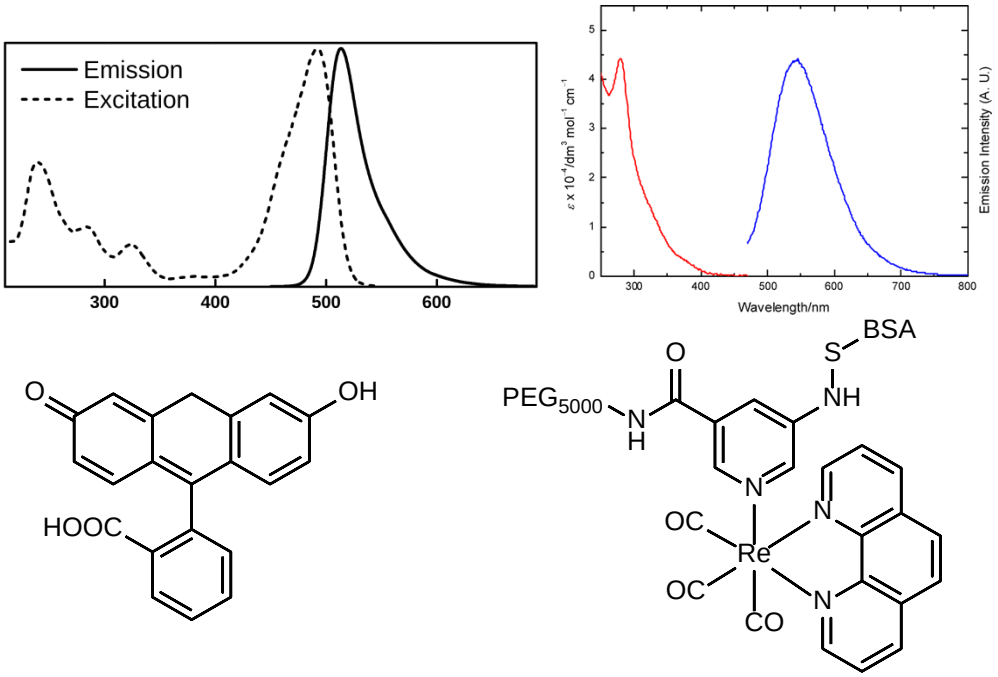

Figure 1. Absorption and emission spectra of fluorescein and the molecular structure (left) and an absorption (red) and emission (blue) spectra and molecular structure of a rhenium (I) phenathroline tricarbonyl complex (right). (BSA = Bovine serum albumin) Adapted from ref[4]

Transition metal complexes exhibit a number of different transitions they can undergo that lead to luminescence, this is due to a number of energetic states being very close in transition metal complexes. These transitions are described based on their electronic transition configuration including: metal centred (MC), ligand centred (LC), metal-to-ligand charge transfer (MLCT), ligand-to-metal charge transfer (LMCT) and ligand-to-ligand or intraligand charge transfer (LLCT or ILCT).[5] Due to the presence of the metal atom in these complexes providing a large spin-orbit coupling, the excited states described almost invariably lead to triplet excited states due to fast

intersystem crossing. A consequence of this is the large Stoke's shift observed in most transition metal complexes.

Metal complexes often exhibit high quantum yields, an imperative for a bioimaging. Furthermore, due to the HOMO and LUMO being located on discreet parts of the molecule, it is possible to colour tuning metal complexes rationally. Conversely, many organic probes are more limited in the tuning of the emission colour due to synthetic limitations. Moreover, the emission wavelength of metal complexes is typically spectrally distinct from the excitation wavelength used as seen in Figure 1, allowing for clear observation of emission. In contrast to organic molecules, which generally have small Stoke's shifts with excitation and emission spectra often overlapping as shown in Figure 3. The difference in excitation and emission also helps to avoids self-quenching through re-absorption by neighbouring luminophores.

2.2.1 Toxicity of Metal Complexes

Even before the discovery of cisplatin, metal containing compounds have been known to be often cytotoxic and this has fuelled the development of complexes for therapeutic applications such as anti-cancer agents[6–9] among others.[10] However, as with all compounds toxicity is concentration dependant and many complexes do not exhibit toxicity at the concentrations used for bioimaging. The general method of assessing toxicity of a probe is via a MTT (3-(4,5-dimethylthiazol-2-yl)-2,5-diphenyltetrazolium bromide) tetrazolium reduction assay which was developed as a homogeneous cell viability for high throughput screening. The MTT is actively converted by viable cells into formazan as shown in Scheme 1, which forms and insoluble precipitate which can be solubilised in DMSO or other organic solvents and the absorbance measured.

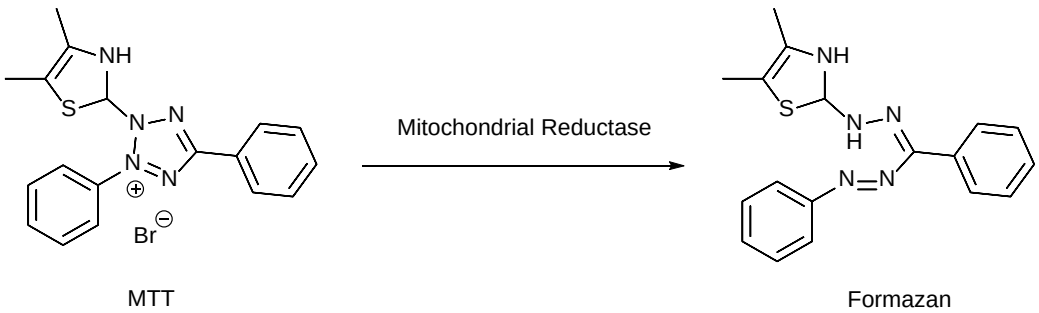

Scheme 1. Reaction scheme of MTT being converted to Formazan.[11]

Some of the complex described below have been proposed as potential anti-cancer agents due to their cytotoxicity but have been included as they offer an interesting insight into the factors that affect localisation of metal complexes *in vitro*.

2.3 Localisation of Metal Complexes

There are a myriad of factors which affect the cellular uptake of any compound. The size[12], charge[13,14], lipophilicity[15] and functional groups present[16,17] all have an effect on the ability of metal complexes to permeate the cell membrane. There are multiple uptake pathways into the cell and these can be categorised in to energy dependant processes, such as endocytosis and energy independent processes, such as passive and facilitated diffusion. The process by which a probe gains entry can have implications for the final destination of the probe. If the probe is taken up by a process like endocytosis then it is likely to be trafficked by the cell to specific locations such as the endosomal system unless the probe can escape the vesicle.[18] Conversely, if the probe enters via diffusion based mechanism, the probe is likely to stain less specifically and accumulate depending on the affinity of the probe to a specific chemical environment. Another factor that has been shown to affect the localisation of molecules into cells is the presences of serum albumin in the media whilst staining is occurring; it is thought that many complexes bind to the large protein and this affects bioavailability and uptake mechnisms.[19–21]

Once inside the cell many of the characteristic highlighted above influence the localisation and accumulation of metal complexes. As mentioned above, specific localisation of a probe is a desirable characteristic and efforts to achieve this vary in approach. One method utilized to achieve specificity involves using functional groups which will react with a specific functional group present within the cell to form a covalent bond.[22] The probe should then accumulate in specific locations rich with the functional group targeted. Another method aims to design the probe so as to mimics the molecules present in an area of interest so that the cell will incorporate it there.[23] Finally, another approach looks to utilise cell penetrating peptides (CPP), short chains of specifically ordered amino acids which are identified by the cell and trafficked to specific locations, allowing compounds which might not usually enter cells to obtain entry and specific localisation.[24,25]

2.3.1 Nucleus

The cell nucleus is a double membrane bound organelle that houses the information essential for the replication of a cell, DNA in the form of chromatin. DNA bound in a nucleus is isolated from the rest of the cell by the nuclear envelope, which is a double membrane with nuclear pores that regulate the transportation of large molecules across the membrane. This is one of the key distinctions between eukaryotic and prokaryotic life and this creates a more complex barrier to entry than the plasma membrane, causing far fewer complexes to localise in the nucleus. The genetic material contained within the nucleus codes for the vast majority of proteins present within the cell and the nucleus is dynamic, regulating the expression of different proteins depending on environmental factor, point in the cell cycle and other factors. Nuclear targeting probes are often simply used to mark each cell as

distinct entities; however these probes can provide information about the dynamics of the cells and provide information about the health and position in the cell cycle of cells.

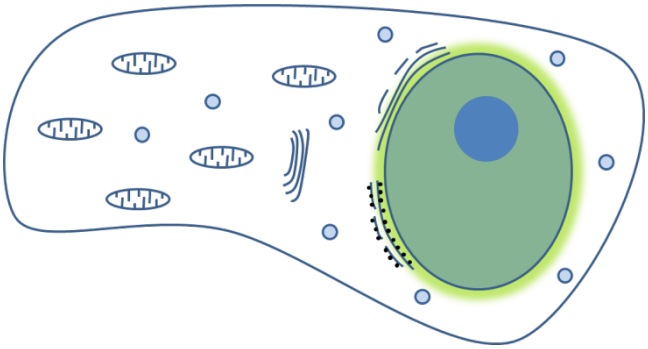

Figure 2. Simplified depiction of a typical eukaryotic cell with its nucleus labelled in green.

Much of the literature on metal complex that stain the nucleus are focused on ruthenium (II) polypyridyl complexes, as they often display the advantageous property of the light switch effect and high affinity for binding DNA.[26] This light switch effect is caused by the quenching of the excited state by hydrogen bonding in solution, which then becomes luminescent when the complex is protected from the solution. It is characterised by the substantial increase in luminescence of these types complexes once bound to DNA.[27,28] Initially this work was primarily done in solutions, with purely photophysical studies characterising the effect of isolated strands of DNA on the photophysics and DNA binding of the complexes.[29] Early experiments performed in cells reported that light switch ruthenium (II) polypyridyls complexes did not stain the nucleus of cells, instead cytoplasmic staining was observed.[21,30] The observed signal was likely mitochondrial due to light switch effect and mitochondria being the primary place outside of the nucleus where DNA is present. However, after these initial results ruthenium (II) complexes which permeated the nucleus started to be reported with Musatkine *et al.* and Gill *et al.* reporting a mono nuclear, ruthenium di(4,7-diphenyl-1,10-phenanthroline) 4,40-dicarboxy-2,20-bipyridine and a dinuclear ruthenium (II) complex, di[ruthenium di(1,10-phenanthroline)] μ-tetrapyrido[3,2-a:20,30-c:300,200-h:2000,3000-j]phenazine which stained the nuclei of cells respectively.[31,32]

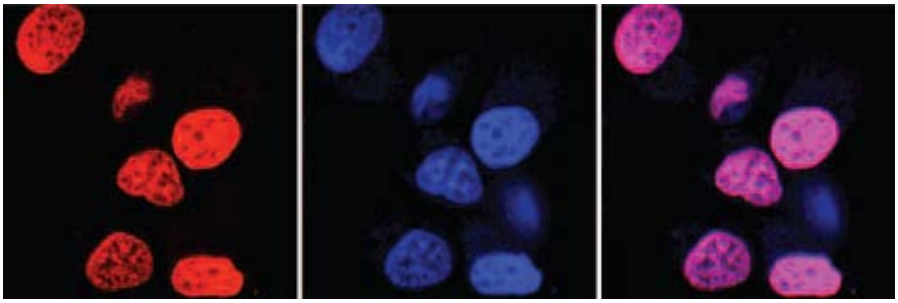

Figure 3. LSCM images of MCF-7 cells stained with the ruthenium (II) polypyridyl complex (emission left) and DAPI (emission centre) with the channels overlaid to show colocalisation(right). Adapted from ref.[32]

Further work by Puckett *et al.* with these types of complexes was combined with that of cell penetrating peptides (CPP), short sequences of amino acids that have been shown to facilitate access in to cell, in an effort to direct these complexes into cells in a designed and desired fashion. A CPP, octaarginine, along with fluorescein was found to direct the localisation of a ruthenium (II) dipyrido-[3,2-a:20,30-c]-phenazine(dppz) polypyridyl to the nucleus and nucleoli of cells.[33] Whereas the complex with only the CPP or fluorescein present only stained the cytoplasm of cells. It was noted however, that these staining patterns were different to that seen of the parent complex. Higher concentrations of the octaarginine complex were found to start localising within the nucleus and this was attributed to the introduction of a competing non-endocytic uptake mechanism.

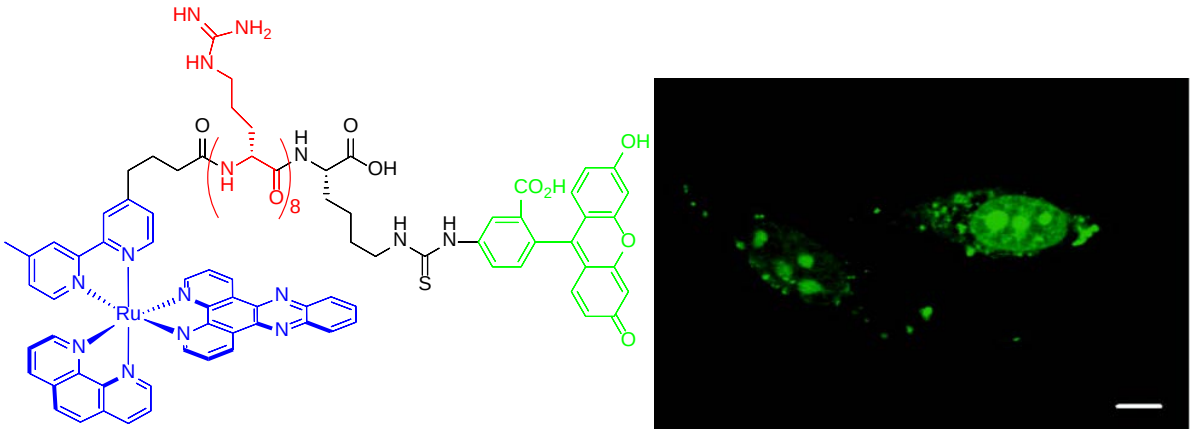

Figure 4. Molecular structure of ruthenium (II) dppz (blue) conjugated to octaagrenine (red) and fluorescein(green)(left) and a LSCM micrograph of HeLa cells treated with the complex.

Further investigation was conducted by these researchers using related complexes, again utilising CPP to aid penetration of these complexes into the cells. It was found that nuclear staining could be achieved by using smaller peptide chain of the nuclear targeting signal RrRK.[34] Curiously, it was also shown that these complexes displayed concentration dependant localisation too, while lower concentrations displayed punctate staining seen in previously reported complexes, at higher concentrations nuclear staining was observed. Changes in incubations time did not affect the localisation of the complex, symptomatic of a change in uptake mechanism that affects the localisation of the complex. Another interesting observation was the affect that serum albumin was

found to have on localisation of the complex. In the absence of serum albumin, much lower concentrations of complex were needed for localisation in the nucleus, suggesting that the complex bound to the large protein, changing it uptake mechanism and localisation. This was further corroborated by another study which found there was a 25-fold increase in complex uptake in serum free incubation vs serum present in the incubation media.[21]

Work by Cosgrave *et al.* found that, in contrast to the work done by Puckett *et al.* that ruthenium (II) polypyridyl complexes could utilize octaarginine peptides to aid in cell penetration while still achieving nuclear localisation by using dppz ligands in place of the 1,10 phenathroline(phen) or bipyridine(bipy) ligands used in previous studies(Fig. 5).[35] Staining with the parent complex was found to only stain the plasma membrane, while staining with the octaarginine conjugate lead to the complex entering cells and staining the nucleus.

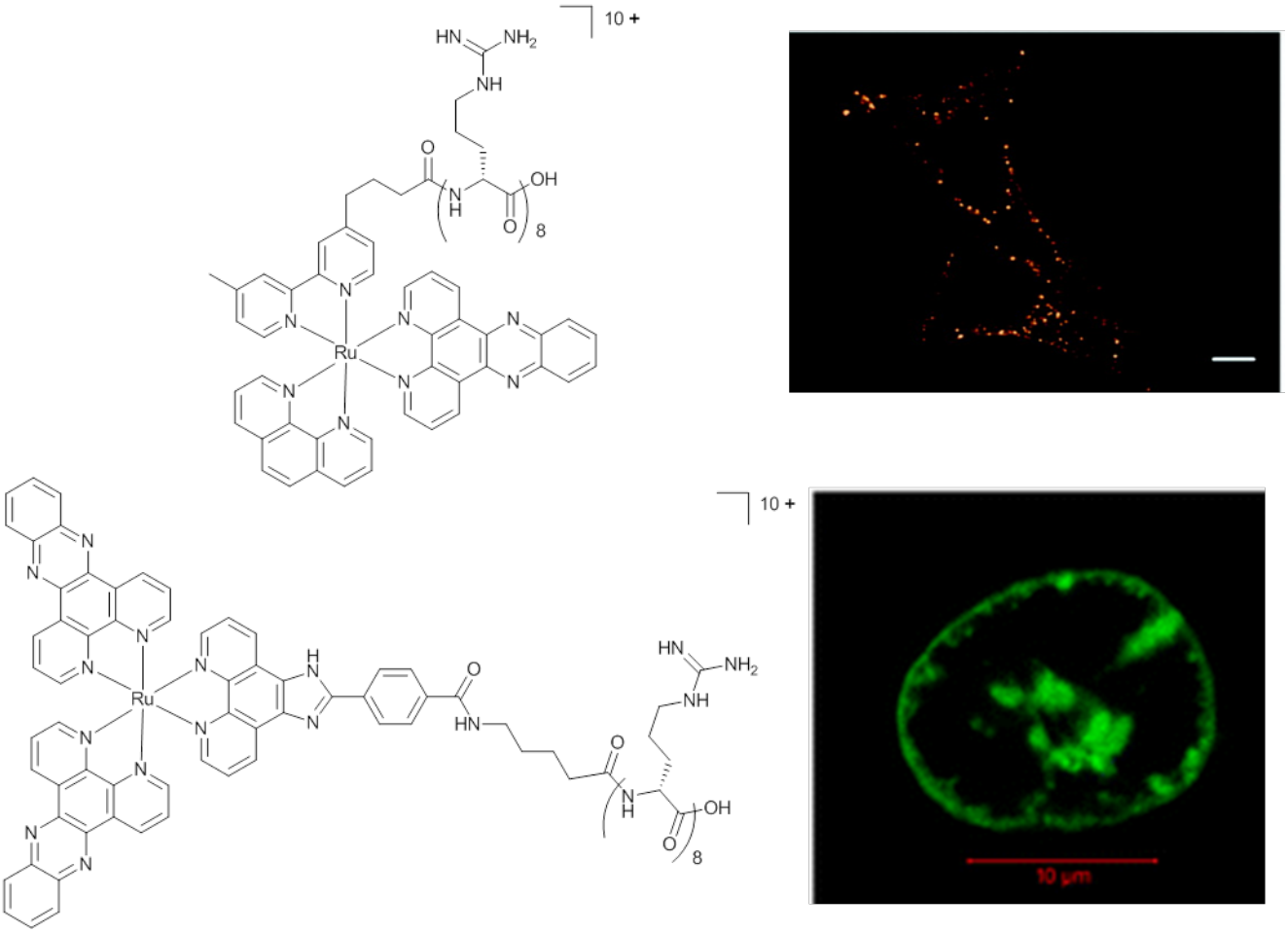

Figure 5. Molecular structure of Ru – D-R8 and the punctate staining pattern observed in HeLa cells (top), molecular structure of [Ru(dppz)2PIC-Arg8]$^{10+}$ and the nuclear staining pattern observed in SP2 myeloma cells. Images adapted from ref.[33,35]

Further developments were reported by Gill e*t al.* utilizing two ruthenium (II) polypyridyl complex using a tetrapyrido[3,2-a:2’,3’-c:3’’,2’’-h:2’’’,3’’’-j]phenazine (tppz) ligand in place of dppz.[36] The

complexes were observed to bind strongly to DNA in solution via an intercalation binding mode and were found to enter MCF-7 cells without the need for any aid from CPP. The complex was shown to accumulate heavily in the nucleus of these cells, confirmed by DAPI (a commercial nucleus stain) co-staining and some diffuse cytoplasmic staining was also observed. Low temperature incubations indicated that the complexes were actively taken up by the cells. The dinuclear mixed metal ruthenium (II)-Iridium (III) complex of the tppz has also been shown to bind strong to DNA, enter cells readily and stain the nucleus of cells.[37]

More recently, ruthenium (II) polypyriyl complexes $[Ru(dpp)_2PIC\text{-}\beta Ala\text{-}NF\text{-}\kappa B]^{6+}$ and $[Ru(bpy)_2PIC\text{-}\beta Ala\text{-}NF\text{-}\kappa B]^{6+}$ that the parent complex had previously been found to not enter cells in purely aqueous media have been shown to enter cells more readily by use of another CPP, nuclear localisation signal NF-κB.[38] The first of these complexes was found to co-localise well with DAPI in the nucleus, whereas the second related complex was observed to stain the nucleoli instead of the nucleus.

The exact binding modes of these ruthenium (II) polypyridyl complexes to DNA have been of interest since the discovery of their DNA binding, as there have been a number of different binding modes observed by different binders. Depending on the charge and ligands present in the complex, multiple binding modes are possible with most being noncovalent for ruthenium (II) polypyridyls.[26] Barton *et al.* have found that large ruthenium (II) complexes containing dppz ligands can discern mismatches in DNA[39] and RNA[40] by changing binding mode in these mismatched sequences(Fig 6.). These mismatches are of particular interest due to their implications and prevalence in cancerous cells.

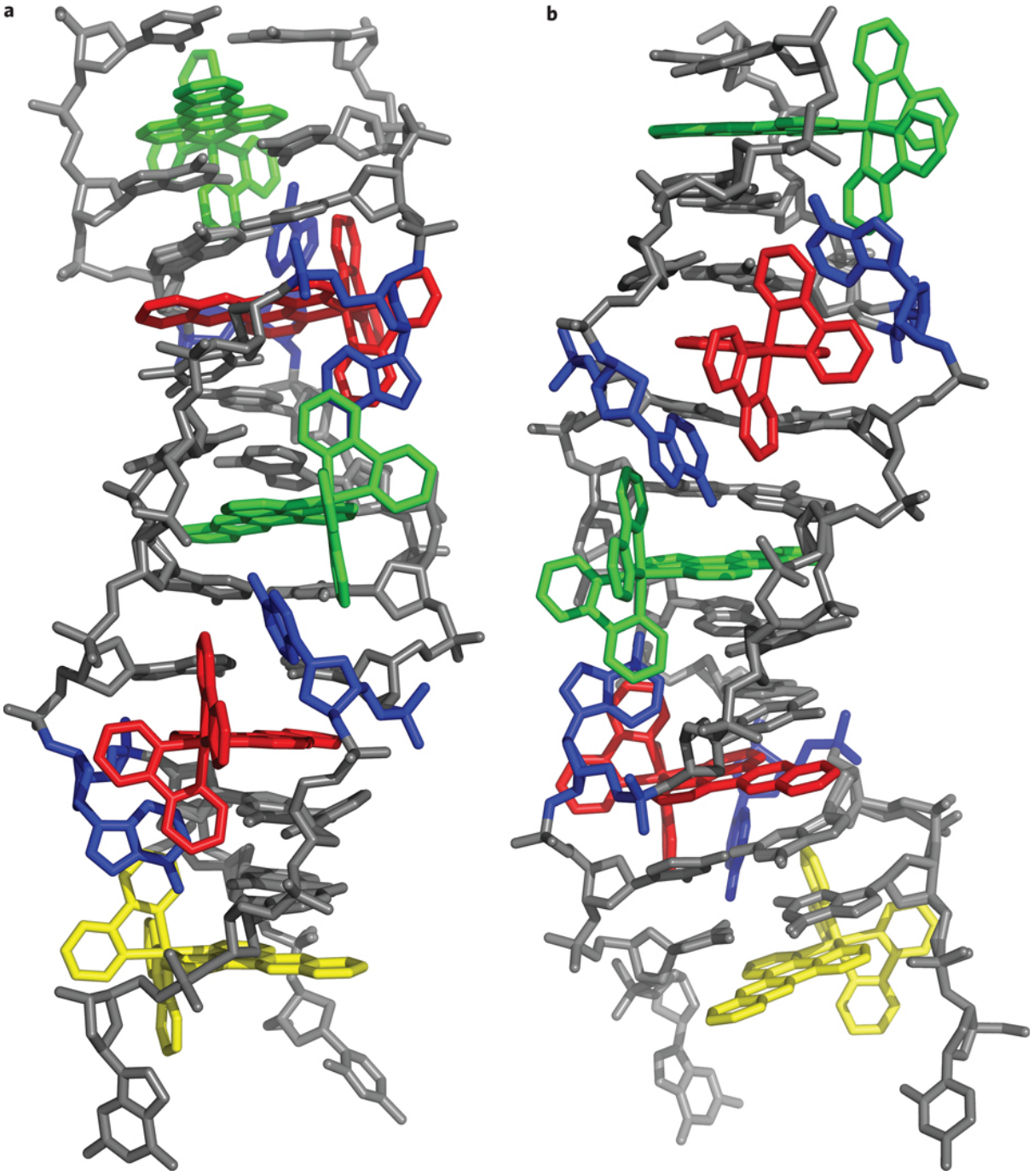

Figure 6. Ruthenium (II) dppz complex binding to an oligonucleotide with mismatched base pairs (blue). The complex is shown to bind in the mismatched area (red), intercalate by well-matched pairs (green) and cap the end of the sequence (yellow). Adapted from ref.[39]

In summary, ruthenium (II) polypyridyl complexes have proven to be potentially useful complexes for nucleus imaging. However, very careful control of ligands and staining conditions has proven key to obtaining the desired localisation. CPP have proven to be very poignant tools for facilitating cell penetration and localisation when coupled with ruthenium (II) complexes but again the effects of these moieties has not always been met with the intended localisation.

After the discovery of Cisplatin there has been steady interest in square planar platinum (II) (II) complex as potential nuclear stains, with many having a flat aromatic structure lending themselves to being good intercalators of DNA.[41] Much like the ruthenium (II) polypyridyl complexes, early square planar platinum (II) complexes were assessed in solution, with binding and photophysical studies being performed. Platinum (II) 2, 2':6'2"-terpyridine(N^N^N) complexes where found to bind strongly to DNA by an intercalative binding mode in solution.[42,43] However, it wasn't until a few decades later that the first microscopy studies started taking place using square planar platinum (II) complexes. One of the first reported by Botchway *et al.* found that a platinum (II) 1,3-di(2-pyridyl)benzene (N^C^N) rapidly entered cells in a 5 minutes and preferentially stained the nucleus(by costaining with DAPI), with some diffuse cytoplasmic staining also observed (Fig 7). DNA titrations of the complex with calf thymus and salmon DNA observed emission enhancement and an intercalation binding mode was suggested due to the structural similarities with the platinum (II) N^N^N complexes. The complex was shown to be applicable with two-photon microscopy and time gating, facilitating high resolution imaging and autofluorescence rejection. The complex was also noted to exhibit excellent photostability during imaging.

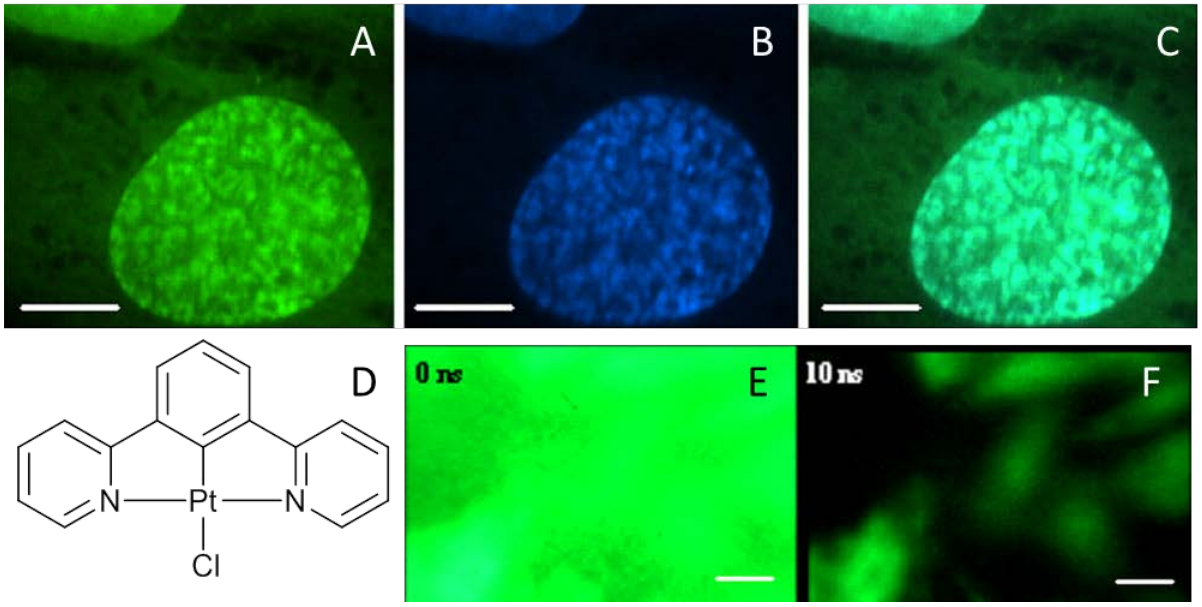

Figure 7. LSCM images of fixed CHO-K1 cells stained with (A) complex X (100 µM, 5 mins) and (B) DAPI (300 nM, 5 mins) with (C) an overlay of the channels showing co-localisation. (D) molecular structure of Pt N^C^N; LSCM time gating images of CHO cells treated with Pt N^C^N and Fluorescein placed in the media,(E) No time delay with emission from both indeterminable, (F) 10 ns time delay showing only Pt N^C^N emission. Images adapted from ref.[44]

Further studies by Kumari *et al.* on square planar platinum (II) complexes designed to be used for anti-tumour uses found a dinuclear complex with two N,N'-bis(salicylidene)-p-phenylenediamine ligands bridging the two platinum (II) atoms stained the nucleus of cells. The complex was found to bind DNA in solution by observed changes in the photophysical properties of the complex and the binding mode was attributed to intercalation.

Further development of the platinum (II) N^C^N complexes was reported by Baggaley *et al.* and Dragonetti *et al.* with a view to making these complexes more water soluble. The work reported by Baggaley *et al.* made use of a amine group to form a HCL salt of Pt N^C^N complex, vastly improving water solubility. The complex was further utilised in TREM to allow lifetime maps of the complex in cells, providing local O_2 environment data from the complex throughout the cell.[45] While Dragonetti *et al.* assess the effects of hydrophobicity/philicity on the uptake on these complex using polyethylene glycol (PEG) chains. It was reported that the more hydrophobic of the complexes, with only a linker and no PEG chain was most readily taken up, while no change in localisation was observed across the complexes.[46]

In summary, a number of different square planar platinum (II) complexes have shown to be good nuclear stains due to their propensity to intercalate DNA. Some compounds such as the Pt N^C^N complexes have been observed to enter cells rapidly and with minimal toxicity while imaging, a key criteria for good bio imaging probes.

Iridium (III) based luminescence complexes typically used for imaging are octahedral complexes with polypyridyl type ligands often employed, however, unlike the ruthenium (II) and platinum (II) complexes that have been discussed earlier, there are few reported examples of Iridium (III) complexes entering the nucleus.[47] Here the few that do permeate the nuclear membrane will be discribed. One elegant example of an Iridium (III) based nuclear stain used an Iridium (III) bis(phenylpyridine) with two DMSO molecules occupying the two vacant co-ordination sites. These sites are labile and were found to react with histidine residues, changing the complex from being non-emissive to strongly luminescent, while also yielding nuclear localisation in live and fixed cells.[48] Uptake of the complex was observed to be swift, with images taken as early as 15 minutes of incubation and the uptake mechanism was also establish to be energy dependant.

Two Iridium (III) complexes, a mono and a dinuclear complex isostructural to previously reported ruthenium (II) complexes by Gill *et al.* with a tpphz present and phenylpyridine(CN) ligands in place of the bipy ligands were assessed in cells for the nucleus staining. As with the ruthenium (II) analogue, the mono nuclear complex permeated cells reasonably quickly and specifically stained the nuclei of cells.[49] Curiously, in contrast to the dinuclear ruthenium (II) analogue, the dinuclear Iridium (III) complex was observed to enter cells and stain the cytoplasm with no nuclear staining observed, whereas the dinuclear ruthenium (II) complex was not found to enter cells at all. The nuclear staining of the mononuclear complex was found to be energy dependant and was not as selective when used in fixed cells, suggesting the cell traffics the complex. This staining mechanism offers interesting alternative to targeted nuclei staining which doesn't require the complex to be a DNA binder, potentially mitigating toxic effects due to DNA damage.

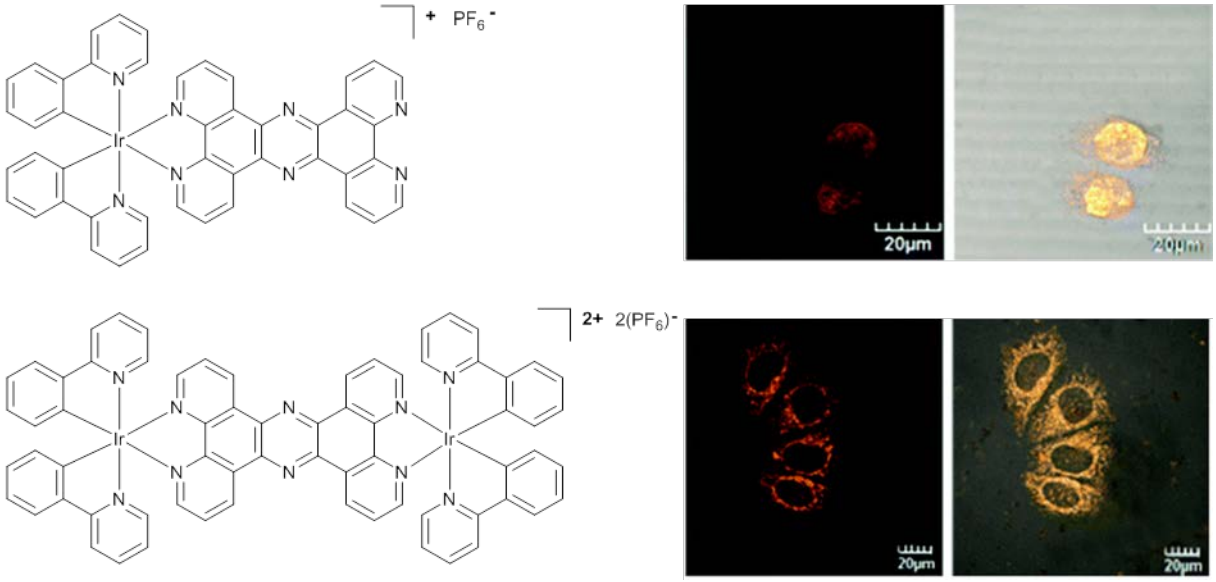

Figure 8. Molecular structure of the mono and dinuclear Iridium (III) complexes (left) and their emission from Hep G2 cells stained with the complexes (right). Adapted from ref.[49]

2.3.2 Nucleoli

The nucleolus is the most prominent subnuclear structure and is often visible by brightfield or DIC microscopy. The nucleolus preforms the crucial role of assembling ribosomes and is essentially a subnuclear factory. The ribosomes within a eukaryotic cell usually number into the millions and are composed to two subunits; this vast number of ribosomes is used to manufacture all the proteins the cell needs. Nucleoli are highly dynamic, with lots of components in transit in and out of the cell and the structure is also highly changeable depending on the activity of the cell. Due to its functions the nucleoli have an abundance of RNA present.

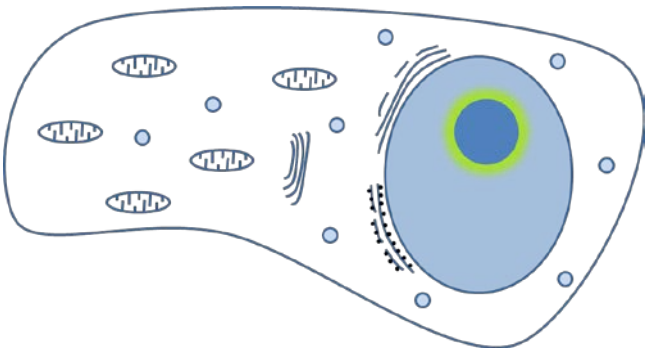

Figure 9. Simplified depiction of a typical eukaryotic cell with its nucleoli labelled in green.

As platinum (II) square planar complexes have already been discussed as good nucleus binder, it is of little surprise that some of these complexes may bind to the nucleoli selectively. Early studies of platinum (II) complexes found a complex with a N^N^C, 2-phenyl-6-(1H-pyrazol-3-yl)-pyridine ligand with a triphenylphosphium pendant group bonded through the nitrogen of the pyrazole

accumulated in the nucleoli of live and fixed HeLa and 3T3 cells.[50] This result is curiously for a number of reasons, firstly the parent complex, while very similar structurally to Pt N^C^N only stained the cytoplasm and not the nucleus[51] and secondly the triphenylphosphonium moiety is well reported as a mitochondrial targeting moiety.[52] Furthermore, the complex was not found to bind DNA or RNA and but instead interacted with proteins strongly, suggesting that its localisation is due to specific interactions with nucleolar proteins. The complex was found to be toxic due to being a transcription inhibitor, causing live cell treated with the complex to quickly display signs of toxicity.

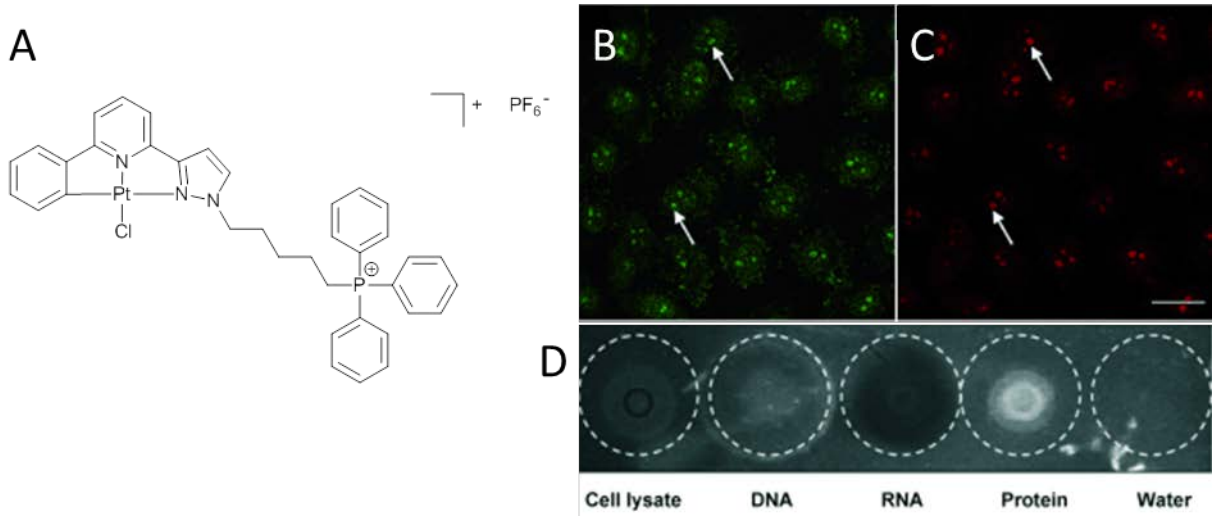

Figure 10. (A) Molecular structure of triphenylphosphonium platinum (II) complex. LSCM images of HeLa cells treated with (B) triphenylphosphonium platinum (II) complex and (C) immunofluorescent labelled fibrillarin(nucleoli specific protein); (D) dot blot assay of complex bound to protein but not DNA or RNA. Images adapted from ref.[50]

Further work on platinum (II) complexes by Septiadi *et al.* found that a platinum (II) complex with a 2,6-bis(3-(tri- fuoromethyl)-1H-1,2,4-triazol-5-yl)pyridine ligand accumulated heavily in the nucleoli of HeLa cells with some diffuse cytoplasmic and nuclear staining.[53] Interestingly, the complex was reported to only stain cells when incubated in PBS and not cell culture media, with protein binding of the complex suggested as the reason for this inhibition. The complex was also shown to form aggregates within cells which improved the photostability of the complex.

As mentioned in the previous section, Iridium (III) complexes typically do not penetrate the nucleus and only a few Iridium (III) complexes have been reported to stain the nucleus and similarly, very few Iridium (III) complexes stain the nucleoli. That being said, there is an example of an Iridium (III) N^C complex with a dipyrido[3,2-*f*:20,30-*h*]quinoxaline (dpq) ligand that has been shown to accumulate in nucleoli with some cytoplasmic staining also present.[54] However, similar to the Pt N^N^C complex discussed above, the localisation of the complex was shown to not be effected by the presence of RNA but instead the complex strongly binds to proteins and the localisation is likely to be due to

interactions with specific nucleolus proteins. Curiously, the complex was also shown to bind readily to DNA but no nuclear staining was observed save for the nucleoli.

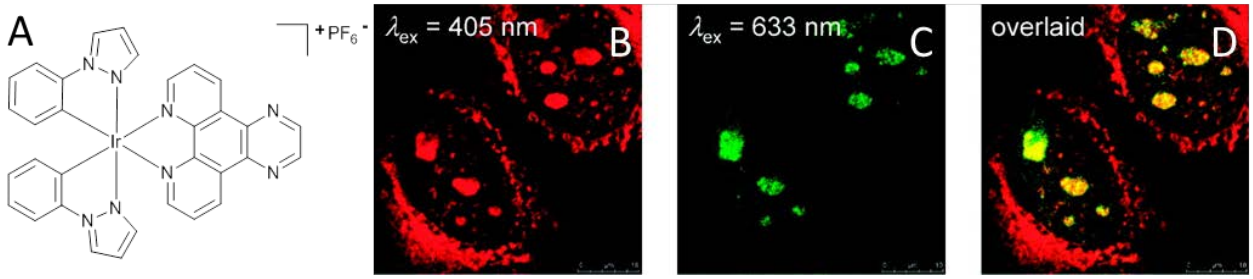

Figure 11. (A) Molecular structure of complex; LSCM images of fixed MDCK cells stained with (B) complex and (C) Fibrillarin antibody, (D) overlayed. Adapted from ref.[54]

Rhenium (I) (I) complexes, much like Iridium (III) complexes have rarely been reported to enter and stain the nucleus of cells. However, there are a handful of examples of complexes that have been reported that have managed to stain the nucleoli of cells and a number of these will be discussed below. The first of these examples is a rhenium (I) (I) N,N-bis(quinolinoyl) complex which has been used in two different studies for its cytotoxic properties for anticancer applications. Both studies used targeting/uptake moieties to aid in uptake and localisation of the complex, with one using vitamin B_{12} and the other using CPPs: nuclear localisation sequence and bombesin. The first of these studies aimed to use vitamin B_{12} as an uptake enhancer but also improve cancer selectivity due to an over expression of transport proteins selective for vitamin B_{12} in cancer cells.[55] The second of the examples looked to use a photolabile protecting group along with a CPP to allow uptake of the compound before using a lower powered laser to uncage the complex and facilitate cell death.[56] Both approaches proved to improve the uptake and selectivity over the parent complex and both complexes accumulated heavily in the nucleoli with some diffuse cytoplasmic staining also observed.

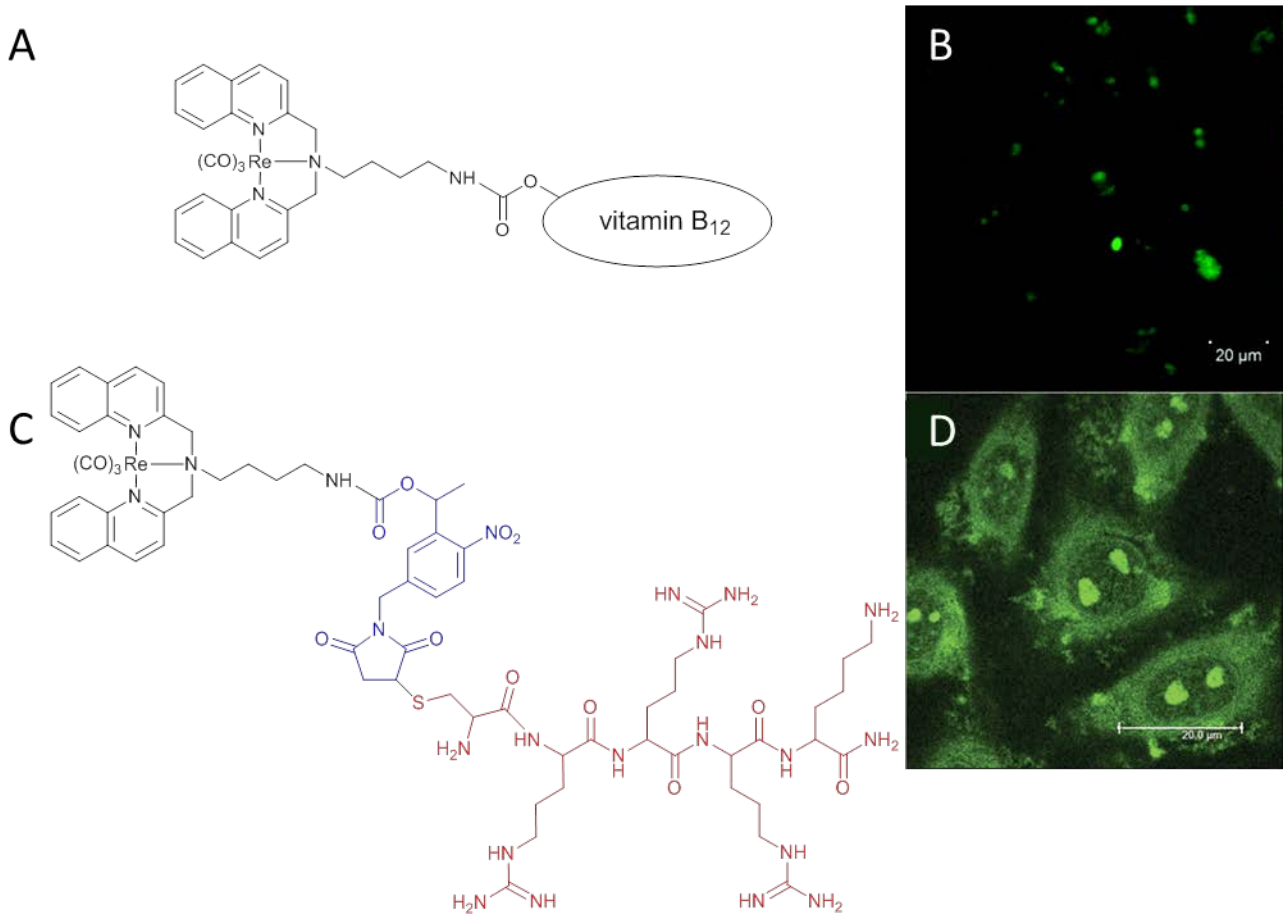

Figure 12. Molecular structure of Re(I) complex coupled to (A) vitamin B_{12} and (C) photolabile group (blue) and nuclear localisation sequence CPP (red); LCSM images of (B) BeWo cell treated with Re (I) vitamin B_{12} and (D) HeLa cells stained with Re (I) CPP complex.

2.3.3 Endoplasmic Reticulum

The endoplasmic reticulum (ER) is made up of a network of flattened membranous cisternae which emanate from the nucleus in to the cell and is responsible for lipid and steroid synthesis, unless studded with ribosomes. In this case, the endoplasmic reticulum is involved in the production and export of proteins. The former is known as the smooth endoplasmic reticulum and the latter is known as the rough endoplasmic reticulum. These functions make the ER an extremely important organelle, with many crucial cargos passing through and being modified inside.[57]

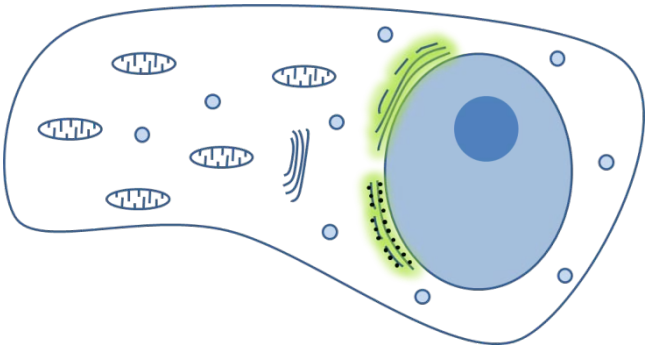

Figure 13. Simplified depiction of a typical eukaryotic cell with its endoplasmic reticulum labelled in green.

Only a small number of complexes have been reported to stain the endoplasmic reticulum, with many being Iridium (III) complexes. Cao *et al.* reported a group of Iridium (III) complexes in which the effects of the ligands on toxicity and uptake were explored. It was found that the most lipophilic complex with a 4,7-diphenyl-1,10-phenanthroline (DIP) ligand was the most toxic when compared to the bipy and phen counterparts and localised in the endoplasmic reticulum of HeLa cells rapidly(Fig. 14).[58] This complex was found to induce endoplasmic reticulum stress and toxicity was likely a result of this, leading to apoptosis. Further work by Yang *et al.* utilising Iridium (III) N^C *N*-heterocyclic carbene (NHC) complexes found that these complexes accumulated specifically in the endoplasmic reticulum.[59] These complexes were also studied for their toxicity and followed a similar trend as the previous Iridium (III) complex, with the more lipophilic complexes displaying greater toxicity compared to the glucose coupled hydrophilic complexes. These complexes were also suggested to cause endoplasmic reticulum stress and as such this is a likely cause of toxicity.

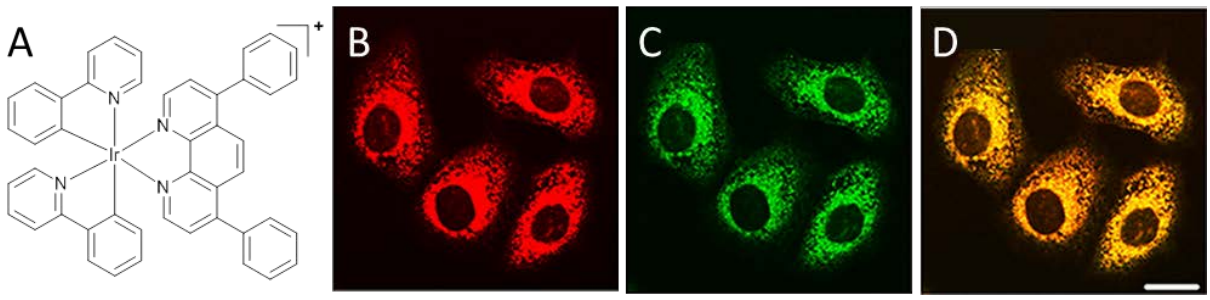

Figure 14. (A) molecular structure of Iridium (III) 4,7-diphenyl-1,10- phenanthroline complex; LCSM images of HeLa cells treated with (B) Iridium (III) complex and (C) ER-tracker and (D) an overlay of the channels displaying the co-localisation. Adapted from ref.[58]

Two dinuclear Iridium (III) complexes which are isostructural to previously reported ruthenium (II) complexes discussed above have been reported recently as G-quadruplex DNA binders. These complexes have either phenylpyridine or benzo(h)quinolone ligands with a tppz ligand bridge between the two Iridium (III) atoms.[60] Much like the ruthenium (II) complexes, these complexes were observed to bind strongly to DNA with an increase in emission intensity upon bind. Interestingly,

when the complexes were used to stain cells both complexes penetrated the cell membrane and stained the endoplasmic reticulum but neither penetrated the nucleus of the cells. This is in contrast to the isostructural ruthenium (II) complexes, where only one penetrated cells and accumulated in the nucleus. These finding are in line with previous observations that Iridium (III) complexes do not typically penetrate the nucleus, although no clear reason has yet been put forward for this phenomenon. These complexes were also found to be toxic to cell at relatively low concentrations (15.6 µM and 18.2 µM).

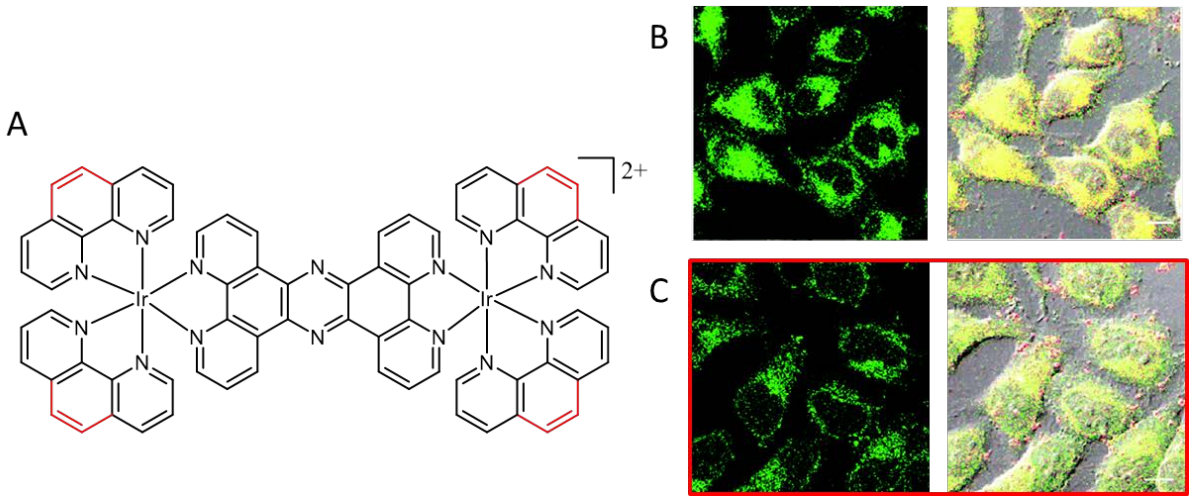

Figure 15. (A) Molecular structure of dinuclear Iridium (III) complexes; (B) emission from NC complex (left) and colocalisation with ER tracker (right), (C) emission from ppy complex (left) and co-localisation with ER tracker (right). Images adapted from ref.[60]

A dinuclear ruthenium (II) complex, di[ruthenium di(4,7-diphenyl-1,10-phenanthroline)] µ-tetrapyrido[3,2-a:20,30-c:300,200-h:2000,300 0-j]phenazine) reported by Gill *et al.* which is structurally very similar to the Iridium (III) complexes just discussed has also been studied *in vitro*, using a tppz ligand to bridge the ruthenium (II) atoms and two DIP ligand bonded to each ruthenium (II). Unlike its comparably phenyl group deficient parent complex, this complex readily enters cells but does not stain the nucleus like the bipy derivative but instead accumulates in the ER of fixed cells as revealed by co-staining with immuno labelled calnexin.[61] Similar to Iridium (III) and ruthenium (II) complexes previously discussed this complex was observed to readily bind to DNA but fails to penetrate the nuclear membrane, as shown by a lack of nuclear staining. Interestingly, this complex much like the others discussed in this section displayed high toxicity to both MCF-7 and HeLa cells with necrosis being the suggested death pathway, counter to the suggested apoptosis in the Iridium (III) complexes.

A platinum (II) NHC complex has also been reported to accumulate rapidly in the ER by co-staining the complex against ER-Tracker in HeLa cells, with similar results to the other complexes of high toxicity seen in the complex across a number of cancer cell lines.[62] However, unlike many of the

complexes discussed above this complex was not found to bind DNA very strongly but instead was observed to bind to proteins. This complex was also discovered to cause apoptosis.

Finally a dinuclear rhenium (I) complex appended with glucose and maltose residues has recently been reported that stain the endoplasmic reticulum of live HeLa cells.[63] These complexes were found to exhibit different localisation pattern to the parent complex, which localised diffusely throughout the entire cell but were slower to enter cells (10 mins vs 1 h).[64] Unlike all the other complexes discussed above that also stain the endoplasmic reticulum, these complexes did not display any reduction in cell viability. This lack of toxicity is likely due to the glucose moieties present in these complexes as they have previously been reported to reduce toxicity compared to parent complexes.[65]

In summary, there have only been a small number of complexes that have been found to localise in the endoplasmic reticulum of cell and of these, the vast majority have been found to be toxic to cell and cause ER stress. A number of the complexes were discovered to be DNA binders but did not display any nuclear staining, suggesting the complexes were not able to penetrate the nuclear membrane.

2.3.4 Golgi Apparatus

The Golgi apparatus is an organelle found in most eukaryotic cells and consists of stacks of membrane bound structures known as cisternae located near the nucleus. The Golgi apparatus is integral for the modifying, sorting and packaging of macromolecules (such as proteins) for use in the cell or secretion. The Golgi apparatus also has a key role in carbohydrate synthesis.

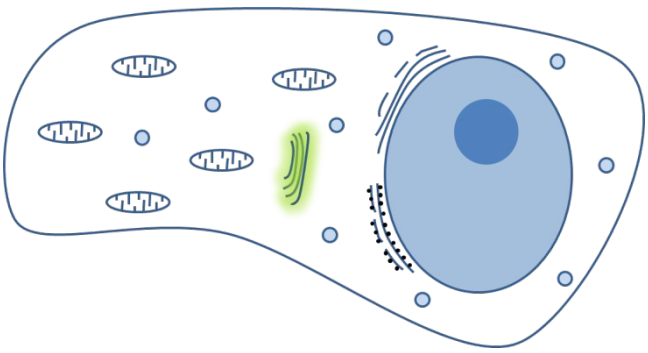

Figure 16. Simplified depiction of a typical eukaryotic cell with its golgi apparatus labelled in green.

Despite the key roles performed by the Golgi apparatus there have been very few reported complexes that stain the Golgi apparatus selectively. This may be explained by the fact that commercial dyes used for staining the Golgi apparatus typically have lipids moieties such as ceramides or sphingolipids as these molecules are sorted in the Golgi apparatus[66] and these moieties are uncommon in

luminescent metal complexes. That being said, there are a handful of examples and one of these was reported by Zhang *et al.* in which they synthesised a series of dendritic Iridium (III) (III) polypyridine complexes.[12] These dendritic Iridium (III) complexes were composed of short peptide chains with bipyridine moieties at the ends of the dendritic chains. Regardless of the large size and high overall charge of the biggest dendritic complexes, which contained eight Iridium (III) complexes, the complexes were observed to enter HeLa cells but at lower concentrations than the monomeric complexes. The large dendritic complexes were observed to co-localise with anti-golgin-97 antibody, demonstrating that the complexes localise within the Golgi apparatus of HeLa cells. Interestingly, while the largest dendritic Iridium (III) complexes did not display the highest logP values, they were observed to have the greatest cytotoxicity of all the dendritic complexes screened and 10-fold greater toxicity than the monomeric complexes, counter to the suggestion of authors that logP was the predominate cause for toxicity.

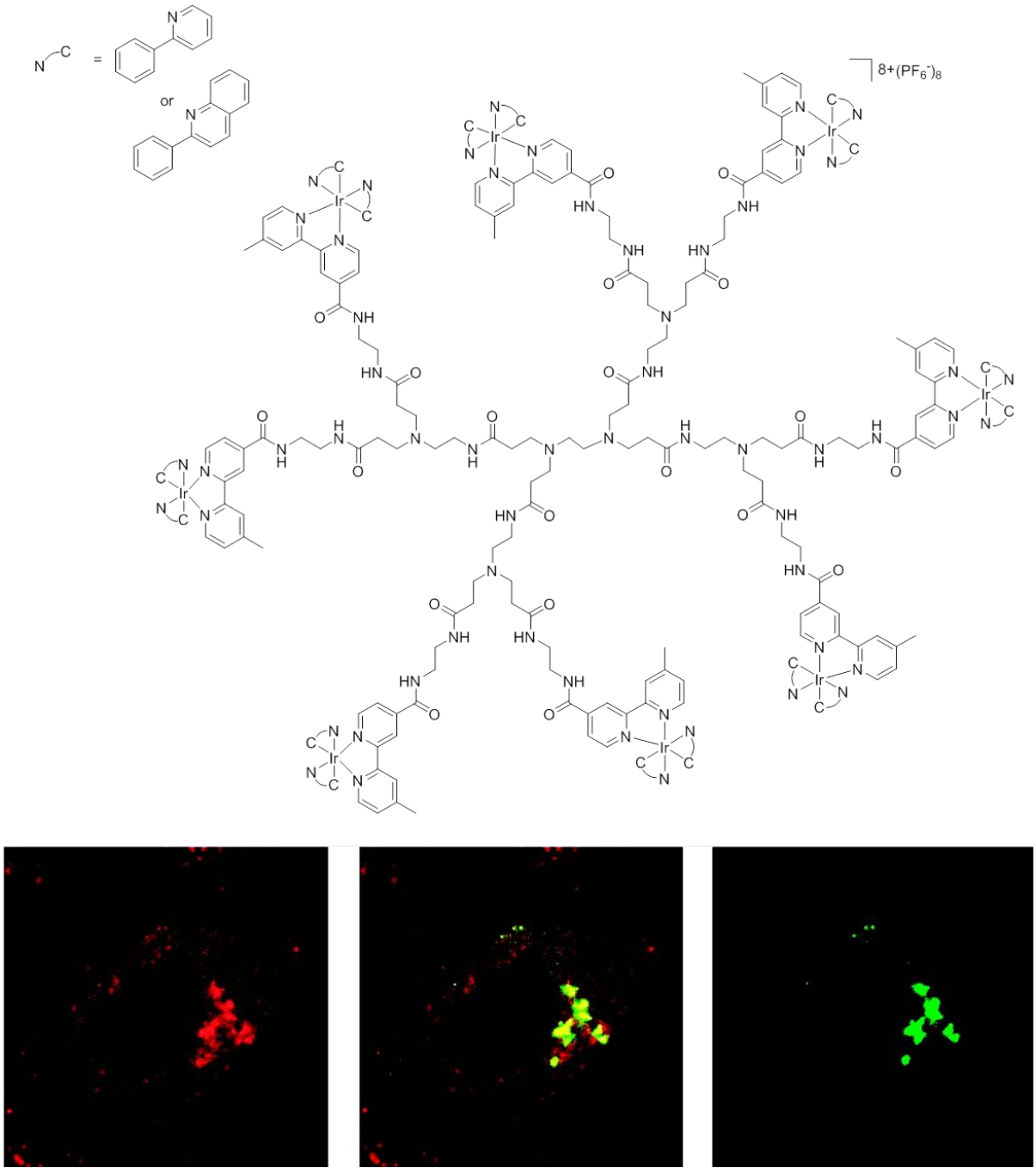

Figure 17. Molecular structure of dendritic Iridium (III) (III) complexes (top) and LSCM images of HeLa cells co-stained with one of the complexes(red) and immunolabelled Golgi apparatus (green) and overlaid. Adapted from ref.[12]

Another Iridium (III) complex was reported to stain the Golgi apparatus by Ho *et al.*, in contrast to the previous example this complex was a mononuclear N^C complex utilizing two N,N-diphenyl-4-(2-pyridinyl)-benzenamine ligands and a 2-[4-[bis(2,4,6-trimethylphenyl)boryl]phenyl]-pyridine ligand.[67] The complex was co-localised with an immunolabelled Alexa Fluor 647 conjugate of HPA (a lectin protein) demonstrating the localisation of the complex in the Golgi apparatus. The complex was also found to exhibit a good two-photon cross section of 340 GM, potentially allowing the complex to be used in two-photon microscopy but no two-photon microscopy images were obtained

in this study. Curiously, this complex exhibited considerably lower toxicity (only 30 % reduction in viability at 100 µM) than the previous complexes discussed above which stained the Golgi apparatus, unlike the complexes which stained the ER, it would appear these complexes may not disrupt the organelle they localise in.

2.3.5 Mitochondria

Mitochondria are often referred to as the "powerhouse" of the cell as they are the organelle where respiration occurs. Mitochondria have a double membrane, a clue of their bacterial origins, with the inner membrane folding in to series of invaginations called cristae. These folds work to increase the surface area inside the mitochondria where proteins crucial to respiration operate. The inner membrane of mitochondria are highly impermeable and consists of densely packed, particularly hydrophobic lipids.[68] The mitochondria also maintain high negative membrane potential as a proton gradient is required for oxidative phosphorylation.[52] In order to maintain this gradient the inner mitochondrial membrane is it necessary for the membrane to be highly effective at excluding molecules and even protons, with special transport machinery utilised often to penetrate it. Mitochondria are responsible for synthesising the majority of the cells ATP and are also play important roles in cell death, cell division cycles, differentiation and signalling.

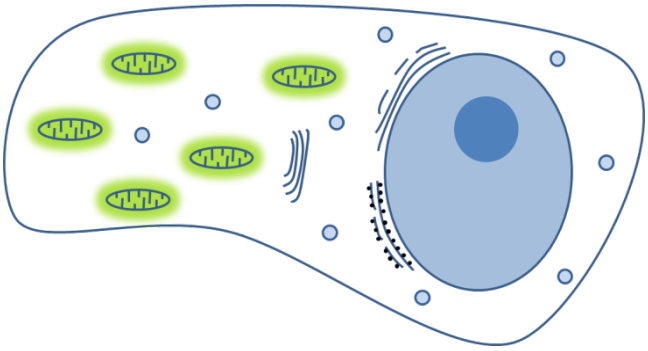

Figure 18. Simplified depiction of a typical eukaryotic cell with its mitochondria labelled in green.

Although the mitochondria are double membrane bound organelles with strong, well defined membranes for maintaining careful balance of molecules with mitochondria, there are a large number of luminescent transition metal complexes which have been found to penetrate and accumulate in mitochondria. This trend can be somewhat explained by the typical properties of metal complex used in cell imaging; most of these complexes are positively changed due to the oxidation state of the metals, leading to these complexes being attracted to the negative potential maintained within the mitochondria. Furthermore, these complexes typically have large aromatic ring systems used to

generate the luminescence in these complexes, thus making the periphery of the complexes lipophilic and helping them penetrate the lipid membranes of the plasma membrane and then the mitochondria.

While there are examples of platinum (II), rhenium (I) and ruthenium (II) complexes localising in mitochondria, the rise of iridium (III) complexes being explored as potential imaging probes has led to plethora of iridium complexes being reported which localise in mitochondria. Many of these examples have been reported recently but one of the early reported iridium (II) complexes using various N^C ligands to occupy four of the ligand sites and a polyamine filling the other two. These complexes were found to exhibit good photophysical properties for imaging and were subsequently found to localise in mitochondria.[69] The studies also investigated the effects of lipophilicity on uptake and toxicity of the complexes, with some of the complexes being attached to PEG linkers of various lengths. It was observed that while the uptake of the more hydrophilic complexes was generally greater, these complexes also exhibited much greater toxicity within cells. Curiously, the PEG chains showed poor uptake, with uptake getting worst the longer the PEG length and toxicity being similarly high for each of the PEG lengths. This goes against conventional wisdom as PEG chains are often considered to help biocompatibility,[70] however the PEGylated complexes where found to be good starting points for potential transfection agents.

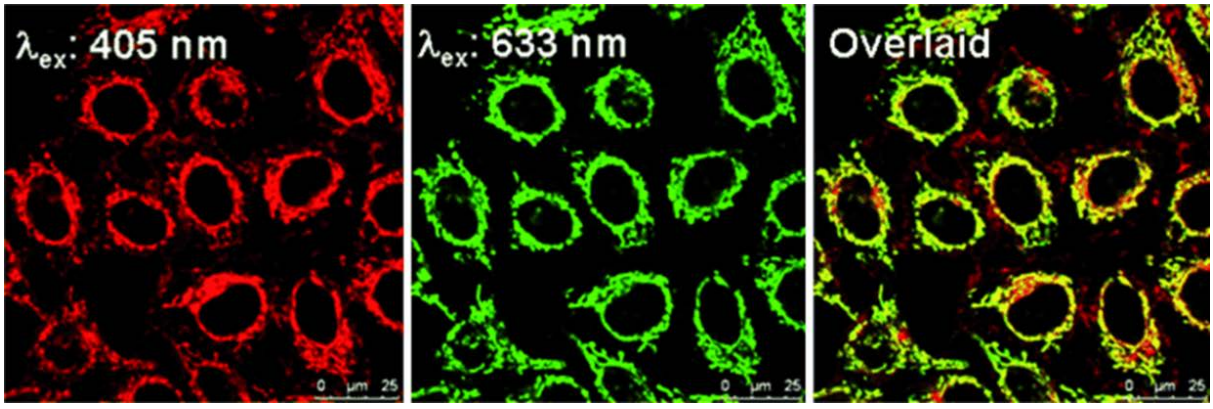

Figure 19. LSCM images of HeLa cells treated with Iridium (III) PEG complex (λ_{ex} = 405 nm) and MitoTracker® deep red FM (λ_{ex} = 633 nm) and an overlay of the channels. Reproduced from ref.[69]

Highlighting the colour tuning potential of transition metal complexes, Chen *et al.* and Zhang *et al.* have reported a number of iridium (III) polypyridyl complexes displaying a wide variety of emission maxima across the visible spectrum.[71,72] Both sets of Iridium (III) complexes where observed to selectively stain the mitochondria of live HeLa cells and exhibited toxicity comparable to other commercially available mitochondria specific probes. Furthermore, these complexes were observed to have excellent photostability when compared to commercially available MitoTracker® dyes. The photostability of these complexes, coupled with the multiple colours offers a range of potential complexes which can be used for mitochondrial tracking experiments in conjunction with other probes.

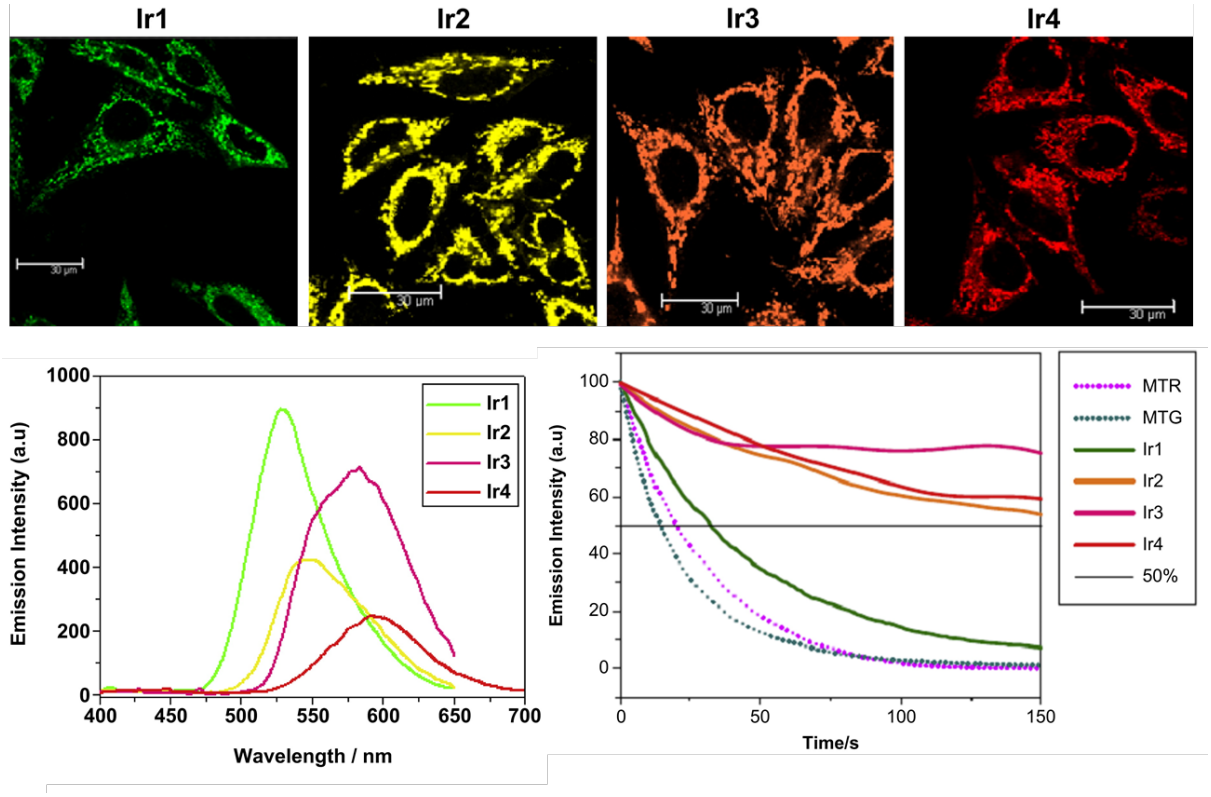

Figure 20. LSCM images of live HeLa cells stained with various Iridium (III) complexes (top). Emission spectra of Iridium (III) complexes (left), and emission intensity over time graph of Iridium (III) complexes versus MitoTracker® green and MitoTracker® red. Adapted from ref.[71]

Further developments in Iridium (III) complexes designed for mitochondrial imaging have looked to incorporate two-photon microscopy to improve the resolution of the imaging, facilitating the imaging of larger, more complex samples. Two set of iridium (III) complexes have been recently reported which have been found to selectively accumulate in the mitochondria of live HeLa cells (Figure 21).[73,74] The complexes were also shown to have reasonable two-photon cross sections between 18.4-65.5 GM at 760 nm), which was adequate to achieve good two-photon microscopy images. Furthermore, these complexes were explored for staining spheroids, large 3D multicellular units used as tumor models as they exhibit phenotypes of tumors more accurately than monolayers. Large z-stacks of up to 200 µM of these spheroids were obtained using two-photon microscopy (Fig 21.). More complexes have also been reported from this group, outlining more mitochondrial specific Iridium (III) complexes which have been used in two-photon microscopy to study spheroid models, highlighting their potential in hypoxia imaging,[75] colour tuning[76] and hypochlorite detection.[77]

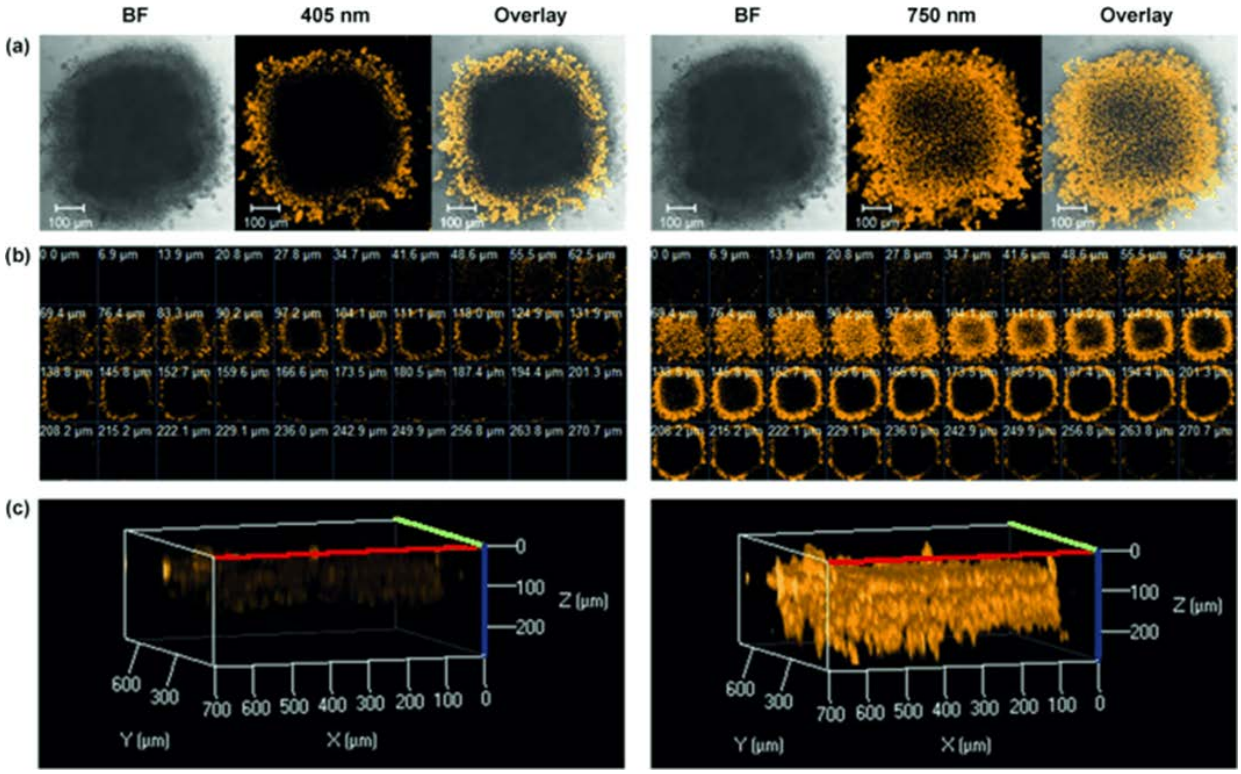

Figure 21. (A) Single photon excitation (left) and two photon excitation (right) microscopy images of spheroids stained with Iridium (III) complex. (B) Z-stack images every 7 µm through the spheroid. (C) 3D projection of the z-stack. Reproduced from ref.[73]

A recent study by Qiu *et al.* has explored a range of iridium (III) phenylpyridine complexes with a morpholine moiety present.[78] These complexes were observed to vary their localisation between the mitochondria or lysosomes and this was found to correlate with the hydrophilicity of the complexes. The more hydrophilic complexes were found to specifically localise in the lysosomes, while the more lipophilic complexes localised in the mitochondria. This localisation was consistent with previous literature which had theorised that that molecules with certain logP values would be like to localise specifically depending on the value of the logP.[79]

While less prevalent than iridium (III) complexes, a reasonable number of platinum (II) based complexes have been reported to selectively stain the mitochondria of cells. One of the earliest examples was reported by Lai *et al.* concerning the development of a thienylpyridyl platinum (II) complex.[80] This complex was observed to accumulate in the mitochondria, with some weak nuclear staining also observed. This complex was also discovered to have an excellent singlet oxygen yield of >90% and it was suggested this complex could be as a photoinduced cytotoxic agent. However, due to the small difference in toxicity of complex in the dark (IC_{50} = 6.12 µM) versus irradiation (IC_{50} = 1.78 µM) it is unlikely this complex could be used as a PDT agent.

Another example of a mitochondrial specific platinum (II) complex was reported by Sun *et al.*, in which a platinum (II) N^N^C complex with a *N*-heterocyclic carbine was explored as a potential

anticancer agent.[81] The complex was discovered to be highly toxic (IC_{50} = 0.057 mM), with considerably higher toxicity observed in cancerous cell lines when compared to non-cancerous cell lines. The complexes were also found to inhibit tumor growth in *in vivo* mouse models, with the complex implicated in the disruption of survivin (apoptosis inhibitor) causing apoptosis in cancerous cells. Curiously, contrary to many other square planar platinum (II) complexes, no nuclear staining was observed and the complex displayed only a small affinity for DNA binding but was shown to be an intercalator. Another platinum (II) complex using a 7-nitro-2,1,3-benzoxadiazole was developed as an anti-cancer agent, however in this study the localisation of the complex *in vitro* and *in vivo* was studied, complementing the previous study by Sun *et al.*[82] In this studies the complex was observed to stain mitochondria with some weak nucleoli staining *in vitro* and was shown to accumulate in the liver of 50 h zebrafish larva. While the complex was proposed as an anticancer agent, no toxicity assays were reported but visual signs of cell toxicity were noted.

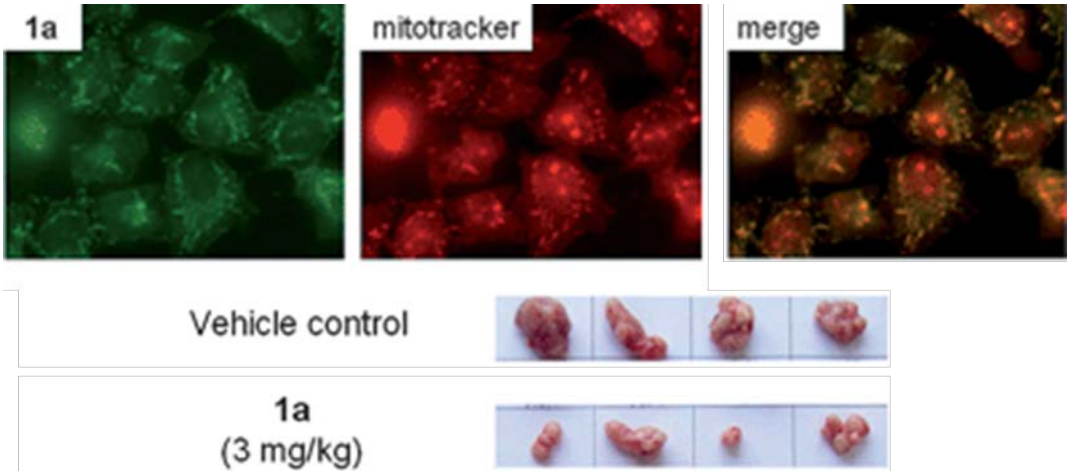

Figure 22. LSCM images of HeLa cells stained with platinum (II) *N*-heterocyclic carbene complex (left) and MitoTracker® red (center) and the channels overlaid (right). Tumor growth without treatment and with platinum (II) complex (bottom). Adapted from ref.[81]

Further work on platinum (II) complexes as anticancer agents led to Mitra *et al.* reporting the use of a platinum (II) complex with a BODIPY attached to a 2-(2-pyridyl)benzimidazole ligand and a catecholate.[83] The BODIPY moiety was utilised to aid in the uptake and localisation of the complex in the mitochondria as disruption of the mitochondria is likely to cause cell death. The complex was found to have excellent singlet oxygen yield and while the complexes toxicity was low in the dark (>100 μM) the toxicity post irradiation was considerably higher (<10 μm = IC_{50}).

Rhenium (I) based complexes were the first of these transition metal complexes to be reported as mitochondrial specific, with Amoroso *et al.* reporting the development of rhenium (I) bipy complex with a reactive methylene chloride moiety.[22] The methylene chloride bonded to a pyridine ring is highly reactive towards thiol groups and due to the large quantity of glutathione present in mitochondria[84] leads to accumulation of the complex in mitochondria (scheme 2). The complex was

tested in yeast as well as MCF-7 cells, highlighting the utility of the complex. Interestingly, while the complex localisation was rationalised by the thiol reactive group the parent complexes with an alcohol group was also found to localise specifically to the mitochondria.[14] It was postulated that this complex might undergo phosphorylation and thus become a thiol reactive species but the authors conceded there was no evidence for this hypothesis.

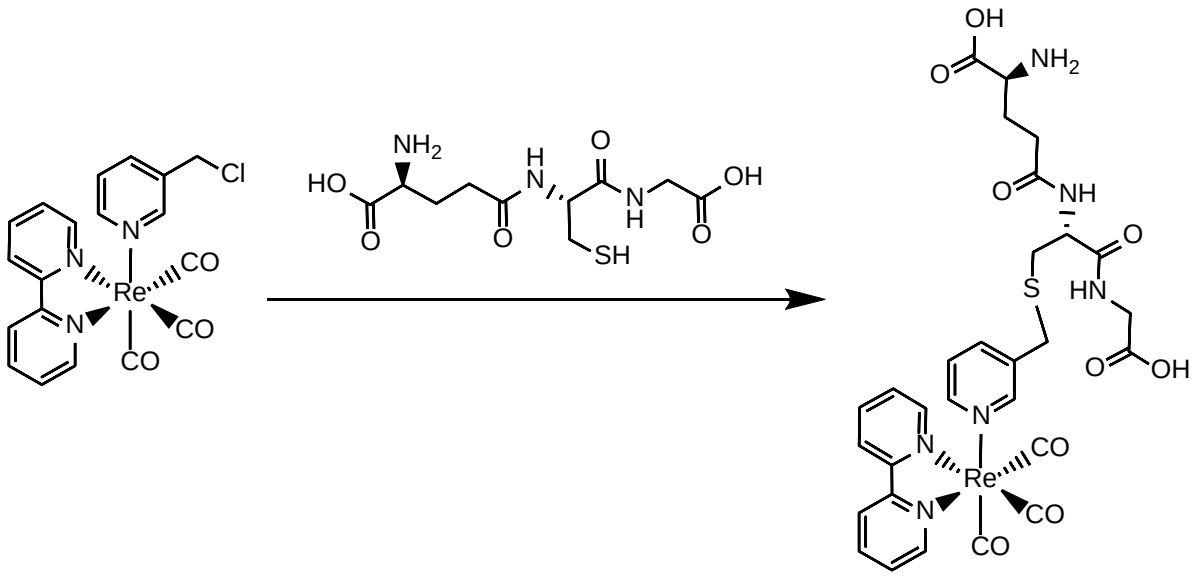

Scheme 2. Thiol reactive rhenium (I) complex shown reacting with glutathione.

Following these advances, Louie *et al.* reported the synthesis and cellular testing of a rhenium (I) phenanthroline complex with a pendant α-D-glucose.[65] The design of this complex was aimed at preferential uptake in cancer cells as many cancer cells are known to overexpress glucose transporter proteins to help fuel their characteristic aggressive growth. Despite glycolysis occurring in the cytosol of cells, the glucose complex was observed to co-localise with MitoTracker® deep red. The inclusion of the glucose moiety was also found to reduce the toxicity of the complex compared to the parent complex. Curiously, the glucose complex was found to be taken up less readily than that of its glucose free parent complex, which was rationalised by the more hydrophobic nature of parent complex by the authors. However, as intended the uptake of the glucose complex was observed to be 2.7 greater in the cancer cell lines HeLa and MCF-7 compared to that of non-cancerous cell lines HEK293T and NIH/3T3.

Further developments in rhenium (I) complexes were reported by Choi *et al.* in the synthesis and bioimaging assessment of a rhenium (I) phenanthroline complex with a pendant PEG moiety.[4] These complexes were readily taken up by Hela cells and observed to colocalise with MitoTracker® deep red as seen in figure 23. Much like the previously discussed PEGylated Iridium (III) complexes, the PEGylated rhenium (I) complexes were found to be considerably more hydrophilic than the parent complexes, leading to lower uptake in cells. Conforming more to expectation than the Iridium (III)

PEG complexes, the PEGylated rhenium (I) complexes were also observed to have generally around half the IC_{50} of the parent complexes. This reduced toxicity was utilised to show that the PEG complex could be used to stain live zebrafish embryos without compromising viability or causing defects but retarding the rate of hatching.

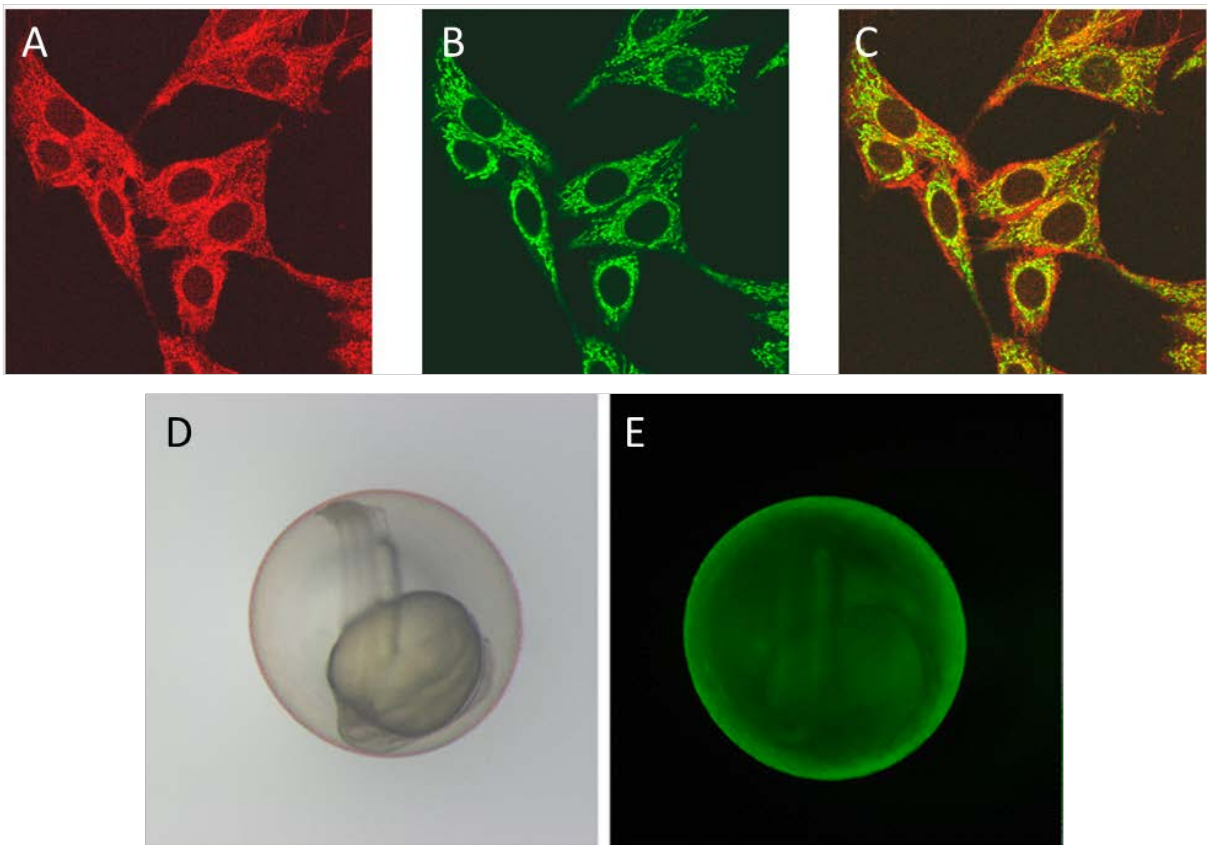

Figure 23. LSCM images of HeLa cells stained with (A) rhenium (I) PEG complex, (B) MitoTracker® deep red, (C) overlay of both channels. Zebrafish embryo stained with rhenium (I) PEG complex (D) brightfield image, (E) Emission from rhenium (I) PEG complex. Adapted from ref.[4]

2.3.6 Lysosomes

Lysosomes are small membrane bound organelles found in animal cells. Lysosomes are the terminal organelles of the endocytic pathway and their primary function is to break down and/or recycle dysfunctional organelles, biomolecules (such as lipids and proteins), cellular debris and other material the cell has internalised. Consequently, lysosomes can vary in size depending on the material being digested. Lysosomes contain many different lytic enzymes which are capable of breaking down carbohydrates, lipids, proteins and even nucleic acids and a pH of 4.5 is maintained inside the lysosomes to maximise the efficiency of these enzymes.[85] Due to the acidic environment of lysosomes, they often sequester molecules that are weak bases by protonating the molecules to become trapped in the lysosomes, thus achieving selective localisation.[86]

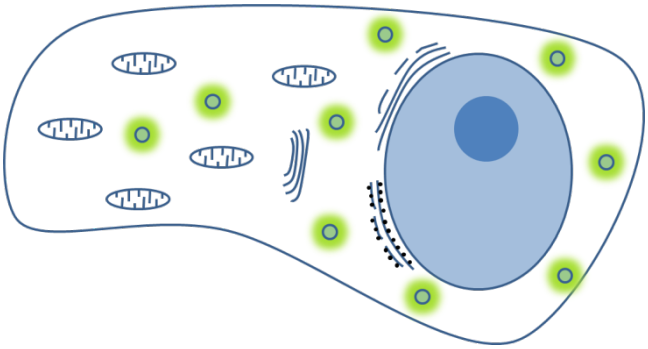

Figure 24. Simplified depiction of a typical eukaryotic cell with its lysosomes labelled in green.

Of the complexes which localise in the lysosomes, they are almost exclusively comprised of platinum (II) and Iridium (III) based complexes. One of the first reported complexes was a complex described by Moromizato *et al.* which was a Iridium (III) (III) complex with 2-(5'-N,N-diethylamino-4'-tolyl)pyridine ligands.[87] This complex displayed pH sensitive light switch effect, with emission increasing below pH 7.4 due to the protonation of the diethylamine group present on the ligands. By virtue of the pH sensitive diethylamine groups the complex was also observed to localise in the lysosomes of HeLa-S3 cells by co-localisation with Lysotracker red. The complex was also noted to be able to produce singlet oxygen by excitation with 377 or 470 nm light in a pH dependant manner, inducing cell death in the irradiated cells.

The next development was reported by Chung *et al.* and focused on the utilisation of a alkynyl platinum (II) (II) terpyridine complex.[88] This complex was also found to be pH sensitive, with a large increase in emission at lower pHs but unlike the previous example is due to the aggregation of the complex, leading to interactions between the complexes and the generation of a metal-metal-to-ligand charge transfer pathway. While the pH is important for the emission of the complex, it also leads to the complex emission being specific to low pH environments such as the lysosomes and as such the complex was found to strongly co-localise with lysosensor green DND-189.

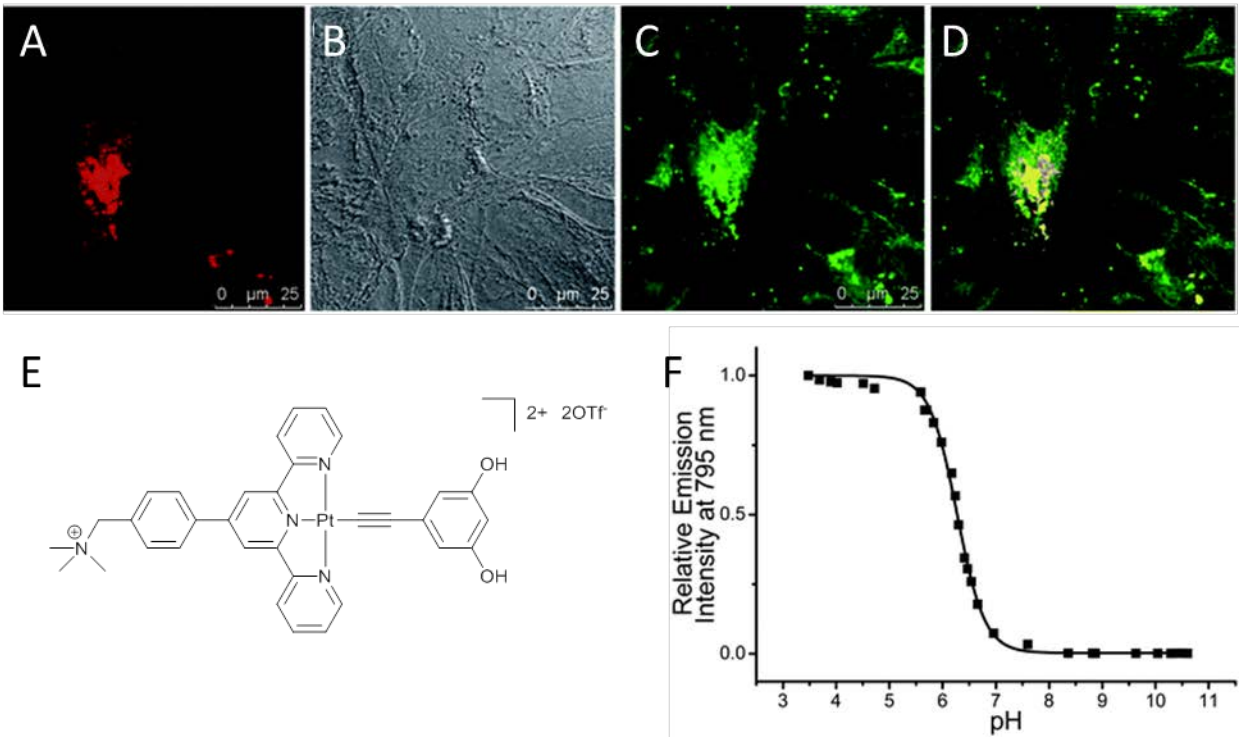

Figure 25. LSCM images of MDCK cells incubated with alkynyl Pt complex (20 µM, 1 h) and Lysosensor green DND-189 (1 µM, 15 mins). (A) emission from Pt complex, (B) brightfield image of cells, (C) emission from lysosensor, (D) overlay of channels. (E) molecular structure of alkynyl Pt complex (F) relative emission intensity vs pH graph displaying the increase in intensity with lower pH. Adapted from ref.[88]

Further developments were reported by Ho *et al.* with two binuclear platinum (II) complexes with CNN ligands on each of the platinum (II) atoms, with a methylene bis(diphenyl phosphine) bridging each platinum (II).[89] These complexes were developed to observe lysosome transportation in neurological cells as there has been evidence that they play a key role in neurodegenerative diseases. Both complexes have a pH sensitive imidiazole group as the outer ligand of the C^N^N, linked through the 2 and 4 positions respectively. As these probes are intended for *in vivo* imaging the two-photon cross sections of the complexes were measured to be 56 and 35 GM, which is ample for two-photon microscopy. Due to the low pK_a of the imidazole groups, the complexes were expected to enter the lysosome and become protonated and trapped. The complexes were observed to stain lysosome in HeLa cells and this was confirmed by co-localisation with Lysotracker red. One of the complexes was also used to demonstrate its ability to monitor the trafficking of lysosomes in live primary dorsal root ganglion and acute brain slices using two-photon microscopy.

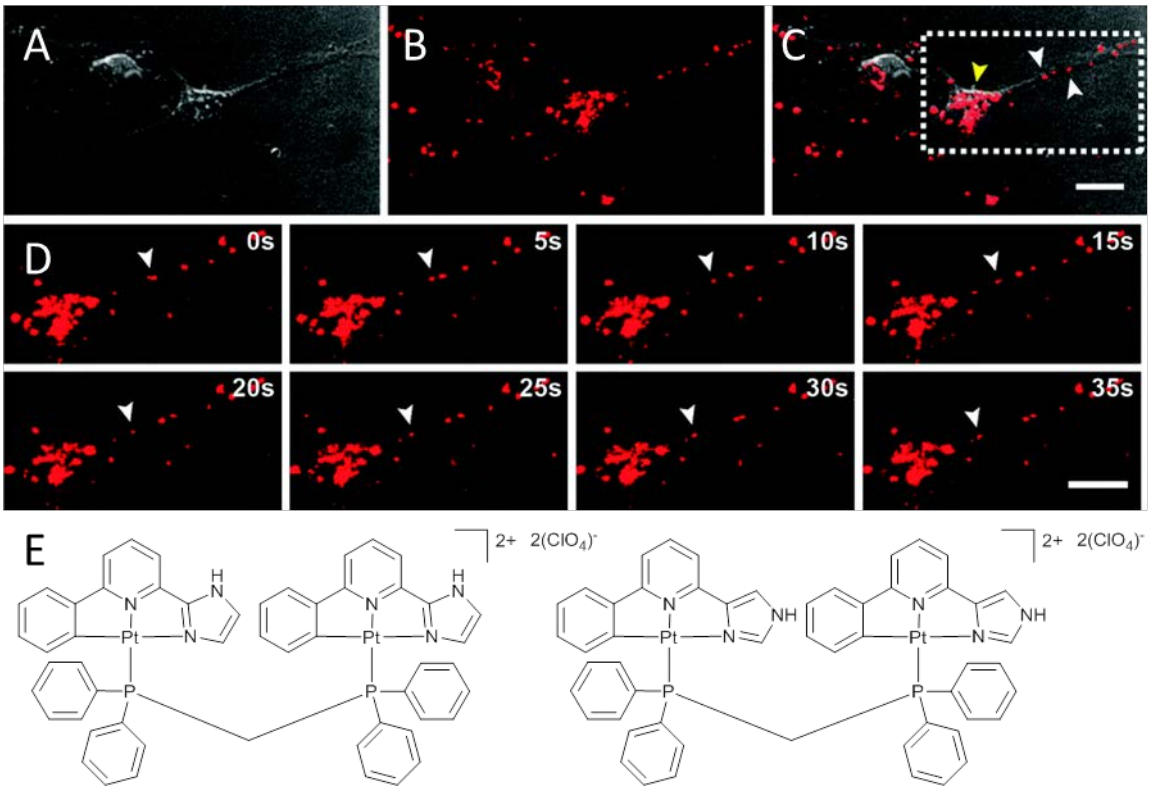

Figure 26. Two-photon microscopy images of live primary dorsal root ganglion neurons. (A) DIC image (B) Emission from the complex (C) overlay of DIC and emission (D) Time-lapse images of lysosomes moving through the axon of the neuron cell (E) Molecular structures of two Pt CNN complexes. Adapted from ref.[89]

Building on this work, Qiu *et al.* have recently reported another complex for long term tracking of lysosomes, this time based on an Iridium (III) (III) phenylpyridine complex with pendant morpholine moieties bonded through the nitrogen atom.[90] As with the other examples above, the complex displayed pH dependant emission properties, with emission intensity observed to increase below pH 7 but not completely quenching at higher pH. The complex was co-localised against Lysotracker red™ using one- and two-photon excitation as the complex was measured to have a reasonably two-photon cross section of 69.5 GM (at 750 nm) and was found to co-localise well with Lysotracker red™. The photostability of the complex was also found to be much greater than that of Lysotracker red™ over a period of continuous irradiation. The complex was also utilised to image 3D tumor spheroids with signal detectable at depths of over 100 µm using two-photon excitation.

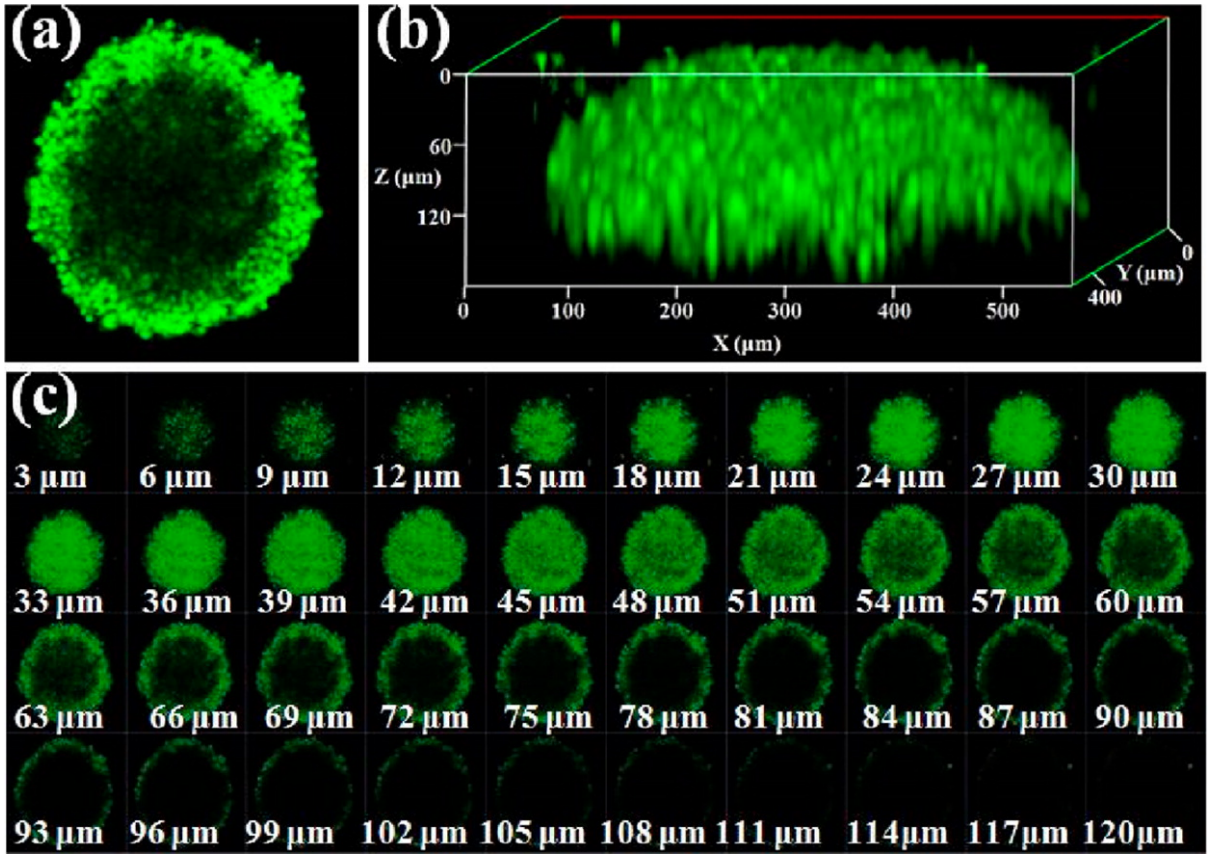

Figure 27. Two-photon microscopy image of 3D spheroid (A) stained with Ir morpholine complex, (B) Z stack of spheroid, (C) Z-stack slices of every 3 µm of the spheroid. Image taken from ref.[90]

Finally, a platinum (II) terpyridine complex and an Iridium (III) phenylpyridine complex have been reported recently by Chung *et al.* and Sansee *et al.* respectively. Both these complexes have alkylamine moieties that afford these complexes pH sensitivity, ideal for localisation and imaging of lysosomes.[91,92] Both complexes where found to localise in the lysosome of live cells when colocalised with commercially available lysosome specific dyes.

2.4 Emission Lifetime Microscopy

The vast majority of luminescent imaging studies rely on differences in wavelength or the variation of intensity of the emission of the probe. There is however another fundamental parameter which can also be utilised, lifetime. Lifetime is normally independent of concentration and can be calibrated absolutely, making fluorescent and phosphorescent lifetime imaging microscopy (FLIM and PLIM, respectfully) powerful tools for detecting the concentration of analytes. Intensity measurements can also be used for certain probes,[93] however they can be complicated by errors stemming from the variations in the efficiency of delivery and detection of light.

Herein lies one of the true strengths of luminescent transition metal complexes as probes for bioimaging, due to their long lifetimes, complexes can be designs to be sensitive to a multitude of important analytes in their environmental. This permits detections and often quantification of key analytes in live cells or even *in vivo* in real time.[94]

2.4.1 Lifetime Imaging Methods

FLIM has been a steadily growing field which offers new information not normally available from optical techniques and has been used for many applications.[93] Fluorescence and phosphorescence lifetimes are state functions and therefore do not depend on the initial trigger conditions such as the excitation wavelength used, duration of the pulse or single- or multi-photon excitation and does not suffer from photobleaching.[95] Instead, lifetimes are affected by the local conditions they experience while in the excited state.[96,97] They are therefore sensitive to the surrounding environment conditions such as temperature, solvent polarity, viscosity and the presence of quenchers such as oxygen. FLIM is currently used mainly on endogenous molecules, such as serotonin,[98] tryphtophan[99] and on dyes such as GFP-tagged proteins.[100] However, these all have lifetimes shorter than fifteen nanoseconds and therefore require very fast excitation sources and detectors to observe sub-nanosecond changes to the lifetimes. FLIM is capable of distinguishing spectrally similar dyes by their characteristic lifetimes but endogenous fluorophores can be a problem if they have similarly short lifetimes.

Time resolved emission microscopy (TREM), unlike FLIM, is not limited to nanosecond lifetimes by employing long-lived metal complexes with lifetimes of hundreds of nanoseconds to milliseconds.[44] This removes the technical requirements of fast detectors and excitation sources and permits rejection of short-lived autofluorescence *via* time gating (Figure 28).

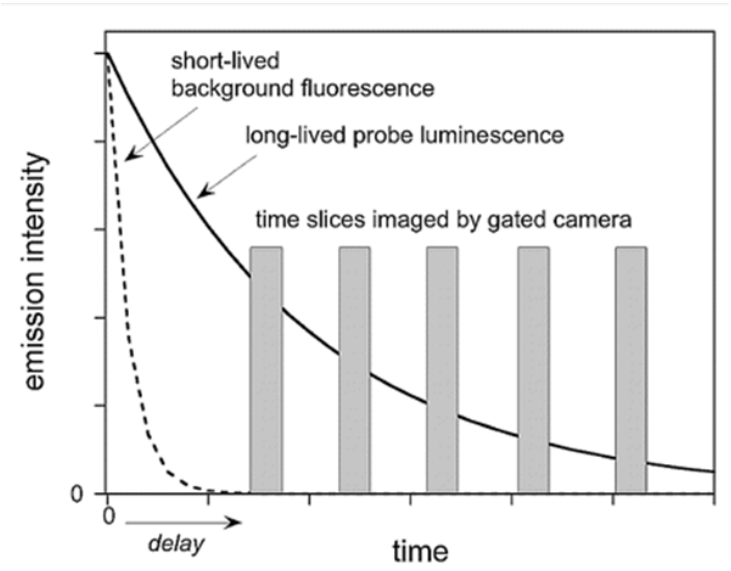

Figure 28. Graph illustrating the concept of lifetime based time-gating. Reproduced from ref.[44]

The first example of a time resolved microscope with the capability of imaging long lived phosphorescence and/or delayed fluorescence was reported using acridine orange.[101] Live 3T3 cells were stained with acridine orange and prompt and delayed fluorescence images were taken. However, the setup used was limited to detecting the delayed fluorescence 50 μs after the excitation pulse. This technological limitation of the time meant that only dyes with lifetimes in excess of 50 μs were feasible. This lead to lanthanide complexes with micro- to millisecond lifetimes being exploited for TREM studies and successful studies using immunostaining were realized.[102,103] The authors however reported issues with lanthanide complexes photobleaching and this meant samples had to be embedded in anti-fade media.

Further improvements were reported on a time resolved microscope with a shorter delay time of 2 μs. This facilitated time resolved studies of platinum (II) porphyrins on silica beads[104], which lead to platinum (II) and palladium (II) porphyrins conjugates being utilized for autofluorescence-free immunostaining[105] and DNA labelling.[106]

Phosphorescence lifetime imaging (PLIM) and TREM are two terms used in the literature, which yield similar results from different set ups, so avoid ambiguity, PLIM and TREM will be described here. Both PLIM and TREM measure the lifetimes of luminophores pixel by pixel in a sample by scanning over each pixel with a laser and measuring the subsequent photons emitted.[45,107] Each pixel is then viewed together as an image much like a standard image generated from a confocal microscope but with a lifetime value, as well as an intensity value measured at each pixel. Thus allowing the production of a lifetime map of a sample. The major difference arises in the laser setup used for these experiments. In TREM the laser is set in cavity dumped mode, the consequence of which is the repetition rate of the laser is reduced so that the gap between each pulse is around 3 μs, instead of ~13 ns. This is important because it allows longer emitters like metal complexes to decay back down to the ground state and measure all the photons emitted before the sample is re-excited by the following pulse. The acquisition of the full decay curve means the lifetime of the sample can more accurately measured. PLIM on the other hand uses the normal 76 MHz repetition but electronically gates the laser out when the lifetime measurements are being made. Therefore, the sample is being excited by a laser with a high repetition rate into its excited state and the laser is then gated to allow the detector to take measurements of the lifetimes. This method give more flexibility than the TREM setup as the measurement window can be changed to different times to better fit the lifetime of the sample used.

2.4.2 Oxygen Sensing *in Vivo*

On absorption of a photon, metal based luminophores become excited into a singlet state which undergoes rapid intersystem crossing to yield an excited triplet state. Relaxation from this state *via* emission is a spin forbidden transition and therefore a long-lived state and it's this long-lived triplet state that can interact with molecular oxygen. Molecular oxygen in its native triplet state can accept energy from the excited triplet state of the luminophore, quenching the emission and generating reactive singlet oxygen.[94] This quenching follows standard stern-volmer kinetics, allowing the concentration of oxygen to be mapped by the measuring the lifetimes of the phosphorescence.

The early examples of phosphorescence lifetimes being used to detect oxygen utilized tin, yttrium, zinc and palladium (II) derivatives of meso-tetra-(4-sulfonatophenyl)-porphine, meso-tetra-(N-methyl-4-pyridyl)-porphine and coproporphyrin.[108] These complexes all have phosphorescence lifetimes of 350 μs or greater in solution and these increased in the presence of bovine calf serum. This was attributed to the binding pockets of the proteins present shielding the complexes from quenchers. The complexes were reported to follow simple pseudo first-order quenching by oxygen as described by stern-volmer kinetics. As such, it was possible to calculate the oxygen concentration within a sample directly by measuring the lifetime of the metal complex present. Prior to this method, measuring oxygen within biological samples required the use of microelectrodes.[109] This method was then expanded to *in vivo* imaging of oxygen concentration in liver tissue using palladium (II) coproporphyrin.[110] The sample was placed in a gas chamber and starved of oxygen, the oxygen concentration was then steadily raised while monitoring the redistribution within the liver tissue.

Further work was done with a palladium (II) meso-tetra (4-carboxyphenyl) porphine which was known to bind in serum albumin. This was advantageous as the phosphorescence lifetime of the compound in physiological condition was relatively independent of pH and ionic composition. Thus allowing the development of a calibration constant for the oxygen-dependant quenching of the complex in the presence of serum.[111] The development of a calibration constant in physiological media laid the groundwork for the use of palladium (II) prophines and porphyrins as oxygen sensors *in vivo*.

Two more palladium (II) porphyrins were developed as non-invasive oxygen sensors, again with calibration constants independent of pH.[112] These polyglutamic palladium (II) porphyrin dendrimers have good solubility in biological fluids but low membrane permeability allowing imaging without the phosphor diffusing out of the blood. The application of these complexes was demonstrated by determination of the oxygen distribution of a subcutaneous tumour in rats (fig 29.). These palladium (II) complexes have also been utilized to measure oxygen concentration in mouse[113,114] and cat[115] eye, mouse[116] and piglet[117] brain and cancerous tumours.[118]

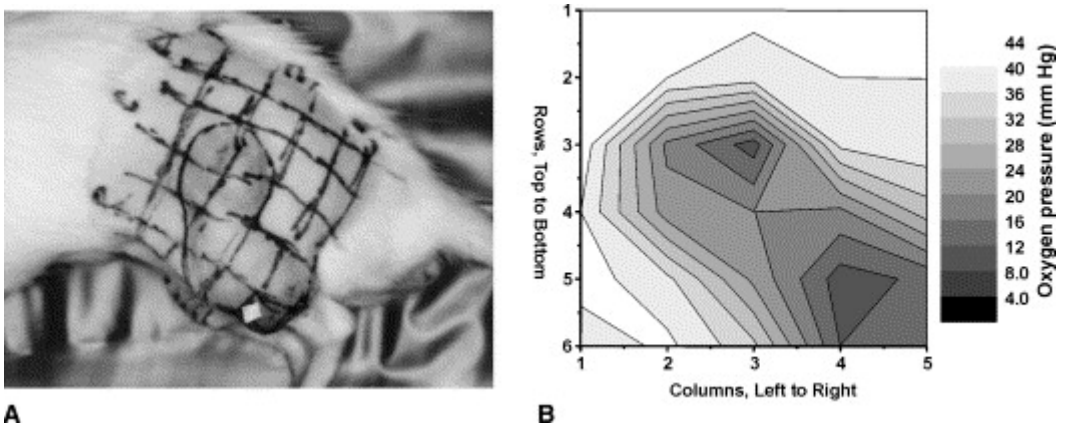

Figure 29. Oxygen measurements in anesthetised Fisher rats with a subcutaneous 9L glioma. (A) Tumour marked by 6 x 5 grid on skin. (B) Contour plot of oxygen concentration with the rows and columns identified. Adapted from ref.[112]

The next development in the field has come from the utilisation of two-photon microscopy. Two-photon microscopy exploits the possibility of molecules to absorb two photons of approximately half the energy required to excite the molecule. The potential of this technique becomes evident when you consider that biological tissue is relatively transparent to infrared radiation, thus allowing greater penetration and less scattering(Fig 30.). Moreover, due to the high photon flux required for two-photon absorption to be likely to occur, only luminophores at the focal plane are excited and luminophores above and below the field of view are not excited by the excitation beam giving greater a signal to noise ratio. However, two-photon absorption is reliant on the luminophore having a reasonable two-photon cross section so that two-photon absorption is sufficient.

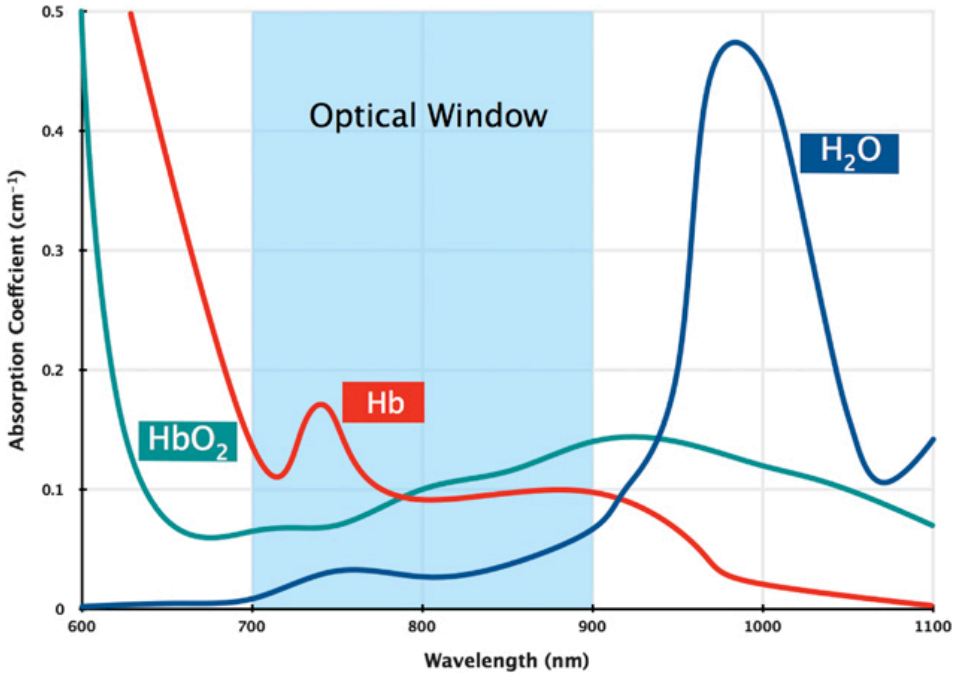

Figure 30. Absorption spectra of major tissue light absorbers highlighting the optical window between 700 nm and 900 nm. From ref.[119]

The widely used palladium (II) porphyrin systems were found to have poor two-photon absorption cross sections. In light of this, a palladium (II) porphyrin dendrimer with coumarins attached to act as two-photon "antenna" dyes which channel two-photon excitation via energy transfer was developed.[120] Coumarins were chosen as the "antenna" as energy transfer between courmarins and dendrimer like porphyrin structures are well understood. Once the energy is channelled, the metalloporphyrin is excited into its oxygen sensitive triplet state. However, the gain in emission from the triplet state of the palladium (II) porphyrin core wasn't directly proportional to the increase in two-photon cross section from the "antenna" dyes. This inconsistency was suggested to be due to energy transfer processes caused by two-photon excitation and the potential for charge transfer to occur, quenching the phosphorescence. The effectiveness of these dendrimers as an oxygen probe was illustrated in a proof of principal experiment on oxygen removal enzymes like glucose oxidase and catalase in a glass capillary and also in human endothelial cells.[121]

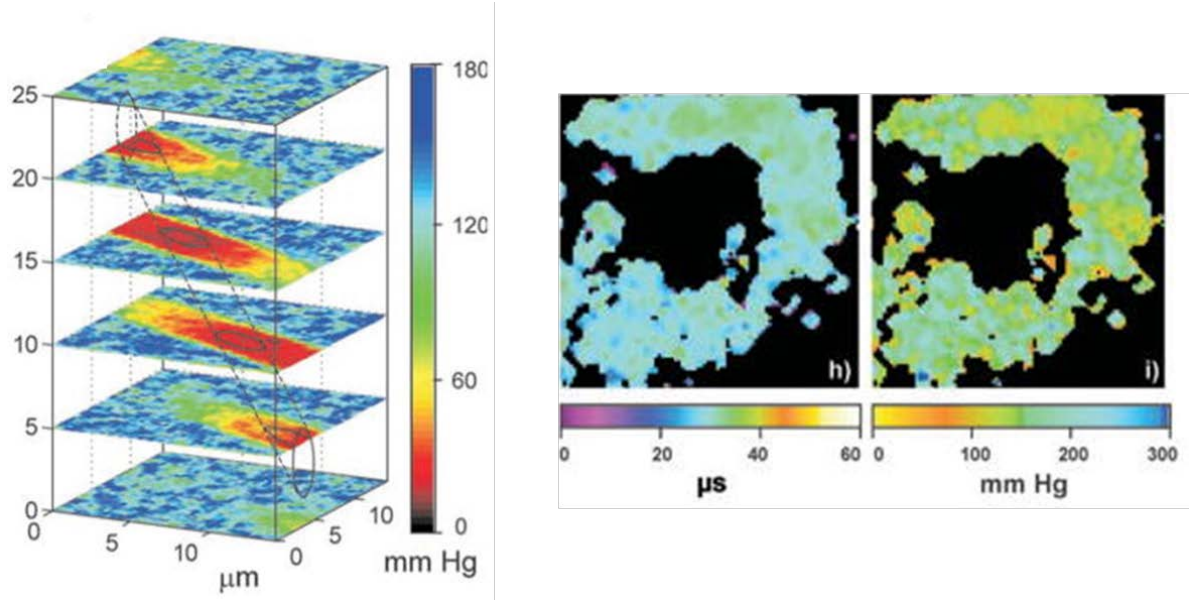

Figure 31. Z-stack of pO_2 images in a glass capillary (left), phosphorescence lifetime image of human umbilical vein endothelial cells (centre) pO_2 image calculated from the lifetime image (right). Adapted from ref.[121]

To overcome the problems that arose with the dendrimer, further development using rhodamine based "antenna" were used. Rhodamine has a much greater two-photon cross section that courmarins (~200 GM vs. courmarins tens of GM) and good photostability making them good antenna candidates. These were also found to suffer quenching by energy transfer but when rigid nonconducting decaproline linkers were used the energy transfer was supressed.[122] This modification showed a linear amplification of two-photon absorption with addition of "antenna" and good oxygen sensitivity.

Following the development of these dendrimers the focus for these oxygen probes has been to utilise the two-photon microscopy's good axial(z) resolution and tissue penetration to map the lifetimes of these dendrimers in the brain[123–127] and bone marrow of live animals,[128] mapping pO_2. These advancements highlight how metal complexes have developed as *in vivo* oxygen monitors.

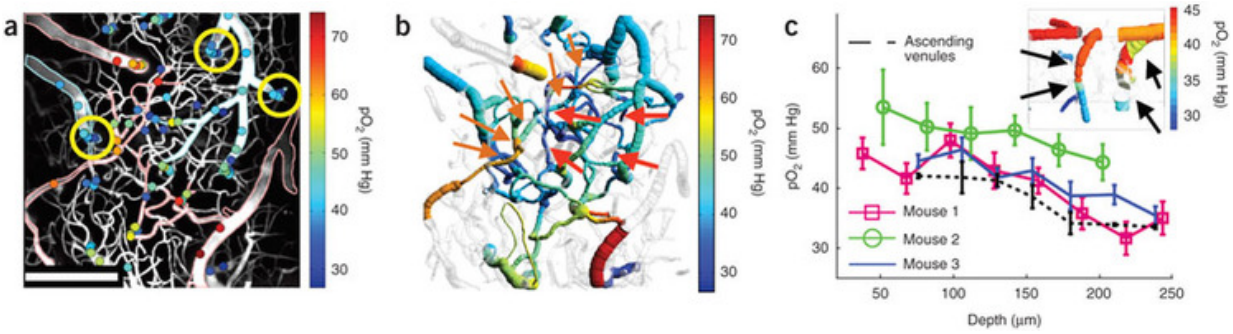

Figure 32. Measurements of oxygen concentration in cortical vasculature (A) Single point measurements of oxygen concentration overlaid on a maximum intensity projection of the vasculature structure. (B) Digitally processed image extrapolating the oxygen concentration in the vasculature. (C) Oxygen concentration dependence with cortical depth. Adapted from ref.[127]

Recently, developments of complexes which were first assessed as oxygen probes *in vitro*[129] have also been reported in *ex vivo* applications as documented by Zhdanov *et al.*[130] This study focused on the oxygen environment of umbrella cells located in the urinary bladder epithelium. The analysis of these umbrella cells found significant heterogeneous oxygen concentrations, with differences of 80 µM observed and radial oxygen gradients of 40 µM across a cell. It was also found that considerable deoxygenation occurred in areas with abundant mitochondria, which could be reduced back to ambient levels by administration of oxidative phosphorylation inhibitor antimycin A.

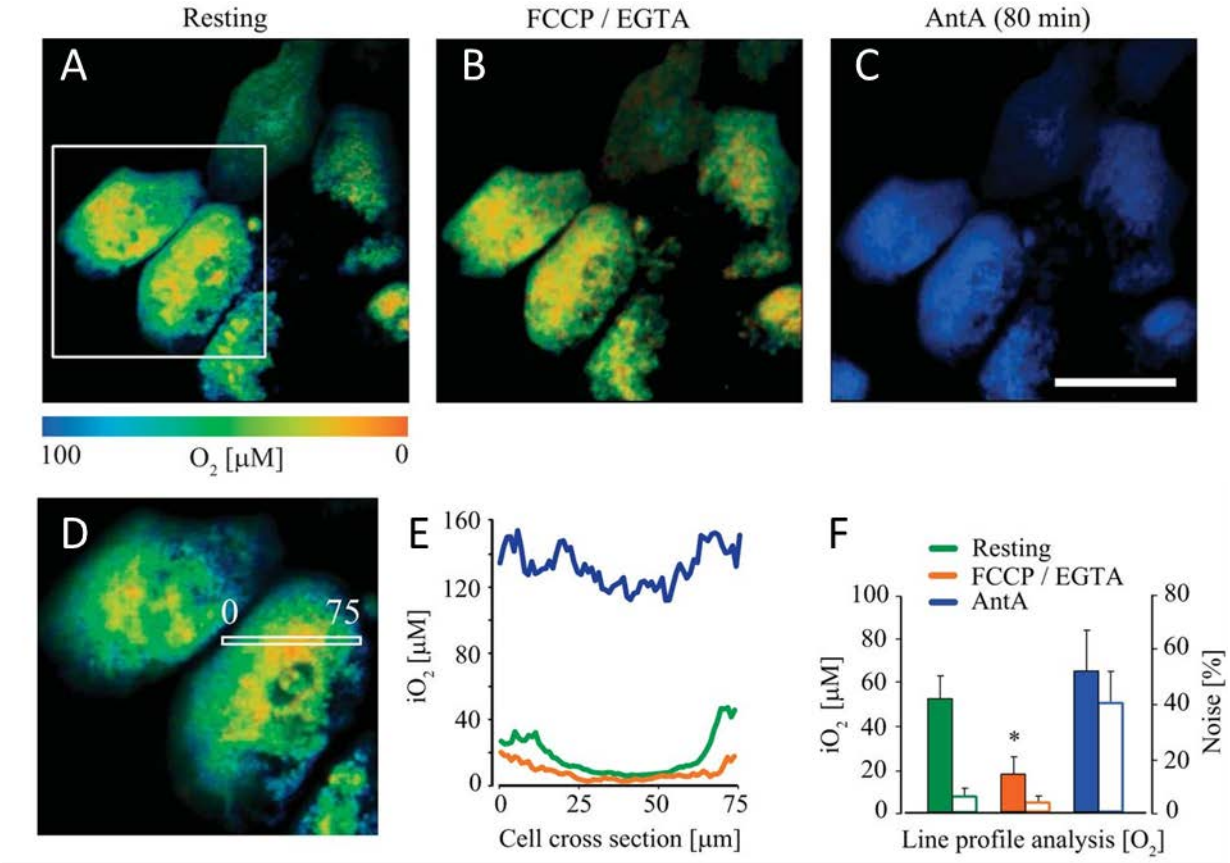

Figure 33. Effects of mitochondrial uncouplers and oxidative phosphorylation inhibitors on the oxygen gradient in umbrella cells. PLIM lifetime maps of umbrella cells (A) respiring normally, (B) After treatment with mitochondrial uncoupler, boosting mitochondria activity, (C) treatment with oxidative phosphorylation inhibitor, reducing mitochondrial activity, (D) Single z-slice of cells at rest used for line profile analysis, (E) intracellular oxygen concentration along line under different conditions, (F) histogram of oxygen concentrations under different conditions. Adapted from ref.[130]

2.4.3 Oxygen Sensing *in Vitro*

While the previous examples have focused on *in vivo* sensing, with complexes required to not penetrate cells so as to stay in the vasculature, there have been a number of complex which have been developed for *in vitro* imaging of oxygen concentration. Using complexes which penetrate cells plasma membranes offers the ability to monitor oxygen concentration intracellularly and analyse

mitochondrial function, metabolic response and the energetic status of cells by monitoring changes on a sub-organelle level.[131]

Initial work on complexes used for oxygen sensing *in vitro* was reported by Dmitriev *et al.* and focused on platinum (II) phophyrin complexes, similar to the complexes that had previously been developed for *in vivo* applications. However, due to the poor uptake of the parent complexes these complexes utilised the CPPs TAT, octaarginine[132] and bactenecin[133] to facilitate uptake of the complexes in to cells. While assessing the localisation of the complexes it was found that the TAT and octaarginine complexes localised in predominately in the secretory pathway but despite this the complexes where still found to sensitive to the cells being treated with mitochondrial uncouplers by measuring the lifetime by fluorescence reader. On the other hand, the bactenecin complex was observed to stain the mitochondria of HCT116 cells and was observed to be sensitive to oxygen concentration and could detect when live cells were treated with a mitochondrial uncoupler by fluorescence plate reader. These results highlighted how complexes could be used to observe changes in oxygen concentration *in vitro* but these experiments would only performed on bulk samples of cells and did not provide subcellular oxygen information.

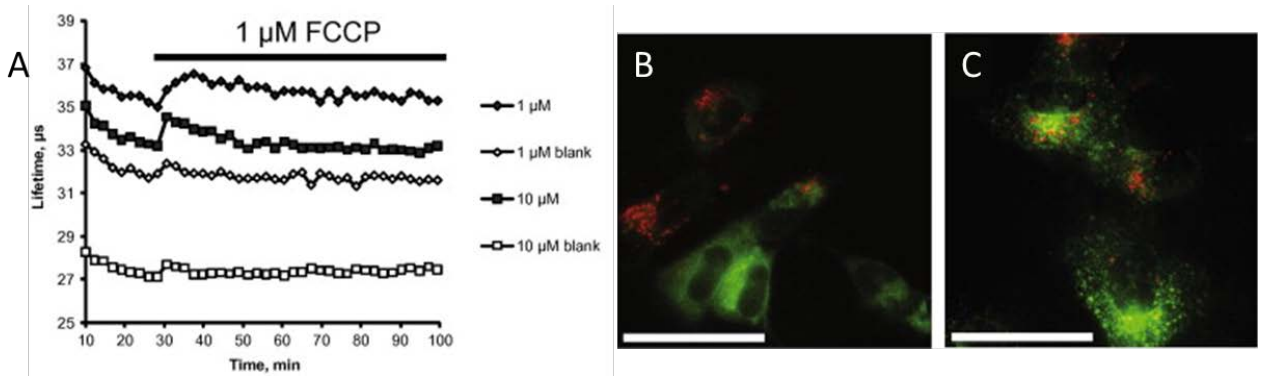

Figure 34. (A) Graph depicting the variation in lifetime of PtCPTE in HepG2 cells when treated with FCCP (mitochondrial uncoupler) (B) widefield micrographs of SH-SY5Y cells treated with PtCPTE (green) and costained with Lysotracker(red) and (C) transferrin-Alexa488(red). Adapted from ref.[132]

Further work by Dmitriev *et al.* screened platinum (II) coproporphyrins with various polypeptide chains and some with PEG chains incorporated to assess the localisation and ability of these complexes to act as intracellular oxygen probes.[18] Although a variety of CPPs were used, such as mitochondrial targeting sequences, the localisation of the complexes were predominantly punctate staining found to be in the secretory system with some also having diffuse cytoplasmic staining. These complexes, much like complexes discussed above were observed to respond to oxygen changes *in vitro* and to mitochondria uncouplers.

As well as platinum (II) based porphyrins, Iridium (III) based porphyrins have also been reported as potential oxygen sensors *in vitro*. As with the platinum (II) porphyrins, the Iridium (III) complexes

utilised two short peptide chains to aid cellular uptake and a short peptide that has been shown to bind to cell membranes of tumor cells.[134] The histidine-tetraarginine complex and truncated bactenecin complex were observed to penetrate various cell types, with partial localisation in the endoplasmic reticulum. However, the complex with the tumor binding sequence was not found to penetrate the cancer derived cell lines, HeLa cells or SH-SY5Y cells and while a number of factors were suggested for this, the authors noted the importance of the CPPs for these type of phorphyrins. These Iridium (III) porphyrins were shown to exhibit $^3O_2$ sensitive emission lifetimes in fixed cells and were observed to be responsive to various uncouplers in live cells.

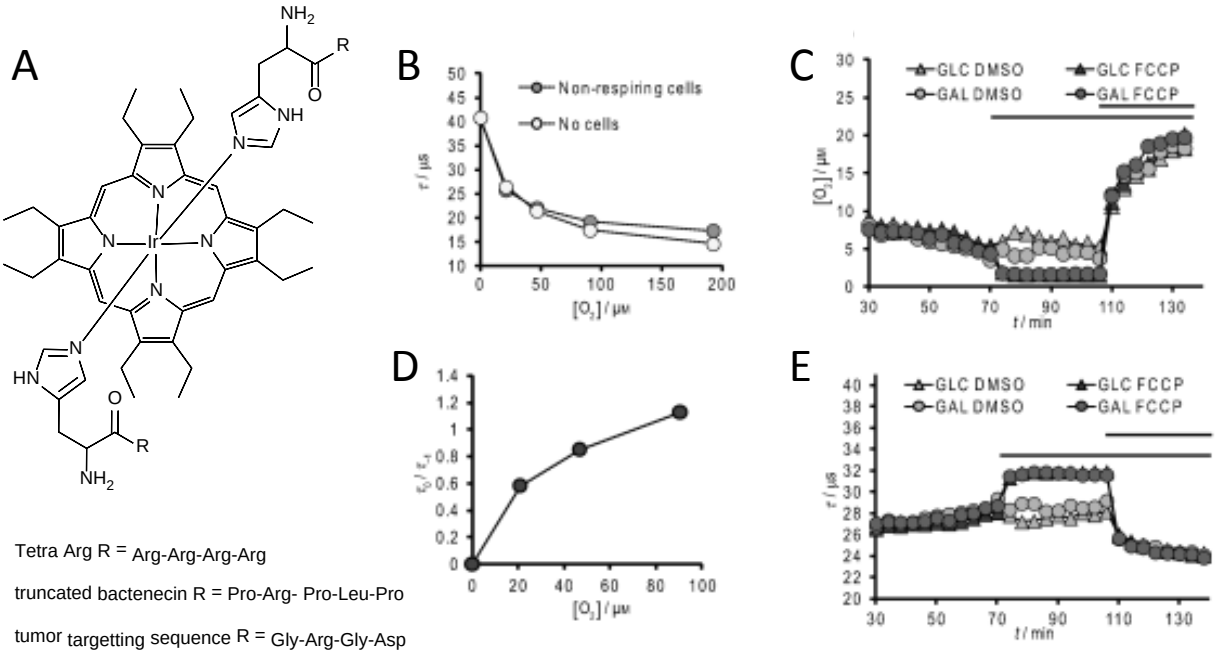

Figure 35. (A)Molecular structure of the Iridium (III) porphyrin oxygen sensor. (B) emission lifetime calibration graph in fixed MEF cells, (C) Profile of intracellular O_2 in MEF cells at rest and under metabolic stimulation, (D) Stern-Volmer plot of complex in fixed MEF cells, (E) Emission lifetimes of cells treated with FCCP or DMSO (long bar) and then AntA (short bar). Adapted from ref.[134]

Further developments looked to combined platinum (II) based porphyrins with nanoparticles, creating anionic poly(methyl methacrylate-co-methacrylic acid) nanoparticles which were used to image culture neural cells and live mouse brain slices using one- and two-photon microscopy.[135] However, development quickly returned to seeking small molecule probes and Dmitriev *et al.* reported the synthesis and exploration of some platinum (II) based fluorinated porphyrins with pendant CPP or sugars bonded to them. These complexes were explored as oxygen probes in MEF cells and multicellular aggregates of PC12 cells and as these spheroid like aggregates it was observed that the interior of these aggregates experience a lower oxygen gradient compared to the ambient O_2 concentration.[129]

In a departure from porphyrin based oxygen sensors, Baggaley *et al.* reported the use of a platinum (II) 3, 5 dipyridylbenzene (NCN) based complexes to explore the intracellular $^3O_2$ concentration of live

CHO-k1, RN22 cells and liver and skin tissue sections.[45,107] These complexes have much shorter emission lifetimes compared to that of platinum (II) and Iridium (III) porphyrins but this was used to their advantage as shorter collection windows could be utilized. The complexes where also shown to be compatible with two-photon microscopy, facilitating the probes use in two-photon PLIM, allowing excellent intracellular resolution (submicron) for oxygen sensing. Due to the oxygen shielding effects afforded by the probe when bound in the nucleus of cells it was also possible to easily discern individual nuclei of cells within tissue samples using two-photon PLIM (fig 36).

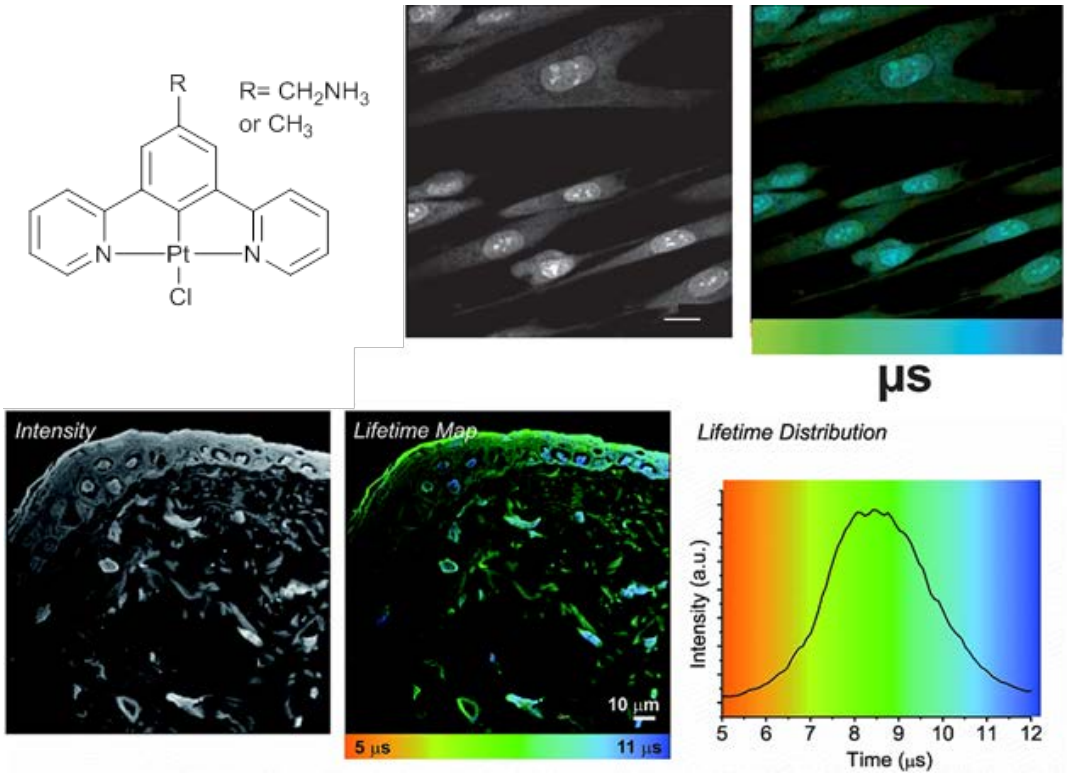

Figure 36. Molecular structure of Pt NCN complexes. Two-photon PLIM image of live human dermal fibroblast cells stained with Pt NCN; intensity image, lifetime map. Two-photon PLIM images of rat skin stained with Pt NCN complex; intensity image, lifetime map, lifetime distribution histogram. Adapted from ref.[45,107]

Following the breakthrough by Baggaley *et al.* of small molecules other than porphyrins being used for oxygen sensing, a flurry of other complexes have been reported for oxygen sensing applications *in vitro*. While complexes not based on porphyrins typically have much shorter emission lifetimes than that of platinum (II) and Iridium (III) porphyrins, the sensitivity of PLIM set-ups is such that the detection of differences in lifetime <100 ns has become routine.[49] Two noteworthy papers reported complexes by Martin e*t al.* and Yoshihara *et al.* developing ruthenium (II) based and Iridium (III) based complexes respectively which localise specifically in the mitochondria of live cells while displaying oxygen sensitivity.[136,137] Like many ruthenium (II) complexes mentioned earlier in this review, the complex contained an octaarginine CPP, facilitating its uptake and localisation with live cells. While the Iridium (III) complexes were based on a phenanthroline ligand with an amine group

attached along with various SC ligands. The sensitivity of the ruthenium (II) complex was such that the effect of antimycin A (mitochondrial uncoupler) could be observed using PLIM. These complexes are big steps towards being able to monitor oxygen concentration almost in real time within mitochondria, the primary oxygen sink within cell, essentially offering the possibility of measure the rate of respiration within live cells.

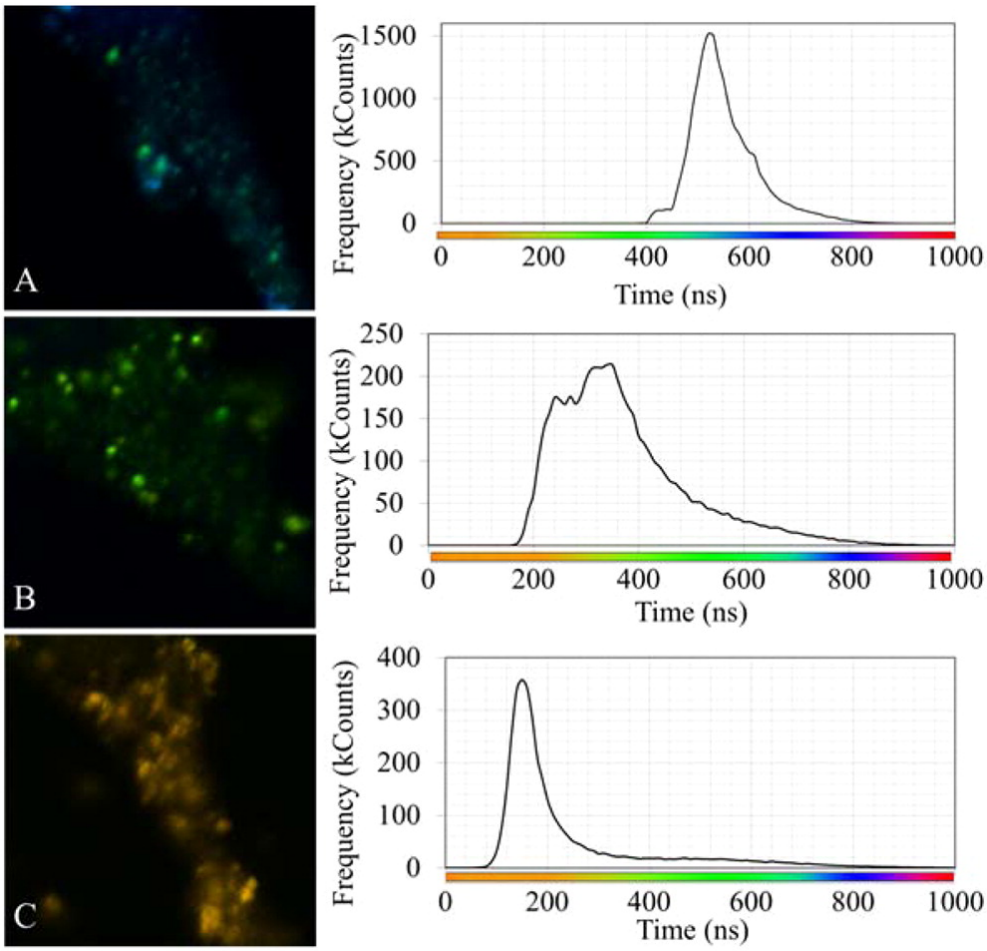

Figure 37. PLIM lifetime maps of Live HeLa cells treated with ruthenium (II) octaarginine conjugate and the lifetime distrobution histiograms. (A) cells images straight after incubation, (B) cells incubated with Antimycin A for 10 mins, (C) cells after 100 mins of incubation with Antimycin A. Reproduced from ref.[136]

Recently Liu *et al.* have reported the development of a dinuclear Iridium (III) complex that displays very strong oxygen sensitivity, with the emission of the complex changing greatly with oxygen concentration.[138] Interesting, while it often mentioned that the long emission lifetimes of transition metal complexes allows background rejection based on lifetime and time-gating, it is not often reflected in the literature. Despite this, the study highlights the reported complexes ability to be time-gated allowing the rejection of shorter lived fluorescent species. Furthermore, the complex was also found to have excellent photostability when compared to the other fluorescence dye Cell tracker blue.

Further advances by Jana *et al.* have been reported in the development of mixed metal Ir^{III}-Ln^{III} (Ln = europium or gadolinium).[139] The gadolinium based complex is a potential multimodal probe due to the luminescence of the Iridium (III) (III) and relaxivity facilitating MRI imaging arising from the gadolinium (III). The isostructural complexes were found to localise specifically in the lysosome of live HeLa cells, and curiously it was noted that despite being isostructural, the uptake of the different mixed metal complexes were distinctly different in both HeLa and MCF -7 cells. Due to the energy transfer present in the IrEu complex the gadolinium complex was used in two-photon PLIM studies and found to be sensitive to oxygen concentrations between 0 - 100 %. Interestingly, the complex was noted to have slightly different lifetimes in the lysosomes and the cytoplasm across the range of O_2 concentrations tested, this was suggested to be due to the differing microenvironments present with the organelles vs the cytoplasmic of the cell, leading to differing amounts of shielding from $^3O_2$ concentration.

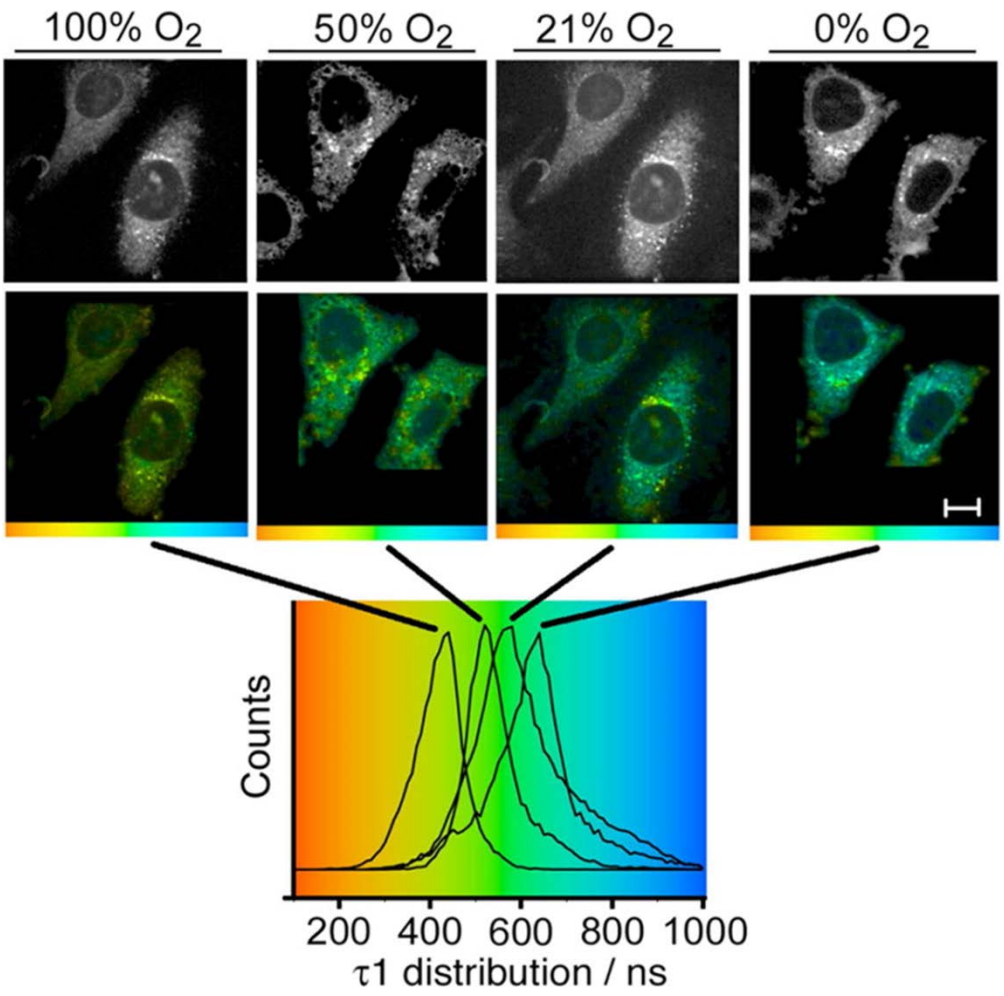

Figure 38. Two-photon PLIM images of HeLa cells treated with IrGd complex under various oxygen concentrations. Reproduced from ref.[139]

2.5 Summary

The rapid development of luminescent transition metal complexes of the last 20 years has now reached a point where the number of complexes available that localise specifically and have a wide colour tuning potential challenge commercial dyes.[1,2,47,140] Many of the complexes discussed above fulfil the ideal criteria of bioimaging probes set out at the beginning of this review. With large numbers of metal complexes only displaying toxicity well above the concentrations used to image samples, metal complexes are beginning to offer real alternative to commercial dyes. One of the keys areas of development still remains the choice of ligand, as this can affect the size, charge and lipophilicity of the complex and ultimately decide the intracellular fate of the complex.

A wide variety of metal complexes have been designed and shown to localise specifically in a whole host of cellular organelles. With this specificity comes the potential to use these complexes to answer biological questions, especially where long term tracking is of interest as these complexes typically exhibit photostability well above that of their commercial organic dye competitors. Ruthenium (II) and platinum (II) based complexes have been shown to be particularly useful for imaging the nuclei of cells and even looking for specific mismatches in the structure of DNA. Imaging nucleoli is dominated by platinum (II) and Iridium (III) complexes which tend to bind proteins associated with the nucleoli over DNA or RNA. Complexes used for imaging the ER of cells was generally achieved using Iridium (III) complex, however the vast majority of complexes that localised in the ER were found to cause ER stress and exhibited toxicity at low concentrations. The imaging of the Golgi apparatus was also dominated by Iridium (III) complexes, including an octanuclear Iridium (III) complex, and high toxicity was noted in some of these complexes. Many complexes have been reported to stain the mitochondria, with Iridium (III) complex dominating but a number of examples of platinum (II) and rhenium (I) complex also being reported. Of the organelles, mitochondrial specific dyes have seen the greatest development, with colour tuning offering a wide colour palette and two-photon microscopy allowing exquisitely detailed images of complex samples to be obtained. Finally, lysosome imaging primarily consist of Iridium (III) and platinum (II) complexes, consistently featuring the presence of pH sensitive groups providing a mechanism to trap complexes in the low pH environment of the lysosome.

Although continued development has now allowed transition metals to compete with commercial dyes in terms of performance, one of their keys advantages is lifetime imaging. While FLIM has been used to superb effect, PLIM offer excellent sensitivity, without the requirement for extremely fast lasers and detectors. Developments in lifetime imaging have progressed now to such a point that the oxygen concentrations of brain, eye and even bone marrow vasculature of live animals can be monitored non-invasively. These achievements have been made possible by the meticulous development of transition metal complexes with specific properties and long lifetimes sensitive to local oxygen concentration.

Coupled with this, the design of probes with high two-photon cross sections, allowing oxygen measurements deep in to tissue. *In vitro* probes have also seen advances with the utilisation of mitochondrial specific probes, which display oxygen sensitivity such that changes in intracellular oxygen concentration can be detected when mitochondrial uncouplers are used. Two-photon microscopy has been used here again to facilitate oxygen sensing at intracellular resolution previously unattainable.

As the developments in microscopy techniques continue and new probes, with improved properties are required, luminescent metal complexes maybe found to have the desired properties.

2.6 References

1 Q. Zhao, C. Huang and F. Li, *Chem. Soc. Rev.*, 2011, **40**, 2508–24.

2 E. Baggaley, J. A. Weinstein and J. A. G. Williams, *Coord. Chem. Rev.*, 2012, **256**, 1762–1785.

3 M. P. Coogan and V. Fernández-Moreira, *Chem. Commun.*, 2014, **50**, 384–99.

4 A. W.-T. Choi, M.-W. Louie, S. P.-Y. Li, H.-W. Liu, B. T.-N. Chan, T. C.-Y. Lam, A. C.-C. Lin, S.-H. Cheng and K. K.-W. Lo, *Inorg. Chem.*, 2012, **51**, 13289–302.

5 M. Mauro, A. Aliprandi, D. Septiadi, N. S. Kehr and L. De Cola, *Chem. Soc. Rev.*, 2014, **43**, 4144–4166.

6 A. J. Pickard, F. Liu, T. F. Bartenstein, L. G. Haines, K. E. Levine, G. L. Kucera and U. Bierbach, *Chemistry*, 2014, 1–15.

7 V. Ramu, M. R. Gill, P. J. Jarman, D. Turton, J. a. Thomas, A. Das and C. Smythe, *Chem. - A Eur. J.*, 2015, **21**, 9185–9197.

8 T. Chen, W.-J. Mei, Y.-S. Wong, J. Liu, Y. Liu, H.-S. Xie and W.-J. Zheng, *Medchemcomm*, 2010, **1**, 73.

9 A. Leonidova, V. Pierroz, L. A. Adams, N. Barlow, S. Ferrari, B. Graham and G. Gasser, *ACS Med. Chem. Lett.*, 2014, **5**, 809–14.

10 D.-L. Ma, H.-Z. He, K.-H. Leung, D. S.-H. Chan and C.-H. Leung, *Angew. Chem. Int. Ed. Engl.*, 2013, **52**, 7666–82.

11 T. L. Riss, A. L. Niles and L. Minor, *Assay Guid. Man.*, 2015, 1–23.

12 K. Y. Zhang, H.-W. Liu, T. T.-H. Fong, X.-G. Chen and K. K.-W. Lo, *Inorg. Chem.*, 2010, **49**, 5432–43.

13 Q. Zhao, M. Yu, L. Shi, S. Liu, C. Li, M. Shi, Z. Zhou, C. Huang and F. Li, *Organometallics*, 2010, **29**, 1085–1091.

14 V. Fernández-Moreira, F. L. Thorp-Greenwood, A. J. Amoroso, J. Cable, J. B. Court, V. Gray, A. J. Hayes, R. L. Jenkins, B. M. Kariuki, D. Lloyd, C. O. Millet, C. F. Williams and M. P. Coogan, *Org. Biomol. Chem.*, 2010, **8**, 3888–901.

15 K. K.-W. Lo, P.-K. Lee and J. S.-Y. Lau, *Organometallics*, 2008, **27**, 2998–3006.

16 U. Neugebauer, Y. Pellegrin, M. Devocelle, R. J. Forster, W. Signac, N. Moran and T. E. Keyes, *Chem. Commun.*, 2008, **2**, 5307–9.

17 K. Y. Zhang, W. H.-T. Law and K. K.-W. Lo, *Organometallics*, 2010, **29**, 3474–3476.

18 R. I. Dmitriev, H. M. Ropiak, G. V Ponomarev, D. V Yashunsky and D. B. Papkovsky, *Bioconjug. Chem.*, 2011, **22**, 2507–18.

19 C. A. Puckett, R. J. Ernst and J. K. Barton, *Dalton Trans.*, 2010, **39**, 1159–70.

20 A. Wragg, M. R. Gill, L. McKenzie, C. Glover, R. Mowll, J. a. Weinstein, X. Su, C. Smythe and J. a. Thomas, *Chem. - A Eur. J.*, 2015, **21**, 11865–11871.

21 C. a Puckett and J. K. Barton, *Biochemistry*, 2008, **47**, 11711–6.

22 A. J. Amoroso, R. J. Arthur, M. P. Coogan, J. B. Court, V. Fernández-Moreira, A. J. Hayes, D. Lloyd, C. Millet and S. J. A. Pope, *New J. Chem.*, 2008, **32**, 1097.

23 C.-K. Koo, K.-L. Wong, C. W.-Y. Man, H.-L. Tam, S.-W. Tsao, K.-W. Cheah and M. H.-W. Lam, *Inorg. Chem.*, 2009, **48**, 7501–3.

24 A. T. Jones and E. J. Sayers, *J. Control. Release*, 2012, **161**, 582–91.

25 K. M. Stewart, K. L. Horton and S. O. Kelley, *Org. Biomol. Chem.*, 2008, **6**, 2242–55.

26 M. R. Gill and J. A. Thomas, *Chem. Soc. Rev.*, 2012, **41**, 3179–92.

27 A. E. Friedman, J.-C. Chambron, J. Sauvage, N. J. Turro and J. K. Barton, *J. Am. Chem. Soc.*, 1990, **112**, 4960–4962.

28 C. Hiort, P. Lincoln and B. Norden, *J. Am. Chem. Soc.*, 1993, **115**, 3448–3454.

29 C. Rajput, R. Rutkaite, L. Swanson, I. Haq and J. A. Thomas, *Chem. - A Eur. J.*, 2006, **12**, 4611–4619.

30 C. A. Puckett and J. K. Barton, *J. Am. Chem. Soc.*, 2007, **129**, 46–7.

31 E. Musatkina, H. Amouri, M. Lamoureux, T. Chepurnykh and C. Cordier, *J. Inorg. Biochem.*, 2007, **101**, 1086–9.

32 M. R. Gill, J. Garcia-Lara, S. J. Foster, C. Smythe, G. Battaglia and J. A. Thomas, *Nat. Chem.*, 2009, **1**, 662–7.

33 C. A. Puckett and J. K. Barton, *J. Am. Chem. Soc.*, 2009, **131**, 8738–9.

34 C. A. Puckett and J. K. Barton, *Bioorganic Med. Chem.*, 2010, **18**, 3564–3569.

35 L. Cosgrave, M. Devocelle, R. J. Forster and T. E. Keyes, *Chem. Commun.*, 2010, **46**, 103–105.

36 M. R. Gill, H. Derrat, C. G. W. Smythe, G. Battaglia and J. A. Thomas, *ChemBioChem*, 2011, **12**, 877–880.

37 A. Wragg, M. R. Gill, D. Turton, H. Adams, T. M. Roseveare, C. Smythe, X. Su and J. a Thomas, *Chem. - A Eur. J.*, 2014, **20**, 14004–14011.

38 L. Blackmore, R. Moriarty, C. Dolan, K. Adamson, R. J. Forster, M. Devocelle and T. E. Keyes, *Chem. Commun.*, 2013, **49**, 2658–2660.

39 H. Song, J. T. Kaiser and J. K. Barton, *Nat. Chem.*, 2012, **4**, 615–20.

40 A. J. McConnell, H. Song and J. K. Barton, *Inorg. Chem.*, 2013, **52**, 10131–10136.

41 J. Lippard, *Acc. Chem. Res.*, 1978, **11**, 211–217.

42 K. W. Jennette, S. J. Lippard, G. A. Vassiliades and W. R. Bauer, *Proc. Natl. Acad. Sci. U. S. A.*, 1974, **71**, 3839–43.

43 C. S. Peyratout, T. K. Aldridge, D. K. Crites, D. R. McMillin and D. R. M. J, *Inorg. Chem.*, 1995, **34**, 4484–4489.

44 S. W. Botchway, M. Charnley, J. W. Haycock, A. W. Parker, D. L. Rochester, J. A. Weinstein and J. A. G. Williams, *Proc. Natl. Acad. Sci. U. S. A.*, 2008, **105**, 16071–6.

45 E. Baggaley, S. W. Botchway, J. W. Haycock, H. Morris, I. V. Sazanovich, J. A. G. Williams and J. A. Weinstein, *Chem. Sci.*, 2014, **5**, 879–886.

46 C. Dragonetti, A. Colombo, F. Fiorini, D. Septiadi, F. Nisic, A. Valore, D. Roberto, M. Mauro and L. De Cola, *Dalt. Trans.*, 2015, **44**, 8478–8487.

47 Y. You, *Curr. Opin. Chem. Biol.*, 2013, **17**, 699–707.

48 C. Li, M. Yu, Y. Sun, Y. Wu, C. Huang and F. Li, *J. Am. Chem. Soc.*, 2011, **133**, 11231–9.

49 S. Liu, H. Liang, K. Y. Zhang, Q. Zhao, X. Zhou, W. Xu and W. Huang, *Chem. Commun.*, 2015, **51**, 7943–7946.

50 C.-K. Koo, L. K.-Y. So, K.-L. Wong, Y.-M. Ho, Y.-W. Lam, M. H.-W. Lam, K.-W. Cheah, C. C.-W. Cheng and W.-M. Kwok, *Chem. A Eur. J.*, 2010, **16**, 3942–50.

51 C.-K. Koo, K.-L. Wong, C. W.-Y. Man, Y.-W. Lam, L. K.-Y. So, H.-L. Tam, S.-W. Tsao, K.-W. Cheah, K.-C. Lau, Y.-Y. Yang, J.-C. Chen and M. H.-W. Lam, *Inorg. Chem.*, 2009, **48**, 872–8.

52 S. R. Jean, D. V Tulumello, S. P. Wisnovsky, E. K. Lei, M. P. Pereira and S. O. Kelley, *ACS Chem. Biol.*, 2014, **9**, 323–333.

53 D. Septiadi, A. Aliprandi, M. Mauro and L. De Cola, *RSC Adv.*, 2014, **4**, 25709.

54 K. Y. Zhang, S. P.-Y. Li, N. Zhu, I. W.-S. Or, M. S.-H. Cheung, Y.-W. Lam and K. K.-W. Lo, *Inorg. Chem.*, 2010, **49**, 2530–40.

55 N. Viola-Villegas, A. E. Rabideau, M. Bartholoma, J. Zubieta and R. P. Doyle, *J. Med. Chem.*, 2009, **52**, 5253–5261.

56 A. Leonidova, V. Pierroz, R. Rubbiani, Y. Lan, A. G. Schmitz, A. Kaech, R. K. O. Sigel, S. Ferrari and G. Gasser, *Chem. Sci.*, 2014, **5**, 4044.

57 M. Smith and S. Wilkinson, *Essays Biochem.*, 2017, **61**, 625–635.

58 R. Cao, J. Jia, X. Ma, M. Zhou and H. Fei, *J. Med. Chem.*, 2013, **56**, 3636–44.

59 C. YANG, F. Mehmood, T. L. Lam, S. L.-F. Chan, Y. Wu, C.-S. Yeung, X. Guan, K. Li, C. Y.-S. Chung, C. Zhou, T. Zou and C.-M. Che, *Chem. Sci.*, 2016, **7**, 3123–3136.

60 T. F. Anjong, G. Kim, H. Y. Jang, J. Yoon and J. Kim, *New J. Chem.*, 2017, **41**, 377–386.

61 M. R. Gill, D. Cecchin, M. G. Walker, R. S. Mulla, G. Battaglia, C. Smythe and J. A. Thomas,

Chem. Sci., 2013, **4**, 4512–4519.

62 T. Zou, C.-N. Lok, Y. M. E. Fung and C.-M. Che, *Chem. Commun.*, 2013, **49**, 5423–5.

63 A. Palmioli, A. Aliprandi, D. Septiadi, M. Mauro, A. Bernardi, L. De Cola and M. Panigati, *Org. Biomol. Chem.*, 2017, **15**, 1686–1699.

64 E. Ferri, D. Donghi, M. Panigati, G. Prencipe, L. D'Alfonso, I. Zanoni, C. Baldoli, S. Maiorana, G. D'Alfonso and E. Licandro, *Chem. Commun. (Camb).*, 2010, **46**, 6255–7.

65 M.-W. Louie, H.-W. Liu, M. H.-C. Lam, Y.-W. Lam and K. K.-W. Lo, *Chem. - A Eur. J.*, 2011, **17**, 8304–8.

66 I. Johnson and M. T. Z. Spence, Eds., *The Molecular Probes handbook. A guide to fluorescent probes and labeling technologies*, Life Technologies, 11th edn., 2010.

67 C.-L. Ho, K.-L. Wong, H.-K. Kong, Y.-M. Ho, C. T.-L. Chan, W.-M. Kwok, K. S.-Y. Leung, H.-L. Tam, M. H.-W. Lam, X.-F. Ren, A.-M. Ren, J.-K. Feng and W.-Y. Wong, *Chem. Commun.*, 2012, **48**, 2525–7.

68 R. A. J. Smith, R. C. Hartley, H. M. Cochemé and M. P. Murphy, *Trends Pharmacol. Sci.*, 2012, **33**, 341–352.

69 S. P.-Y. Li, T. S.-M. Tang, K. S.-M. Yiu and K. K.-W. Lo, *Chem. - A Eur. J.*, 2012, **18**, 13342–54.

70 H. Petersen, P. M. Fechner, D. Fischer and T. Kissel, *Macromolecules*, 2002, **35**, 6867–6874.

71 Y. Chen, L. Qiao, L. Ji and H. Chao, *Biomaterials*, 2014, **35**, 2–13.

72 Q. Zhang, R. Cao, F. Hao and M. Zhou, *Dalt. Trans.*, 2014, **43**, 16872–16879.

73 C. Jin, J. Liu, Y. Chen, L. Zeng, R. Guan, C. Ouyang, L. Ji and H. Chao, *Chem. - A Eur. J.*, 2015, **21**, 12000–12010.

74 K. Qiu, H. Huang, B. Liu, Y. Liu, P. Zhang, Y. Chen, L. Ji and H. Chao, *J. Mater. Chem. B*, 2015, **3**, 6690–6697.

75 L. Sun, Y. Chen, S. Kuang, G. Li, R. Guan, J. Liu and L. Ji, *Chem. - A Eur. J.*, 2016, **22**, 8955–8965.

76 H. Huang, L. Yang, P. Zhang, K. Qiu, J. Huang, Y. Chen, J. Diao, J. Liu, L. Ji, J. Long and H. Chao, *Biomaterials*, 2016, **83**, 321–331.

77 G. Li, Q. Lin, L. Sun, C. Feng, P. Zhang, B. Yu, Y. Chen, Y. Wen, H. Wang, L. Ji and H. Chao, *Biomaterials*, 2015, **53**, 285–295.

78 K. Qiu, Y. Liu, H. Huang, C. Liu, H. Zhu, Y. Chen, L. Ji and H. Chao, *Dalt. Trans.*, 2016, 1–4.

79 R. Horobin and F. Rashid-Doubell, *Biotech. Histochem.*, 2013, **88**, 461–476.

80 S.-W. Lai, Y. Liu, D. Zhang, B. Wang, C.-N. Lok, C.-M. Che and M. Selke, *Photochem. Photobiol.*, 2010, **86**, 1414–1420.

81 R. Wai-Yin Sun, A. Lok-Fung Chow, X.-H. Li, J. J. Yan, S. Sin-Yin Chui and C.-M. Che, *Chem. Sci.*, 2011, 2, 728.

82 S. Wu, C. Zhu, C. Zhang, Z. Yu, W. He, Y. He, Y. Li, J. Wang and Z. Guo, *Inorg. Chem.*, 2011, **50**, 11847–9.

83 K. Mitra, S. Gautam, P. Kondaiah and A. R. Chakravarty, *ChemMedChem*, 2016, **11**, 1956–1967.

84 M. Marí, A. Morales, A. Colell, C. García-Ruiz, N. Kaplowitz and J. C. Fernández-Checa, *Biochim. Biophys. Acta*, 2013, **1830**, 3317–28.

85 J. A. Mindell, *Annu. Rev. Physiol.*, 2012, **74**, 69–86.

86 B. Zhitomirsky and Y. G. Assaraf, *Cancer Cell Microenviron.*, 2015, 3–9.

87 S. Moromizato, Y. Hisamatsu, T. Suzuki, Y. Matsuo, R. Abe and S. Aoki, *Inorg. Chem.*, 2012, **51**, 12697–706.

88 C. Y.-S. Chung, S. P.-Y. Li, M.-W. Louie, K. K.-W. Lo and V. W.-W. Yam, *Chem. Sci.*, 2013, **4**, 2453.

89 Y.-M. Ho, N.-P. B. Au, K.-L. Wong, C. T.-L. Chan, W.-M. Kwok, G.-L. Law, K.-K. Tang, W.-Y. Wong, C.-H. E. Ma and M. H.-W. Lam, *Chem. Commun.*, 2014, **50**, 4161–3.

90 K. Qiu, H. Huang, B. Liu, Y. Liu, Z. Huang, Y. Chen and L. Ji, *Appl. Mater. Interfaces*, 2016, **8**, 12702–12710.

91 C. Yik-Sham Chung, S. Po-Yam Li, K. Kam-Wing Lo and V. Wing-Wah Yam, *Inorg. Chem.*, 2016, **55**, 4650–4663.

92 A. Sansee, S. Meksawangwong, K. Chainok, K. J. Franz, M. Gál, L.-O. Pålsson, W. Puniyan, R. Traiphol, R. Pal and F. Kielar, *Dalt. Trans.*, 2016, **45**, 17420–17430.

93 M. Y. Berezin and S. Achilefu, *Chem. Rev.*, 2010, **110**, 2641–84.

94 M. Quaranta, S. M. Borisov and I. Klimant, *Bioanal. Rev.*, 2012, **4**, 115–157.

95 Y. Chen and A. Periasamy, *Microsc. Res. Tech.*, 2004, **63**, 72–80.

96 K. Suhling, P. M. W. French and D. Phillips, *Photochem. Photobiol. Sci.*, 2005, **4**, 13–22.

97 A. J. Lam, F. St-Pierre, Y. Gong, J. D. Marshall, P. J. Cranfill, M. A. Baird, M. R. McKeown, J. Wiedenmann, M. W. Davidson, M. J. Schnitzer, R. Y. Tsien and M. Z. Lin, *Nat. Methods*, 2012, **9**, 1005–12.

98 S. W. Botchway, A. W. Parker, R. H. Bisby and A. G. Crisostomo, *Microsc. Res. Tech.*, 2008, **71**, 267–73.

99 Y. Chen and M. D. Barkley, *Biochemistry*, 1998, **37**, 9976–82.

100 B. Treanor, P. M. P. Lanigan, K. Suhling, T. Schreiber, I. Munro, M. A. A. Neil, D. Phillips, D. M. Davis and P. M. W. French, *J. Microsc.*, 2005, **217**, 36–43.

101 G. Marriott, R. M. Clegg, D. J. Arndt-jovin and T. M. Jovin, *Biophys. J.*, 1991, **60**, 1374–1387.

102 L. Seveus, M. Väisälä, S. Syrjänen, M. Sandberg, A. Kuusisto, R. Harju, J. Salo, I. Hemmilä, H. Kojola and E. Soini, *Cytometry*, 1992, **13**, 329–38.

103 R. R. de Haas, N. P. Verwoerd, M. P. van der Corput, R. P. van Gijlswijk, H. Siitari and H. J. Tanke, *J. Histochem. Cytochem.*, 1996, **44**, 1091–1099.

104 E. J. Hennink, R. de Haas, N. P. Verwoerd and H. J. Tanke, *Cytometry*, 1996, **24**, 312–20.

105 R. R. de Haas, R. P. M. van Gijlswijk, E. B. van der Tol, H. J. M. a. a. Zijlmans, T. Bakker-

Schut, J. Bonnet, N. P. Verwoerd and H. J. Tanke, *J. Histochem. Cytochem.*, 1997, **45**, 1279–1292.

106 R. R. de Haas, R. P. M. van Gijlswijk, E. B. van der Tol, J. Veuskens, H. E. van Gijssel, R. B. Tijdens, J. Bonnet, N. P. Verwoerd and H. J. Tanke, *J. Histochem. Cytochem.*, 1999, **47**, 183–196.

107 E. Baggaley, I. Sazanovich, J. A. G. Williams, J. Haycock, S. W. Botchway and J. A. Weinstein, *RSC Adv.*, 2014, **4**, 35003–35008.

108 J. M. Vanderkooi, G. Maniara, T. J. Green and D. F. Wilson, *J. Biol. Chem.*, 1987, **262**, 5476–82.

109 B. R. Duling, W. Kuschinsky and M. Wahl, *Pflügers Arch. Eur. J. Physiol.*, 1979, **383**, 29–34.

110 W. Rumsey, J. Vanderkooi and D. Wilson, *Science (80-.).*, 1988, **241**, 1649–1651.

111 L. W. Lo, C. J. Koch and D. F. Wilson, *Anal. Biochem.*, 1996, **236**, 153–60.

112 I. Dunphy, S. a Vinogradov and D. F. Wilson, *Anal. Biochem.*, 2002, **310**, 191–8.

113 R. D. Shonat and A. C. Kight, *Ann. Biomed. Eng.*, 2003, **31**, 1084–1096.

114 D. F. Wilson, S. a Vinogradov, P. Grosul, M. N. Vaccarezza, A. Kuroki and J. Bennett, *Appl. Opt.*, 2005, **44**, 5239–48.

115 R. D. Shonat, D. F. Wilson, C. E. Riva and M. Pawlowski, *Appl. Opt.*, 1992, **31**, 3711–8.

116 R. D. Shonat, E. S. Wachman, W. Niu, A. P. Koretsky and D. L. Farkas, *Biophys. J.*, 1997, **73**, 1223–31.

117 D. F. Wilson, A. Pastuszko, J. E. DiGiacomo, M. Pawlowski, R. Schneiderman and M. Delivoria-Papadopoulos, *J. Appl. Physiol.*, 1991, **70**, 2691–6.

118 L. S. Ziemer, W. M. F. Lee, S. a Vinogradov, C. Sehgal and D. F. Wilson, *J. Appl. Physiol.*, 2005, **98**, 1503–10.

119 T. G. Phan and A. Bullen, *Immunol. Cell Biol.*, 2010, **88**, 438–444.

120 R. P. Briñas, T. Troxler, R. M. Hochstrasser and S. a Vinogradov, *J. Am. Chem. Soc.*, 2005, **127**, 11851–62.

121 O. S. Finikova, A. Y. Lebedev, A. Aprelev, T. Troxler, F. Gao, C. Garnacho, S. Muro, R. M. Hochstrasser and S. A. Vinogradov, *Chemphyschem*, 2008, **9**, 1673–9.

122 O. S. Finikova, T. Troxler, A. Senes, W. F. DeGrado, R. M. Hochstrasser and S. A. Vinogradov, *J. Phys. Chem. A*, 2007, **111**, 6977–90.

123 S. Sakadzić, S. Yuan, E. Dilekoz, S. Ruvinskaya, S. A. Vinogradov, C. Ayata and D. A. Boas, *Appl. Opt.*, 2009, **48**, D169-77.

124 J. Lecoq, A. Parpaleix, E. Roussakis, M. Ducros, Y. Goulam Houssen, S. A. Vinogradov and S. Charpak, *Nat. Med.*, 2011, **17**, 893–8.

125 L. E. Sinks, E. Roussakis, S. Sakadžic, G. P. Robbins, D. A. Hammer, A. Devor, D. A. Boas and S. A. Vinogradov, *Proc. SPIE*, 2011, **7903**, 79032A–79032A–8.

126 S. M. S. Kazmi, A. J. Salvaggio, A. D. Estrada, M. a Hemati, N. K. Shaydyuk, E. Roussakis, T. a Jones, S. a Vinogradov and A. K. Dunn, *Biomed. Opt. Express*, 2013, **4**, 1061–73.

127 S. Sakadzić, E. Roussakis, M. A. Yaseen, E. T. Mandeville, V. J. Srinivasan, K. Arai, S. Ruvinskaya, A. Devor, E. H. Lo, S. A. Vinogradov and D. A. Boas, *Nat. Methods*, 2010, **7**, 755–9.

128 J. A. Spencer, F. Ferraro, E. Roussakis, A. Klein, J. Wu, J. M. Runnels, W. Zaher, L. J. Mortensen, C. Alt, R. Turcotte, R. Yusuf, D. Côté, S. A. Vinogradov, D. T. Scadden and C. P. Lin, *Nature*, 2014, **508**, 269–73.

129 R. I. Dmitriev, A. V. Kondrashina, K. Koren, I. Klimant, A. V. Zhdanov, J. M. P. Pakan, K. W. McDermott and D. B. Papkovsky, *Biomater. Sci.*, 2014, **2**, 853.

130 A. V Zhdanov, A. V. Golubeva, I. A. Okkelman, J. F. Cryan and D. Papkovsky, *Am. J. Physiol. - Cell Physiol.*, 2015, **2**, ajpcell.00121.2015.

131 R. I. Dmitriev and D. B. Papkovsky, *Methods Appl. Fluoresc.*, 2015, **3**, 34001.

132 R. I. Dmitriev, A. V Zhdanov, G. V Ponomarev, D. V Yashunski and D. B. Papkovsky, *Anal. Biochem.*, 2010, **398**, 24–33.

133 R. I. Dmitriev, H. M. Ropiak, D. V Yashunsky, G. V Ponomarev, A. V Zhdanov and D. B. Papkovsky, *FEBS J.*, 2010, **277**, 4651–61.

134 K. Koren, R. I. Dmitriev, S. M. Borisov, D. B. Papkovsky and I. Klimant, *Chembiochem*, 2012, **13**, 1184–90.

135 R. I. Dmitriev, S. M. Borisov, A. V. Kondrashina, J. M. P. Pakan, U. Anilkumar, J. H. M. Prehn, A. V. Zhdanov, K. W. McDermott, I. Klimant and D. B. Papkovsky, *Cell. Mol. Life Sci.*, 2014, **72**, 367–381.

136 A. Martin, A. Byrne, C. S. Burke, R. J. Forster and T. E. Keyes, *J. Am. Chem. Soc.*, 2014, **136**, 15300–9.

137 T. Yoshihara, S. Murayama, T. Masuda, T. Kikuchi, K. Yoshida, M. Hosaka and S. Tobita, *J. Photochem. Photobiol. A Chem.*, 2015, **299**, 172–182.

138 S. Liu, Y. Zhang, H. Liang, Z. Chen, Z. Liu and Q. Zhao, *Opt. Express*, 2016, **24**, 15757–15764.

139 A. Jana, B. J. Crowston, J. R. Shewring, L. K. Mckenzie, H. E. Bryant, S. W. Botchway, A. D. Ward, A. J. Amoroso, E. Baggaley and M. D. Ward, *Inorg. Chem.*, 2016, **55**, 5623–5633.

140 Y. Chen, R. Guan, C. Zhang, J. Huang, L. Ji and H. Chao, *Coord. Chem. Rev.*, 2016, **310**, 16–40.

Research objectives

The microscopy revolution is here. As discussed in Chapter 1, super resolution microscopy techniques and CLEM are emerging techniques that place tougher demands on conventional probes. One of the key requirements of super resolution microscopy is photostability, whereas correlative microscopy demands probes that can be viewed by both emission and electron microscopy techniques, without compromising one for the other. Good-to-excellent photostability is a necessary trait for application of transition metals complexes in bio-imaging applications, of which there have been many published examples over the past 5-10 years. More recently, there have been reports on a handful of complexes that also provide contrast in electron microscopy. This research will focus on exploring the ability of luminescence metal complexes as probes for super resolution microscopy and CLEM. The aims of this work can be summarised in to three key points:

(I) The assessment and development of luminescent transition metal complexes as potential CLEM probes by exploring their ability to act as contrast agents in TEM. An important facet of this will be the ability to use complexes at concentrations that are visible in both techniques without causing cytotoxicity, or compromising image quality or resolution.

(II) Explore a series of bio-compatible complexes as potentials for super resolution microscopy, comparing them to commercially available probes to assess their viability. Finding complexes that can be utilised for super resolution microscopy and electron microscopy at the same working concentration, will open up the possibility of these complexes for super resolution CLEM.

(III) To develop and / or identify luminescence metal complexes that exhibit specific cellular localisation, as well as all the necessary photophysical properties for both super resolution and electron microscopy.

If luminescent transition metal complexes can be used with the same simplicity as commercial organic dyes in super-resolution imaging, but also provide contrast in TEM, this would reduce the complexity of CLEM protocols considerably. Furthermore, if it is also possible to utilise the long emission lifetimes obtain environmental data from these complexes then these probes may be truly multimodal probes, offering a wealth of information.

Chapter 3. Exploring Pt N^C^N as a Dual Probe

3.1 Introduction

Platinum (II)(II) complexes have attracted interest in biological applications ever since the discovery of cisplatin. Interest in luminescent complexes as bioimaging probes has been an expanding over the past two decades. [1–3] These complexes typically have relatively high quantum yields of a few % or more, long emission lifetimes and good photostability, the characteristics that makes them attractive candidates for bio-imaging and lifetime based microscopy techniques. A number of these complexes have also been reported to have good two-photon cross sections, facilitating their use in two-photon microscopy, yielding improved spatial resolution.[4–10] The long emission lifetimes, often in excess of hundreds of nanoseconds or more, have also been utilised to obtain data on the local environment experienced by the probe, the most common analyte being oxygen *in vitro*[4,5,11,12] and *in vivo*[13–16] as the emission of these probes is quenched by molecular oxygen.

One such example is a class of platinum (II)(II) complexes which are derivatives of a tridentate 3,5-dipyridyl benzene ligand, that has been shown to preferentially accumulate in nuclei. These compounds have been utilised in confocal, two-photon and TP-TREM microscopy *in vitro*.[4,6] This complex is well defined and established in cells with the complex accumulating in cells within 5 minutes, while having a bright and photostable emission *in vitro*. Platinum (II) is also a third row metal and therefore has a large nucleus with which to scatter electrons effectively, potentially acting a good contrast agent. Due to these favourable properties and the well studied nature of the probe, it was decided that this complex would be used as a model complex to test as a potential dual probe. Furthermore, luminescent metal complexes as of yet, have only been reported in a single type of super resolution microscopy, STED[17] and therefore due to its previously reported excellent photostability this complex will be explored as a potential 3D SIM probe.

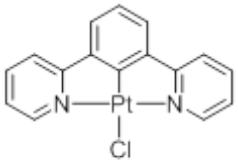

3.1

Figure 1. Molecular structure of Pt NCN, complex 3.1

The aim for this Chapter was to explore the potential for complex **3.1** to act as a contrast agent, and to assess its suitability as a label in super resolution microscopy

The complex used in this chapter were synthesised and characterised by Dr Elizabeth Baggaley, while the first report of its use in cells was reported by Botchway *et al.*[1]

3.2 Establishing Intracellular Localisation of Pt(N^C^N)Cl, Compound

The first task was to establish the localisation pattern more precisely than had been achieved previously using light microscopy. Previous work has shown that the complex strongly stains the nucleus as confirmed by its co-localisation with DAPI, that it binds DNA, and that it is a potential DNA intercalator.[6] It was also suggested to be a RNA binder as DNA and RNA have similar structures, potentially allowing the platinum (II) complex to bind in a similar fashion. Syto 82 is a commercially available nucleic acids stain which luminesces when bound to DNA or RNA, and as such seemed to be an ideal co-stain for the complex to assess it DNA and RNA binding. HeLa cells stained with complex **3.1** (100 μM in DMEM media with <1% DMSO) were found to have bright nucleus and nucleoli staining with diffuse, heterogeneous staining of the cytoplasm as previously reported.[6] Co-staining cells with complex **3.1** and Syto 82 revealed a striking similarity in their staining patterns, whilst the Pearson's coefficient for the overlaid images was calculated to be 0.96, indicating a very high correlation between the localisations and intensity of the signals between both images. This confirmed that Pt N^C^N does indeed stain DNA and RNA present within cells, indicated by strong staining of the nucleus where the vast majority of DNA is present and the nucleoli, where there is a large amount of RNA present. The diffuse staining with the cytoplasm as mentioned is heterogeneous, suggesting there could be some specific localisation of the complex within the cytoplasm in areas of high concentrations of nucleic acids.

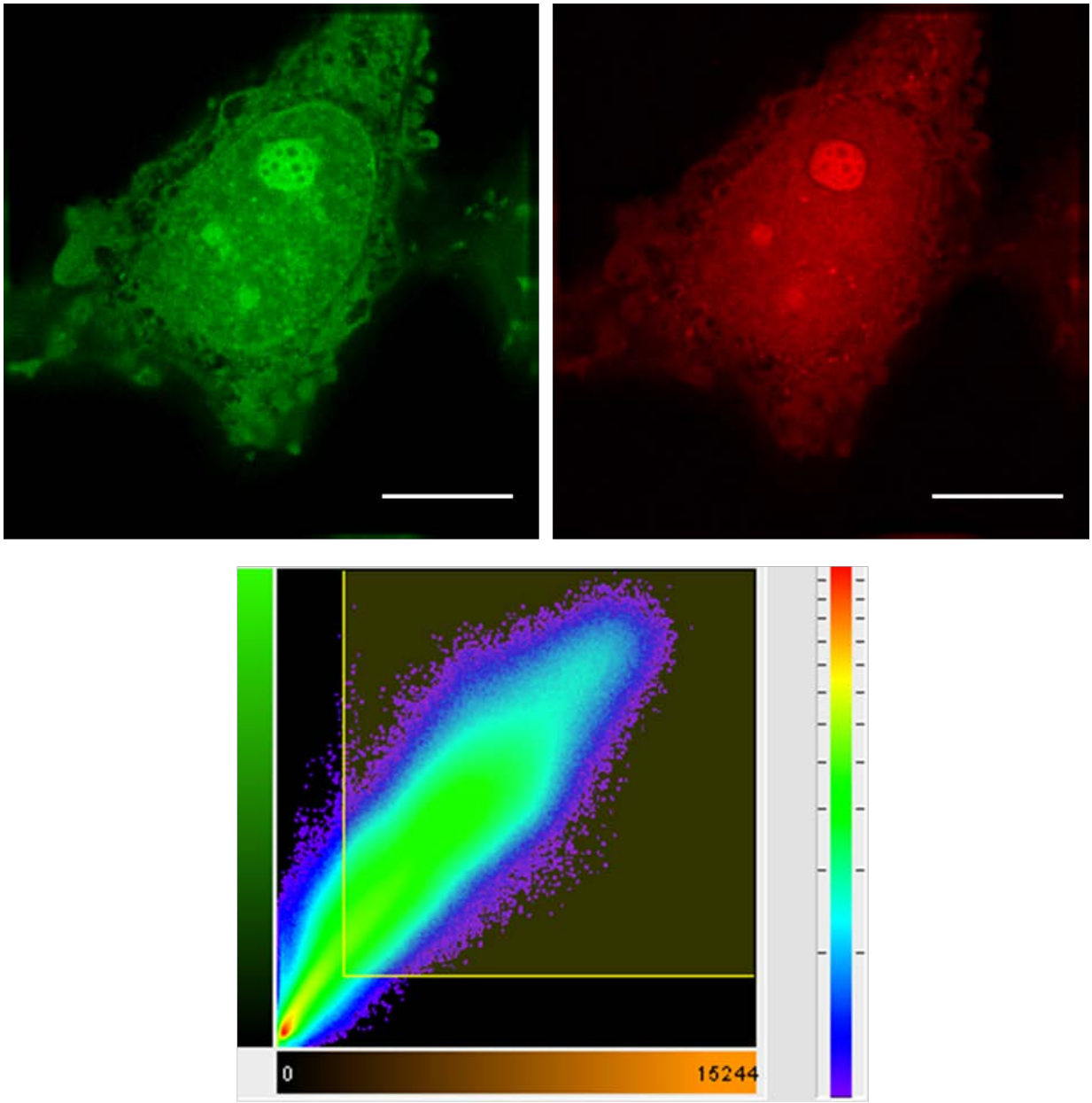

Figure 2. Widefield microscopy images of HeLa cells stained with (A) 3.1 at 100 µM, 5 mins (λ_{ex} = 405 nm) and (B) Syto 82 2.5 µM, 35 mins (λ_{ex} = 561 nm) (scale bar = 10 µm); 2D histogram

3.3 TEM Imaging

Transmission electron microscopy (TEM) functions by sending a beam of electrons through a sample. While the electrons pass through the sample they interact in a number of ways, by various types of scattering, as a result, a reduced number of electrons exit the sample and are focused onto a detector. The key attribute of atoms defining the strength of scattering is the atomic weight and therefore the heavier the atoms, the greater the scattering by that atom. Typically osmium, lead and uranyl salts are used as strong electron scatterers which bind to biomolecules, accumulating in specific areas of the

cell to provide cellular context to the electron micrographs. If the complex in this study accumulates sufficiently in cells, then this should result in sufficient scattering to be clearly visible by TEM. While standard TEM contrast agents have been established for many decades there have been a handful of studies that have used other stains as contrast agents. Platinum (II) blue has been reported as a potential substitution for uranyl acetate, utilising a multinuclear platinum (II) complex to provide contrast.[2] However this complex is non emissive and therefore not useful for CLEM applications. Emissive complexes have also be demonstrated to function as contrast agents, however these complexes have predominately been multinuclear and used in concentrations well above those used for light microscopy imaging.[3–5] Here a mononuclear, emissive complex will be assessed for potential use as a contrast agent in TEM

The first experiments were conducted under the exact conditions used for emission based imaging, where the same concentration of 3.1 was used for incubating the cells, and no additional heavy metal stains were added, to see only where the platinum (II) was visible. Live cells were treated with platinum (II) complex as described above and then fixed with glutaraldehyde (3 %) in PBS, dehydrated in an ethanol gradient, placed in propylene oxide and then covered in Araldite resin before being cured in an oven at 60 °C. These were then sectioned on a microtome and the sections viewed on a TEM. No osmium tetroxide, uranyl acetate or lead citrate were used to provide any contrast within the samples. Control cells were also prepared using the method explained above but without cells being treated with platinum (II) complex, and thus these cells demonstrate what totally unstained cells look like.

Unstained control cells displayed very little contrast in EM, with the nucleus and nucleoli faintly visible in the micrograph but no structural detail visible in the cytoplasm. This was as expected, since the most abundant atoms present with biological samples will be hydrogen, carbon, nitrogen, sulfur and phosphorus, all of which are light elements with low numbers of electrons, and therefore scatter electrons poorly. Some modest improvement in the image contrast was observed in the cells treated with platinum (II) complex compared to unstained cells: the nucleus is slightly more defined, the double membrane of the nuclear membrane visible and nucleoli more defined. This staining pattern is in agreement with the stronger staining of the nucleus and nucleoli detected by emission microscopy. None of the cytoplasmic structures were visible, which is not unexpected as the complex doesn’t stain the cytoplasm very strongly. This result was encouraging; however, it was clear that more complex was needed to be present inside the cell for contrast to be high enough to discern cytoplasmic details.

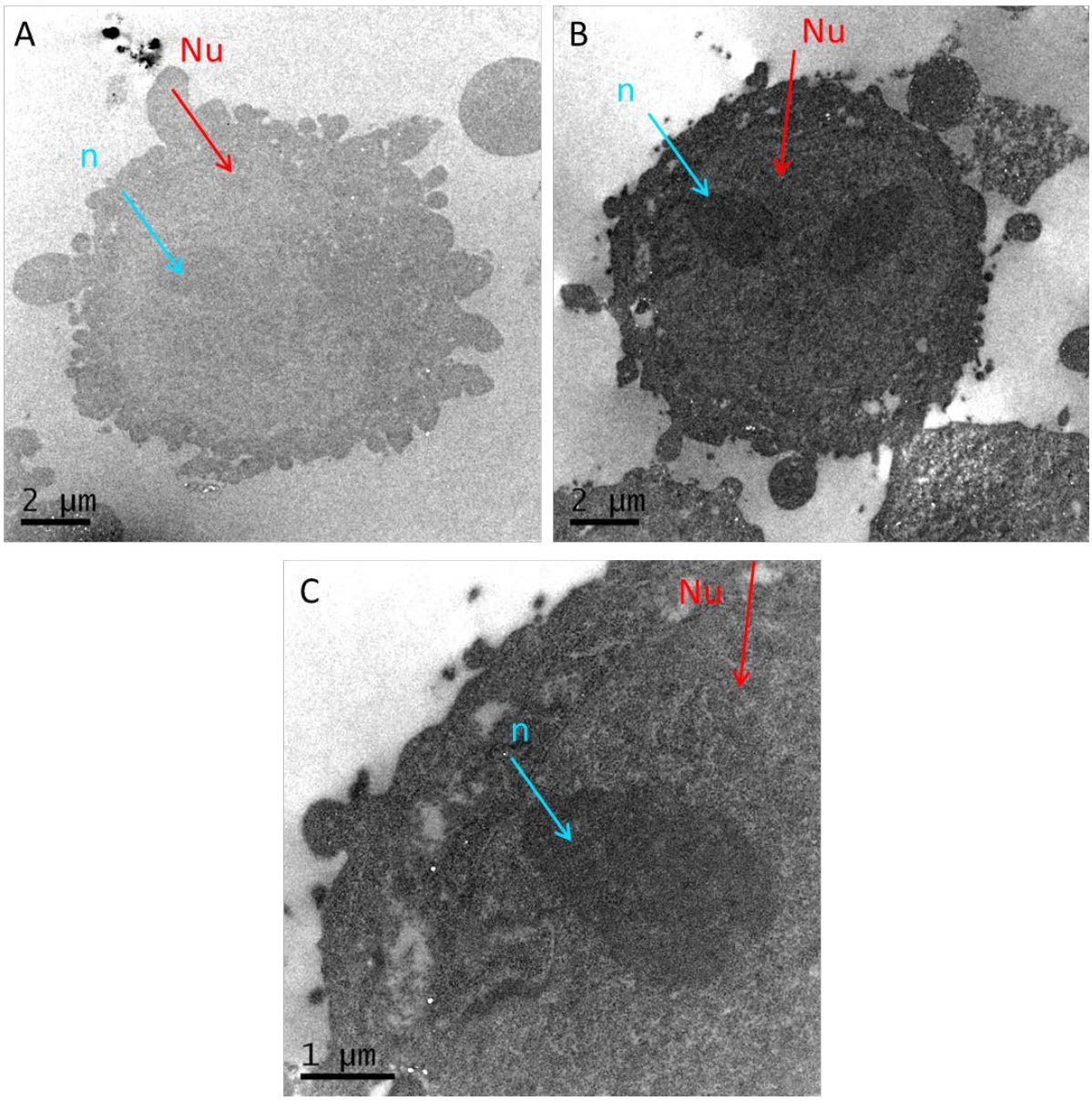

Figure 3. Electron micrograph of HeLa cells (A) with no contrast agents, (B+C) stained with complex 3.1 (100 µM, 5 mins). (Nucleus = red arrows, nucleoli = blue arrows)

The concentration that we initially used was reasonably high in comparison to other platinum (II) (II) complexes in emission based microscopy but incubations times were shorter.[18–20] Other probes have been used at much higher concentrations for TEM imaging (200 µM- 2mM)[21–24] but the complex have been found to be toxic over concentrations of 100 µM.[6] The clear choice for increasing the amount of complex present in the cell was therefore to increase incubations time, giving more of an opportunity for the complex in solution to diffuse into the cell.

It was also noted that because there was not any secondary fixative present the cells were being extracted during the dehydration steps of the TEM preparation of the samples, causing white spots in the sample where no material is left to give contrast (Fig. 4, green arrows). This could prove to be a problem if the preservation of the sample is compromised by lack of a secondary fixative. However,

the majority of the sample does appear to be retained but some extraction is apparent.

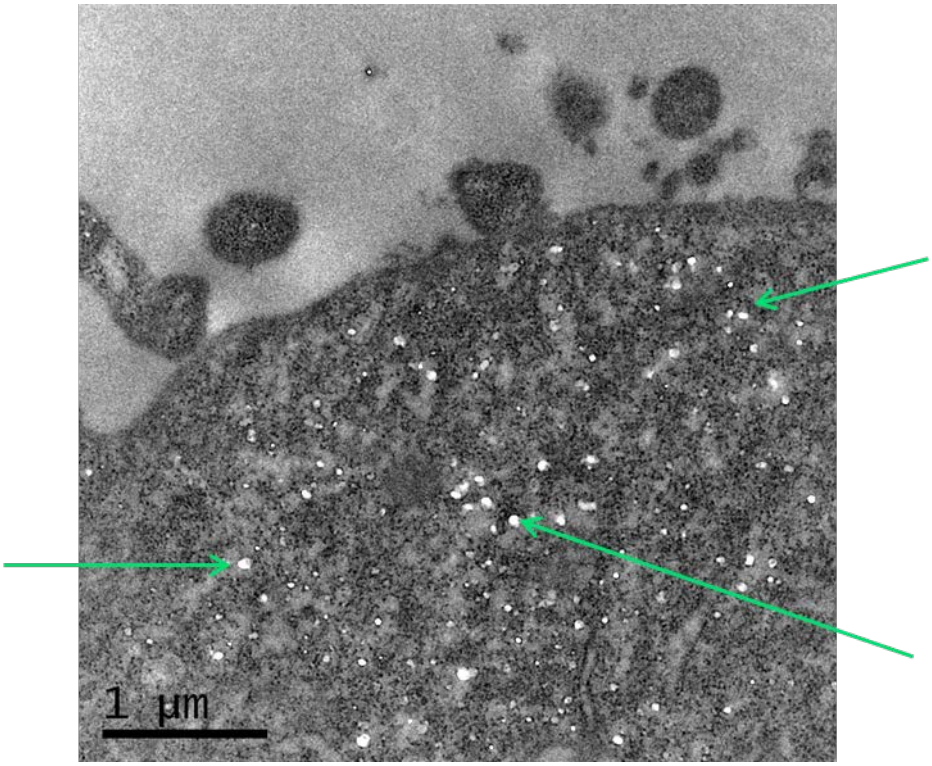

Figure 4. Electron micrograph of Hela cells showing signs of extraction due to lack of secondary fixative (green arrows).

Increasing the incubation time to 20 minutes, and thus allowing more complex to accumulate in the cells, allowed for much sharper EM images, with the nucleus being more defined, and euchromatin and heterochromatin (loosely bound and tightly bound chromatin) clearly distinguishable. The nucleoli and nuclear membrane are also much more clearly defined and the cytoplasm is much more heterogeneous with organelles starting to become visible. These results were promising but it was difficult to discern what exactly the platinum (II) complex was staining within the cytoplasm where the staining was more diffuse.

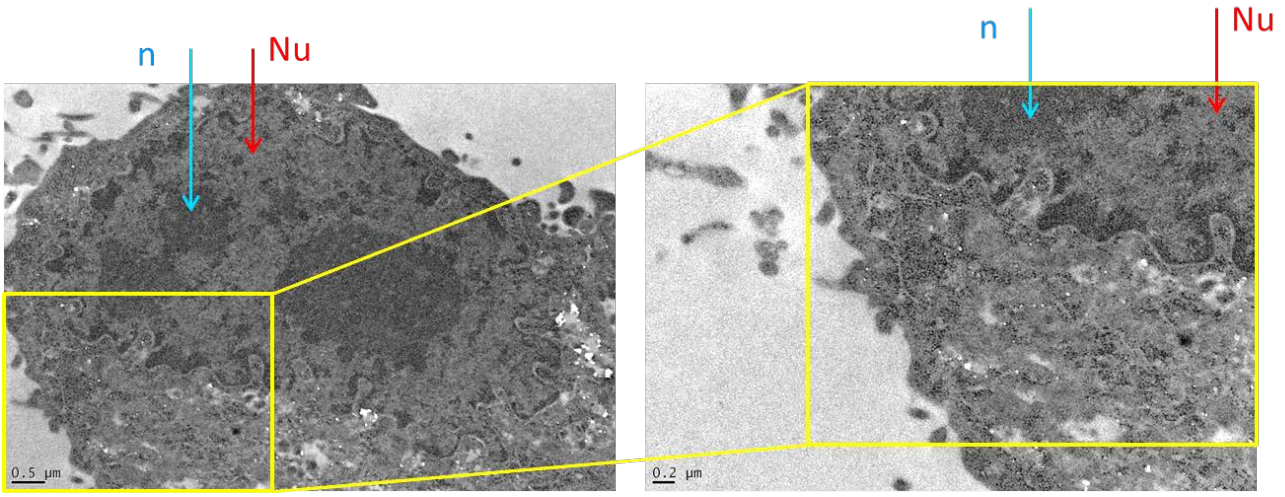

Figure 5. Electron micrograph of HeLa cells stained only with complex 3.1 (100 µM, 20 mins). (Nucleus = red arrows, nucleoli = blue arrows)

To further help elucidate the platinum (II) complex accumulation in cells it was decided that standard TEM contrast agents would be used in addition to the Pt complex to give more cellular context. It was expected that area where the platinum (II) complex were accumulating would exhibit increased contrast compared to cells stained with the standard agents. Control cells were also prepared with the same typical stains used in TEM here as a comparison to cells stained with platinum (II) complex to help determine where levels of contrast were greater.

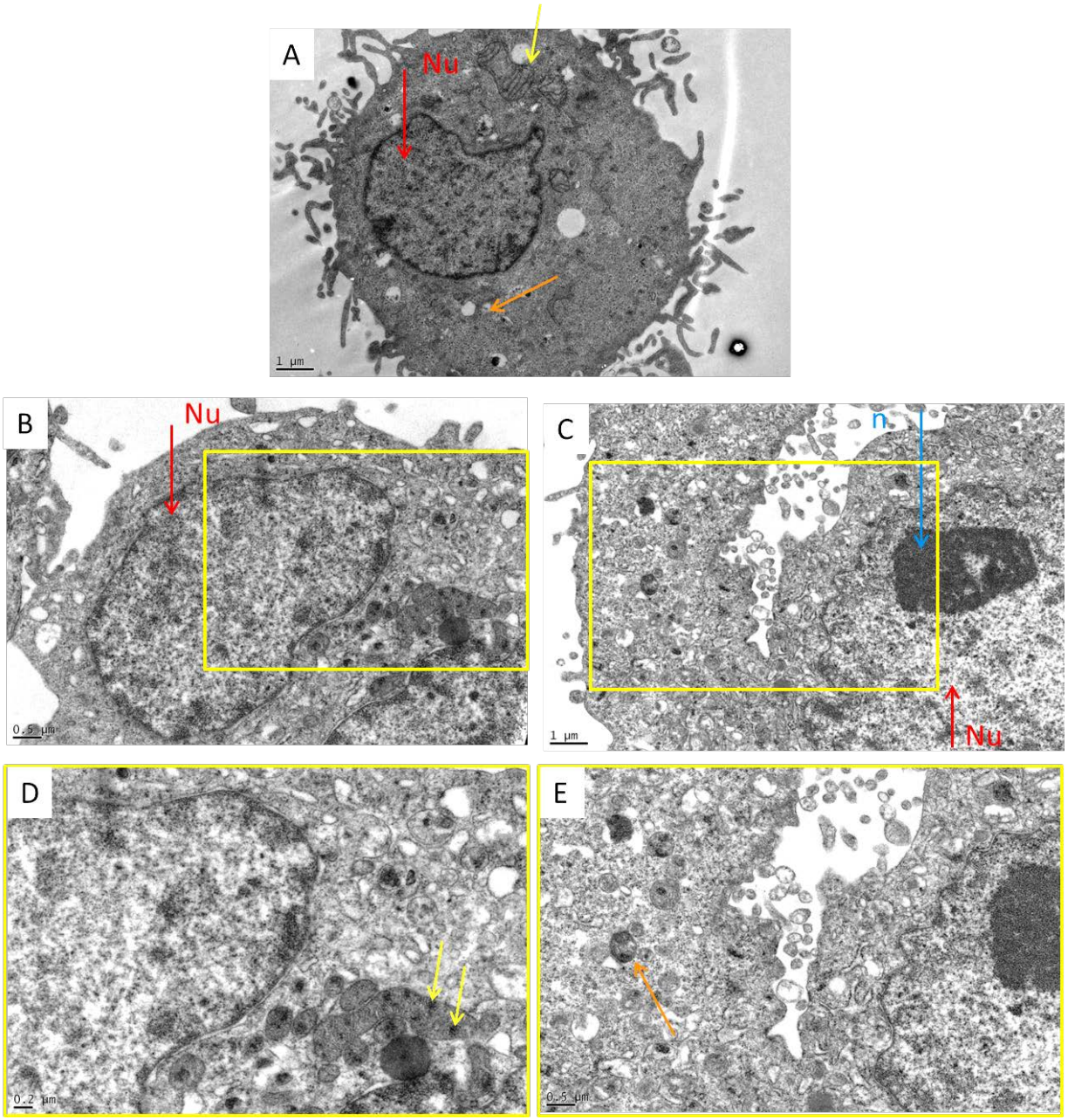

Figure 6.Electron micrograph of Hela cells stained with osmium tetroxide (A) control cells, stained with complex 3.1 (100 µM, 20 mins) displaying (B+D) punctate staining within the mitochondria (yellow arrows) and (C+E) some lysosomal (orange arrows) and nucleoli staining (blue arrow).

Cells were treated as above with complex **3.1** (100 µM, 20 mins), fixed and stained with osmium tetroxide, which acts as a secondary fixative but also deposits osmium in membranes providing cellular context. Once organelles became visible from the osmium staining it became apparent that the platinum (II) complex was staining some areas in the cytoplasm specifically. One of the striking features were the small, high contrast circles present within the mitochondria (yellow arrows): these "circles" appeared to be slightly asymmetrical, with average dimensions of 131 ± 15 nm by 110 ± 13 nm. These circles when compared to structures present in the mitochondria match well nucloids, mitochondrial DNA rings present with all mitochondria, for which sizing was done by super

resolution microscopy.[25–27] This finding fits well with the previous studies showing that the platinum (II) complex binds to DNA strongly and is a DNA intercalator. It has also been previously speculated that the complex might stain mtDNA on the basis of emission light microscopy studies.[6] However, as mentioned the mtDNA nucloids are around 100 nm in size which is too small to resolve with diffraction limited light microscopes, especially with the non-specific cytoplasmic staining complicating precise co-localisation.

A somewhat greater contrast observed in some lysosomes present in the micrographs (Fig 6., orange arrow) could be evidence of the cell attempting to destroy/ traffic the probe out of the cell. It was also noted that with the addition of osmium tetroxide to the TEM preparation, the extraction of the cells appeared to stop as the osmium tetroxide was acting as a secondary fixative.

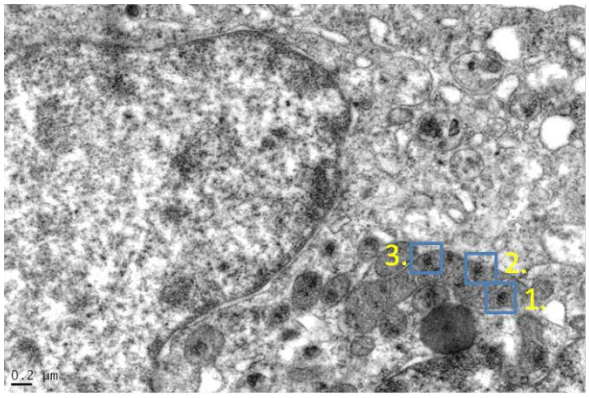

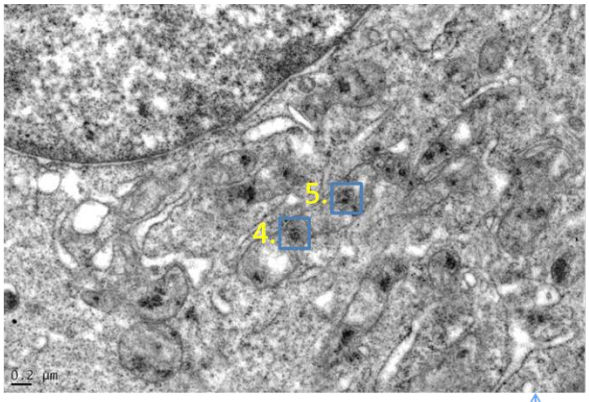

	Y - axis	x - axis
	1. 136 nm	1. 109 nm
	2. 125 nm	2. 109 nm
	3. 118 nm	3. 98 nm
	4. 120 nm	4. 103 nm
	5. 155 nm	5. 131 nm
Averages	y = 131 ± 15 nm	x = 110 ± 13 nm

Figure 7. Electron micrographs of HeLa cells treated with osmium tetroxide and complex 3.1 (100 µM, 20 mins) depicting which punctate staining was taken for sizing analysis in imagej. Table of the sizes of the puncta measure (y axis was always denoted as the longest axis)

In general, TEM protocols for cell preparation also include treatment with uranyl acetate and lead citrate in addition to osmium tetroxide, as these 3 compounds stain different regions of the cell. Therefore to add more cellular context, cells treated with platinum (II) complex **3.1** were also stained with uranyl acetate and lead citrate after sectioning, as well as osmium tetroxide. These cells displayed the same staining pattern as was observed in the osmium tetroxide stained cells, with high

contrast seen in the nucleoli, small circles present in the mitochondria and more heavily staining seen in some but not all lysosomes.

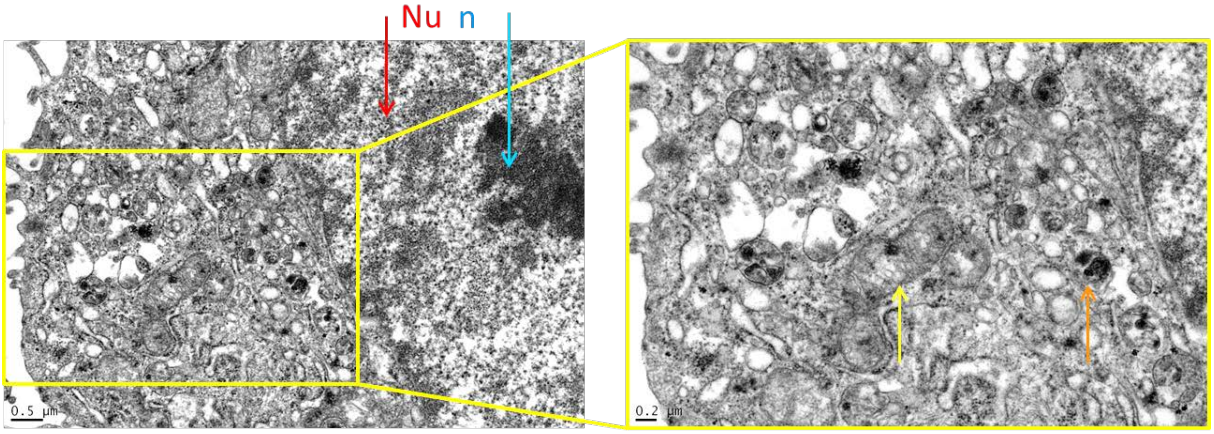

Figure 8. Electron micrographs of HeLa cells stained with the typical contrast agents osmium tetroxide, uranyl acetate and lead citrate as well as complex 3.1 (100 µM, 20 mins) again displaying puncta in the mitochondria (yellow arrows) and staining in the lysosomes (orange arrows) and nucleoli (blue arrows)

When comparing images of cell stained with osmium tetroxide, uranyl acetate and lead citrate with cell that have also been treated with platinum (II) complex it is clear that the mtDNA staining is only present in cells which have been stained with platinum (II) complex. This provides evidence that these circles of high contrast are platinum (II) complex staining the circular mtDNA which is not resolvable in standard confocal or widefield imaging.

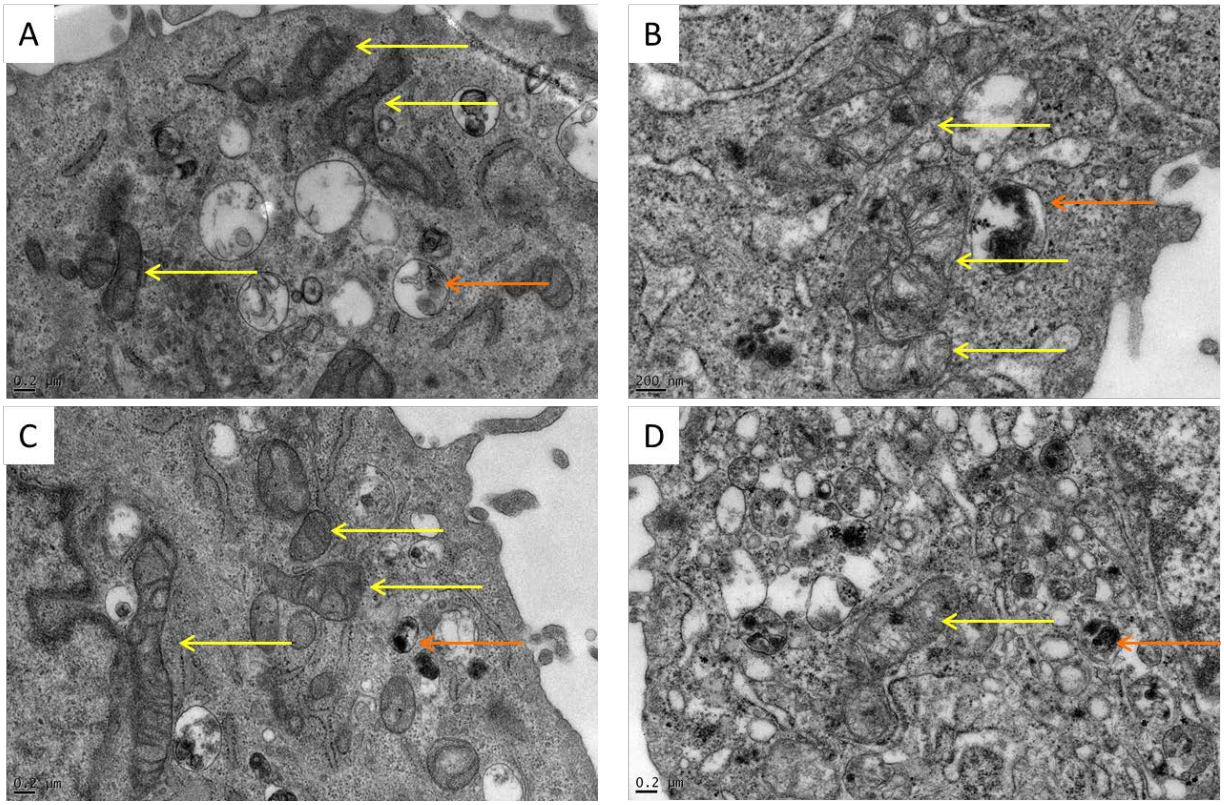

Figure 9. Electron micrographs of HeLa cells displaying the difference between cells stained (A+C) with just typical contrast agents and (B+D) cells stained with typical contrast agents and complex 3.1 (100 µM, 20 mins). (mitochondria = yellow arrows, lysosomes = orange arrows)

3.4 Super Resolution Imaging

In previous studies it has been noted repeatedly that metal complexes often display excellent photostability and this property is very desirable for imaging probes but this becomes paramount for super resolution techniques, as the they are all typically more laser intense than other imaging methods.[28] As the complex **3.1** had previously been reported to exhibit excellent photostability it was decided that complex would be explored as a potential 3D SIM probe.

All cells for these experiments were HeLa cells grown on n 1.5 high precision cover slips to minimise spherical aberrations from variable distances from the objective, which can be compounded during the reconstruction. HeLa cells were treated with the amount of complex stated in full media and immediately fixed using paraformaldehyde (4 %) in PBS. No difference was seen when compared to cells stained in complex in PBS, however it has been previously reported that serum albumin can affect the toxicity and localisation of complexes.[29] All cells were mounted on microscope slides in prolong gold antifade media to give a better refractive index as glycerol has a higher refractive index than water and as a photoprotectant.

Initially, the staining procedures from Baggaley *et al.* that were also used to co-stain against Syto 82 were used for consistency. The 3D SIM showed the HeLa cells in exquisite detail, with the nucleus very clearly shown with nucleoli staining visible. The diffuse staining of the cytoplasm is mostly homogenous with some areas of the cytoplasm devoid of any complex and some bright punctate staining observed. Some of the larger punctate staining is likely the lysosomal staining visible in the TEM but the rest of the punctate staining is smaller than expected for lysosome staining and could potentially be the mtDNA seen in the TEM.

The photostability of the complex was also assessed using SIMcheck, a free plugin for image j, which evaluates the reconstruction of SIM data to search for any inconsistencies.[30] From this plugin it is possible to generate graphs of the mean intensity of each raw image in a Z-stack, the gradient of the line illustrates how much photobleaching is occurring and the plugin also estimates the percentage photobleaching. The raw images are organised into three groups from each of the angles of illumination and a reduction in mean intensity through the Z-stack is indicative of photobleaching. As can be seen in the mean intensity graph (Fig. 10), the mean intensity of each angle of illumination of the 3D SIM images are straight lines, thus the platinum (II) complex did not show any photobleaching under the conditions used, with the plugin estimating 0 % intensity decay. This illustrates remarkable photostability of this compound with sustained illumination with a 405 nm excitation laser. There is a drop between each of the angles but this is due to variation in the light path for each angle of illumination creating slight variation in the illumination strength and detection.

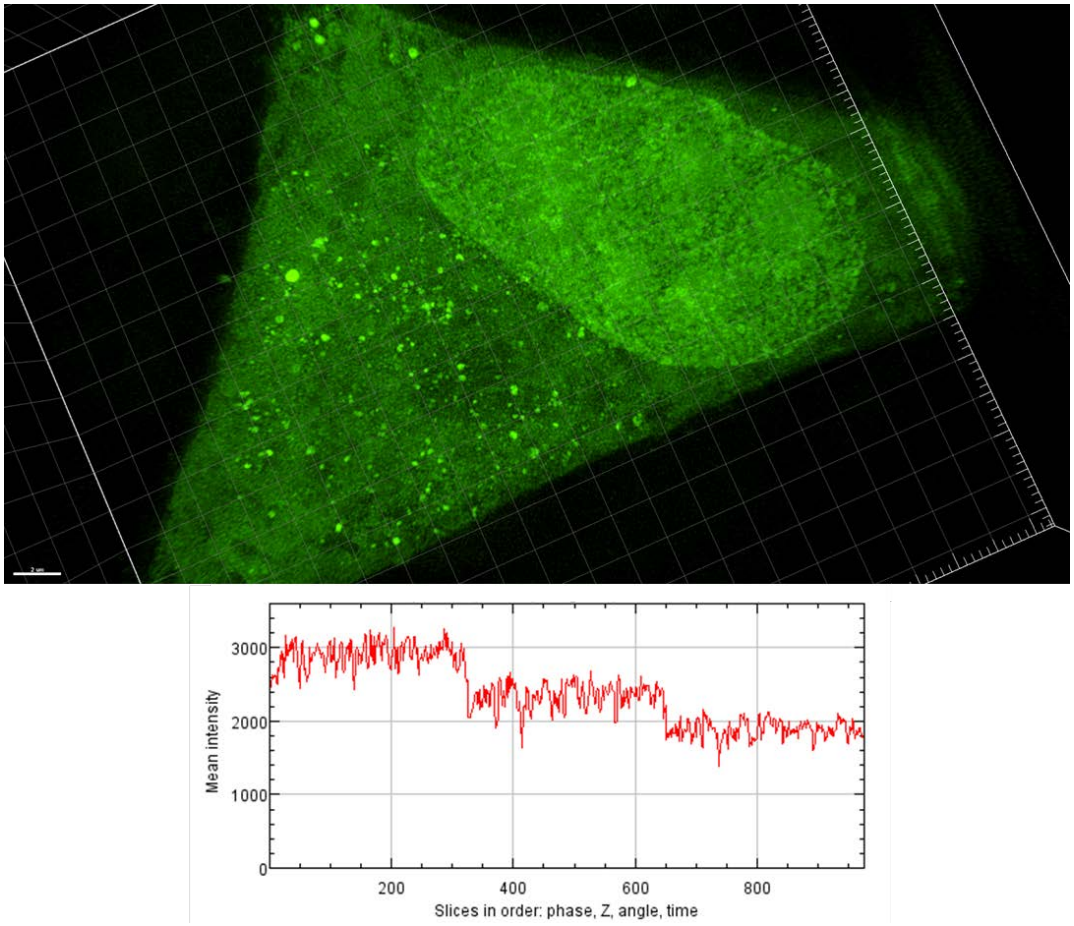

Figure 10. 3D SIM image of HeLa cells stained with complex 3.1 (100 µM,5 mins) (top) and a graph of mean intensity from the raw data of the SIM image (bottom). Scare bar = 2 µm

Once the initial conditions had been used it was decided to further test concentrations and incubation time. First of all, the staining conditions used for TEM were tested as this would ease correlating between both techniques. As such, HeLa cells were treated with platinum (II) complex **3.1** (100 µM, 20 mins), fixed and imaged on the 3D SIM. Very bright signal was seen in the nucleus but the nucleoli staining was difficult to see in the 3D rendered images as the signal from the nucleus was so strong. When looking at the central images from the z-stack it was apparent the nucleoli staining was still present (Fig. 11, white arrows). The diffuse cytoplasmic staining was very similar to the lower incubation time sample, with some small bright punctate staining present.

The total mean intensity shows a slight negative gradient for this image, showing that some photobleaching was occurring in this sample. The estimates intensity decay was 8.5 % which is still very low, highlights the photostability of this complex. The variation between each angle is not as pronounced in this sample.

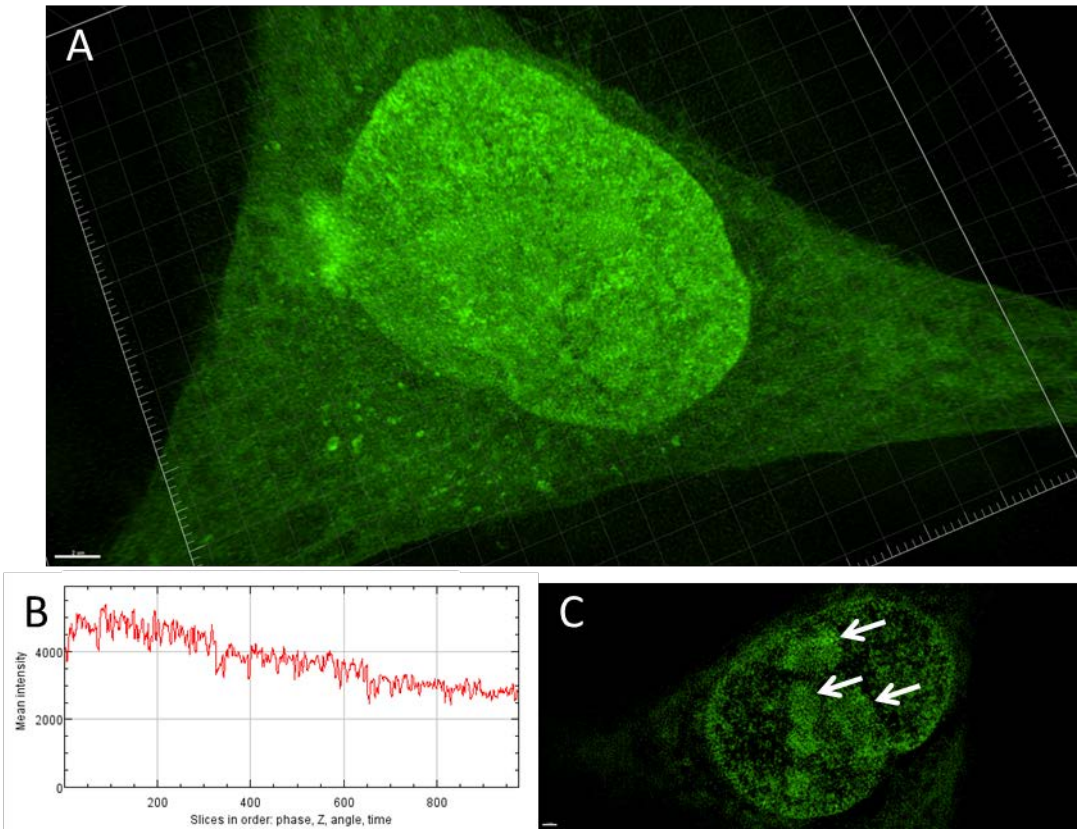

Figure 11. 3D SIM image of HeLa cells treated with complex 3.1 (100 µM, 5 mins). (A) 3D rendered image of a whole cell, (B) total mean intensity graph from the raw data, (C) single slice of z-stack highlighting the nucleoli staining (white arrows).

To further test the photostability of the complex, multiple image stacks of the same area were taken to observe the intensity decay between different image stacks as well as through a single z-stack. The same area was imaged three times taking large raw imaging stacks of 1335 images to yield 89 reconstructed 3D SIM images with identical setting of illumination and exposure in each instance. Sufficient data was obtained to reconstruct a super resolution image for each of the image stacks. The estimated intensity decays for each image set were 3 %, 0 % and 0 % respectively suggesting that very little photobleaching was occurring. However, as can be seen in the comparison of each mean intensity graph there is a drop in intensity between each image set when compared to the corresponding angle. The last angle in each image set, which has the smallest variation image to image, have average intensity values of approximately 2200, 1900 and 1700 counts respectively, thus displaying a 14 % reduction in mean intensity between the first and second image stack and a further 10 % reduction to the third image stack from the original intensity (Fig. 12). This suggests that the plugin underestimated the amount of photobleaching occurring, however this amount of photobleaching is still relatively low over such large image stacks and doesn't compromise the strength of the reconstruction.

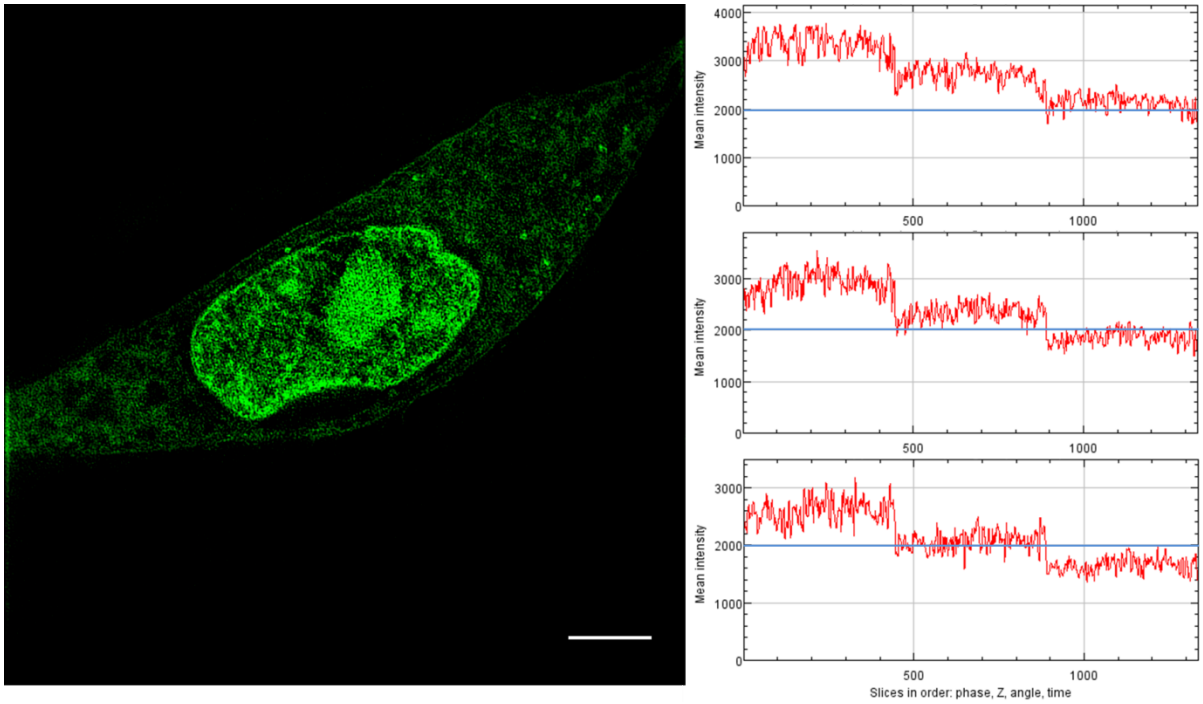

Figure 12. 2D slice of a 3D SIM z-stack of HeLa cells stained with complex 3.1 (100 µm, 5 mins)(left), total intensity graphs from 3 sequential runs on the same cell(right). (scale bar = 5 µm)

HeLa cells were also screen at lower concentrations utilising the same incubations times as the 3D SIM has excellent sensitivity, therefore allowing less complex to be used which lowers the possibility of the complex affecting the normal function of cells. HeLa cells were treated with 25 µM of platinum (II) complex for 5 and 20 minutes. Both sets of conditions provided suitable intensity for reconstruction, however nucleus, nucleoli and cytoplasmic staining was clearer in the cell that were incubated for longer. However, the estimated decays for each image stack were 14.6 % and 3.3 % for the 5 minute and 20 minute respectively. This is a considerable difference and reflects the varying amounts of compounds present in the cells while imaging, affecting the initial intensities and amount of signal lost, as seen in the intensity decay graphs (Fig 13.). From these images it is clear that staining for longer at lower concentrations gives clearer images and less signal loss is observed.

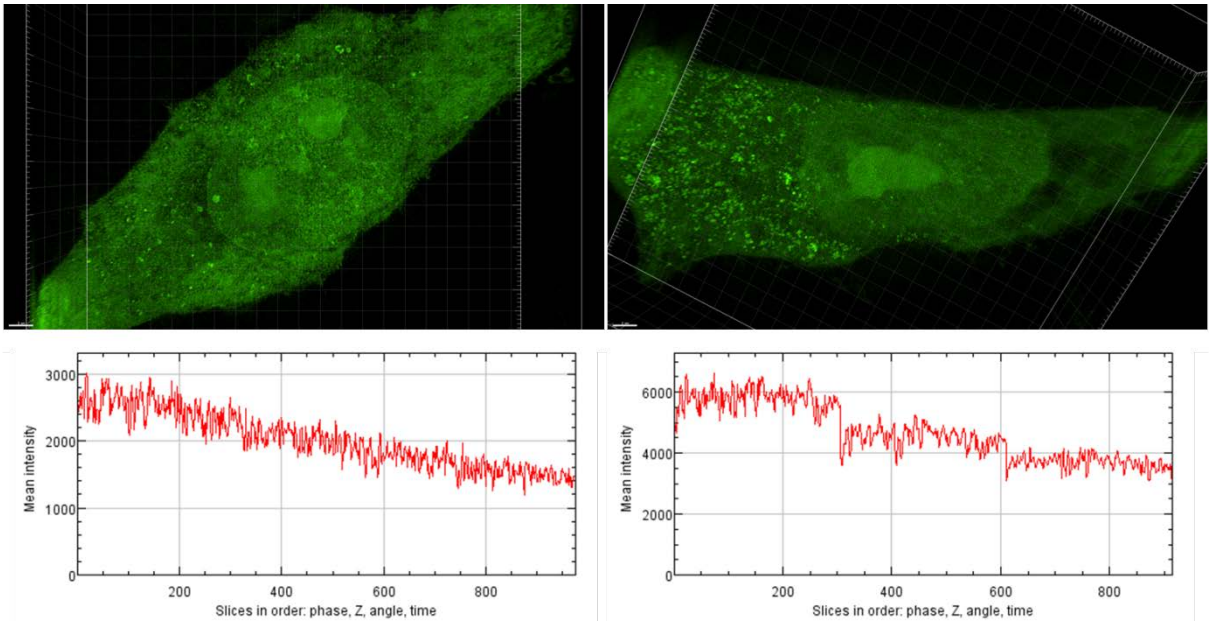

Figure 13. 3D SIM images of Hela cells stained with 25 µM of complex 3.1 for 5 mins (left) and 20 mins (right) with corresponding total mean intensity graphs from the raw data below each image. Scare bar = 2 µm

Multiple image stacks of the same cells were collected on cells treated with 25 µM for 20 minutes, as above, to further test the photostability of the complex at different concentrations. Raw z-stacks of 975 images were taken for each run, with illumination power and time kept consistent to yield a 65 image z-stack of reconstructed super resolution images. The mean intensity graphs show minimal negative gradient, suggesting very low levels of photobleaching and the estimated decay intensity was calculated by SIMcheck to be 3.94 %, 1.94 % and 0 % for each run respectively, further confirming that the photobleach was extremely minimal during image acquisition. However, upon comparison between the third angle, which is the least variable of each angle, the mean intensity was recorded as 5300, 4700 and 4400 counts respectively (Fig. 14). This indicates an 11.3 % reduction in mean intensity between the first and second image acquisition and a further 5.7 % reduction in mean intensity, again suggestion that the SIMcheck plugin potentially underestimates the level of photobleaching occurring. These reductions in mean intensity are however still small and highlight the photostability of the complex to prolonged periods of irradiation.

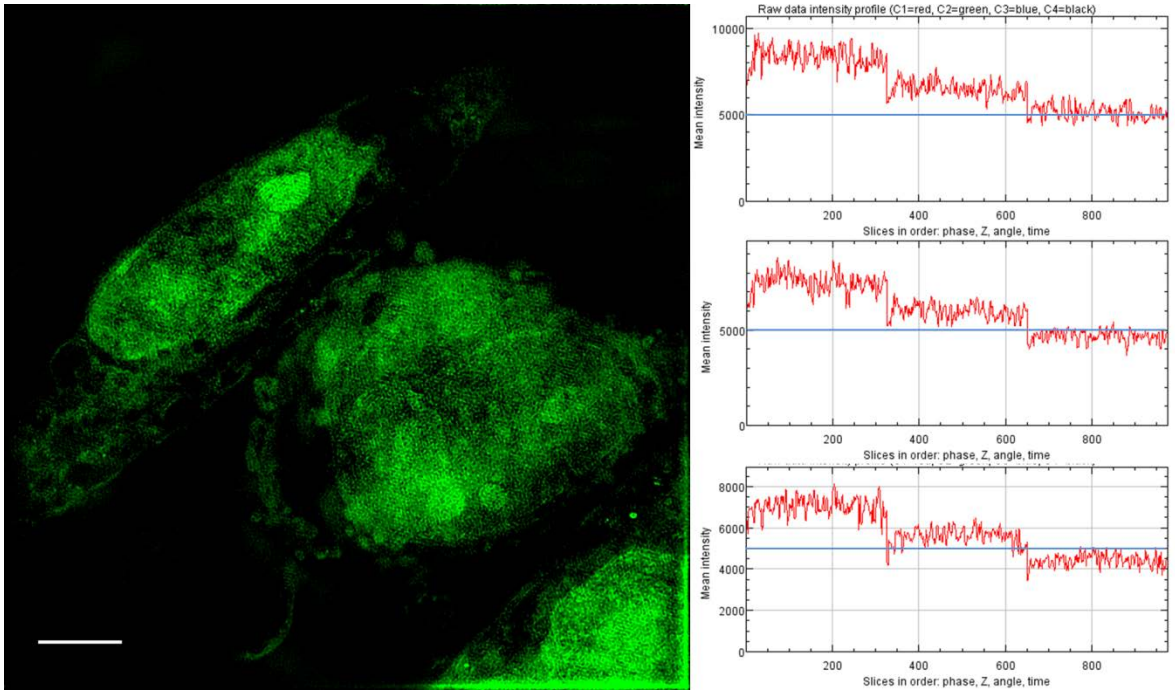

Figure 14. 2D slice of a 3D SIM z-stack of HeLa cells stained with complex 3.1 (25 µm, 20 mins)(left), total intensity graphs from 3 sequential runs on the same cell(right). (scale bar = 5 µm)

3.4.1. Co-Staining

Next the photostability of complex was assessed against commercially available dyes Hoechst and Syto 82 as these dyes stain similar area of the cells to the platinum (II) complex. Furthermore, better localisation information was hoped to be obtained through co-localising in the super resolution technique. Hoechst was the first dye used which is a commercially available nuclear stain and binds DNA strongly, much like the platinum (II) complex. As previously reported, the platinum (II) complex **3.1** stains the nucleus heavily and therefore overlaps well with the Hoechst staining, however as the platinum (II) complex also has lots of nonspecific cytoplasmic staining, using statistics like Pearson's coefficient to evaluate the colocalisation would yield low correlation values.

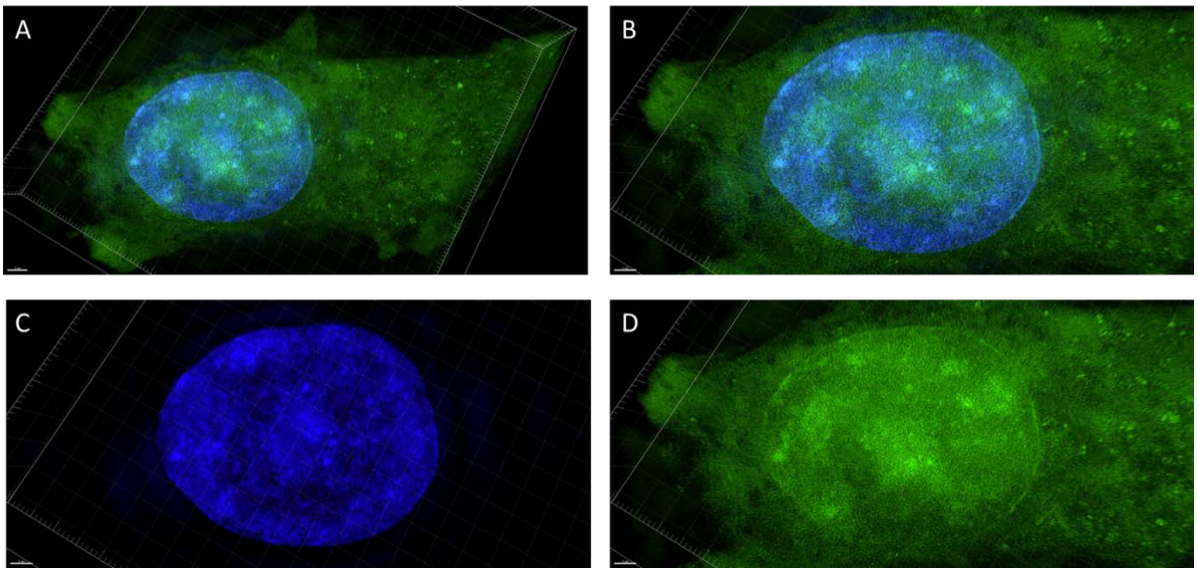

Figure 15. 3D SIM images of HeLa cells stained with complex 3.1 (100 µM, 5 mins) and Hoechst (3µM, 20 mins); (A) channels overlaid, (B) zoomed in, (C) Hoechst emission only, (D) complex 3.1 emission only.

Next, cells treated with the platinum (II) complex **3.1** were costained with Syto 82 as this has been shown to correlate well with staining pattern of the platinum (II) complex. The Syto 82 was found to photobleach very readily while imaging in SIM mode, as shown by the mean intensity graph (Fig. 16), with an estimated intensity decay of 54 % and this compromised the reconstruction. The poor reconstruction can be seen in Fig. 15, as the nucleoli staining (blue arrows) in the raw image can be seen clearly but this staining is not very visible in the SIM reconstruction. Furthermore, artefacts are visible where signal is visible in the top of the reconstruction image that is not present in the raw image. The low photostability of Syto 82 while being imaging in SIM hindered the acquisition of good raw data such that no data was taken that was good enough for SIM reconstruction without artefacts. This highlights the need for photostable dyes for use in SIM to attain data of a suitable quality for reconstruction.

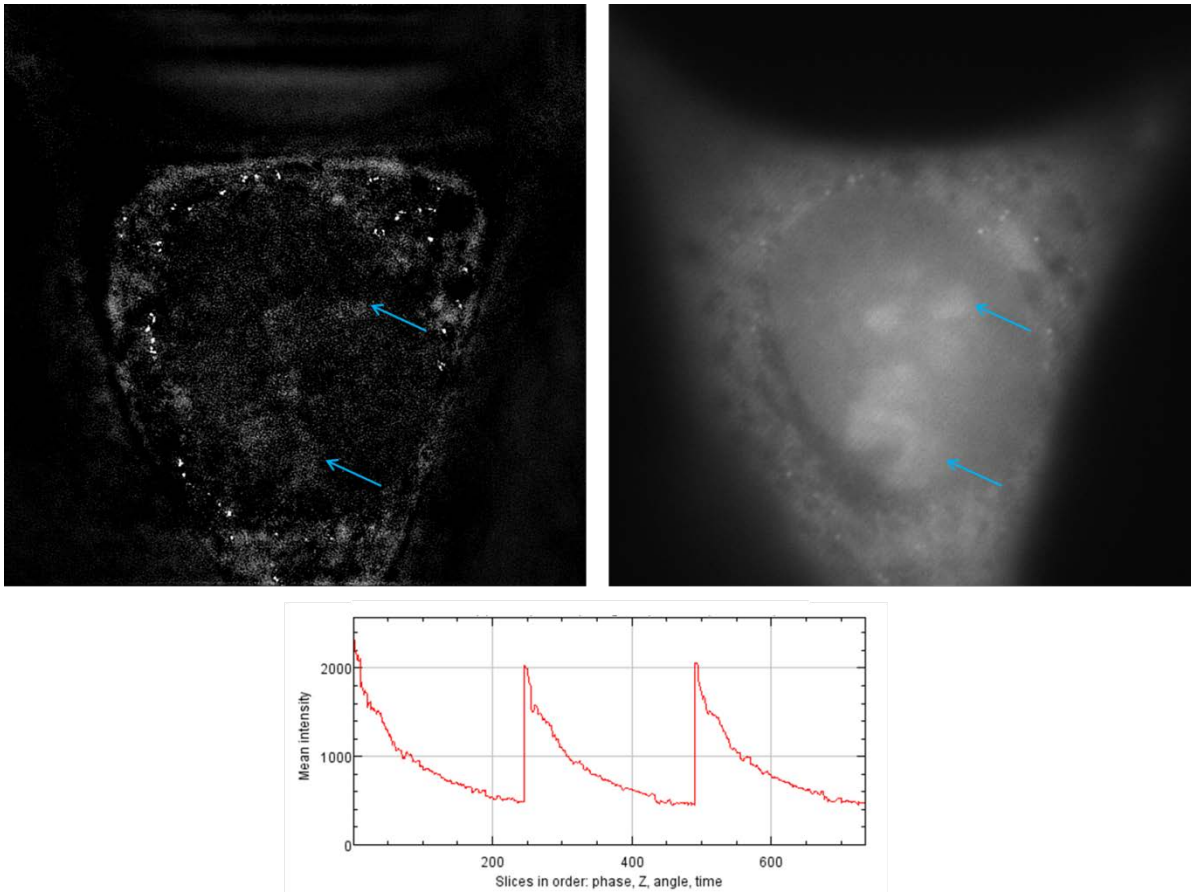

Figure 16. 2D slice of 3D SIM Z-stack of a HeLa cell treated with Syto 82 displaying a poor reconstruction with loss of nucleoli staining (Blue arrow)(left), raw data used for reconstruction with nucleoli staining clearly visible(right), total mean intensity graph of raw data showing sharp drop in intensity from Syto 82.

Finally, HeLa cells stained with the platinum (II) complex **3.1** were costained with MitoTracker® orange to observe if any of the small bright punctate staining visible in the cytoplasm co-localises within the mitochondria and therefore are likely to be mtDNA as seen in the TEM. Curiously, as can be seen in Figure 16. the small punctate doesn't overlap with any of the MitoTracker® orange signal. However, upon measurement of the small punctate generally measured approximately 200-300 nm in size, which is in agreement with the mtDNA ring with complex present throughout the ring (Fig. 17).

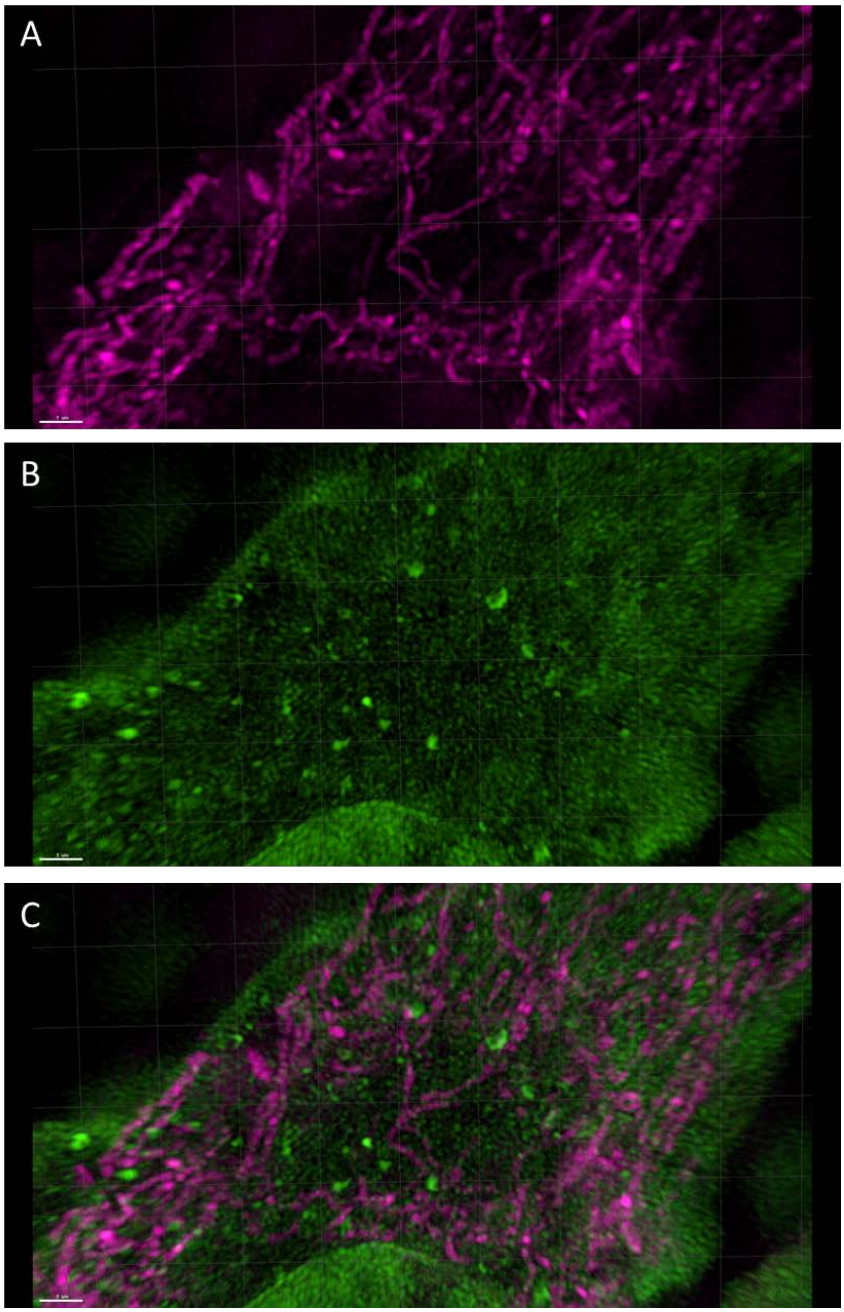

Figure 17. 3D SIM images of HeLa cells stained with (A) MitoTracker® orange (100 nM, 20 mins) and (B) complex 3.1 (100 µM, 5 mins), (C) channels overlaid; (D) Diagram depicting the localisation of complex in mtDNA leading to 200-300 nm spots.

3.5 Summary

We report here the first use of any transition metal complex in the super resolution microscopy technique 3D SIM, in addition to TEM contrast enhancement at the same concentration. It was observed that the complex provided contrast in TEM and stained the nucleus and nucleoli heavily, which is in agreement with emission based microscopy. Small structures in the mitochondria were also noted in TEM, and are tentatively assigned as mitochondrial DNA. While the complex was also known to weakly stain the cytoplasm, no other contrast enhancement was noted, showing that only in areas of sufficient accumulation provide contrast.

The complex was found to function well as a 3D SIM probe, with excellent photostability noted, with SIMcheck estimating the total intensity decay of samples to be generally ≤ 5% over 1000 images. However, it was noted that after further analysis, that it was likely underestimating the amount of decay but the values were still only found to be ≤ 10 %. The commercial stain Syto 82, which localised in the same localisation pattern the complex proved problematic to image due to photobleaching, with estimated intensities decay of 54 %. However, when the cells were costained with the complex 3.1. and MitoTracker® orange, no punctate staining from the mitochondrial DNA was observed in 3D SIM emission images despite its localisation in mitochondria confirmed by TEM, suggesting that the emission of the complex was quenched when present in this environment.

This work confirms that luminescent metal complexes have the potential to be useful tools for CLEM applications by providing luminescence for emission based microscopy and contrast in TEM, a property not found in other small luminescence molecules. However, this specific complex suffers from a lack of specificity, making comparison and correlation between techniques difficult and reduces its true usefulness in applications. Thus this study has been a proof of concept that luminescent transition metal complexes can provide contrast in TEM, and at the same concentrations and conditions used to image them using super resolution microscopy techniques, such as 3D SIM. A further strength of these types of probes is the requirement of the probe to accumulate sufficiently to provide contrast in TEM, thus eliminating background/ off target staining that does not have the required concentration of metal complex present.

As mentioned in Chapter 1, emission of these types of complexes is sensitive to the environment, potentially offering a wealth of information from a sample stained with a single probe. Further work should explore at using complexes which stain specific organelles, where environmental and correlative information could be obtained, which would be more useful for potential applications.

3.6 References

1 E. Baggaley, J. A. Weinstein and J. A. G. Williams, *Coord. Chem. Rev.*, 2012, **256**, 1762–

1785.

2 M. Mauro, A. Aliprandi, D. Septiadi, N. S. Kehr and L. De Cola, *Chem. Soc. Rev.*, 2014, **43**, 4144–4166.

3 M. Patra and G. Gasser, *Chembiochem*, 2012, **13**, 1232–52.

4 E. Baggaley, S. W. Botchway, J. W. Haycock, H. Morris, I. V. Sazanovich, J. A. G. Williams and J. A. Weinstein, *Chem. Sci.*, 2014, **5**, 879–886.

5 E. Baggaley, I. Sazanovich, J. A. G. Williams, J. Haycock, S. W. Botchway and J. A. Weinstein, *RSC Adv.*, 2014, **4**, 35003–35008.

6 S. W. Botchway, M. Charnley, J. W. Haycock, A. W. Parker, D. L. Rochester, J. A. Weinstein and J. A. G. Williams, *Proc. Natl. Acad. Sci. U. S. A.*, 2008, **105**, 16071–6.

7 C.-K. Koo, K.-L. Wong, C. W.-Y. Man, H.-L. Tam, S.-W. Tsao, K.-W. Cheah and M. H.-W. Lam, *Inorg. Chem.*, 2009, **48**, 7501–3.

8 Q. Zhang, X. Tian, G. Hu, P. Shi, J. Wu, S. Li, H. Zhou, B. Jin, J. Yang, S. Zhang and Y. Tian, *Biochemistry*, 2015, **54**, 2177–2180.

9 C.-K. Koo, L. K.-Y. So, K.-L. Wong, Y.-M. Ho, Y.-W. Lam, M. H.-W. Lam, K.-W. Cheah, C. C.-W. Cheng and W.-M. Kwok, *Chem. Eur. J.*, 2010, **16**, 3942–50.

10 Y.-M. Ho, N.-P. B. Au, K.-L. Wong, C. T.-L. Chan, W.-M. Kwok, G.-L. Law, K.-K. Tang, W.-Y. Wong, C.-H. E. Ma and M. H.-W. Lam, *Chem. Commun.*, 2014, **50**, 4161–3.

11 R. I. Dmitriev, A. V. Kondrashina, K. Koren, I. Klimant, A. V. Zhdanov, J. M. P. Pakan, K. W. McDermott and D. B. Papkovsky, *Biomater. Sci.*, 2014, **2**, 853.

12 R. I. Dmitriev, S. M. Borisov, A. V. Kondrashina, J. M. P. Pakan, U. Anilkumar, J. H. M. Prehn, A. V. Zhdanov, K. W. McDermott, I. Klimant and D. B. Papkovsky, *Cell. Mol. Life Sci.*, 2014, **72**, 367–381.

13 V. Tsytsarev, H. Arakawa, S. Borisov, E. Pumbo, R. S. Erzurumlu and D. B. Papkovsky, *J. Neurosci. Methods*, 2013, **216**, 146–51.

14 S. S. Howard, A. Straub, N. G. Horton, D. Kobat and C. Xu, *Nat. Photonics*, 2012, **7**, 33–37.

15 J. Lecoq, A. Parpaleix, E. Roussakis, M. Ducros, Y. Goulam Houssen, S. A. Vinogradov and S. Charpak, *Nat. Med.*, 2011, **17**, 893–8.

16 A. Parpaleix, Y. Goulam Houssen and S. Charpak, *Nat. Med.*, 2013, **19**, 241–6.

17 A. Byrne, S. Burke and T. E. Keyes, *Chem. Sci.*, 2016, **0**, 1–12.

18 D. Septiadi, A. Aliprandi, M. Mauro and L. De Cola, *RSC Adv.*, 2014, **4**, 25709.

19 C. Dragonetti, A. Colombo, F. Fiorini, D. Septiadi, F. Nisic, A. Valore, D. Roberto, M. Mauro and L. De Cola, *Dalt. Trans.*, 2014.

20 S. Wu, C. Zhu, C. Zhang, Z. Yu, W. He, Y. He, Y. Li, J. Wang and Z. Guo, *Inorg. Chem.*, 2011, **50**, 11847–9.

21 M. R. Gill, J. Garcia-Lara, S. J. Foster, C. Smythe, G. Battaglia and J. A. Thomas, *Nat. Chem.*, 2009, **1**, 662–7.

22 X. Tian, M. R. Gill, I. Cantón, J. A. Thomas and G. Battaglia, *Chembiochem*, 2011, **12**, 548–

51.

23 M. R. Gill, D. Cecchin, M. G. Walker, R. S. Mulla, G. Battaglia, C. Smythe and J. A. Thomas, *Chem. Sci.*, 2013, **4**, 4512.

24 A. Wragg, M. R. Gill, C. J. Hill, X. Su, A. J. H. M. Meijer, C. Smythe and J. A. Thomas, *Chem. Commun.*, 2014, **50**, 14494–7.

25 T. A. Brown, A. N. Tkachuk, G. Shtengel, B. G. Kopek, D. F. Bogenhagen, H. F. Hess and D. A. Clayton, *Mol. Cell. Biol.*, 2011, **31**, 4994–5010.

26 C. Kukat, C. A. Wurm, H. Spåhr, M. Falkenberg, N.-G. Larsson and S. Jakobs, *Proc. Natl. Acad. Sci. U. S. A.*, 2011, **108**, 13534–13539.

27 C. Kukat, K. M. Davies, C. A. Wurm, H. Spåhr, N. A. Bonekamp, I. Kühl, F. Joos, P. L. Polosa, C. B. Park, V. Posse, M. Falkenberg, S. Jakobs, W. Kühlbrandt and N.-G. Larsson, *Proc. Natl. Acad. Sci.*, 2015, **112**, 11288–11293.

28 L. Schermelleh, R. Heintzmann and H. Leonhardt, *J. Cell Biol.*, 2010, **190**, 165–175.

29 A. Wragg, M. R. Gill, L. McKenzie, C. Glover, R. Mowll, J. a. Weinstein, X. Su, C. Smythe and J. a. Thomas, *Chem. Eur. J.*, 2015, **21**, 11865–11871.

30 G. Ball, J. Demmerle, R. Kaufmann, I. Davis, I. M. Dobbie and L. Schermelleh, *Sci. Rep.*, 2015, **5**, 15915.

Chapter 4. Investigation of an Iridium (III) Complex as Dual Probe

4.1 Introduction

The results of Chapter 3 demonstrate that a platinum (II) based luminescent metal complex was capable of providing contrast in TEM and being used as a luminescent probe for 3D SIM. However, the drawback of this complex is that it lacked specific localisation, making it difficult to resolve cellular features seen in both techniques but also highlighted the fact that only areas where the complex accumulated in a significant quantity could be seen by TEM. On a positive note, the lack of specificity does mean that lifetime imaging yields a snapshot of the oxygen environment across an entire live cell. These shortcomings could be overcome by finding a luminescent complex with organelle-specific localisation which would be more useful in potential applications. Another criterion also shown to be important by the studies of the platinum (II) based probes was toxicity, as high concentrations were necessary to obtain goof Image contrast any potential transition metal complexes would also need to exhibit low toxicity at higher concentrations to yield contrast in TEM, or localise with specificity to give high local concentrations.

Lifetime imaging can offer a wealth of information about a probes environment *in vitro*[1–3] and *in vivo*[4–6] and while it has predominantly been used to measure oxygen concentration it can also be used to observe other conditions depending on what environmental analytes the probe is sensitive too (Fig 1).[7,8] Luminescent transition metal complexes are generally oxygen sensitive, but it is also possible to design complexes which are sensitive to other environmental conditions, such as pH. Complexes which localise specifically to certain organelles which are sensitive to these kinds of biologically important analytes offer the opportunity to monitor these conditions on an intracellular level in real time. This coupled with the potential for super resolution CLEM provides a wealth of information on a sample not usually obtainable with a single molecule.

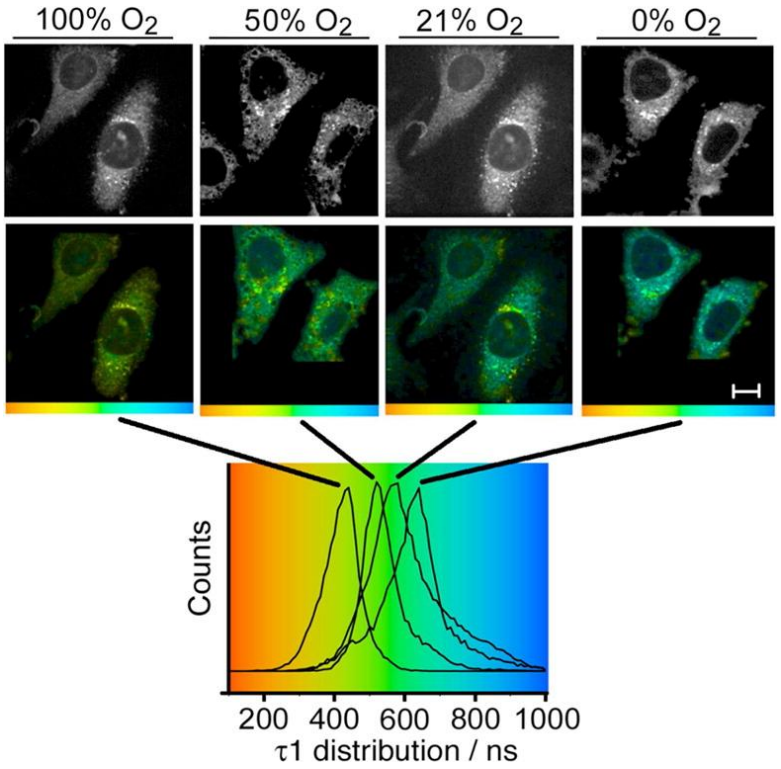

Figure 1. Two-photon PLIM of an Ir-Gd complex displaying O_2 sensitivity in Live HeLa cells. Figure adapted from ref.[9]

To this end it was decided that not just platinum (II) but other third row metals could also act as potential contrast agents if they accumulated in suitable concentrations. Therefore promising luminescent iridium (III), platinum (II) and rhenium (I) complexes could be explored, as the photophysical properties, as discussed in Chapter 2, are potentially favourable for bioimaging applications. Photostability is often reported as a strength of these types of molecules,[10] which is particularly advantageous for use in super resolution microscopy techniques.

The aim of this work was to find a complex which meets the majority of criteria for a bioimaging probe but must also have specific localisation, which is a key criteria for CLEM.

4.2 Screening Potential Complexes

A number platinum (II) and iridium (III) complex were considered for screening to find new potential CLEM probes as many of these complexes have photophysical properties suitable for imaging applications.[11,12] In order to achieve more specific localisation of the probes, several methods have been attempted. A number of complexes were selected because of their lipophilic cationic nature, as these properties are known to cause molecules to localise specifically in mitochondria.[13] Complexes with Brønsted basic moieties were also considered as these could offer a way to sequester the label in acid compartments, potentially offering specific localisation as well as provide environmental data

through changes in photophysical properties.

Complexes were initially tested by emission imaging of Chinese hamster ovary (CHO) cells. CHO cells were treated with a complex at a concentration and incubation times typical for imaging with such complexes from reported literature, localisation and uptake were monitored using confocal microscopy. Due to the time restriction on the availability of the TREM set up in the Rutherford Appleton laboratory, toxicity of complexes was initially assessed simply by looking for visible signs of damage or malfunction of the cells.

These complexes were graciously supplied by Professor Gareth Williams, Durham University, having been synthesized and characterized there and the initial screening was done in conjunction with Luke McKenzie.

4.2.1 Platinum (II) Complexes

In Chapter 3 it was noted that the ease with which the platinum (II) NCN complex entered cells was an advantage, whilst its lack of specificity reduced its utility as a contrast agent and a CLEM probe. Therefore, similar complexes were considered instead of [Pt(N^C^N)], which bear ligands aiding specific intracellular localisation. The first compound to be tested was complex **4.1**, another square planar complex with a 6-phenyl(2,2' bipyridine) (N^N^C), ligand in place of the N^C^N ligand, and with a dihexyl urea group present. It was hypothesised that this Pt(NNC-urea) complex would have similar uptake characteristics to Pt N^C^N, but have a more selective localisation within the cell. Incubation of CHO cells with Pt(N^N^C-urea) at 100 μM required 12 hours incubation (vs. 5 min with Pt N^C^N) to achieve accumulation sufficient for emission imaging. This suggests that the complex does not enter cells as readily as Pt N^C^N despite the structural similarity. The Pt N^N^C-urea complex was found to localise in the nucleoli and perinuclear region with some weaker nuclear staining also observed. This suggests the complex preferentially binds to RNA, as large quantities of DNA are transcribed in the nucleoli. The complex binding to RNA is similar to the Pt N^C^N complex **3.1** which follows as the complexes are structurally very similar but the lack of strong nuclear staining suggests it does not have such a strong preference for DNA, unlike the Pt N^C^N and the previously studied Pt(II) terpyridine complex.[14] The cells did not show any obvious signs of toxicity, such as blebing of the membrane or considerable changes to their morphology while imaging so the complex was considered not toxic on the timescale of imaging, and therefore detailed TREM experiemnts have been undertaken.

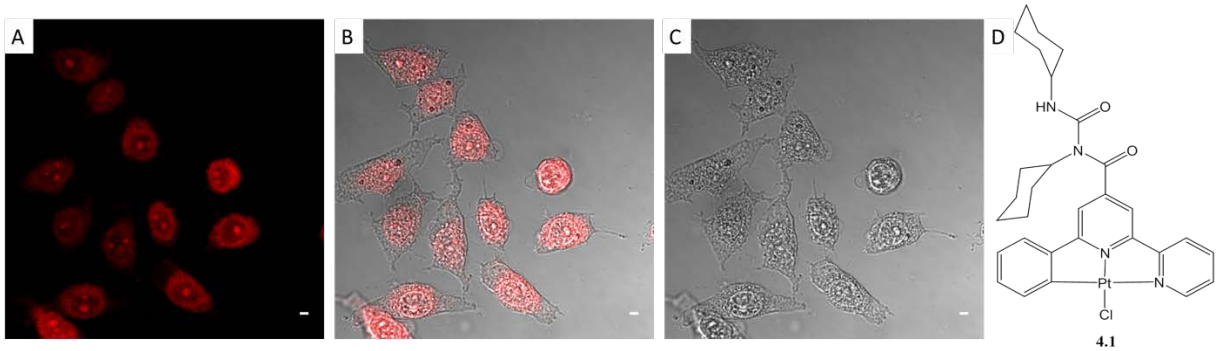

Figure 2. LCSM images of live CHO cells stained with complex 4.1 (100 µM, 12 h), (A) emission (λ_{ex} = 405 nm), (B) overlay, (C) brightfield; (D) structure of complex 4.1. Scale bar = 10 µm

Another related, charge-neutral platinum (II) complex **4.2,** with a cyclometallating tetradentate CNNC ligand, was also explored. It was hypothesised that similar to the NCN and NNC-urea complexes, **4.2** would potentially intercalate into DNA and RNA due to its planar structure and potential for aromatic interactions with the nuclear bases, and accumulate in the nucleus and nucleoli. CHO cells were treated with complex **4.2** at 50 µM in PBS buffer. The complex was found to accumulate within CHO cells faster than the N^N^C-urea complex, but slower than Pt (II) N^C^N complexes, with accumulation sufficient for imaging achieved after 3 hours incubation. To our surprise, the complex was not found to localise in the nucleus or the nucleoli but instead a punctate perinuclear staining pattern was observed, with some diffuse cytoplasmic staining. This suggests that either the complex is unable to penetrate the nuclear membrane or that it does not have an affinity for DNA or RNA. No obvious signs of toxicity were noted while imaging cells treated with complex **4.2**. Due to its low uptake, it was decided that there would not be sufficient concentration within cells to perform EM imaging, and this complex was not studied any further.

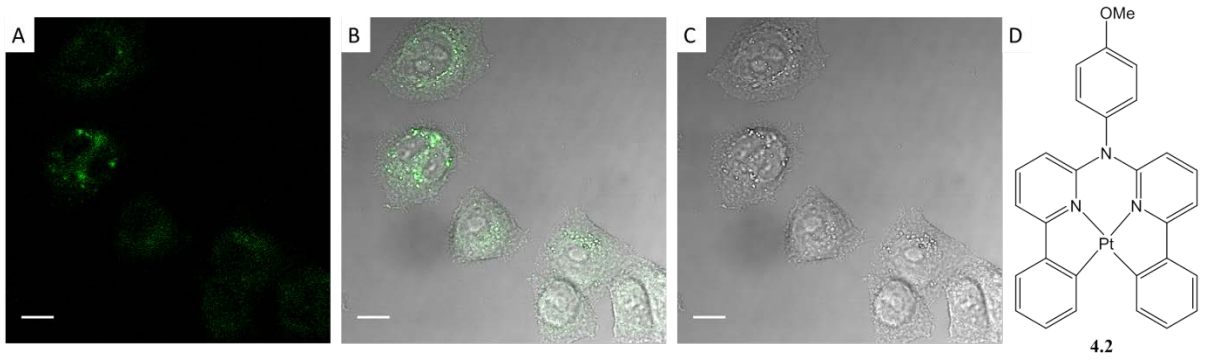

Figure 3. LSCM images of live CHO cells treated with complex 4.2 (50 µM, 3 h), (A) emission (λ_{ex} = 405 nm), (B) overlay, (C) brightfield; (D) molecular structure of complex 4.2. Scale bar = 10 µm

4.2.2 Iridium (III) Complexes

Many luminescent complexes of Ir(III) use cyclometallating di(phenylpyridine) ligands, with various bypyridine derivatives occupying the remaining 2 coordination sites. As discussed in Chapter 2, these

types of complexes typically display good photophysical properties for imaging.

Singly positively charged Ir(III) complex **4.3**, which includes one bipyridine ligand and two 2-(4-fluoro-phenyl)-pyrydine ligands, has been used as a typical representative of Ir(III) cyclometallated emissive complexes. CHO cells were incubated with complex **4.3** at 20 µM in DMEM media (DMSO < 1%). The complex was found to localise rapidly within cells, emission images could be obtained after only 10 minute incubation at 37 °C. The staining pattern of the complex appeared reminiscent of mitochondrial staining due to the small tubular/punctate nature of the staining. Thus providing an excellent starting point for the development of mitochondrial specific luminescent complexes.

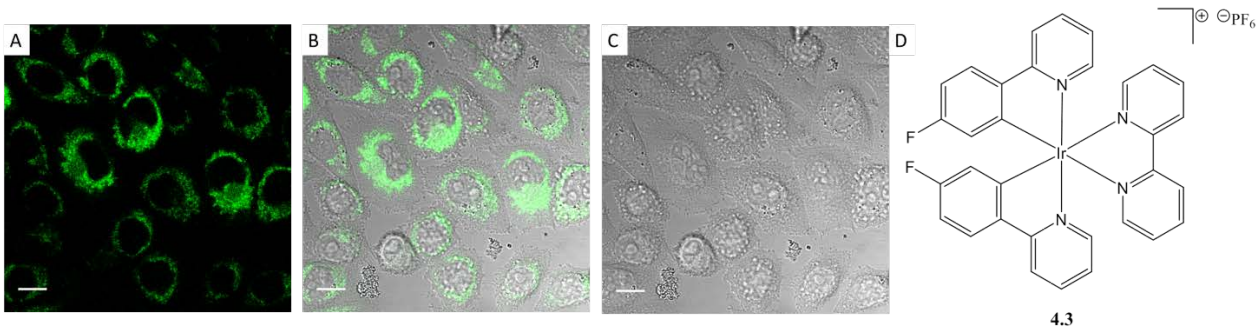

Figure 4. LSCM images of live CHO cells treated with complex 4.3 (20 µM, 10 mins), (A) emission (λ_{ex} = 405 nm), (B) overlay, (C) brightfield; (D) molecular structure of complex 4.3. Scale bar = 10 µm

Unfortunately, the complex displayed signs of toxicity at the concentration used, with large vesicles forming throughout the cell as seen in Figure 5(red arrows), and while lower concentrations could potentially be explored for emission imaging, the inability to use higher concentrations would limit its utility as a contrast agent in TEM. As this complex does not appear to localise with complete specificity in a particular organelle, it would likely not have accumulated in sufficient concentration to function as a CLEM probe. However, it does suggest that other complexes based on a similar moiety could potentially be selective to mitochondria, and are promising CLEM agents, as long as they are not toxic.

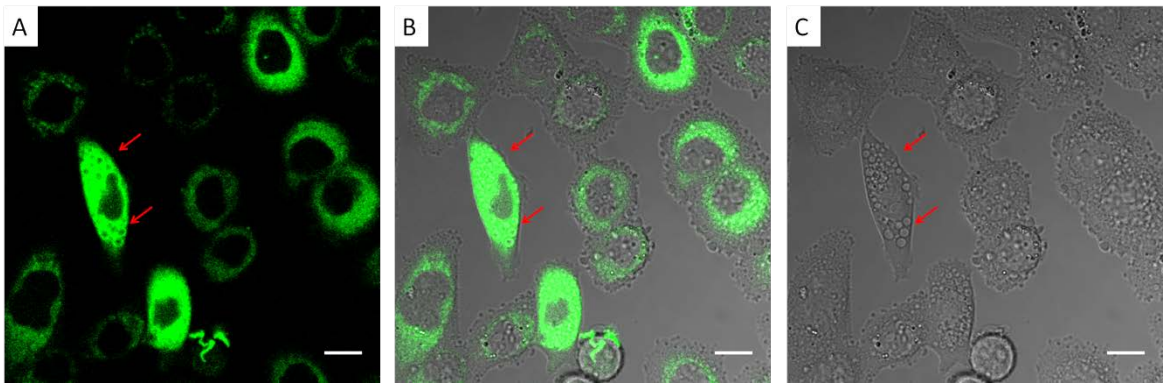

Figure 5. LSCM images of live CHO cells treated with complex 4.3 (50 µM, 3h) displaying signs of toxicity (A) emission (λ_{ex} = 405 nm), (B) overlay, (C) brightfield. Scale bar = 10 µm

In order to improve intracellular localisation, another set of iridium (III) NC-complexes was

investigated which bear diimine ligands that could potentially improve localisation. Specifically, benzimidazole ligands were considered, as these moieties have been reported as novel adenosine receptors antagonists[15] and could have pKas suitable to undergo protonation over physiological pH, potentially yielding specific localisation. Positively charged Ir(III) complexes with two phenylpyridine ligands and quinoline or isoquinoline benzimidazole as a neutral diimine ligand have been tested for intracellular localisation, complex **4.4** and its structural isomer **4.5**. Diffuse staining in the cytoplasm was seen in the cells stained with either complex, with no nuclear staining observed which is common for most iridium (III)-NC complexes. There was also bright punctate perinuclear staining seen with both complexes which is typically associated with lysosomal and/or endosome staining, this could be due to the low pH of the lytic vesicles(4-5 pH) protonating the complexes and trapping them inside. No clear signs of toxicity were observed while imaging was performed with either complex.

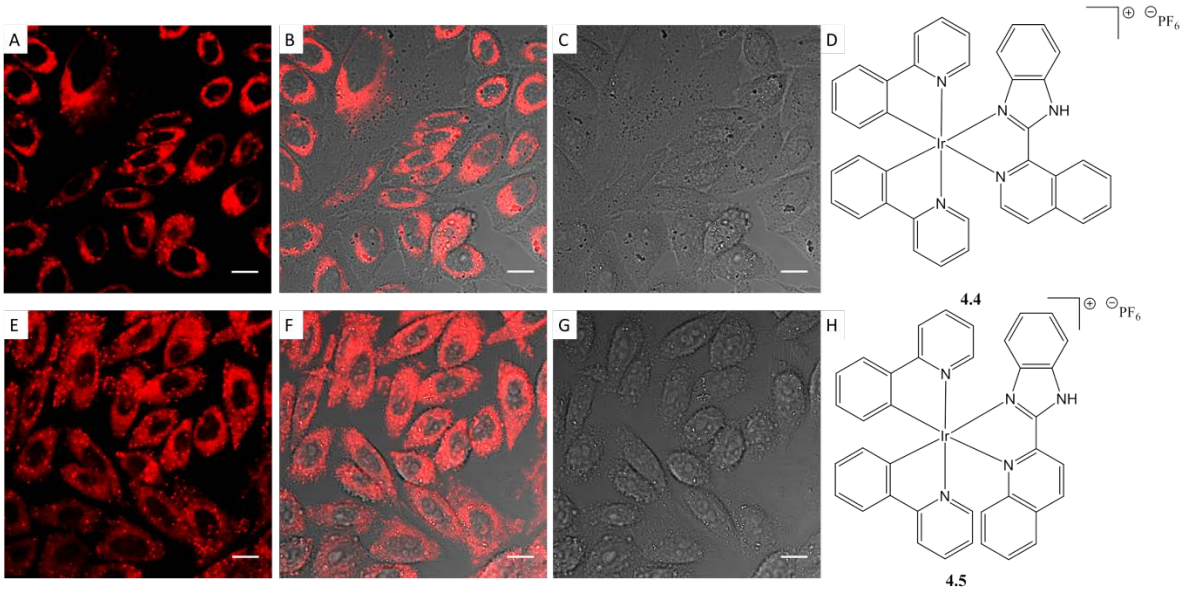

Figure 6. LSCM images of live CHO cells treated with complex 4.4 (A-C) or complex 4.5 (E-G)(50 µM, 3h), (A + E) emission (λ_{ex} = 405 nm), (B + F) overlay, (C + G) brightfield; (D) molecular structure of complex 4.4 (H) molecular structure of complex 4.5. Scale bar = 10 µm

While these complexes look like potential candidates for further work solubility of the complexes was something of a problem as the complexes would often precipitate from solution while staining cells. This affected in-situ concentrations in solution leading to inconsistent staining and non-reproducible results due to unknown concentrations in solution. Due to these problems it was decided that more water soluble complexes needed to be explored.

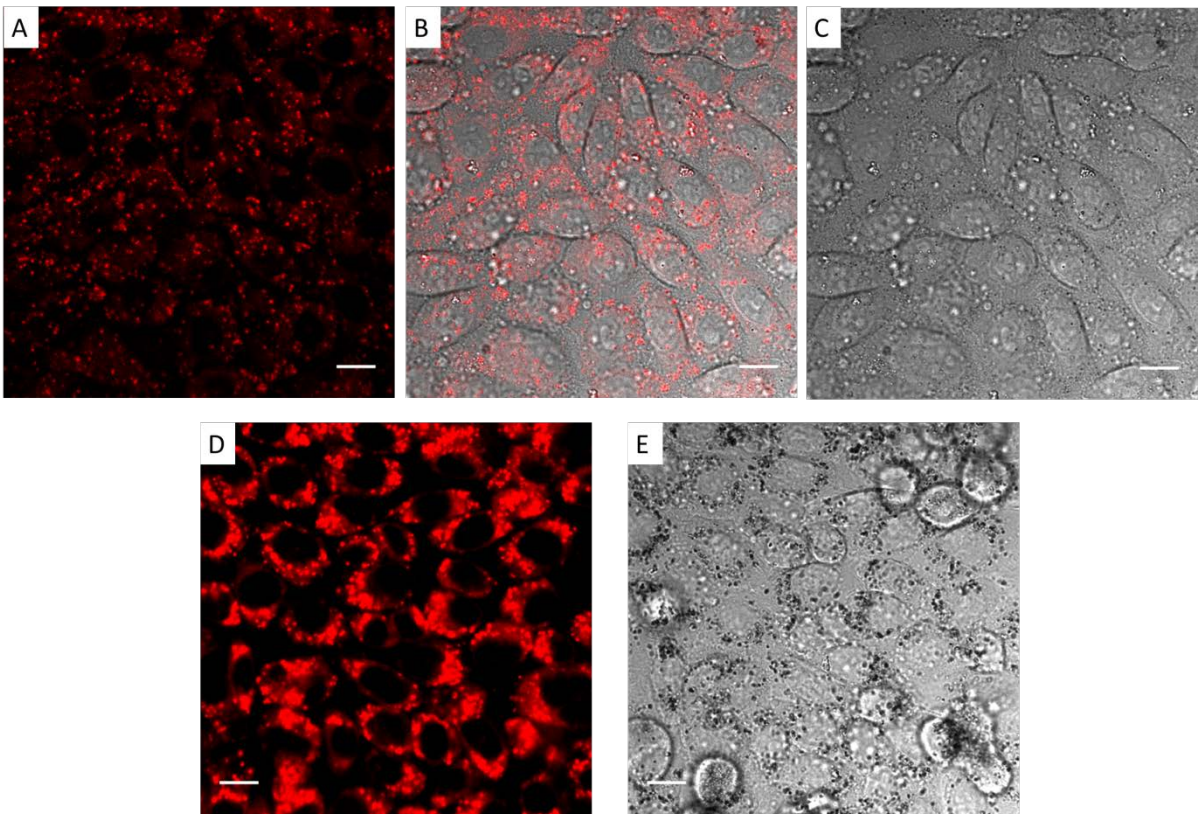

Figure 7. LSCM images of live CHO cells treated with complex 4.4 (top) or complex 4.5 (bottom) (50 µM, 3 h) displaying large amounts of precipitated material around the cells. (A + D) emission (λ_{ex} = 405 nm), (B) overlay, (C + E) brightfield. Scale bar = 10 µm

To build on the design of complexes **4.4** and **4.5,** complexes with a bisbenzimidazole instead of a benzimidazole ligand has been used in the $[Ir(N\hat{}C)(N\hat{}N)]^+$ motif. It was proposed that is complex could potentially localise specifically via the protonation of the benzimidazole as the pK_a of the second bisbenzimidazole group is 5.7. CHO cells were stained with 5 µM (in DMEM media, DMSO < 1%) of complex **4.6** for 12 hours before imaging. The localisation of the complex was observed to be bright puncta in the perinuclear region of the cell with some diffuse cytoplasmic staining also seen. The complex displayed no obvious signs of toxicity after the long incubation period. Thus it was decided that this complex that this complex could be taken forward for further study.

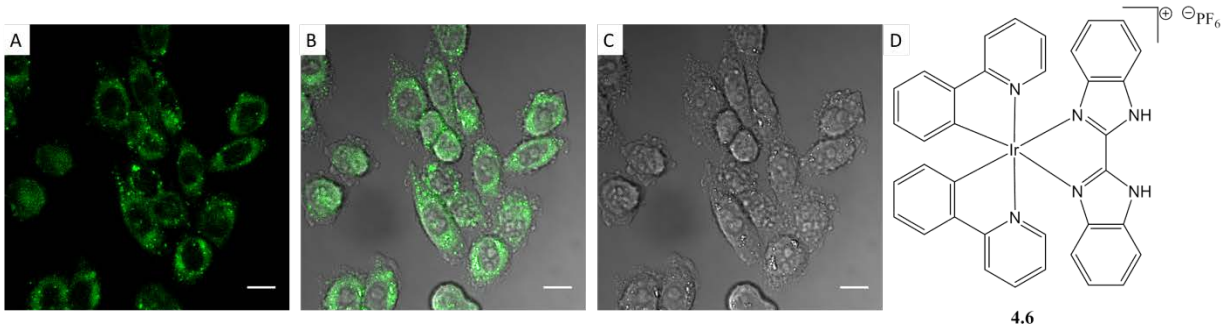

4.6

Figure 8. LSCM images of live CHO cells treated with complex 4.6 (5 µM, 12 h), (A) emission (λ_{ex} = 405 nm), (B) overlay, (C) brightfield; (D) molecular structure of 4.6. Scale bar = 10 µm

Finally, one more class of emissive iridium (III) complexes with cyclometallating ligands is one based on 2-(2-thienyl) pyridines. These complexes have gained interest of the last decade for LED applications due to their high emission quantum yields, and emission maxima being shifted towards red part of the spectrum.[16] These complexes, however, have not been investigated as bioimaging probes. The complex $[Ir(thp)_2(acac)]^+[PF_6]$, **4.7**, was investigated here for that purpose. When CHO cells were treated with 100 µM (in DMEM media, DMSO < 1%) of complex **4.7** for 1 hour, the complex was found to accumulate reasonably rapidly in cells, allowing images to be taken after 1 hour incubation. Punctate perinuclear staining was observed with some diffuse cytoplasmic staining also present, suggesting that the complex is being sequestered in the endosomal system. While no obvious signs of toxicity were observed, the sequestering of the complex into the endosomal system suggests the cells are attempting to traffic the complex out of the cell. This could be due to potentially toxicity or simply the areas of the cell the complex preferentially accumulated in.

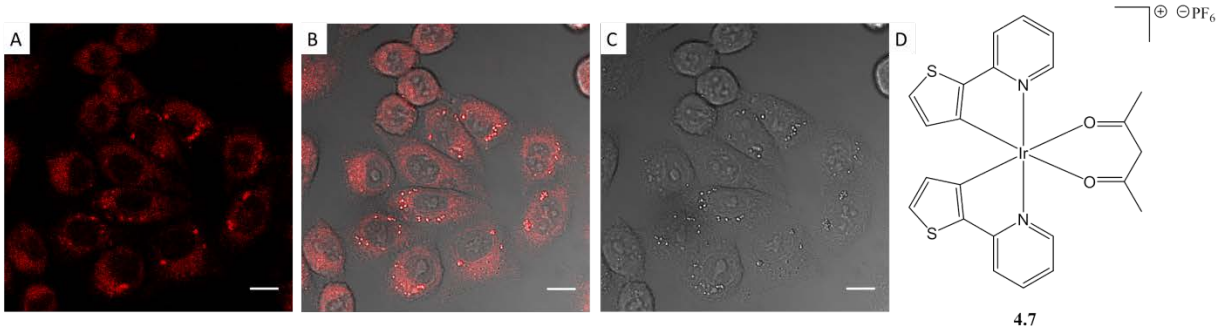

4.7

Figure 9. LSCM images of live CHO cells treated with complex 4.7 (100 µM, 1 h), (A) emission (λ_{ex} = 405 nm), (B) overlay, (C) brightfield; (D) molecular structure of 4.7. Scale bar = 10 µm

4.2.3 Time Resolved Emission Microscopy Studies

Three complexes shown in Figure 10 were found to be promising upon initial screening, and as such further experiments were undertaken to observe if any of these complexes display environmental sensitivity which was measurable using TREM. While the long emission lifetime of the first platinum (II) complex studied, Pt(N^C^N)Cl, gave excellent sensitivity for oxygen, shorter lifetimes on the order of a few hundred nanoseconds would be desirable for future probes. Shorter emission lifetimes would yield higher relative brightness as more photons are emitted per unit time, therefore requiring less irradiation and reducing any phototoxicity. On the other hand, the lifetime should be sufficiently long for the differences in lifetimes induced by the analyte of interest (H^+, metal ions, etc) under physiological conditions to be still measurable with a high degree of certainty.

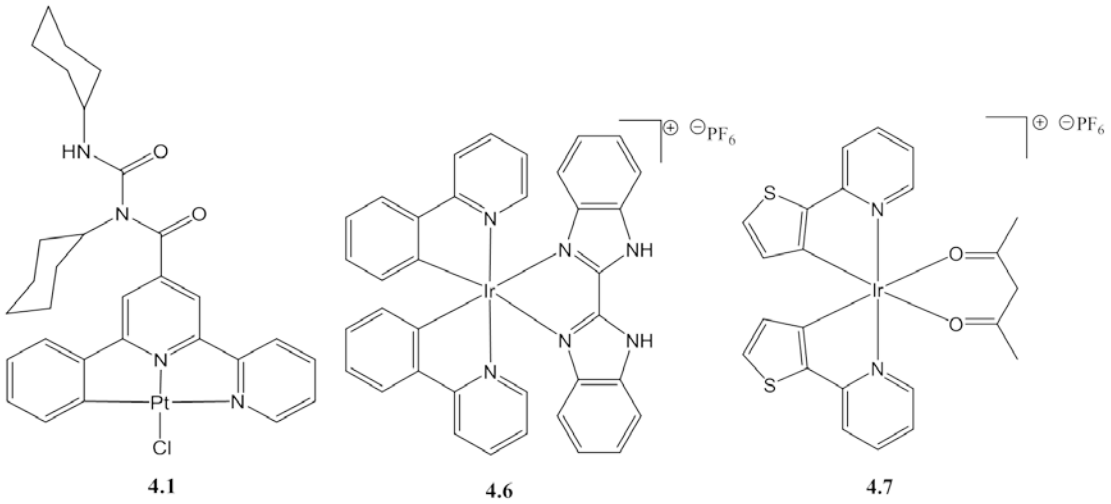

Figure 10. Molecular structures of complexes selected for TREM experiments.

The Pt(N^N^C-urea) complex, **4.1** was found to localise throughout the cytoplasm and the nucleus, without any obvious signs of cytotoxicity observed. As such the complex was scrutinised under TP-TREM to see if any interesting variations in emission lifetime could be observed throughout the cell. Similar to the Pt(N^C^N) complex in Chapter 3, complex **4.1** was expected to show oxygen sensitivity due to emission originating from the triplet state in these complexes. TP-TREM studies were performed on live CHO cells incubated with complex **4.1** at 100 μM for 12 h. The lifetime data collected was fitted to a bi-exponential model with a very short component (autofluorescence) and a longer lived component ranging between 300 - 800 ns, corresponding to the lifetime of the complex in the cellular environment. The complex was observed to have shorter emission lifetimes on the periphery of the cell with steadily increasing lifetime towards the nucleus and nucleoli. Curiously, the longer lifetimes of ~750 ns were observed just outside of the nucleus, in what would appear to be the endoplasmic reticulum/golgi apparatus of the cell, whereas lifetimes of ~670 ns were recorded within the nucleus. It would appear likely that, much like some examples in the literature,[17,18] this complex actually exhibits a preferences for binding proteins over DNA, supported by the lack of strong nucleus staining and the lengthening of lifetimes in protein rich areas of the cell. The increase in lifetime in the protein rich areas of the endoplasmic reticulum suggests that this complex binds to pockets with proteins, shielding the complex from intracellular oxygen and thus reducing quenching.

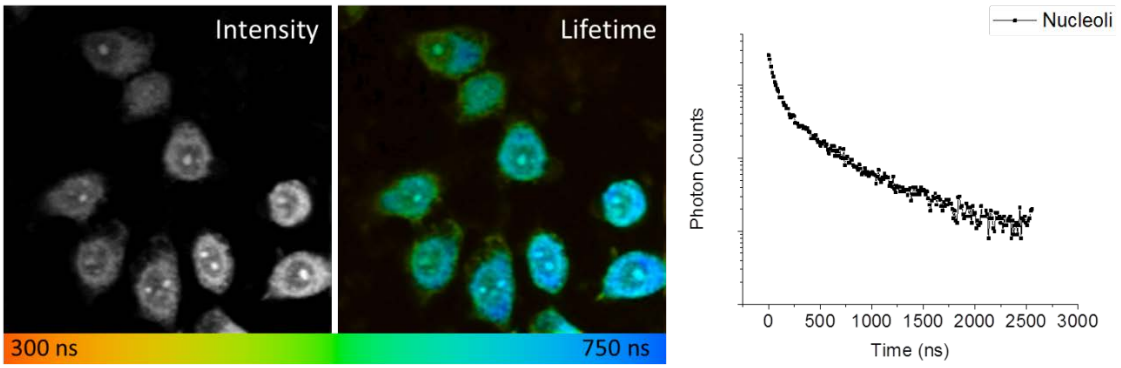

Figure 11. TP-TREM images of live CHO cells treated with complex 4.1 (100 µM, 12 h). In-vitro decay trace from nucleoli region.

Complex **4.1** does appear to display an oxygen gradient within live cells, as the lifetimes steadily increase from the cell periphery in towards the nucleus. However these results also suggest the complex interacts with proteins present within the cell, changing the observable lifetime of the complex and thus affecting the complexes ability to provide reliable oxygen sensitive lifetimes. For this reason the complex was not pursued for further study.

The iridium (III) complex **4.6** that was observed to have punctate staining with a diffuse staining of the cytoplasm was hoped to display some pH sensitivity *in vitro* as the bisbenzimidazole of the complex could be protonated in solution at physiological pH. Previous work done by Gareth Williams and co-workers has also shown that the complex can exist in three different formed depending on the pH of the environment which dictates if the complex is mono or diprotonated. With a calculated pK_a of 5.7, this complex was thought to be ideal for observing physiological conditions and similar to other commercial probes for lysosome and pH sensing.[19] Differences in emission lifetime were also observed between the mono and diprotonated forms of the complex in solution, suggesting that intracellular lifetimes of the complex should vary as a function of pH of the local environment.

TP-TREM studies were undertaken using live HeLa cells stained with complex **4.6** at 5 µm (in DMEM media, DMSO < 1%) for 12h. The cells were imaged pixel by pixel with a emission decay and an intensity value recorded for each pixel. The decay data were best fitted to a monoexponential decay law, and a lifetime distribution map of the imaged area was created with lifetimes depicted by a rainbow chart, red being short (330 ns), blue being long (750 ns). From this data it became clear there were 2 distinct lifetimes present within the cell in line with the different staining, a longer lifetime was measured in the cytoplasmic staining and a shorter lifetime was measured in punctate staining. The average lifetime of the cytoplasmic staining was 513 ns and the average lifetime of the punctate staining was 426 ns, the difference of ~90 ns is indicative of 2 different forms of the complex being present in the different localisation. This is in agreement with solution data where the monoprotonated complex exhibited an emission lifetime of 240 ns and the diprotonated an emission lifetime of 340 ns, thus a difference of ~100 ns is expected. This also suggests that the environment which leads to the

punctate staining is in more acidic locations within the cell, suggesting the complex is localising in the lysosome as these organelles are the most acidic organelles in the cell, at ~4.5 pH.[20]

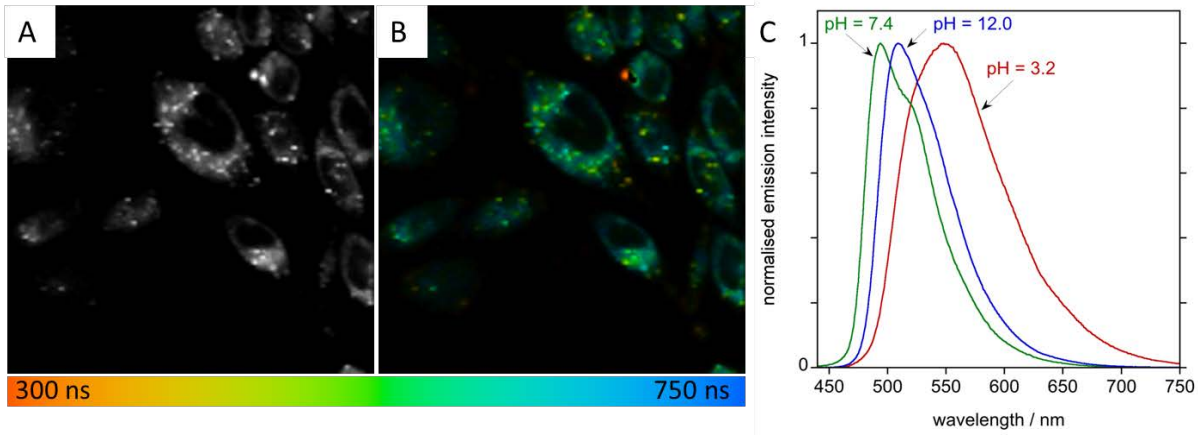

Figure 12. TP-TREM images of live CHO cells treated with complex 4.6 (5 µM, 12h) and emission spectra from solution with complex 4.6. (A) intensity image, (B) lifetime map fitted to a continuous rainbow scale, (C) normalised emission spectra of complex 4.6 at 3 different pHs (pH changes achieved using HCL and NaOH)

Upon imaging, live HeLa cells in both the green (500-550 nm) and red channel (600-700 nm) it was noted that some longer wavelength emission was observed from the bright punctate staining, as shown by the white colour observable in the overlay (Fig. 13). This also suggests that the complex is in its protonated state in these locations as the complex is redshifted when protonated, thus the complex appears to be localising in acidic compartments within the cells.

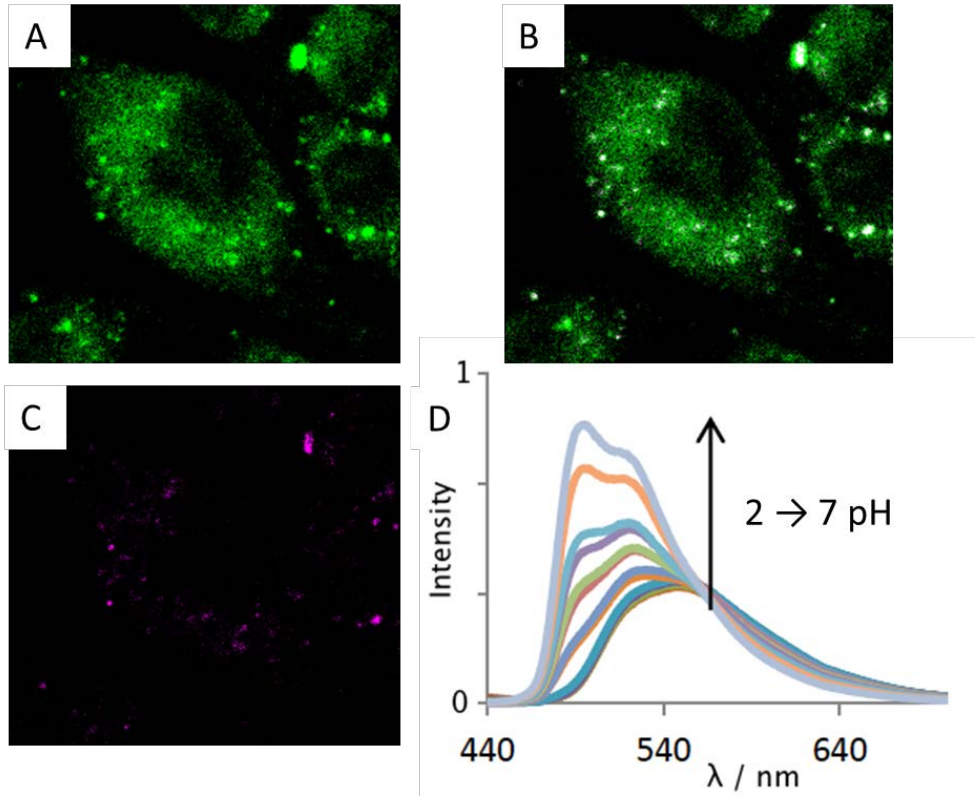

Figure 13. LSCM images of live CHO cells treated with complex 4.6 (5 µM, 12h) displaying emission from (A) 500/25 filter, (B) overlay, (C) 650/50 filters and (D) variation in emission spectra from solution data of complex X by pH from 2 → 6.9 pH units.

The iridium (III) complex **4.7** was also observed to have a punctate localisation pattern with some diffuse cytoplasmic staining also present. The cells treated with this complex did not display any obvious signs of toxicity and therefore **4.7** has been considered for TP-TREM experiments. The emission of this complex was expected to be oxygen sensitive due to emission originating from the triplet state. TP-TREM was performed on live CHO cells incubated with complex **4.7** at 100 µM for 1 h. The lifetime data was best fitted to a mono-exponential decay and a lifetime map was calculated. In the initial false coloured lifetime map no dependence of the lifetime on the localisation of the complex was observed.

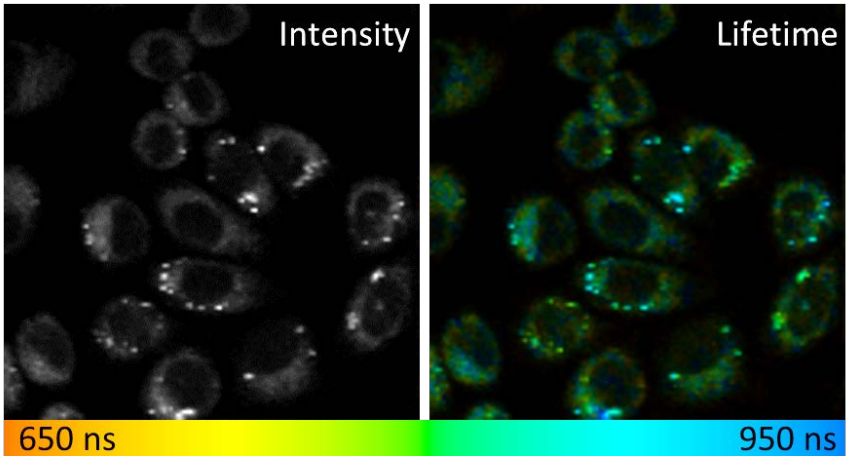

Figure 14. TP-TREM images of CHO cells treated with complex 4.7 (100 µM, 1 h)

Further analysis of the difference in lifetime between the punctate and cytoplasmic staining was performed by taking lifetimes of specific regions using a pixel bin of 5. Pixel binning utilizes surrounding pixel values of a point of interest depicted below (Fig. 15), to add statistical robustness to the data. From these values it became clear that there was very small differences between the regions and both values were found to have large errors associated with them, essentially making the values indistinguishable. This suggests that the lifetime of complex **4.7** is likely to be sensitive to many different factors *in vitro* and so would not be a good candidate for use as TP-TREM dye for oxygen sensing due to the inability to ascribe changes in lifetime to specific environmental changes.

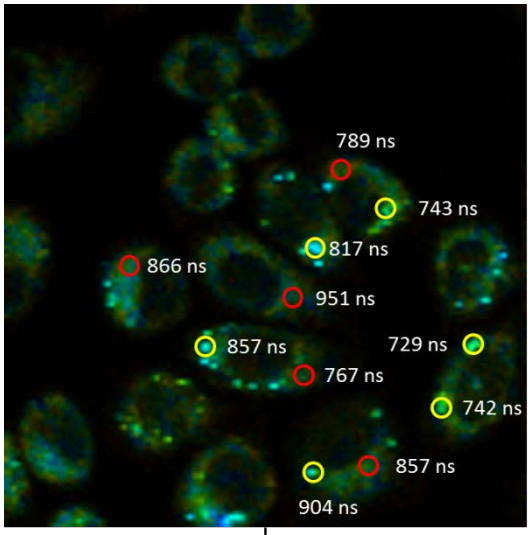

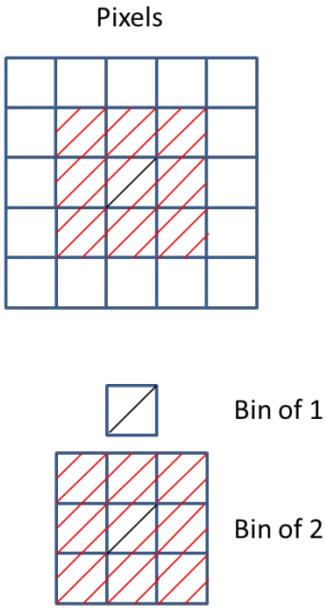

Punctate staining	Cytoplasmic staining
742 ns	767 ns
743 ns	789 ns
817 ns	857 ns
857 ns	866 ns
904 ns	951 ns

Figure 15. TP-TREM lifetime map depicting the specific regions lifetimes were taken for analysis (left). Graphical representation of pixel binning (right).

From these TP-TREM studies it was clear that the best candidate to be taken forward as a multimodal dye is complex **4.6** due to its good photophysical properties, and pH sensitivity. Complex **4.1** was found to display sensitivity to oxygen but the lifetime data also suggested the complex binds to proteins within the cell, therefore more than one factor affects the lifetime. Complex **4.7** was observed to have a very complicated lifetime map that did not display any obvious lifetime patterns associated with the localisation of the complex, suggesting that the lifetime of the complex is sensitive to multiple analytes *in vitro*. This reduces the effectiveness of the complex to be a probe for specific environment data.

4.3 Uptake and Localisation of 4.6.

After selecting **4.6** for further study it was thought the incubation times and localisation could be further optimised and with further work done by Luke McKenzie it was found that the complex changed it localisation over the period of 24 hours. The staining pattern after 15 min incubation has been primarily diffuse cytoplasmic staining, with the typical punctate staining steadily growing in overtime as the cytoplasmic staining steadily disappearing. In light of this information it was decided that after two hours incubation the complex appeared to have mixed localisation between some punctate staining and some cytoplasmic staining which appeared to potentially have specific

localisation too. As such this time point was decided as an interesting feature to study the complex further.

Due to the pH sensitivity of the complex it was suspected that the punctate perinuclear staining was likely to be protonated complex trapped in the lysosomes, as lysosomes typically have a pH of ~4.5.[20] This phenomenon of complex trapping has been observed in other molecules with pH sensitive moieties present.[21] Furthermore, initial two-photon TREM experiments were suggestive that the punctate staining was of more acid compartments/organelles due to the difference in lifetime observed. Upon incubating cells with complex **4.6** and LysoTracker™ Red it was clear that the punctate staining of the complex colocalised with that of the LysoTracker™ Red (Fig 16. white arrows). While colocalisation is usually accessed by use of statistical methods, such as the Pearson's coefficient or Manders coefficient, it is not a sensible measure here as the cytoplasmic staining would reduce the value obtained.

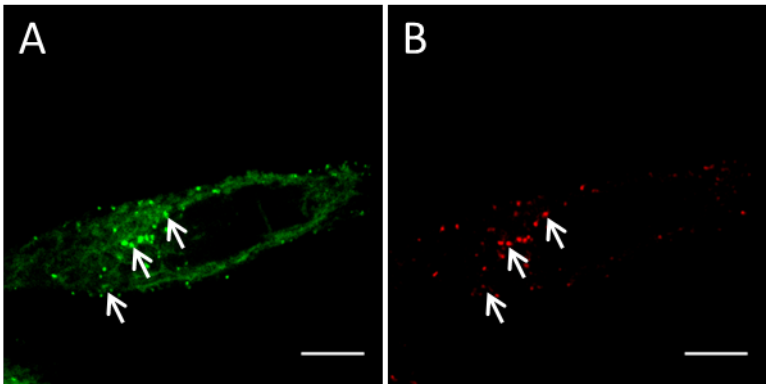

Figure 16. LSCM images of live HeLa cells treated with complex 4.6 (10 µM, 2 h) and LysoTracker™ Red (50 nM, 35 mins) with lysosome staining pattern highlighted by white arrows (A) emission from complex 4.6 (λ_{ex} = 405 nm), (B) emission from LysoTracker™ Red (λ_{ex} = 561nm). Scale bar = 10 µm

The complex was also assessed as a potential two photon dye as this would allow images to be taken in live cells with reduced phototoxicity and better z resolution. The two-photon cross section was measured using the comparative method using fluorescein as a standard and was calculated by Dr Elizabeth Baggaley to be 112 GM at 760 nm excitation.[22] This value is reasonable for this type of complex and adequate to obtain good quality emission images under two photon excitations. Live HeLa cells stained with complex **4.6** and were imaged using a two photon microscope, providing exquisite detail of the staining with the punctate staining well defined (Figure 17).

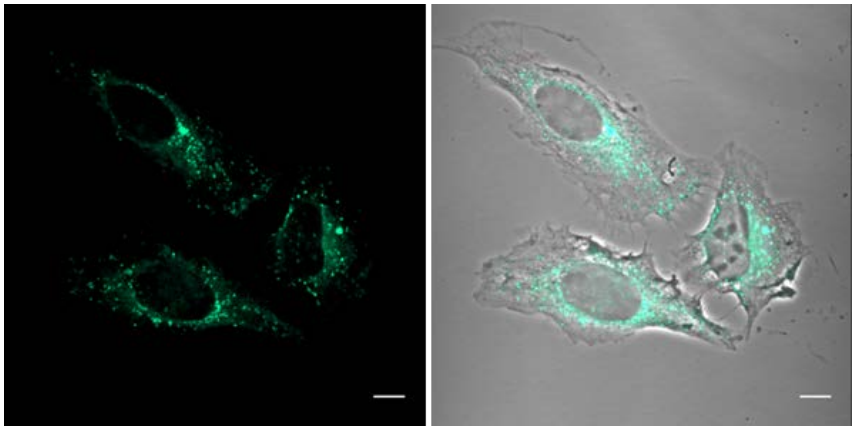

Figure 17. Two-photon microscopy Images of live HeLa cells treated with complex 4.6 (10 µM, 2 h) with the emission image (left) and the overlay of the emission and brightfield (right). Scale bar = 10 µm

The diffuse cytoplasmic staining appeared to have its own pattern, and therefore may be indicative of specific localisation in some formations in the cytoplasm. Due to the expansive nature of the staining it was first considered that the complex could be staining the vesicle networks of the endoplasmic reticulum and therefore the complex was co-stained against ER tracker. While some overlap was observed there were areas in the cytoplasm where the complex was clearly located but the ER stain was not present (white arrows). 3D SIM studies have been undertaken since the improved resolution could potentially yield any clues as to the cytoplasmic localisation of the complex.

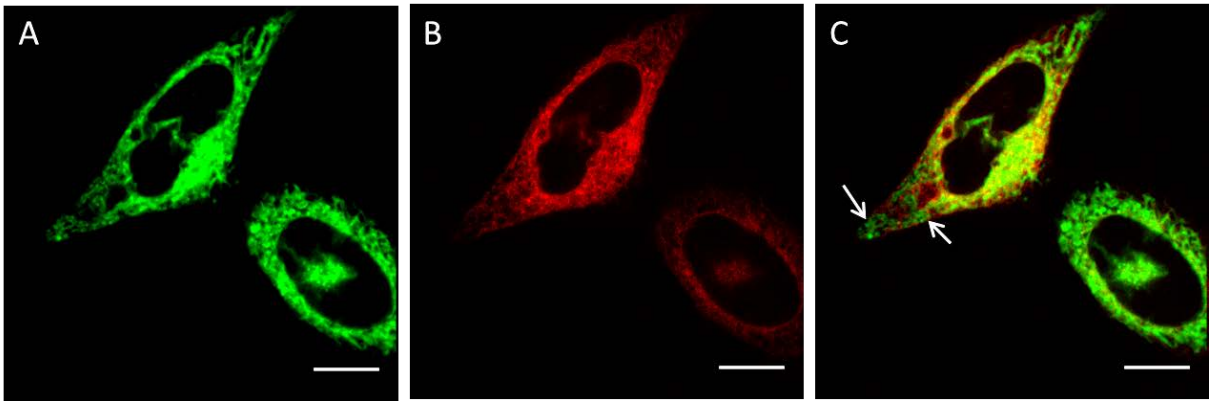

Figure 18. LSCM images of live HeLa cells treated with complex 4.6 (10 µM, 2 h) and Cellight®ER-RFP, BacMam 2.0 at 30 p/c.(A) Emission from complex 4.6 (λ_{ex} = 405 nm), (B) emission from RFP (λ_{ex} = 561 nm), (C) overlay. Scale bar = 10 µm

Although complex **4.6** had not shown any obvious signs of being toxic to cells, the complex was accessed via a MTT ((3-(4,5-dimethylthiazol-2-yl)-2,5-diphenyltetrazolium bromide) tetrazolium) reduction assay to confirm the effects of the complex to the viability of the cells (Figure 19). An MTT assay works by providing the cells with a compound that is broken down by healthy cells to yield an insoluble product which strongly absorbs in the visible range in solution. The cells are then permeabilised, the product dissolved in DMSO and a direct comparison to healthy cells is used to assess the viability of the cells. The lower the cells metabolic activity, the lower the amount of MTT converted to the product and thus lower optical density of the solution measured. As the complex is

dissolved in DMSO as a stock and DMSO can also have effects on cell viability these were also compared. The MTT assay was carried out immediately after cells had been stained with complex **4.6** (10-100 µM, 2 h) or the corresponding concentration of DMSO (0.2-2 %). No change in cell viability was observed at 10 µM compared to the control or 0.2 % DMSO and a small reduction in viability was seen at 100 µM in comparison to control and 2 % DMSO. This data suggests that the complex is not particularly cytotoxic unless used at concentrations above 100 µM, which is well above the concentration needed for optical imaging.

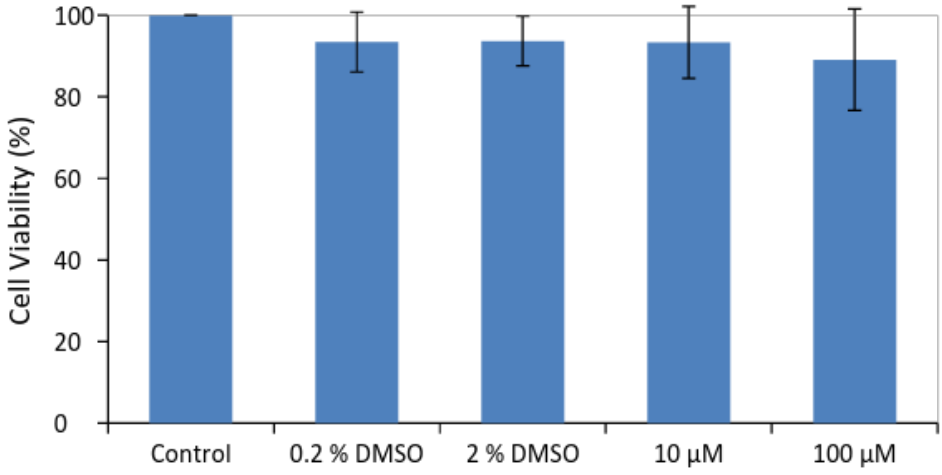

Figure 19. Histogram displaying MTT toxicity data of HeLa cells treated with complex 4.6 (2 h) with error bars. Error bars = 2SD

4.4.1 *In Vitro* Lifetime Mapping with 4.6.

Due to the change in incubation time and cell type from CHO to HeLa cells, the TP-TREM studies were repeated for the complex in HeLa cells and the new staining conditions developed were utilised. Emission from live HeLa cells stained with **4.6** displaying localisation concordant with the localisation pattern observed in live CHO cells with confocal and two-photon microscopy of CHO cells stained with the same complex, displaying a combination of bright punctate lysosomal staining and diffuse cytoplasmic staining being observed. Emission spectra from specific areas of the cells were obtained using a spectrometer attached to the microscope to assess emission behavior at the sub-cellular resolution in addition to the emission lifetime (Figure 20). The emission profile from the cytoplasm was found to match solution data for the singly protonated form of the complex. While the emission spectrum from the punctate lysosomal staining corresponds to a mixture of the single and double protonated forms. This mix of profiles is likely to be due to some emission from the cytoplasm-accumulated complex above and below the lysosome being measured as well, as the pKa of 5.7 suggests that the doubly protonated form should predominate in the acidic conditions.

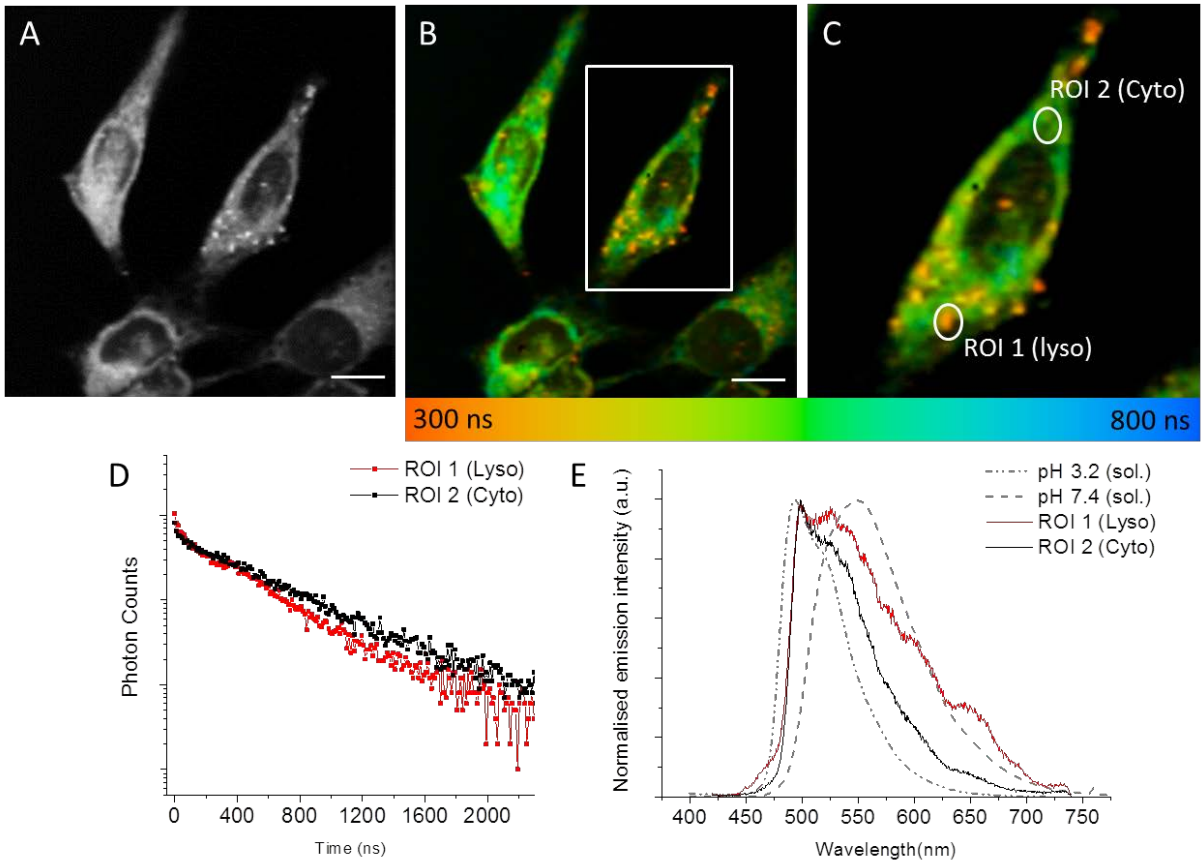

Figure 20. TP-TREM imaging and emission spectra of HeLa cells treated with 4.6 (10 µM, 2 h). (a) total intensity image; (b,c) lifetime maps fitted to continuous rainbow scale; (d) in-vitro decay profiles taken from lysosome (region of interest, ROI 1, red) and cytoplasm (ROI 2, black); (e) normalised emission spectra recorded from live HeLa cells at two locations: lysosome (1, red), cytoplasm (2, black); solution spectra at pH 4.2 and 7.4 (grey lines) are included for comparison. Scale bar = 20 µm.

Lifetime distribution mapping of the HeLa cells stained with complex **4.6** were consistent with the patterns observed in the CHO cells. Average lifetimes of the lysosome and cytoplasm were found to be 415 ns and 530 ns respectively. The difference between the lysosome and cytoplasm lifetimes is slightly larger than observed in the CHO cells, however they remain within the error margins of the initial CHO measurements. This shows that the lifetime differences between the two cellular locations are clearly defined for the different protonated form of this complex and allow pH sensitive data to be obtained by lifetime mapping.

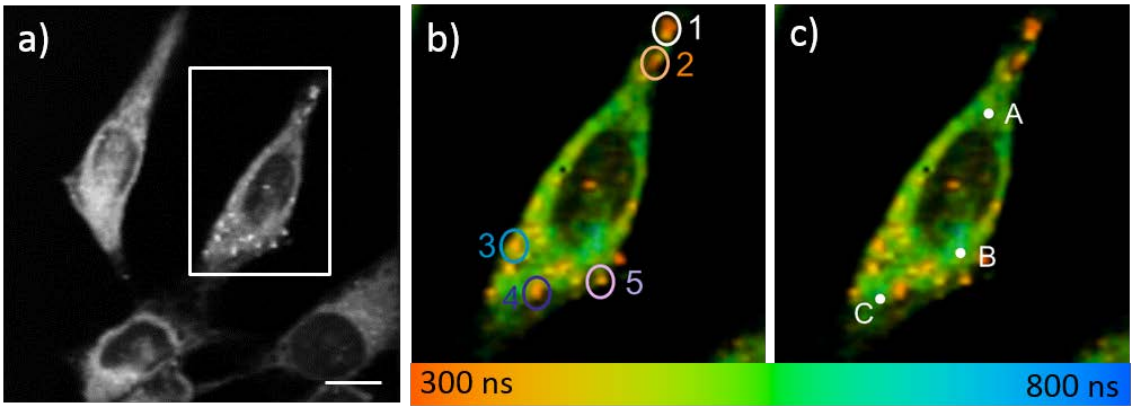

Cellular location	ROI	Lifetime / ns	Average τ / ns
Lysosome	1-5	407, 400, 436, 406, 416	415
Cytoplasm	A-C	532, 541, 527	530

Figure 21. Two-photon TREM ROI analysis of punctate (b) and diffuse (c) ROI's.

4.4 3D SIM Imaging with 4.6

Little photobleaching was observed whilst using **4.6** for confocal and lifetime microscopy, potentially making complex **4.6** ideal for use in super resolution microscopy applications. As the localisation was also still uncertain, it was anticipated that the improved resolution provided by 3D SIM might give further insight. Live HeLa cells were prepared for SIM in the same way as was described in Chapter 3, the incubation conditions used as above (10 μM, 2 h).

Seen in confocal and two-photon images, the bright punctate staining of the complex was exquisitely clear when imaged using the SIM. In contrast to the other techniques however, the diffuse cytoplasmic staining also appeared structured, as small vesicle/tubular networks that was reminiscent of mitochondrial staining. The photobleaching of complex **4.6** was analysed using the SIMcheck plugin for ImageJ. The relative intensity decay was estimated to be 4.5 %, highlighting that the complex displays excellent photostability while almost 700 individual images were taken to provide a 43 image z-stack of super resolution images. However, the relative intensity fluctuation (which gives an value of the variance in signal between each slice) was calculated to be 26.5 %, this value is usually attributed to illumination flicker and the greater the number the worst the illumination. Based on Chapter 3, this does appear to be a problem with metal complexes as this was observed with complex **3.1** too but not to the same degree as with the organic dyes. This can be seen in the mean intensity graph as the highest and lower mean intensity for each angle varies quite unpredictably,

which is contrary to what is expected as more complex would be predicted to be in the central parts of the cells.

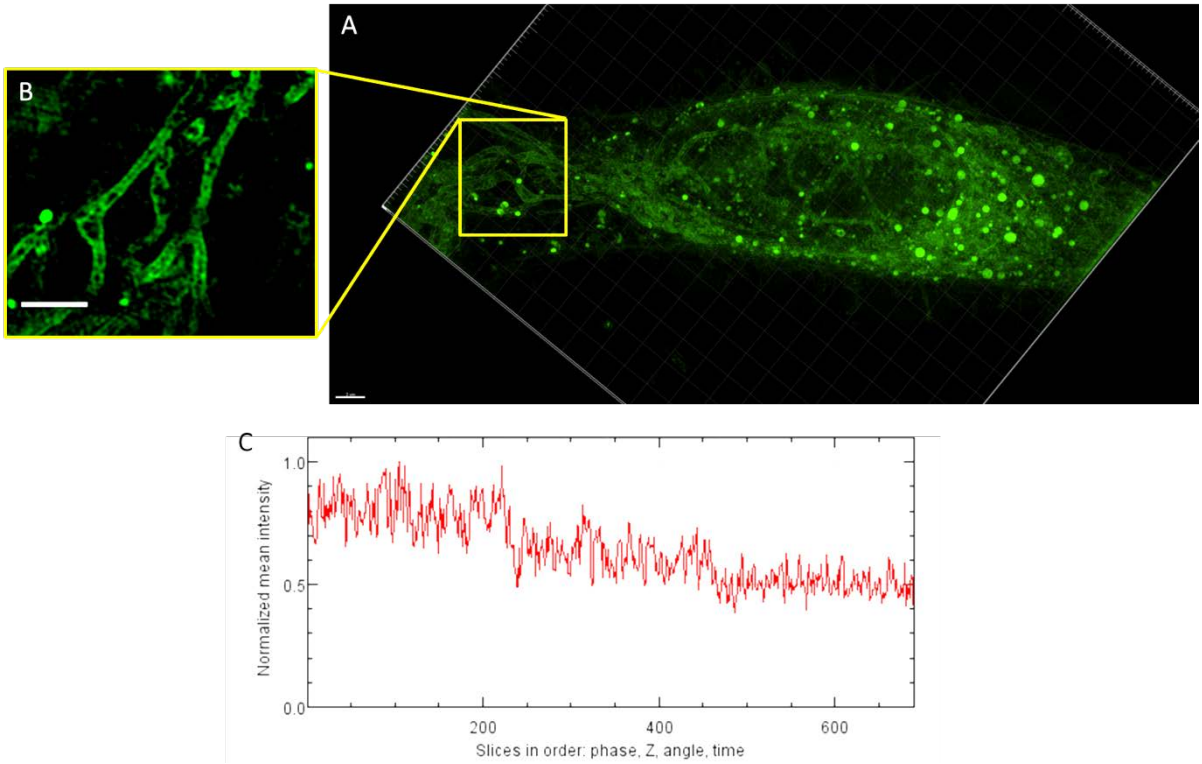

Figure 22. 3D SIM images of fixed HeLa cells stained with complex 4.6 (10 µM, 2h) (A) 3D rendered Z-stack of emission, (B) single slice of tubular network (C) mean intensity graph of all raw slices. (Scale bar = 2 µm)

4.4.1 Co-staining

3D SIM imaging had provided valuable insight into the diffuse cytoplasmic staining of **4.6** after 2 hours incubation. Thus mitochondria co-staining experiments were undertaken to confirm the localisation pattern. Live HeLa cells were stained with complex **4.6** (10 µM, 2 hours) and MitoTracker™ Orange (100 nM, 20 mins) and then fixed (PFA 4%) and mounted for imaging. As expected, the MitoTracker™ Orange was found to co-localise well with complex **4.6** confirming that the complex also localises in mitochondria. As can be seen from the line profile in Figure 24, the majority of the MitoTracker™ emission comes from the center of the mitochondria, whereas the Ir^{III} emission tends to come from the edges of the mitochondria. This opens a number of possibilities as to why this occurs: potentially the complex predominantely binds to the membrane of the mitochondria while MitoTracker™ binds within the mitochondrial matrix. Another possibility is that the complex binds competitively with the MitoTracker™ for sites within the mitochondria and so becomes displaced by the MitoTracker™.

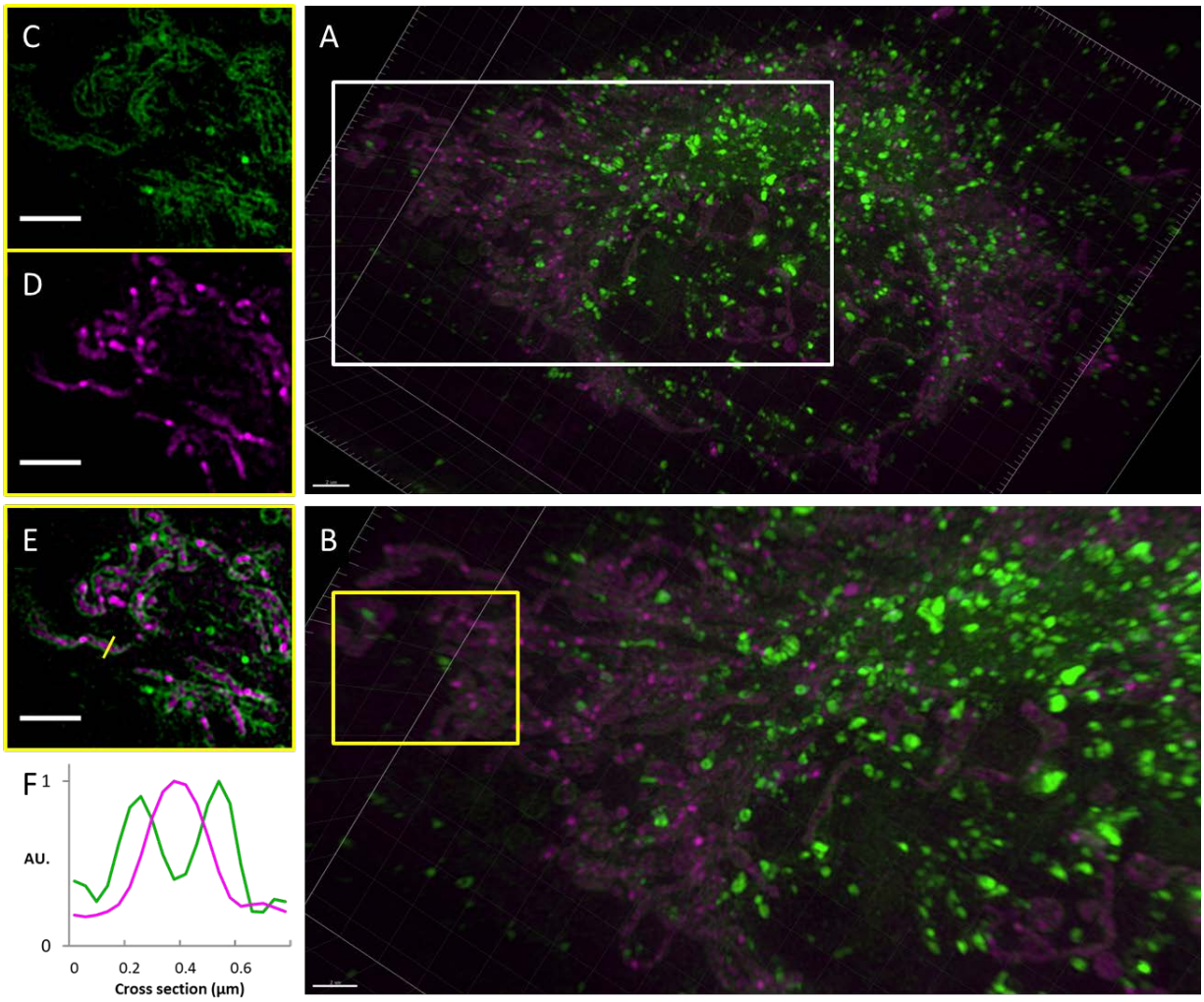

Figure 24. 3D SIM images of fixed HeLa cells stained with complex 4.6 (10 µM, 2 h) and MitoTracker™ Orange (100 nm, 20 mins) (A) 3D rendered image of whole cell with emission from both probes (complex = green, MitoTracker™ = magenta), (B) Zoomed in 3D rendered image of stained cell, (C) single Z-slice showing emission from complex in the mitochondrial membrane, (D) single Z-slice showing MitoTracker™ orange staining mitochondria (E) single Z-slice overlay, (F) Emission line profile from yellow line on overlay demonstrating the complex in the mitochondrial membrane. Scale = 3 µm

To further investigate the potential effects of MitoTracker™ on the localisation of the complex, images of cells treated solely with complex were analysed for comparision. By looking at a number of different cells, it became clear that cells treated with complex did not display uniform staining of their mitochondria. Generally there was a small reduction of intensity in the center of the mitochondria, indicating that the complex exhibits a preference for binding to the mitochondrial membrane (Fig. 24). However, the observed reduction in intensity was not as pronounced as the cells that had also been stained with MitoTracker™ Orange, suggesting that the MitoTracker™ is having an effect on the localisation of the complex.

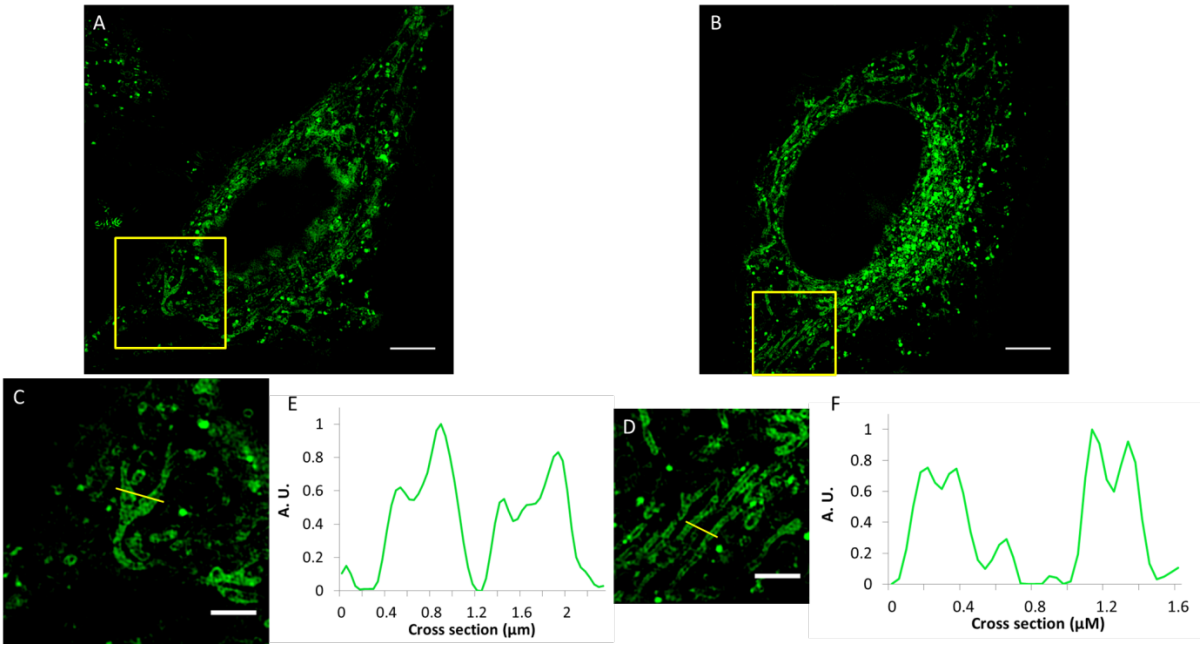

Figure 24. 3D SIM images of fixed HeLa cells stained with complex 4.6 (10 µM, 2 h) with examples of mitochondrial staining using line profiles. (A + B) single image slices of 3D SIM images stacks, (C + D) zoomed in areas of mitochondrial staining with area of line profile marked in yellow, (E + F) emission line profiles of mitochondrial staining demonstrating only minor reductions in the centre of mitochondria. Scale = 5 µm (A + B) or 2 µm (C + D).

While imaging dual labelled samples, it was noted that the MitoTracker™ Orange was photobleaching far in advance of complex **4.6** and so the photostability of both complex **4.6** and MitoTracker™ were analysed using SIMcheck. Analysis showed that MitoTracker™ displayed almost double the loss of % mean intensity compared to complex **4.6** under the same number of images taken. The highest % intensity decay observed for MitoTracker™ was 42.5 % while complex **4.6** was only seen reach 24.5 %, with stacks as large as 930 images taken for a single channel. Also due the fragile nature of MitoTracker™ Orange to shorter wavelength excitation, these image stacks had to be collected sequentially or the MitoTracker™ orange would photobleach completely before image acquisition was complete, complicating multicolour imaging with it.

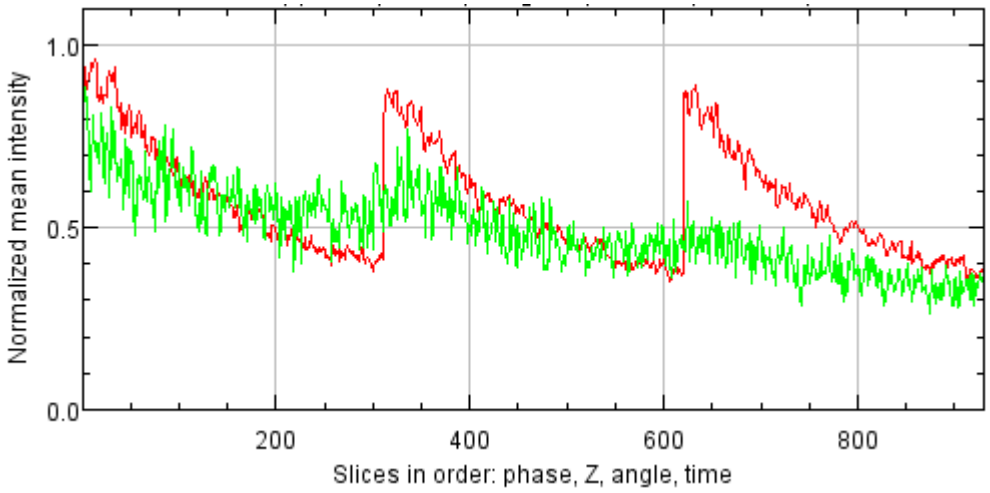

Figure 25. Mean intensity graph of all the raw images taken for a 3D SIM reconstruction of HeLa cells stained with complex 4.6 (green) and MitoTracker™ orange (red).

Co-localisation studies were also performed using LysoTracker™ Red to test the photostability and image reconstruction quality in comparison complex **4.6**. As with the MitoTracker™ orange, when image acquisition was attempted with both illumination wavelengths simultaneously the LysoTracker™ Red photobleached such that image processing was not possible without severe artefacts. Sequential imaging of cells labelled with LysoTracker™ Red and complex **4.6** were also found to suffer problems due to the photobleaching and general low intensity of the LysoTracker™ Red staining, leading to poor image quality. While this data was poorly reconstructed due to the photobleaching of lysostracker red, overlays from cells co-stained with both stained were found to exhibit colocalisation as seen in Figure 26**.**

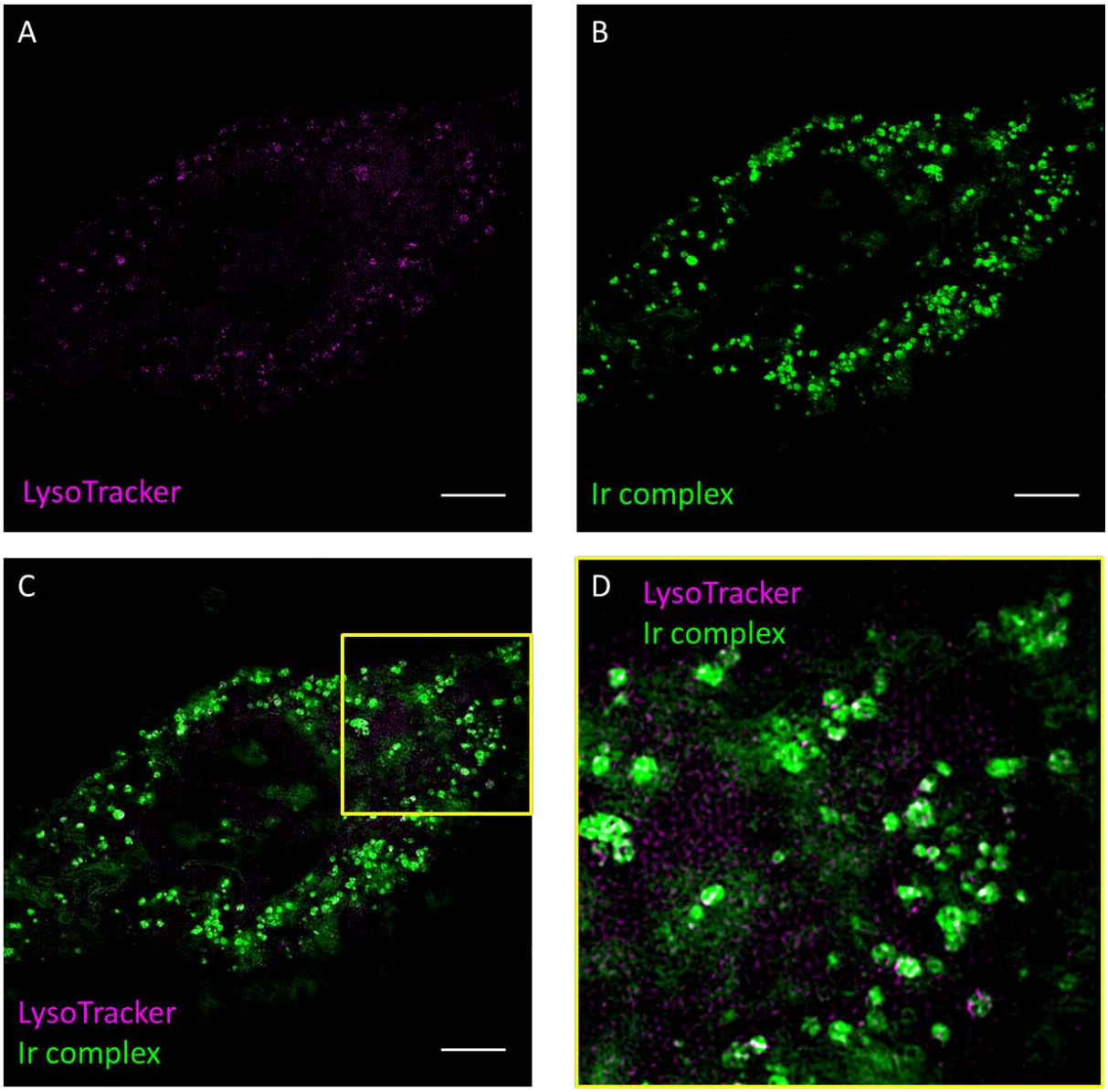

Figure 26. 3D SIM images of fixed HeLa cells stained with complex 4.6 (10 µM, 2 h) and LysoTracker™ Red (50 nm, 35 mins) (A) Lysotracker emission(λ_{ex} = 561 nm), (B) Complex 4.6 emission(λ_{ex} = 405 nm), (C) Overlay of A and B, (D) zoomed in ROI demonstrating colocalisation of the Lysotracker and complex 4.6 seen as white areas. (Scales bar = 3 µm)

Further analysis of the LysoTracker™ Red data shows how the signal to noise ratio is such that the data is not suitable for reconstructions. The images below are modulation contrast-to-noise ratio (MCNR) images generated in SIMcheck and they provide a visual depiction of the ratio of structured illumination pattern strength to noise strength, a key metric for the strength of a SIM reconstruction. Values >3 are shown in purple and are considered inadequate for reconstruction, values around 6 are shown in red and these are adequate for reconstruction and the values twelve to twenty four are rated as good to excellent (Fig. 27). As can be seen in the lysotracker MCNR images, there is very little adequate signal and there is also some off-target background staining visible too. Comparatively, the MCNR image from complex **4.6** exhibits a much higher proportion of orange and yellow pixels,

especially in the lysosomal staining. The mitochondrial staining is seen to be weaker and is predominantly red, indicating that these pixels are only adequate for SIM reconstruction. It was also clear from the total mean intensity graph that the LysoTracker™ was considerably dimmer compared to complex **4.6** which impacts on the signal-to-noise ratio of the images obtained and as such create problems for the reconstruction. Ideally probes for SIM should have good and consistent brightness over the course of the image acquisition to maximise the strength of the reconstruction and avoid artifacts introduction.

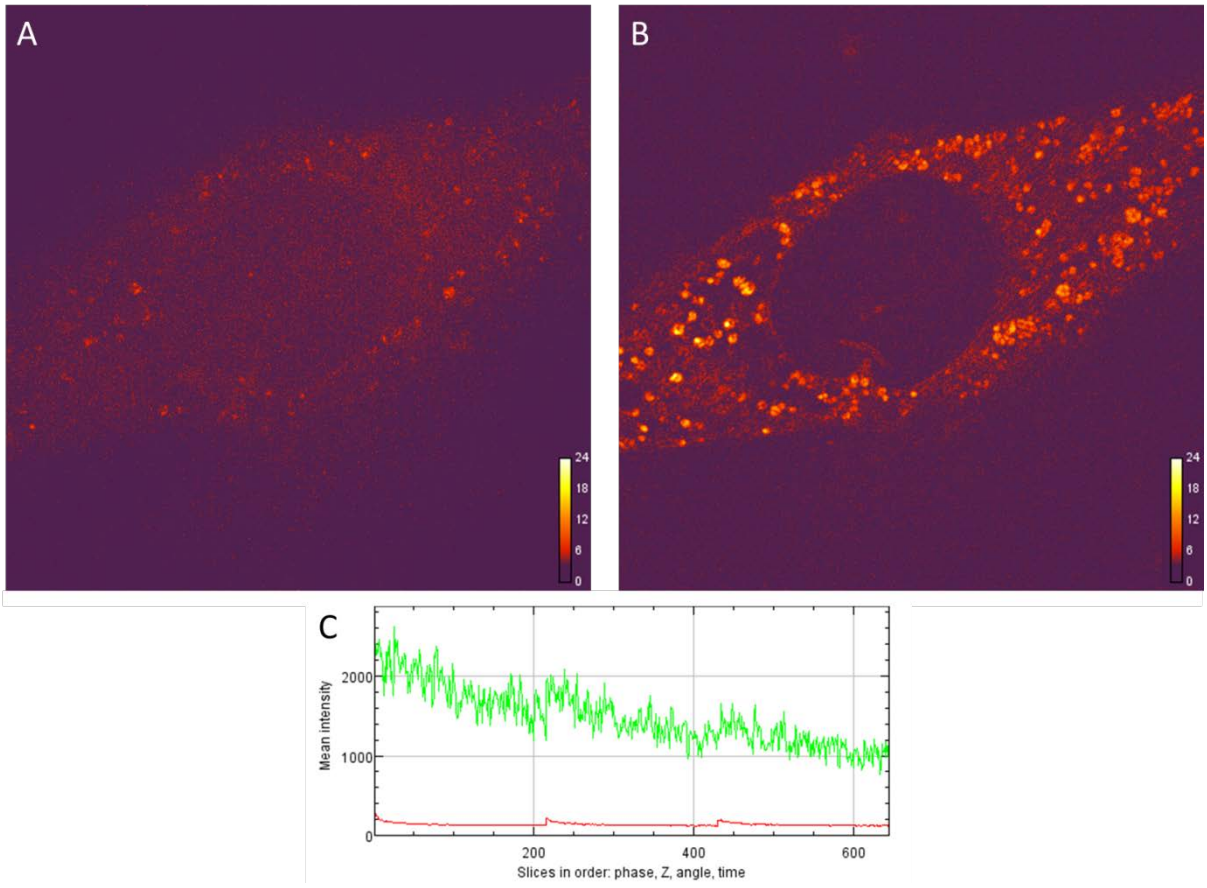

Figure 27. Modulation contrast-to-noise ratio images of fixed HeLa cells treated with (A) LysoTracker™ Red (50 nm, 35 mins) and (B) complex 4.6 (10 µM, 2 h); (C) mean intensity graph of the raw images (green = complex 4.6, red = LysoTracker).

From this 3D SIM data it is clear that complex **4.6** stains the lysosome and mitochondria in HeLa cells, with particular preference for the membrane of mitochondria. It is also clear that currently available commercial probes for mitochondria and lysosomes are not ideal for use in SIM due to the ease with which they photobleach, which adversely affects image reconstruction of the data and therefore causing artefacts. However, complexes such as complex **4.6** are promising candidates to fill this void of dyes which lack the photostability to be used in laser intensive applications such as super resolution microscopy.

4.4.2 Further Cell Lines

As this complex is being tested for its potential as a possible CLEM probe it was decided that it would be prudent to test the complexes behaviour in other cell lines to see if the accumulation and localisation of the complex remained intact. As such two other cell line were chosen to test the wider applicability of complex, U-2 OS an osteosarcoma cell line and SHEP-1, a neuroblastoma cell. These cell lines along with HeLa cells provide a diverse set of cells types with which to test the complex.

These cell lines were prepared in the same fashion as the HeLa cells for 3D SIM to test the ease of use of the complex. Both the U-2 OS and SHEP-1 cells were found to have the same bright punctate staining of the lysosome seen in the HeLa cell and the tubular network of that were observed in HeLa cells (Fig 28.). While no toxicity assays were performed on these cell lines there was no visual signs of toxicity such as blebing of membranes or radical changes in morphology were present after incubation with complex **4.6**.

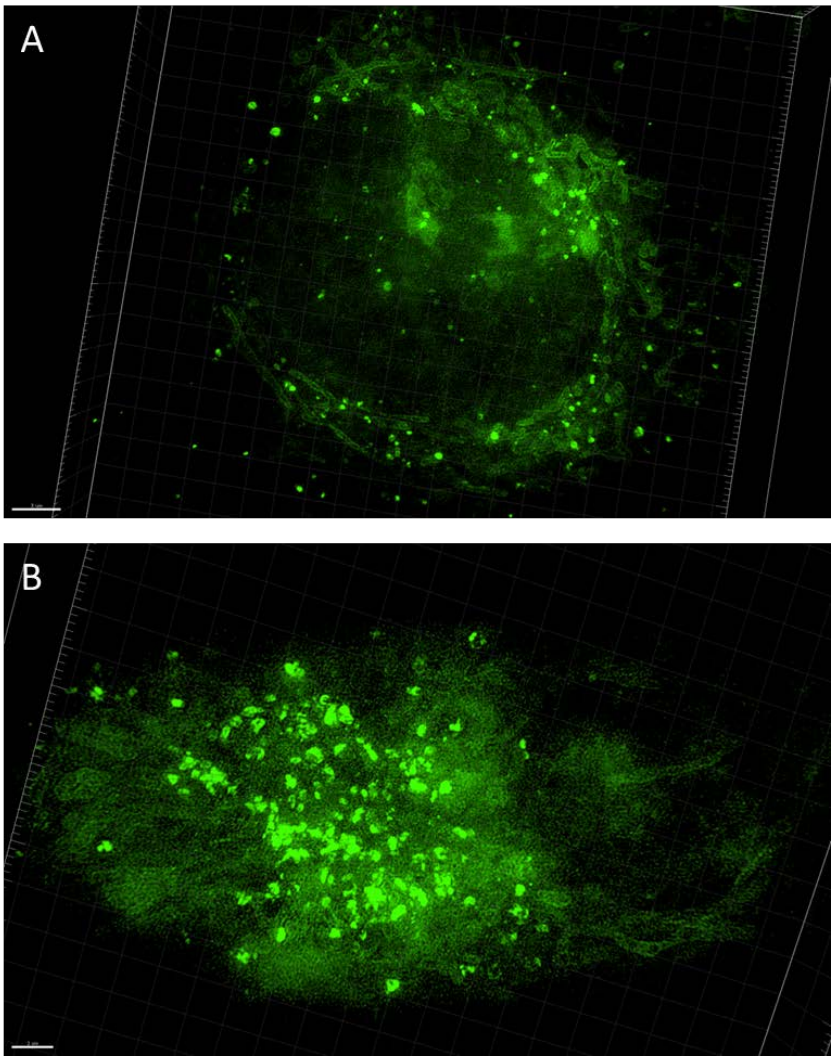

Figure 28. 3D SIM images of various cell lines treated with complex 4.6 (10 µM, 2 h) to display applicability of the complex. (A) U 2-OS cells, (B) SHEP-1 cells

4.5 TEM Imaging

As with the platinum (II) complex in the previous Chapter, the starting point was to establish if the complex would provide contrast in EM and ideally at concentrations usable for emission based imaging. Due to the previous work done using confocal, two-photon and 3D SIM methods, the localisation of the complex was well understood and the contrast was expected to be found in the lysosomes and the mitochondria.

Initially, the complex was used at the 10 µM for 2 hours (in DMEM, DMSO < 2%) on HeLa cells to be concordant with the emission based microscope experiments and no further contrast agents were used to establish where contrast from the complex could be observed. However, at 10 µM no contrast enhancement was observed within the cell when the images were compared to unstained control cells (Fig. 29.). Other complexes that have been recorded providing contrast have been used at considerably higher concentrations than this (200 µM- 2mM).[23-28]

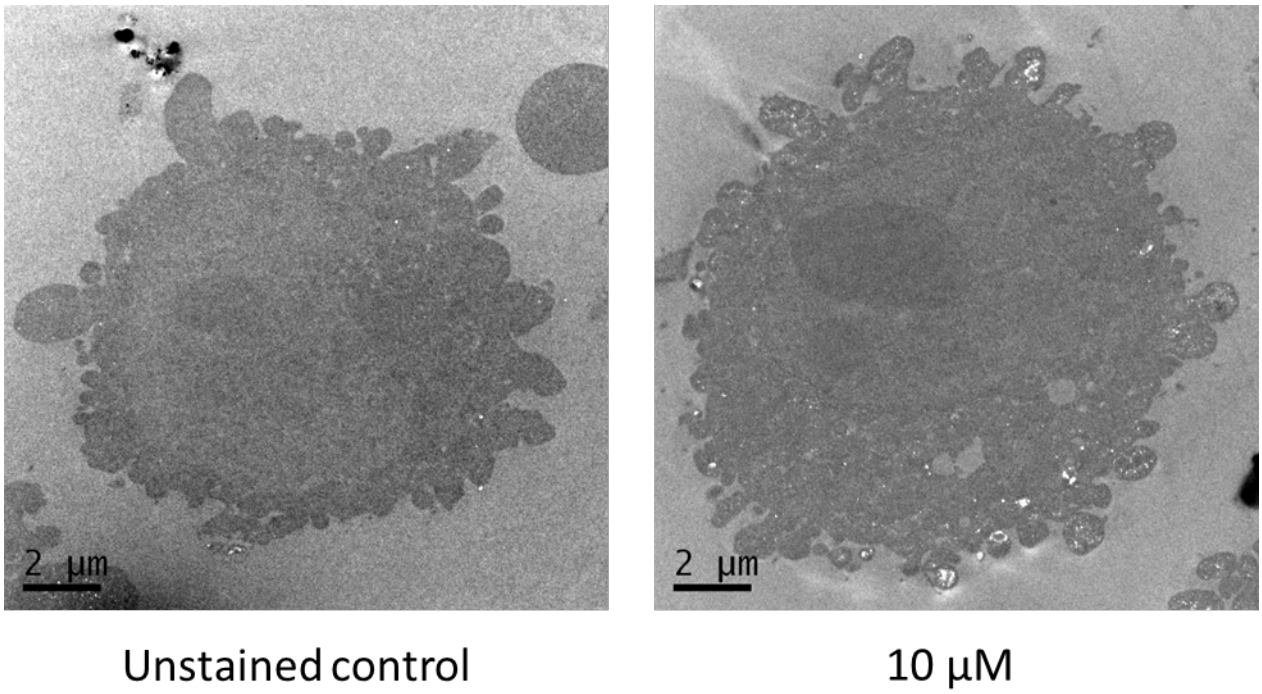

Figure 29. TEM micrographs of HeLa cells, complexly unstained cells (left) and cell stained with complex 4.6 (10 µM, 2 h)(right).

Due to the lack of observed contrast and lower concentration used higher concentrations of complex **4.6** were screened to see if contrast enhancement could be observed. 50, 75 and 100 µM concentrations were chosen as this covers the range at which the cell viability will not be affected.

These concentrations were selected due the potential cytotoxicity from the complex above 100 µM and the platinum (II) complex from Chapter 3 was found to provide contrast at the concentration of 100 µM. In comparison to unstained control cell, cells stained with 50 µM of **4.6** displayed some improvement in contrast with mitochondria and lysosomes just becoming visible in the cytoplasm. However, cells stained with 75 and 100 µM concentrations displayed clear staining of the tubular mitochondria and punctate lysosomes within the cytoplasm of cells only stained with complex **4.6**. The staining of mitochondria and lysosomes is consistent with the localisation pattern observed in 3D SIM, however no perceivable difference is observed in the staining of mitochondrial membranes in comparison to the mitochondrial matrix. This provides further evidence that the presence of MitoTracker™ does affect the localisation of the complex.

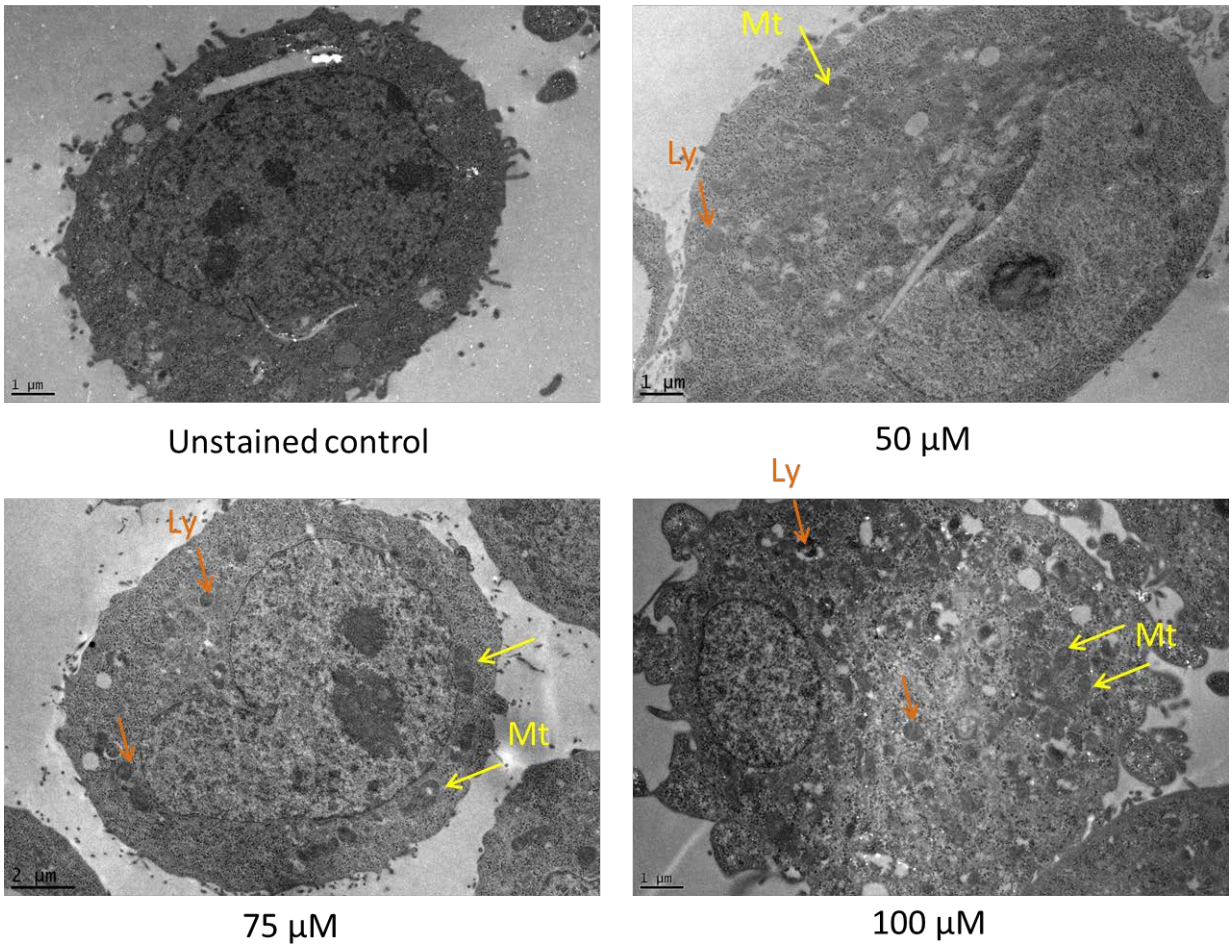

Figure 30.TEM micrographs of HeLa cells stained only with complex 4.6 (concentrations shown, 2 h) without any typical contrast agents used. (example mitochondrial shown by yellow arrows and example lysosomes highlighted by orange arrows)

To further explore the staining of cellular compartments, cells were also prepared using standard EM contrast agents in addition to staining with complex **4.6**. It is also important to establish what complex

4.6 looks like in conjunction with typical staining conditions using osmium tetroxide, uranyl acetate and lead citrate as this is close to the conditions used for CLEM applications as the rest of the cellular context would still be required or at the very least desirable. As in the unstained cells, the HeLa cells stained with 50 µM of **4.6** for 2 hours do not display much difference in contrast to normally stained cells but the cristae of the mitochondria, which would normally be visible, are obscured, due to the presence of the Ir^{III} complex homogenising the staining contrast. There is some clear lysosomal staining in comparison to the control cells treated with typical contrast agents. The HeLa cells treated with 75 and 100 µM show much clearer staining of the mitochondria, with the cristae obscured by the presence of the complex. The lysosomal staining present in the 75 and 100 µM samples are extremely clear punctate staining see throughout the cytoplasm.

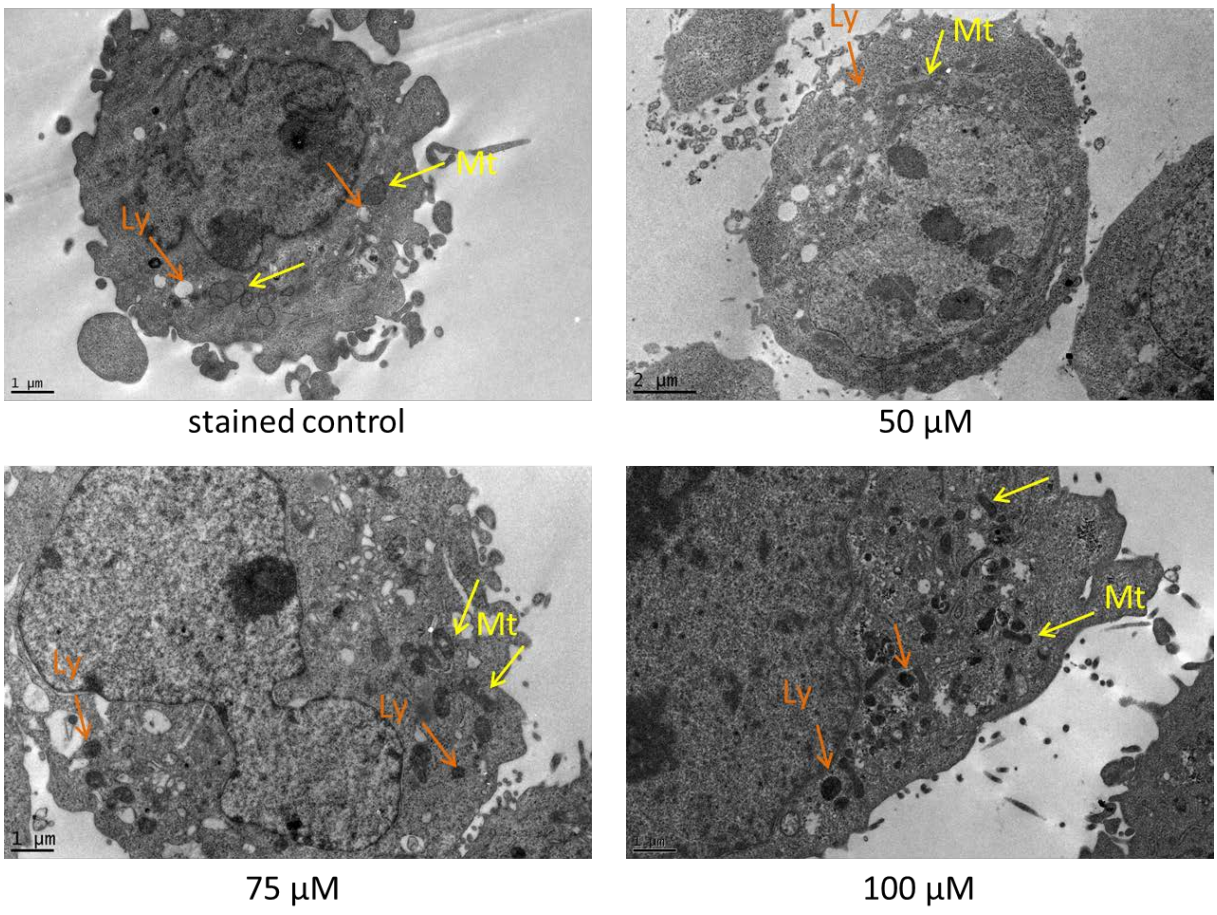

Figure 31. TEM micrographs of HeLa cells stained with typical contrast agents and complex 4.6 (concentrations shown, 2 h). (example mitochondrial shown by yellow arrows and example lysosomes highlighted by orange arrows)

Contrast is not typically assessed in TEM as the techniques is considered qualitative for biological samples, however by applying the equation for optical density it maybe be possible to attempt to gain some semi-quantitative using some assumptions. The equation for optical density is

$$OD = -log_{10}(\frac{p_{out}}{P_{in}})$$

where P_{in} is the amount of light entering the sample and P_{out} is the amount of light exiting the sample and while we don't have a measurement for the amount of electrons entering the sample we can use an area of the sample that is only passing through the resin as a measure of maximum electrons passing through the sample, e_{in}. This will cause the contrast to be artificially reduced as it will underestimate the number of electrons entering the sample. However, it does provide an internal reference for each sample, as each image was taken under different illumination conditions and so can not be compared simply by comparing the difference in grey values of the images. The mean intensity of the region of interest can then be used as the number of electrons getting through, e_{out}. Using these it is possible to change the equation to contain these terms to give

$$EC = -log_{10}(\frac{e_{out}}{e_{in}})$$

where ED is the electron contrast and e_{in} and e_{out} the electrons entering and leaving the sample respectively. While this might offer some possible values it is unlikely to yield absolute values due to the variables that can affect these measurements. Therefore as a simpler method of relative comparison can be made by using the following equation

$$RC = 1 - (\frac{e_{out}}{e_{in}})$$

where RC is the relative contrast between the region of interest and the resin and and e_{in} and e_{out} the electrons entering and leaving the sample respectively. With this equation the e_{in} is assumed to be the maximum intensity and by dividing the e_{out} by this you obtain the percentage of electrons getting through the region of interest. Finally, by subtracting this value from 1 you obtain a relative measure of the difference in contrast between the ROI and the resin.

A large area of resin, depicted by the blue box in each image (Fig. 32) is taken as a control for the intensity of electrons making it through the sample without passing through and cellular material. The mean intensity value of this area is taken as the reference intensity, I_r which is given as the maximum number of electrons able to pass through the sample. Variation in this number across a sample should be only a few percent as the section thickness should only vary by +/- 2 nm in a 85 nm section, giving a variation of ~5 %.[29] A large area of cytoplasm, represented by a blue box is also taken as a comparison to the organelles that the complex is known to stain. The mean intensities of each area were calculated by taking a ROI in imagej and analysing the histogram.

The area of interest, in this case the mitochondria were selected using the ROI tool in imagej shown by the green boxes (fig. 32), and the histogram of the organelle taken yielding the mean intensity. For

each of the different concentrations, three different mitochondria were selected and their mean intensities averaged to provide more statistically robust data. Areas of cytoplasm with no obvious membranes or organelles present were also selected, illustrated by a blue box and histograms of these area were calculated to obtain mean intensities for the cytoplasm of each cell.

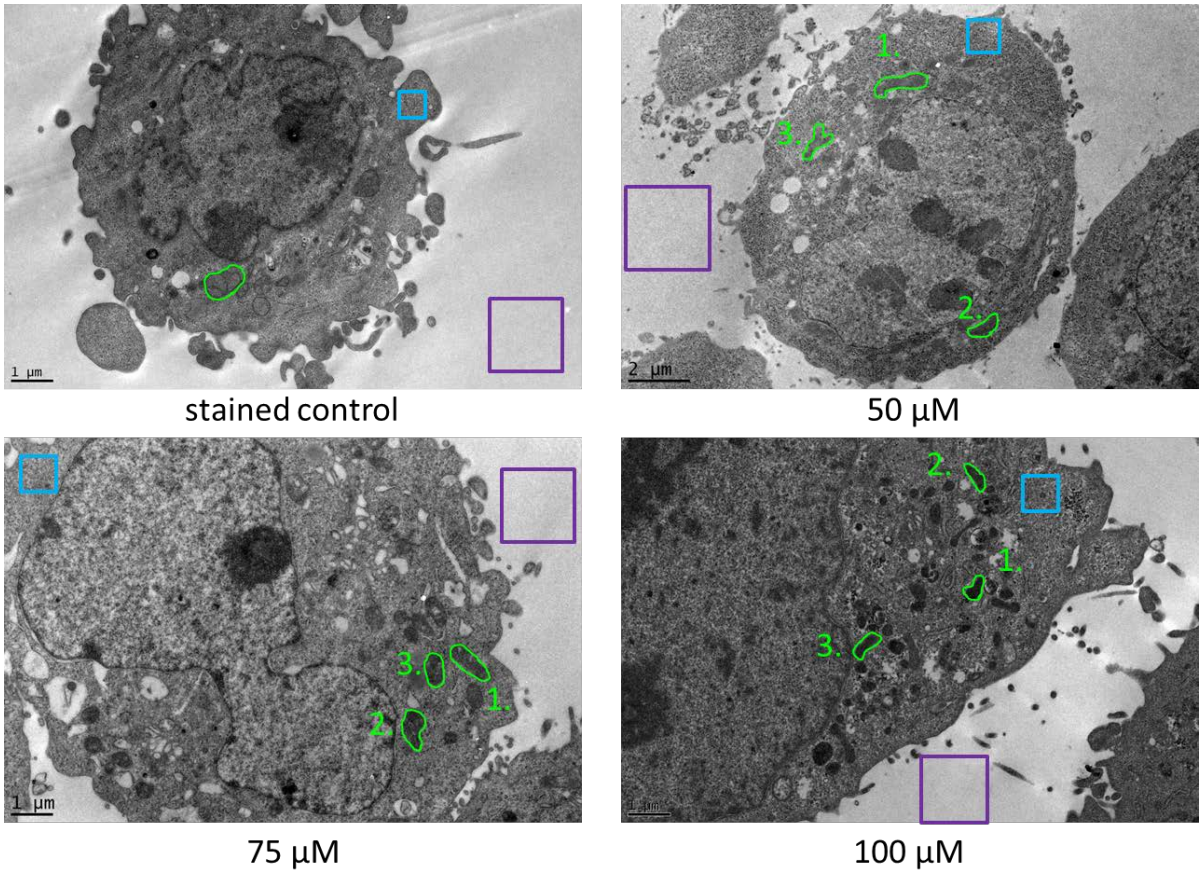

Figure 32. TEM micrographs of HeLa cells stained with typical contrast agents and complex 4.6 (concentrations shown, 2 h) with area of analysis shown. (purple box = control area, blue box = cytoplasm area, green = mitochondria taken for analysis)

It should be noted that this analysis is a considerable simplification and only offers some insight into the changes of contrast and without rigourous testing of many samples taken under exactly the sample conditions, which is extremely difficult to achieve on an electron microscope, this data should only be taken as a guide to give rough trends in place of using subjective visual analysis. Furthermore, due to the variation in image acquisitions for these images and the variation in staining efficiency of the typical stains and the complex these images are best compared by looking at the difference between the cytoplasm and the mitochondria and not directly comparing the changes in relative contrast, as this helps take into account the variation in staining efficiencies.

The control cell stained with typical contrast agents when analysed using this equation were found to have mitochondria with slightly more contrast than the cytoplasm, with 4.4 % greater relative contrast. This is in line with visual observations as previously noted the contrast doesn't appear much greater but the cristae are clearly stained. In the HeLa cells stained with 50 µM of the complex it was

calculated that there was only a small amount of relative contrast difference between cytoplasm and mitochondria of 1.6 %, less than that seen in the control cell. There is however some obscuring of the cristae, suggesting that complex is present but is simply not imparting much contrast. HeLa cells treated with 75 µM, unlike the 50 µM cell displayed much clearer difference between the cytoplasm and the mitochondria with a 9.8 % relative contrast difference between the two regions, indicating much clearer staining of the mitochondria. The cytoplasm, curiously, displays less contrast than seen in the cells stained with the complex **4.6**, when it would be assumed that more complex would also be seen in the cytoplasm due to the increased concentration, raising the contrast seen in the cytoplasm. This is likely due to the differing conditions of the image acquisitions and the potential variation in cells staining differently while being prepared for TEM. Finally, the HeLa cells treated with 100 µM were seen to have a very clear difference in relative contrast between the cytoplasm and the mitochondria, with a 14 % difference. This is made more considerable when the relative contrast of the cytoplasm is taken into account, which is ~13% higher than the stained control cell. The rising in cytoplasmic relative contrast is in line with the assumption that as the concentration of complex is increased, the greater the amount of complex that is likely to be in the cytoplasm.

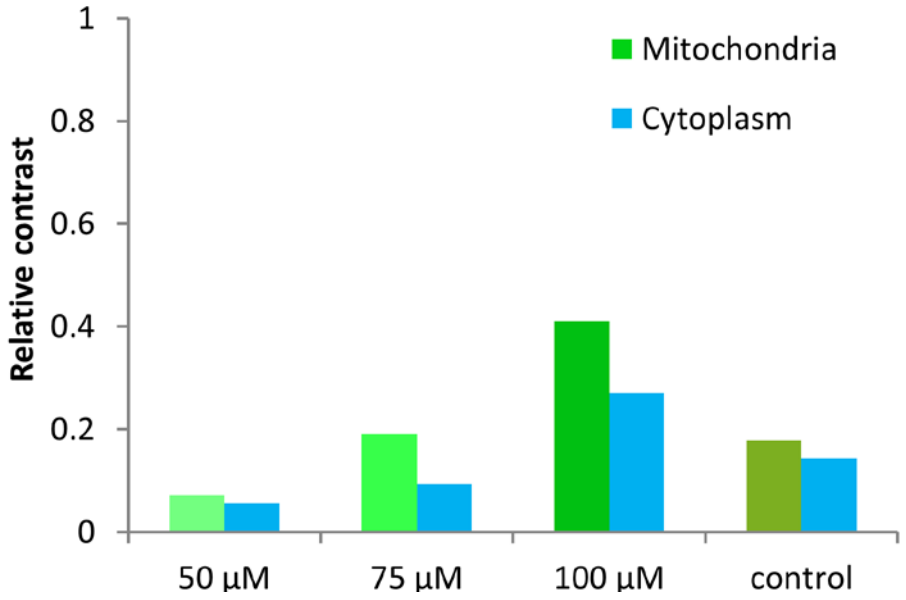

Figure 33. Histogram displaying the relative contrast of different areas of the cell at different concentrations of complex 4.6. (No error bars are present because this data is a difference of a difference, making error bars mute)

The same kind of analysis was considered for the lysosomes too, however the dynamic nature of the lysosomes and the variety of contrast that can be observed due to different cargos being broken down at the time of fixation means that the values could vary wildly.[30] This would mean that obtaining any significant results out of the analysis would be unlikely, due to the natural variation in the contrast observed typically complicating analysis.

4.6 Summary

A collection of platinum (II) and iridium (III) complexes were screened for use as potential CLEM probes and of these, the most promising were used in TREM experiments to try and observe any variation in emission lifetime with intracellular localisation. The primary lead that came out of this screen was found to be iridium (III) complex **4.6** which uptake localisation was found to be predominantly in the lysosomes. Two-photon TREM studies showed that the complex exhibited a lifetime change in the lysosomes consistent with the formation of the protonated form of the complex, highlighting the complex's pH sensitivity in the physiologically relevant range.

3D SIM study revealed that the complex also stained the mitochondria and displayed superior photostability when compared to the commercial dye ,MitoTracker™ Orange. The Ir complex was also compared to the commercial dye LysoTracker™ Red which stains lysosomes but obtaining 3D SIM images without artefacts proved problematic due to the comparably dim LysoTracker™ Red and its rapid photobleaching during image acquisition.

TEM undertaken on cells incubated with the same concentration of **4.6** as used in the original emission based microscopy studies, 10 μM, did not show any contrast enhancement in the mitochondria or lysosomes. Screening at higher concentrations found that 50 μM was a minimum concentration necessary to start observing some enhancement in TEM images, but 75 and 100 μM concentrations displayed much clearer contrast enhancement. Utilising a semi-quantitative analysis of the contrast enhancement in cells stained with typical contrast agents and complex **4.6** found that there was very little difference between control cells and the 50 μM stained cells, while 75 and 100 μM demonstrated much greater values for contrast enhancement. Complex **4.6** was shown to operate simultaneously with typical contrast agents while displaying clear contrast in the organelles it was shown to accumulate in. This suggests that complexes such as this could be used as CLEM probes alongside normal contrast agents to provide ultrastructural data while staining areas of interest.

This study has built on Chapter 3 and has demonstrated that luminescent transition metal complexes, which have often found use as probes for luminescence based microscopy, can also function as contrast agents, providing contrast in a predictable fashion, Ideal for CLEM. This property can also potentially lead to more in-depth knowledge of the localisation and accumulation of complexes within cellular environments. Furthermore, the potential of these complexes as sensors of their environment offer unparalleled amounts of data on a single sample from a single small molecule probe that can be used a simply as a commercial dye. Their photostability and super resolution microscopy compatibility opens up the possibility for other emission based microscopy, facilitating even greater scrutiny of samples at improved resolution and closing the gap between EM and LM.

However, complex **4.6** does not have perfectly desirable properties, as staining multiple organelles is

not ideal as this would confuse correlation between two different techniques, which is ultimately the end goal. Also the lack of contrast at emission based microscopy concentration reduces the effectiveness of the complex as a greater amount is required.

4.7 References

1 A. Martin, A. Byrne, C. S. Burke, R. J. Forster and T. E. Keyes, *J. Am. Chem. Soc.*, 2014, **136**, 15300–9.

2 G. Li, Q. Lin, L. Sun, C. Feng, P. Zhang, B. Yu, Y. Chen, Y. Wen, H. Wang, L. Ji and H. Chao, *Biomaterials*, 2015, **53**, 285–295.

3 R. I. Dmitriev, H. M. Ropiak, D. V Yashunsky, G. V Ponomarev, A. V Zhdanov and D. B. Papkovsky, *FEBS J.*, 2010, **277**, 4651–61.

4 J. Lecoq, A. Parpaleix, E. Roussakis, M. Ducros, Y. Goulam Houssen, S. A. Vinogradov and S. Charpak, *Nat. Med.*, 2011, **17**, 893–8.

5 S. S. Howard, A. Straub, N. G. Horton, D. Kobat and C. Xu, *Nat. Photonics*, 2012, **7**, 33–37.

6 X. Zheng, X. Wang, H. Mao, W. Wu, B. Liu and X. Jiang, *Nat. Commun.*, 2015, **6**, 1–12.

7 D. B. Papkovsky and R. I. Dmitriev, *Chem. Soc. Rev.*, 2013, **42**, 8700–32.

8 R. I. Dmitriev and D. B. Papkovsky, *Cell. Mol. Life Sci.*, 2012, **69**, 2025–2039.

9 A. Jana, B. J. Crowston, J. R. Shewring, L. K. Mckenzie, H. E. Bryant, S. W. Botchway, A. D. Ward, A. J. Amoroso, E. Baggaley and M. D. Ward, *Inorg. Chem.*, 2016, **55**, 5623–5633.

10 E. Baggaley, J. A. Weinstein and J. A. G. Williams, *Coord. Chem. Rev.*, 2012, **256**, 1762–1785.

11 M. Mauro, A. Aliprandi, D. Septiadi, N. S. Kehr and L. De Cola, *Chem. Soc. Rev.*, 2014, **43**, 4144–4166.

12 Y. You, *Curr. Opin. Chem. Biol.*, 2013, **17**, 699–707.

13 S. R. Jean, D. V Tulumello, S. P. Wisnovsky, E. K. Lei, M. P. Pereira and S. O. Kelley, *ACS Chem. Biol.*, 2014, **9**, 323–333.

14 J. Lippard, *Acc. Chem. Res.*, 1978, **11**, 211–217.

15 B. Cosimelli, S. Taliani, G. Greco, E. Novellino, A. Sala, E. Severi, F. DaSettimo, C. LaMotta, I. Pugliesi, L. Antonioli, M. Fornai, R. Colucci, C. Blandizzi, S. Daniele, M. L. Trincavelli and C. Martini, *ChemMedChem*, 2011, **6**, 1909–1918.

16 S. Lamansky, P. Djurovich, D. Murphy, F. Abdel-Razzaq, H. E. Lee, C. Adachi, P. E. Burrows, S. R. Forrest and M. E. Thompson, *J. Am. Chem. Soc.*, 2001, **123**, 4304–4312.

17 C. K. Koo, L. K. Y. So, K. L. Wong, Y. M. Ho, Y. W. Lam, M. H. W. Lam, K. W. Cheah, C. C. W. Cheng and W. M. Kwok, *Chem. Eur. J.*, 2010, **16**, 3942–3950.

18 K. Y. Zhang, S. P.-Y. Li, N. Zhu, I. W.-S. Or, M. S.-H. Cheung, Y.-W. Lam and K. K.-W. Lo, *Inorg. Chem.*, 2010, **49**, 2530–40.

19 I. Johnson and M. T. Z. Spence, Eds., *The Molecular Probes handbook. A guide to fluorescent*

probes and labeling technologies, Life Technologies, 11th edn., 2010.

20 J. A. Mindell, *Annu. Rev. Physiol.*, 2012, **74**, 69–86.

21 B. Zhitomirsky and Y. G. Assaraf, *Cancer Cell Microenviron.*, 2015, 3–9.

22 L. K. McKenzie, I. V. Sazanovich, E. Baggaley, M. Bonneau, V. Guerchais, J. A. G. Williams, J. A. Weinstein and H. E. Bryant, *Chem. Eur. J.*, 10.1002/chem.201604792.

23 M. R. Gill, J. Garcia-Lara, S. J. Foster, C. Smythe, G. Battaglia and J. A. Thomas, *Nat. Chem.*, 2009, **1**, 662–7.

24 M. R. Gill, H. Derrat, C. G. W. Smythe, G. Battaglia and J. A. Thomas, *ChemBioChem*, 2011, **12**, 877–880.

25 X. Tian, M. R. Gill, I. Cantón, J. A. Thomas and G. Battaglia, *Chembiochem*, 2011, **12**, 548–51.

26 A. Wragg, M. R. Gill, C. J. Hill, X. Su, A. J. H. M. Meijer, C. Smythe and J. A. Thomas, *Chem. Commun.*, 2014, **50**, 14494–7.

27 Q. Zhang, X. Tian, G. Hu, P. Shi, J. Wu, S. Li, H. Zhou, B. Jin, J. Yang, S. Zhang and Y. Tian, *Biochemistry*, 2015, **54**, 2177–2180.

28 M. R. Gill, D. Cecchin, M. G. Walker, R. S. Mulla, G. Battaglia, C. Smythe and J. A. Thomas, *Chem. Sci.*, 2013, **4**, 4512.

29 D. M. D. De Groot, *J. Microsc.*, 1988, **151**, 23–42.

30 J. P. M. Schellens, W. T. Daems, J. J. Emeis, P. Brederoo, W. C. De Bruijn and E. Wisse, in *Lysosomes: A laboratory handbook*, ed. J. T. Dingle, North-Holland Biomedical press, Oxford, 2nd edn., 1977, pp. 147–208.

Chapter 5. Mitochondrial Specific Iridium (III) Complex for CLEM

5.1 Introduction

Due to the success with using iridium (III) complexes for both emission and TEM imaging as described in Chapters 3 and 4, and the general favourable photophysical properties of iridium (III) (III) complexes, it was considered desirable to explore more iridium (III) complex motifs for CLEM assessment. Achieving specific intracellular localisation of any new complexes was paramount, as previous complexes have lacked the specificity required for CLEM applications.

In collaboration with Professor Michael Ward and his group, a new set of promising complexes were obtained as shown in figure 1. These complexes had shown promise in preliminary studies carried out by Dr Elizabeth Baggaley, in which specific localisation was observed in preliminary imaging studies, but not confirmed. The complexes were designed, synthesised and characterised by AJ Cankut. These Ir(III) triazol-pyridine complexes, Figure 1, have a short pendant PEG chains on the NC ligands to improve solubility, and a pyridyl (complex 5.1) or tolyl group (complex 5.2) located on the 2-(1H-1,2, 4-triazol-5-yl)-pyridine ligand. The pyridine group was hypothesised to aid localisation due to its Bronsted basic nature, whilst the complex bearing the tolyl group in place of pyrydine was used as a control. Complex **5.1** was previously found to undergo protonation of the pyridyl nitrogen between pH 6 and pH4, which is an ideal range to observe physiological conditions; this protonation was accompanied by a reduction in emission intensity of 63% and a reduction in emission lifetime from ca. 550 to ca.350 ns. The emission of the tolyl complex **5.2** did not display any notable changes in emission characteristics across a wide pH range, corroborating that the protonation of the pyridyl group in complex **5.1** was responsible for the changes in photophysical properties, and not the triazole group present in both complexes.

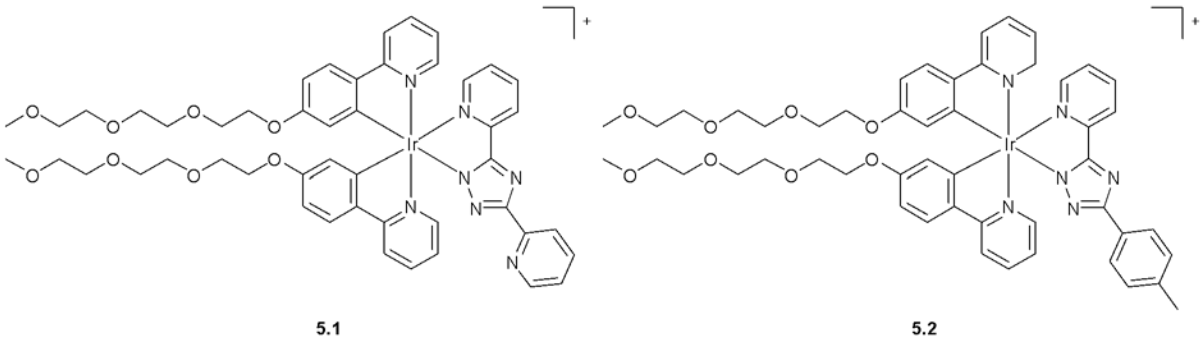

Figure 1. Molecular structure of complex 5.1 and 5.2

The aim of the work presented in this Chapter was to assess the ability of these two new promising iridium (III) complexes as potential super resolution CLEM probes.

5.2 Localisation of Complexes

Before the assessment of the complexes as potential CLEM probes the localisation of the complexes needed to be monitored, to observe if it would be sufficiently specific. Initial time dose studies had revealed that the uptake of the complexes at 50 µM was sufficient to obtain images after 4 hours of incubation. To confirm these finding, HeLa cells were treated with complex **5.1** and **5.2** at 50 µM for 4 hours and imaged on a confocal microscope. As can be seen in figure 2, complex **5.1** clearly stains structures throughout the cytoplasmic region of the cell without any staining observed within the nucleus. Complex **5.2** was curiously found to have a very similar staining pattern to **5.1** with stained structures observed throughout the cytoplasm but no nuclear staining seen despite lacking the pyridyl nitrogen, suggesting that the protonation of the complex was not affecting localisation. As can be seen in figure 2, there were also some problems with complex **5.2** precipitating out of solution while staining the cells due to poor solubility, however it was discovered that if the solution was filtered before staining the cells, then no precipitate was observed.

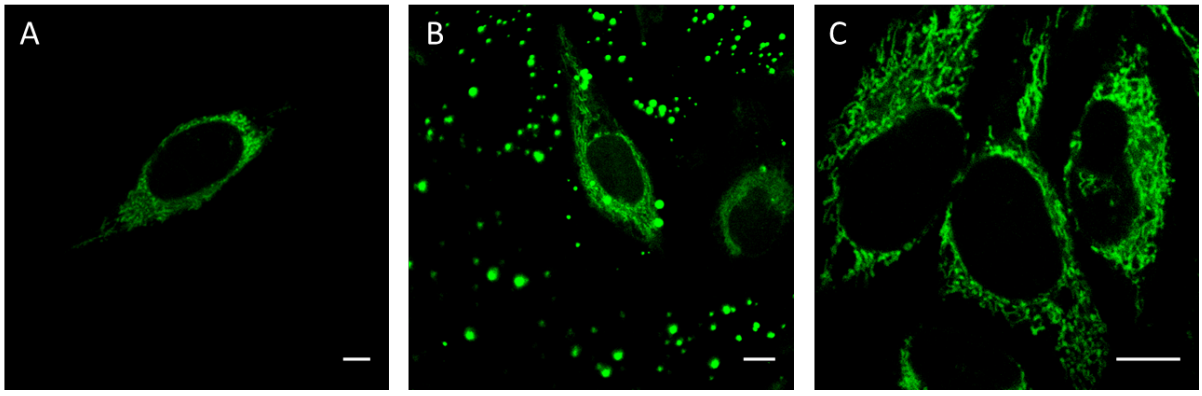

Figure 2. LSCM images of HeLa cells stained with (A) complex 5.1 (50 µM, 4 h), (B) complex 5.2 (50 µM, 4 h) the large punctate staining across the image is precipitated complex, (C) complex 5.2 (50 µM, 4 h) which was filtered before staining. Scale bar = 10 µm

5.2.1 Lysosomal Co-Staining

With initial uptake conditions confirmed, the localisation of complex was the next key property to be explored. While the complex did appear to be potentially localising in a single organelle it was not clear which; as complex **5.1** had been shown to be pH sensitive over the physiological range the first co-localisation was against LysoTracker™ Red. The localisation of **5.1** and **5.2** was not found to match well with LysoTracker™ Red (fig 3.). A Pearson's coefficient of 0.58 was calculated for **5.1**, which is an ambiguous intermediary value, however 0.51 of this was below threshold, meaning the majority of the Pearson's consists of lower brightness pixels or likely background. The threshold Mander's coefficient was found to be 0.041, suggesting that very little co-occurrence was present between the two channels. While the complex had been observed to be pH sensitive in solution it had also been shown that the emission was quenched when protonated which would likely make localisation in the lysosomes difficult to observe but the analysis does suggest that the complex does not localise in lysosomes.

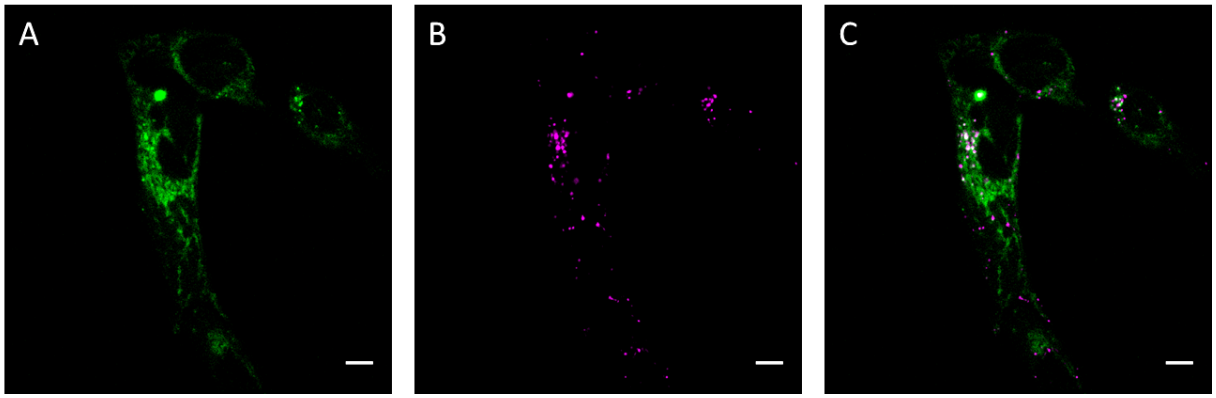

Figure 3. LSCM micrographs of HeLa cells treated with complex 5.1 (50 µM, 4 h) and LysoTracker™ Red (50 nM, 35 mins). (A) complex 5.1 emission, (B) LysoTracker™ Red emission (C) overlay. Scale bar = 10 µm

5.2.2 Endoplasmic Reticulum Co-Staining

To establish where complex **5.**1 was accumulating in Hela cells, further co-localisation were conducted using CellLight ER-RFP, as the endoplasmic reticulum is made up of a network of membranes throughout the cell and it was believed this could match the observed staining pattern from initial experiments. Both complex **5.1** and **5.2** were used in co-localisation experiments using cellLight ER-RFP (fig 4.). The Pearson's coefficient for complex **5.1** and **5.2** were found to be 0.38 and 0.29 respectively, which indicates that the colocalisation is poor as it can be assumed that Pearson's coefficient should be high if they colocalised well. The threshold Mander's coefficient for both complexes were considerably high however at 0.66 and 0.59, indicating that while there might not be a very good fit for correlation there is a reasonable amount of co-occurrence, this suggests that the complex may localise in closely associated organelles.

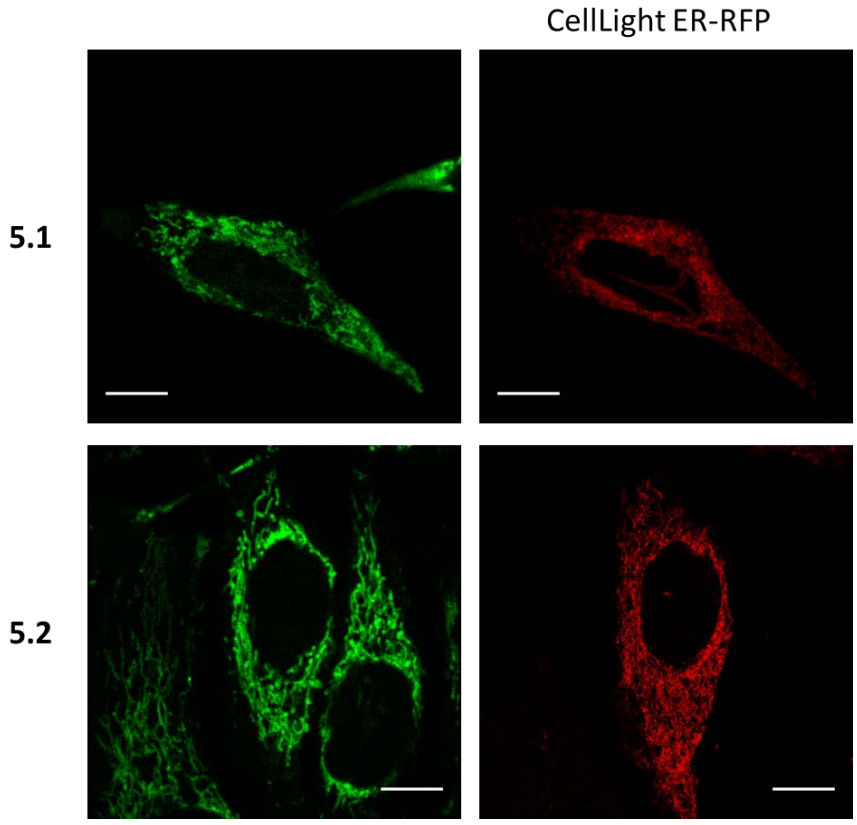

Figure 4. LSCM micrographs of HeLa cells treated with complex 5.1 (top) (50 µM, 4 h) or 5.2 (bottom) (50 µM, 4 h) and cellLight ER-RFP tracker (30 p/c). Scale bar = 10 µm

5.2.3 Mitochondrial Co-Staining

Due to the observation that the complex was likely in organelles closely associated with the endoplasmic reticulum the next organelle to investigate was the mitochondria, as links between mitochondria and the endoplasmic reticulum have been well documented.[1] Both complexes were co-stained against MitoTracker™ Orange to assess the possible accumulation of the complexes in the mitochondria. Despite there being some off target staining of the nucleoli by the MitoTracker™ Orange, the staining patterns of the two complexes were very similar (fig 5.) and this was supported by the Pearson's coefficients which were 0.72 and 0.73 for complex **5.1** and **5.2** respectively. These values strongly suggest that these complexes accumulate in the mitochondria of cells, with the value likely to be higher if off target staining had not been present. The threshold Mander's coefficients for both complexes were also exceptional with values of 0.91 and 0.96 for complex **5.1** and **5.2** respectively, highlighting a high degree of co-occurence between the complexes and the MitoTracker™ Orange. Despite complex **5.1** being pH sensitive at physiologically relevant pH this does not appear to affect the localisation of the complex. Instead it would appear that the dominating factors directing cellular localisation for this class if complexes is their lipophilic cationic nature. Molecules with these characteristics have been reports to typically easily permeate cellular membranes and are the sequestered into the mitochondria due to the negative potential maintained within the mitochondria for oxidative phosphorylation.[2,3]

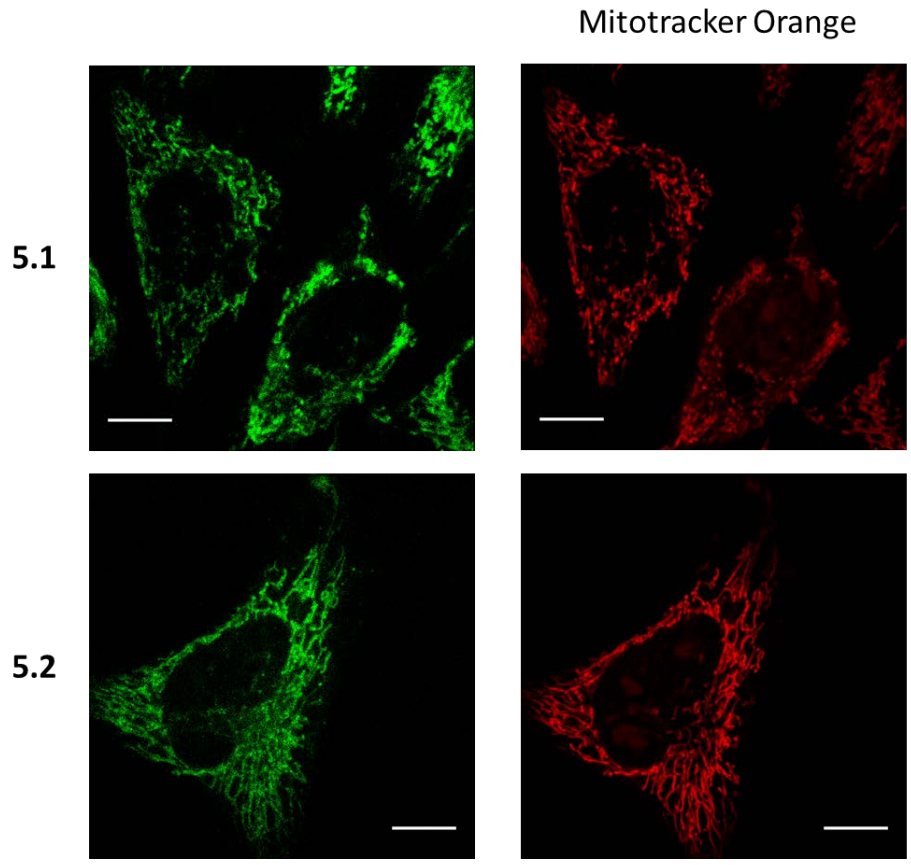

Figure 5. LSCM micrographs of HeLa cells stained with complex 5.1 (top) (50 µM, 4 h) or 5.2 (50 µM, 4 h) (bottom) and MitoTracker™ Orange (200 nM, 35 mins). Scale bar = 10 µm

Although the absorption and emission spectra of complexes **5.1**, **5.2** and MitoTracker™ Orange are such that there should not be any crosstalk or bleed through, control experiments were done to ensure the co-localisation results were representative of the staining. HeLa cells solely treated with MitoTracker™ Orange were imaged using 405 and 561 nm excitation and the cellular emission recorded in both the green (525/50 nm) and red channels (>590 nm). As expected, the MitoTracker™ Orange provided the clearest image using 561 nm excitation while observing the emission in the red channel (fig. 6). However, some MitoTracker™ Orange emission was observed in the red channel under 405 nm excitation, however as no light was detected in the was also observed while being excited by the 405 nm laser but no emission was observed in the green channel. So while there was some cross talk observed there was no bleed through of the signal from the red channel into the green channel and therefore the colocalisation data is not compromised.

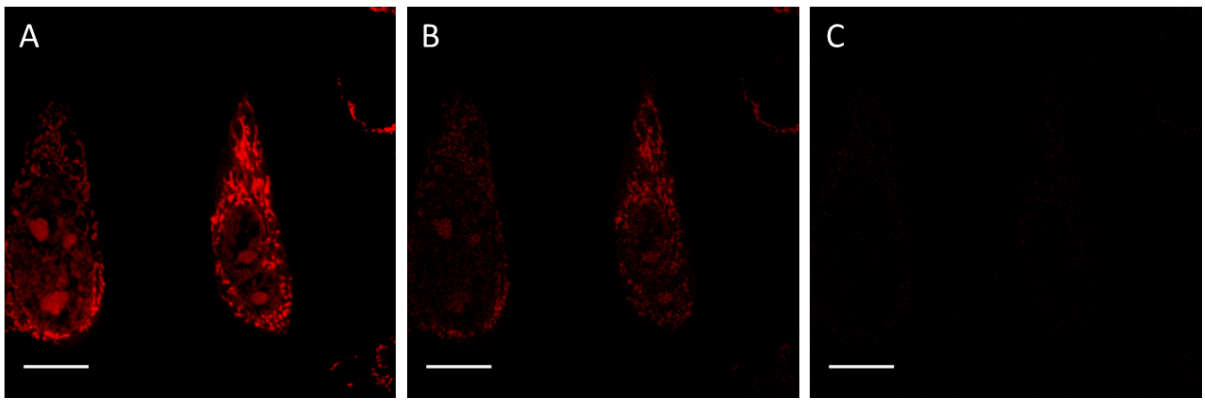

Figure 6. LSCM images of HeLa cells treated with Mitotracker red 200 nM for 35 mins. (A) Mitotracker emission under 561 nm excitation(filter< 590 nm), (B) under 405 nm excitation (filter< 590 nm) and (C) under 405 nm excitation (filter 475-575 nm). Scale bar = 10 µm

5.2.4 Toxicity Studies

Once the localisation of complexes had been established, the toxicity of the complexes needed to be assessed although no obvious signs of toxicity were observed while imaging live cells. An MTT assay was conducted on live cells treated with complex **5.1** and **5.2** over a range of concentrations for the typical incubations period of 4 hours(in DMEM media, DMSO < 2%). For both complexes there was very little change in cell viability over the concentration range (10-75 µM) including those well above the concentrations used for imaging. This suggests that the complexes have very little adverse effect on the cell metabolism, which is ideal for molecules intended for cell imaging and also suggests that higher concentrations could be used if necessary.

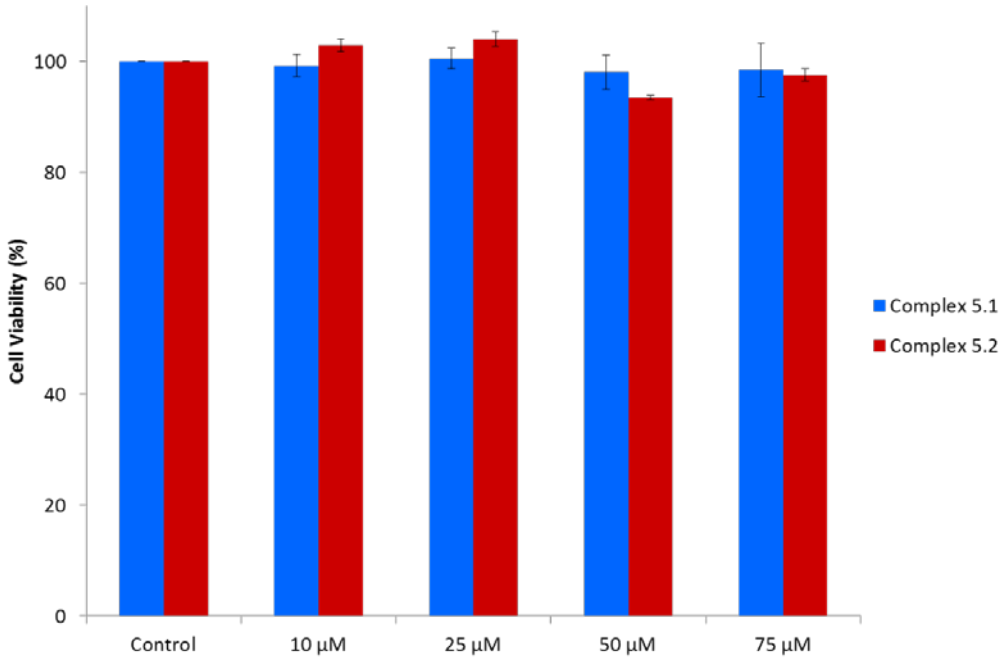

Figure 7. A graph to show the cell viability of cells treated with complex 5.1 and 5.2 by MTT assay. Error bars = 2SD.

5.3 TEM Imaging

While complex **5.1** and **5.2** had shown promising specificity for mitochondria and displayed very little toxicity, the next important test was to observe if the complexes could provide specific contrast in TEM, preferentially at the concentration used for luminescence based imaging.

As in the previous Chapters, the initial experiments aimed to assess the ability of the complexes to provide contrast in TEM without the use of any other contrast agents so that any contrast observed could be ascribed to the complex alone. According to confocal microscopy studies, both complexes should be observed solely in the mitochondria of HeLa cells. To prepare cells for TEM imaging live HeLa cells were treated with complex **5.1** or **5.2** at 50 μM for 4 hours and then fixed using glutaraldehyde (3 %) in PBS. The cells were then dehydrated and embedded in araldite resin before being sectioned and imaged. No other contrast agents were added to the sample in this process. While the other complexes, discussed in Chapters 3 and 4 required modified incubation conditions to optimise the contrast seen in TEM, it was hoped that the longer incubation time of these complexes (4 h vs 2 h) with the reasonable concentration might yield good results. TEM images obtained using complexes **5.1** and **5.2** only are show in figure 8. Clear contrast enhancement was observed matching the tubular structures of the mitochondria (yellow arrows) in comparison to the cytoplasm. No further in the cytoplasm displayed any contrast enhancement, which is consistent with the co-localisation investigations carried out using confocal microscopy. Due to the lack of the secondary fixative osmium tetroxide there is some notable damage to the section visible in figure 8 (green arrows). However, osmium tetroxide also provides contrast so it was necessary to omit this reagent it to confidently assign the contrast enhancement brought about by complexes **5.1** and **5.2** only.

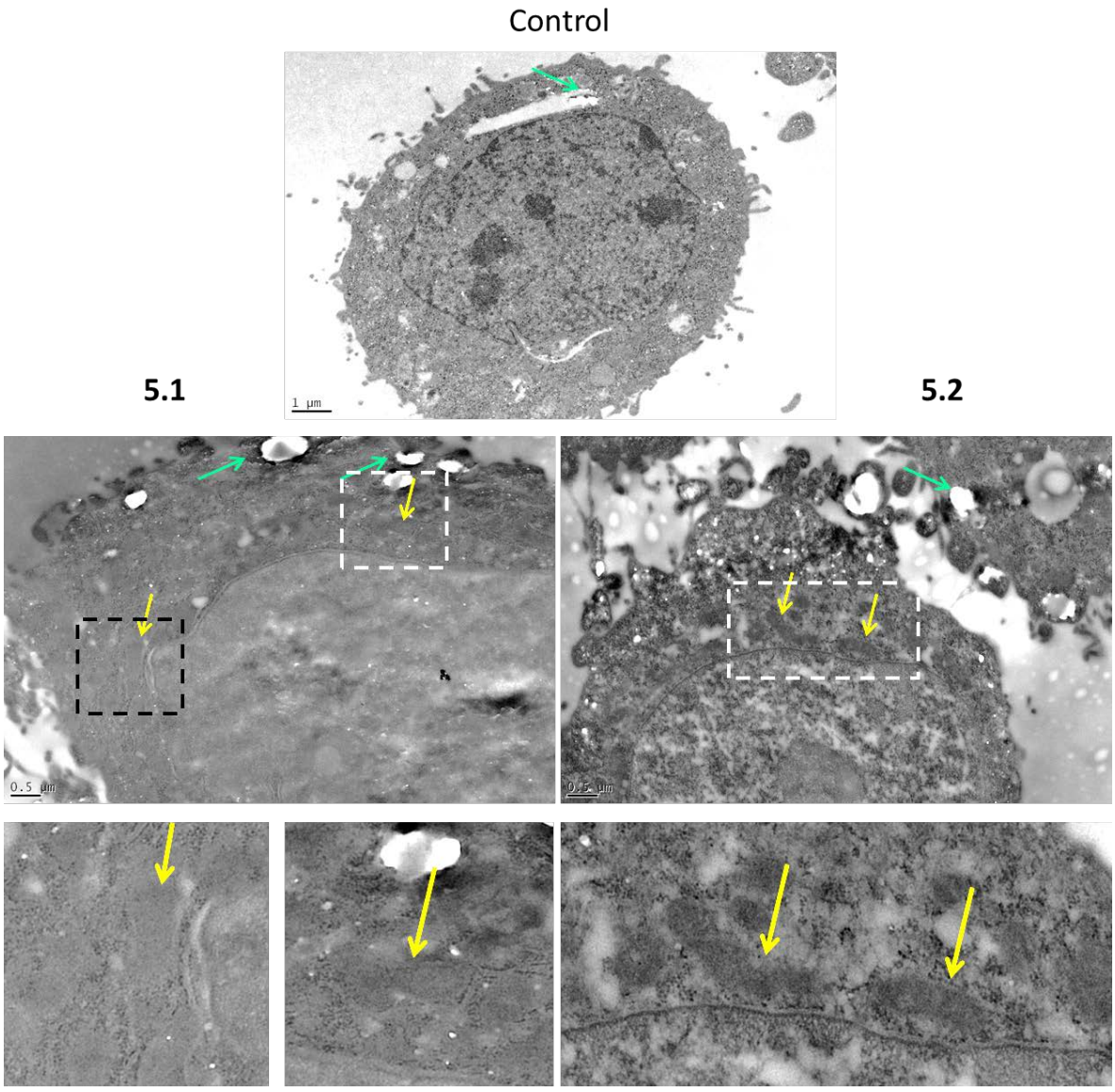

Figure 8. TEM micrographs of unstained HeLa cells imaged (top) and unstained Hela cells treated with complex 5.1 (left) or 5.2 (right). Yellow arrows = mitochondria, green arrows = section damage

Following the observation of good contrast enhancement in unstained cells, samples were prepared using typical contrast agents osmium tetroxide, uranyl acetate and lead citrate to further explore the accumulation of the complexes in better cellular context and assess the effects of the presence of other contrasts agents. Live HeLa cells treated with complex **5.1** or **5.2** and then prepared for TEM using typical contrasts agents were imaged. Contrast enhancement was observed in the mitochondria for both complexes when compared to control cells which had not been treated with complex (fig 9.), while the rest of the cell appear to display normal staining patterns for cell prepared for TEM. This shows that these complexes can be used in tandem with typical contrast agents to provide contrast enhancement of areas of interest without interfering with the normal ultrastructural data obtained in TEM, a key requirement for CLEM. This is boosted further by the ability to use incubation conditions that are ideal for both luminescence based microscopy and electron microscopy without change to the

preparation methods of either technique.

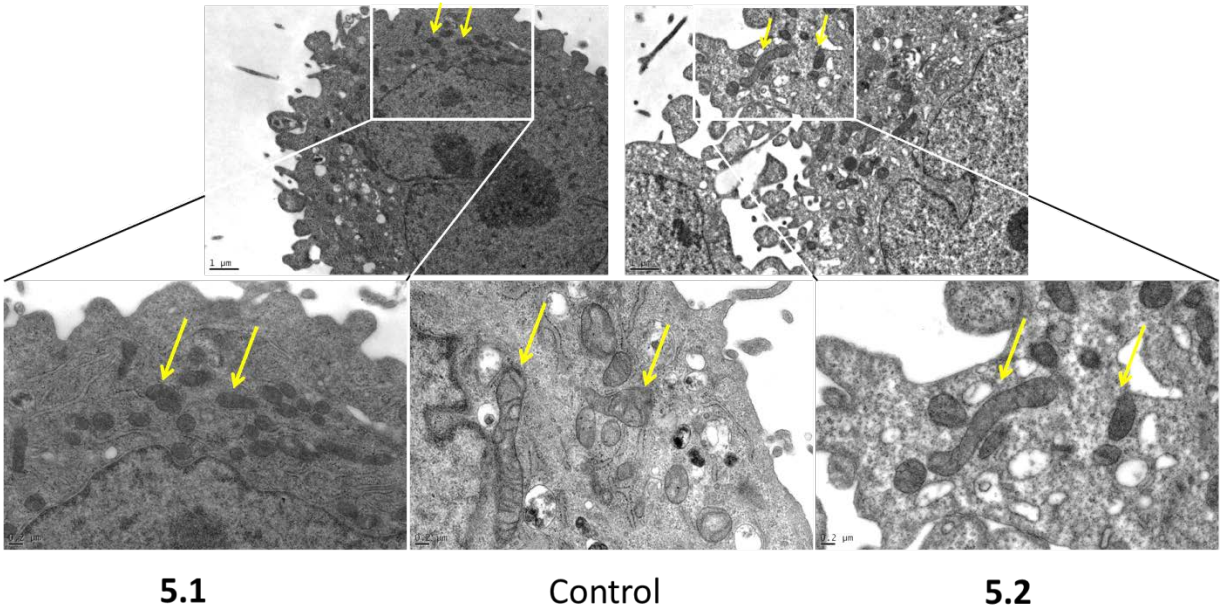

Figure 9. TEM micrographs of HeLa cells stained with typical contrast agents osmium tetroxide, uranyl acetate and lead acetate and complex 5.1 (left) or complex 5.2 (right) with unstained control cells (bottom centre). Yellow arrows = mitochondria

The equation used to analyse TEM images from Chapter 4 was also used to quantify the contrast enhancement observed for **5.1** and **5.2**. TEM images in Figure 10. were analysed by taking grey values from the background (shown by purple box), the cytoplasm (shown by blue box) and the mitochondria (shown by green boxes). As described in Chapter 4, by assuming the average background grey values are essentially the maximum amount of electrons passing through the sample, the relative contrast of the cytoplasm and mitochondria can be assessed from their grey values. The differences in the value of the cytoplasm and the mitochondria for each individual sample are the important statistic as the direct comparison of mitochondrial values or cytoplasmic values between samples is not comparable due to different imaging conditions of each image.

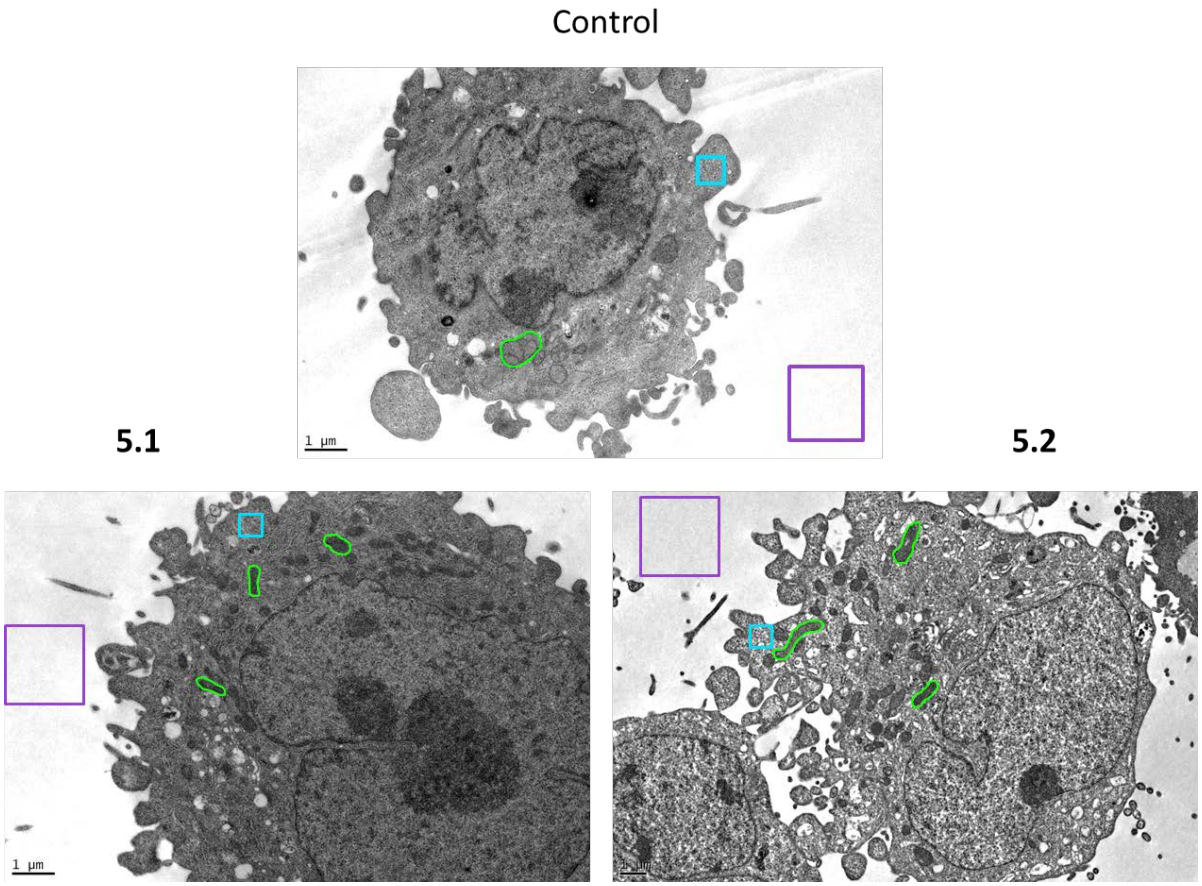

Figure 10. TEM micrographs of HeLa cells stained with typical contrast agents and complex 5.1 or 5.2 (50 µM, 4 h) with area of analysis shown. (purple box = control area, blue box = cytoplasm area, green = mitochondria taken for analysis)

Utilizing the stained control cells from Chapter 4 (Fig. 11), the relative contrast difference observed between the cytoplasm and the mitochondria was 3.4 % and this is due to only the membranes of the mitochondria exhibiting greater contrast relative to the cytoplasm. In the image of HeLa cells treated with complex **5.1** the relative difference between the cytoplasm and mitochondria was found to be 6.3 % and as can been seen in the images (Fig. 9 & 10) the mitochondria clearly appear as dark filled organelles when compared to the control. Cell treated with complex **5.2** were actually found to exhibit greater levels of contrast with respect to **5.1** with the relative contrast difference between cytoplasm and mitochondria observed to be 10 %. This suggests that although the complex does display solubility problems, complex **5.2** might actually accumulate more heavily in the mitochondria that complex **5.1**.

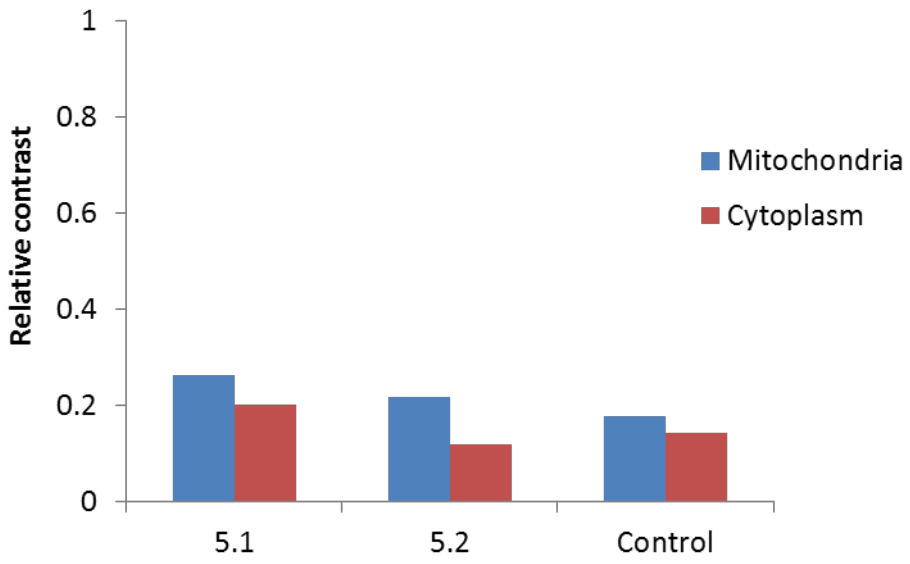

Figure 11. Histogram displaying the relative contrast of different areas of the cell treated with complex 5.1 or 5.2 in comparison to control cells. (No error bars are present because this data is a difference of a difference, making error bars mute)

5.4 Super Resolution Imaging

With the uptake and localisation of the complexes explored using confocal microscopy and the TEM corroborating that the complexes localise and provide enhanced contrast in the mitochondria as expected, the next step was to assess the complexes as 3D SIM probes.

Using the incubation conditions established for confocal microscopy and TEM, HeLa cells were stained with complex **5.1** or **5.2** and then fixed and prepared for 3D SIM. Both complexes were co-stained against MitoTracker™ Orange to observe co-localisation at the improved resolution and to compare the photostability of both complexes against MitoTracker™ Orange. Unfortunately, the solubility problems initially seen in complex **5.2** became untenable when it came to preparing HeLa cells for 3D SIM, as small amounts of precipitate were found in the samples, compromising the SIM reconstructions (fig. 12.). Although conditions for SIM reconstruction were not ideal, it was possible to observe some of the mitochondrial staining present in the HeLa cells treated with complex **5.2** (Fig 12, yellow arrows). To avoid complications in imaging reconstruction from complex precipitation problem, complex **5.1** was selected to be the focus for SIM investigations.

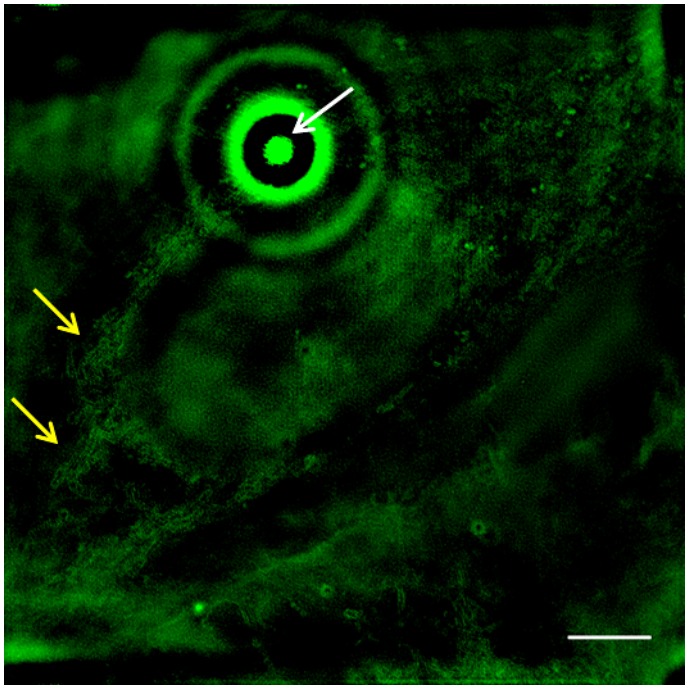

Figure 12. 2D slice from a 3D SIM reconstruction of fixed HeLa cells treated with complex 5.2 (50 µM, 4 h) showing precipitate (white arrow) and the mitochondrial staining of the complex (yellow arrows). Scale bar = 5 µm

HeLa cells stained with complex **5.1** and co-stained against MitoTracker™ Orange displayed the expected staining pattern, with complex **5.1** and MitoTracker™ Orange exhibiting co-localisation throughout the cytoplasm of the cell (fig. 13, white arrows). It was also noted that while there appears to be some staining of the nucleus is it actually visible from the z-stack and the 3D image that the complex actually only stains the nuclear membrane (blue arrows) and does not penetrate the nucleus itself as is true of most iridium (III) N^C complexes.[4]

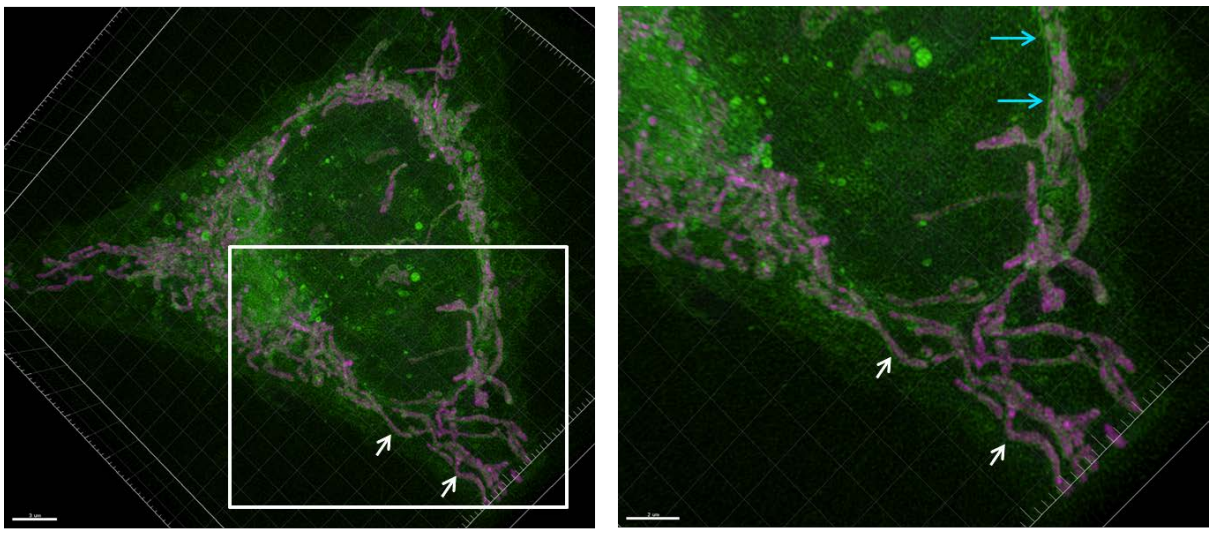

Figure 13. 3D rendered SIM images of fixed HeLa cells treated with complex 5.1 (50 µM, 4 h, green) and MitoTracker™ Orange (100 nm, 20 mins, magenta), with a full cell view (left) and zoomed view of mitochondrial staining in the cytoplasm (right). White arrow = mitochondrial co-staining.

Further analysis of staining of the mitochondria when compared to that of complex **4.6** in the Chapter

4, which saw the complex be excluded from the centre of the mitochondria when MitoTracker™ Orange was present. As can be seen from the line profile in figure 14, the localisation of **5.1** was not perturbed by the presence of MitoTracker™ Orange. The behaviour was opposite to that observed with complex **4.6**, suggesting that they are likely to bind to different biomolecules within the mitochondria once they accumulate there due to the different response to the presence of MitoTracker™ Orange.

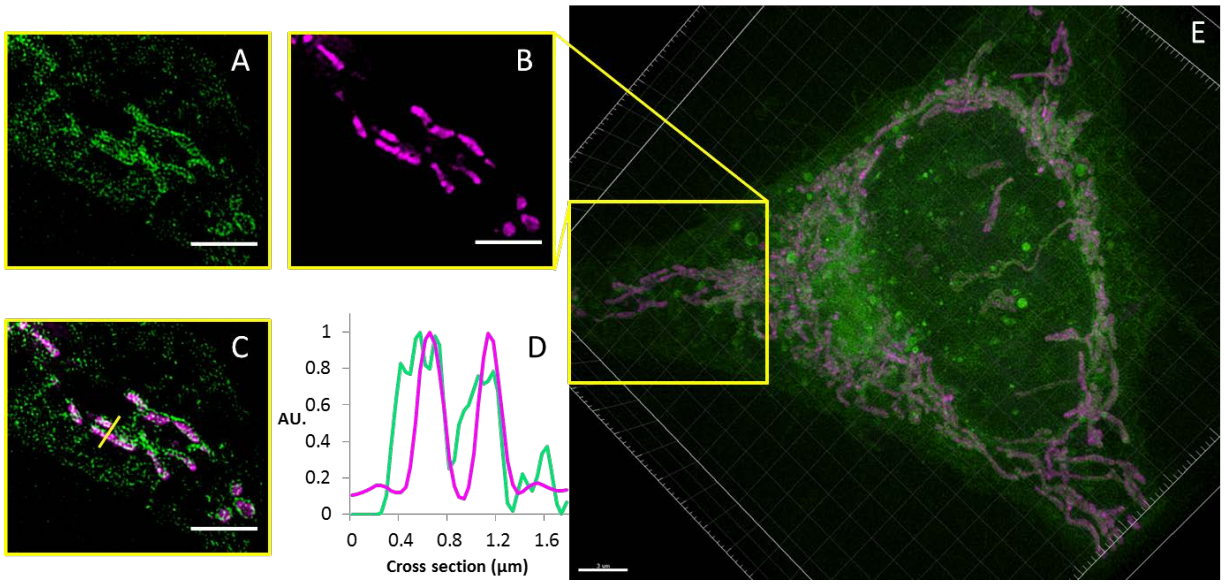

Figure 14. 3D SIM images of HeLa cells treated with complex 5.1 (50 µM, 4 h, green) and MitoTracker™ Orange (100 nM, 20 mins, magenta). (A) single Z-slice displaying emission from complex 5.1, (B) single Z-slice displaying emission from MitoTracker™ Orange, (C) single Z-slice displaying overlay of both channels, (D) Emission line profile from yellow line on overlay image demonstrating full colocalisation (E) 3D render image of whole cell with emission from both probes (complex 5.1 = green, MitoTracker™ Orange = magenta). Scale bar = 3 µm

The photostability of complex **5.1** was also assessed against MitoTracker™ Orange, as photostability is a key factor in the quality of the SIM reconstruction. The images were assessed using SIMcheck and the complex was found to exhibit an intensity decay of 2.63 % after almost 700 raw images were acquired, whereas the MitoTracker™ Orange was found to exhibit 32.1 % intensity decay over the same number of raw images. This shows that complex **5.1** has photostability over 10-fold greater compared to that of MitoTracker™ Orange, although it has been shown in previous Chapters that SIMcheck can underestimate the amount of intensity decay of a sample. However, as can be seen I figure 15, the intensity fluctuation between angles and within angles for complex **5.1** is quite large, these appear to be systemic phenomena for metal complexes as each complex tested for 3D SIM has displayed these kinds of signal fluctuations. This suggests that the phenomena observed is likely due to intrinsic properties of luminescent metal complexes such as the long emission lifetimes of the complexes compared to commercial organic fluorophores.

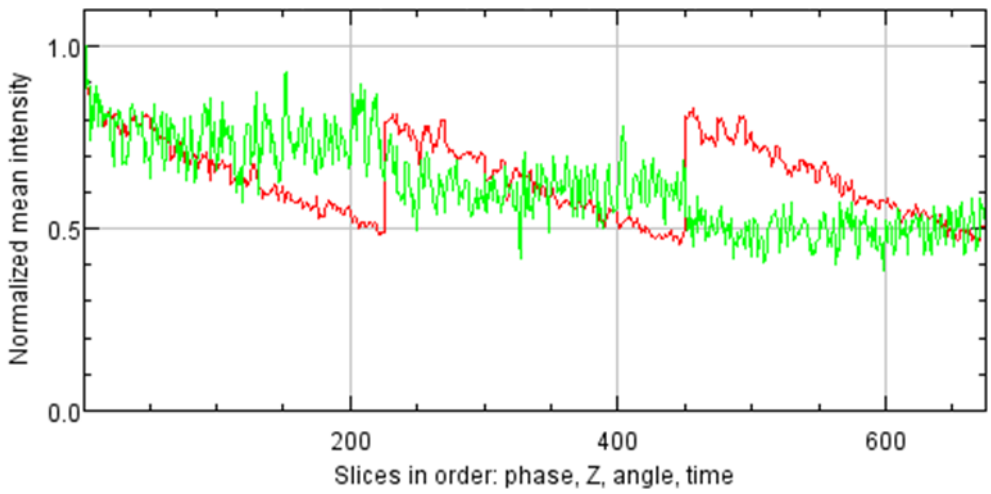

Figure 15. Mean intensity graph of raw slice of 3D SIM Z-stack of HeLa cells treated with complex 5.1 (50 µM, 4 h, green) and MitoTracker™ Orange (100 nM, 20 mins, red).

While the superior photostability of complex **5.1** suggests that the complex is a more ideally suited probe for 3D SIM, the modulation contrast-to-noise ratio images reveal the reconstruction data is not as good as the MitoTracker™ Orange. This is because the emission from **5.**1 is less bright, therefore only just enough photons are being detected to perform a SIM reconstruction. This is likely due to the lower emission quantum yield of complex **5.1** and was not a problem for complex **4.6** as this complex was recorded as having a greater quantum yield. While these results do not render this complex useless for 3D SIM, is does mean that the complex requires harsher imaging conditions with greater laser powers to obtain as good reconstruction data as that available by complex **4.6**.

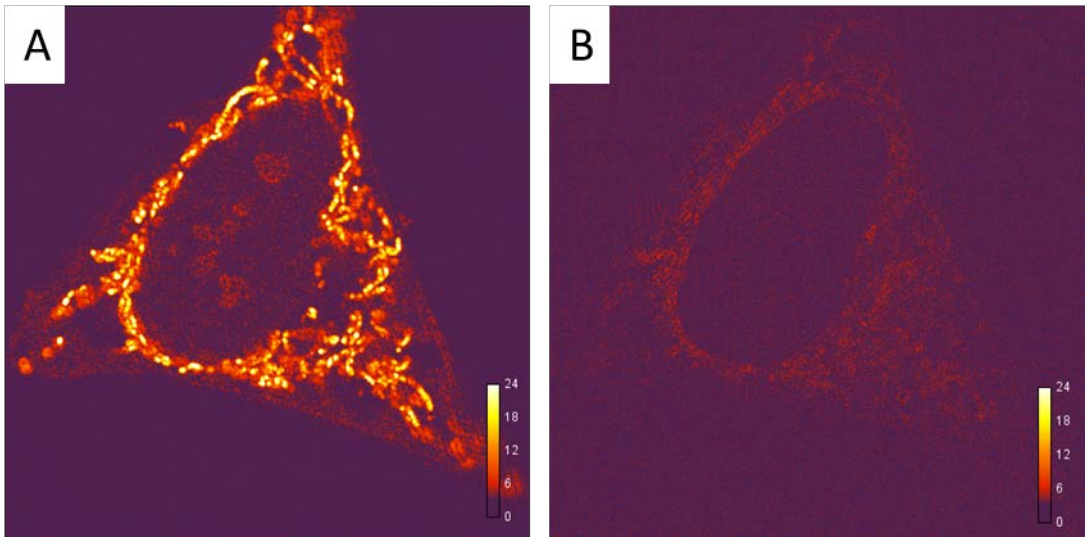

Figure 16. Modulation contrast-to-noise ratio images of fixed HeLa cells treated with (A) MitoTracker™ Orange (100 µM, 20 mins) and (B) complex 5.1 (50 µM, 4 h).

5.5 Summary

The promising Ir(III) triazol-pyridine complexes studied in collaboration with Professor Mike Wards' group were found to enter cells readily and localise specifically in the mitochondria of HeLa cells which was confirmed via co-staining with MitoTracker™ Orange. These complexes were also observed to have very low toxicity, with no change in cell viability up to 100 μM by MTT assay, double the imaging concentration. There was however some solubility issues seen with complex **5.2**, as the complex was observed to precipitate out of solution when diluting with aqueous solutions. This was mitigated by filtering solutions before staining cells with solution of complex.

TEM studies were performed with the complexes using the same concentration as used for emission microscopy experiments and, as predicted contrast enhancement of the mitochondria was observed in HeLa cells, without the need for additional contrast agents. Further TEM experiments found that the complexes could also be used in conjunction with typical contrast agents and still yield observable contrast enhancement in the mitochondria of HeLa cells. While complex **5.2** was observed to have solubility issues it was noted in the analysis that it had greater contrast enhancement than **5.1.** This could be due to the complex accumulating more heavily in the mitochondria than **5.1** or it could be due to the **5.1** undergoing some extraction while the cells are being prepared for TEM due to its greater solubility.

Poor solubility of **5.2** has precluded its use in 3D SIM as precipitate was affecting the reconstruction of the images. Complex **5.1** however functioned reasonably well as a 3D SIM probe. The photostability of the complex was noted to very good when compared with MitoTracker™ Orange, with intensity decay being measured at 2.63 % compared to Mitotrackers 32.1 %. However, because the emission of the complex is not as bright as that of the MitoTracker™, the contrast-to-noise ratio achieved with **5.1** was only just acceptable for reconstruction, while MitoTracker™ Orange was found to have an excellent ratio. Interestingly, when analysis of the localisation of the complex within the mitochondria was performed, it was found that the complex was not affected by the presence of MitoTracker™ Orange, unlike the bisimidazole Ir(III) complex **4.6** from the Chapter 4, suggesting the mechanism of binding of these two complexes to the mitochondria is different to one another.

These complexes have displayed the potential to be useful CLEM probes with staining visible in both light and electron based microscopy, with the signal seen in the same organelles across techniques. Complex **5.1** has also displayed reasonable propensity to act as a 3D SIM probe, with excellent photostability but with lower than desired brightness, which was reducing the strength of reconstructions when compared to the other luminescent transition metal complexes used in these studies. Therefore, while it would not be a perfect probe, complex **5.1** could function as a super resolution CLEM probe for applications where mitochondrial dynamics are the interest of the study, without the need for changes to the cell preparation for light or electron microscopy or the use of

differing concentrations of probe.

5.6 References

1 S. Marchi, S. Patergnani and P. Pinton, *Biochim. Biophys. Acta - Bioenerg.*, 2014, **1837**, 461–469.

2 R. A. J. Smith, C. M. Porteous, A. M. Gane and M. P. Murphy, *Proc. Natl. Acad. Sci. U. S. A.*, 2003, **100**, 5407–12.

3 S. R. Jean, D. V Tulumello, S. P. Wisnovsky, E. K. Lei, M. P. Pereira and S. O. Kelley, *ACS Chem. Biol.*, 2014, **9**, 323–333.

4 Y. You, *Curr. Opin. Chem. Biol.*, 2013, **17**, 699–707.

Chapter 6. Correlative microscopy with luminescent metal complexes

6.1 Introduction

Light microscopy and electron microscopy have been two cornerstones of the life sciences, facilitating the visualisation of complex cellular processes, organisation and structure. However, due to the conflicting sample preparation and differences in probe requirements, samples are usually prepared separately and information inferred between samples. Correlative light and electron microscopy (CLEM) seeks to bridge the gap between light microscopy and electron microscopy, allowing imaging of a single sample across different modalities, giving greater depth of than either modality can provide alone.[1,2] Due to the differences in sample preparation and probe requirement, CLEM generally requires special methods and the use of novel probe systems to achieve its aims. While CLEM has started to facilitate new strides in understanding of biological systems,[3–5] there is still more development required to make this a mainstream technique.

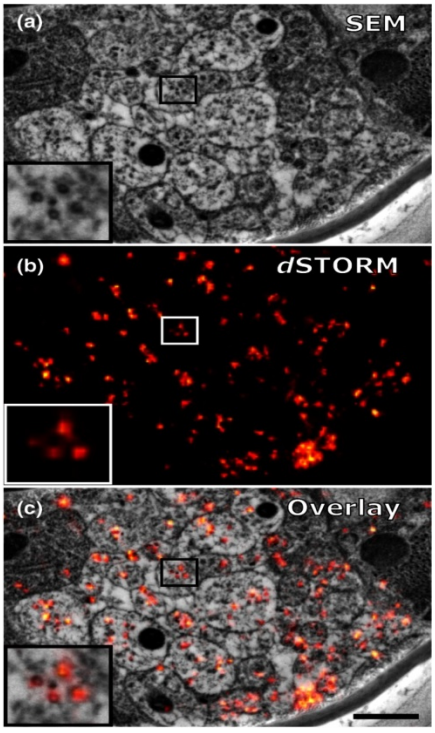

Figure 1. Correlated dSTORM and SEM micrographs of *C. elegans.* Reproduced from ref.[6]

In the previous chapters we have evaluated the potential of luminescent transition metal complex to potentially act as CLEM agents through their use in luminescence microscopy and electron microscopy. However, there are multiple methods currently used by researchers to perform CLEM on

various samples, ranging in the type of sample preparation and a variety probe choices.[7] Sample preparation has a huge effect on cellular preservation of samples, with different fixation methods offering differing levels of protection of ultrastructure from extraction from the dehydration steps and the preservation of protein localisation.[8] The choice of sample preparation is also informed by the type of probe(s) that are intended to be used, with ideally a single probe being used for both techniques to avoid uncertainty in co-localisation.[9–11]

On the choice of how best to approach CLEM, ideally, simplest methods are desirable due to low throughput of the method. Probes without complicated sample preparation associated with their use are considered better for general applications. Some of the common methods use genetic based probes which offer excellent tracking of proteins of interest, however these structures are not typically visible in EM and require further preparation such as additional contrast agents to improve electron scattering.[12,13] Another common method is immunostaining, which utilizes the exquisite precision of antibodies to bind specifically to proteins of interest. These methods also have pitfalls, such as in order to prepare cells for immunostaining they have to be fixed and then permeabilised using strong detergent, which can often extract cellular components and change protein location.[8] Other approaches such as Quantum Dots (QDs) offer a more straightforward way of using probes, but QDs are quite large and have surface properties that can perturb cell function.[14,15] Overall, there are various approaches using diverse probes, each with their advantages and disadvantages. While much has been achieved with these probes, there is still a niche to be filled for probes which have a greater accessibility by functioning similarly to commercial organic dyes. If probes could be used to stain cells and imaged without further complex cell preparation, but unlike organic dyes would also be visible in EM, this would simplify preparations for CLEM imaging and allow the choice of CLEM preparations to be ideal for the sample in question and would not be constrained by the probe used.

As shown in chapter 3, 4, and 5, luminescent metal complexes have the potential to fill this niche and allow CLEM to become routine by simplifying the preparation of samples, while maintaining visibility in both imaging modalities. However, as discussed above there are many ways to prepare cells for CLEM and these are often dictated by the probes being used. While metal complexes should in theory be compatible with preparing samples for pre- and post-TEM preparation, light imaging it was also realised that these probes could also serve as an *in situ* probe for high pressure freezing (HPF) applications. For all these samples preparations it should also be possible to use the best available fixation conditions without fear of damaging fluorescent proteins, maintaining the structure of epitopes or the need to permeablise the sample to allow antibodies access to the protein of interest.

The aim of this chapter was to assess the type of EM preparations that the luminescent transition metal complexes (explored in the previous chapters) could be subjected to, in order to achieve fully correlative images of cells stained with such complexes.

6.2 Correlative Light and Electron Microscopy on TEM Grids

As mentioned in the introduction, there are many different ways of sample preparation to achieve correlative images of samples, and one of the simplest ways is to use samples prepared for TEM with luminescent probes already present or added post embedding. This allows samples that are ready to be viewed in EM which can either be modified to be visible in LM or are already emissive. This means there will be no changes made to the sample between imaging the sample in EM or LM due to sample preparation, allowing easier correlation with a greatly reduced chance of artefact introduction before imaging in another modality. This type of preparation has already been utilised in studies concerned with potential therapies for eye regeneration.[16]

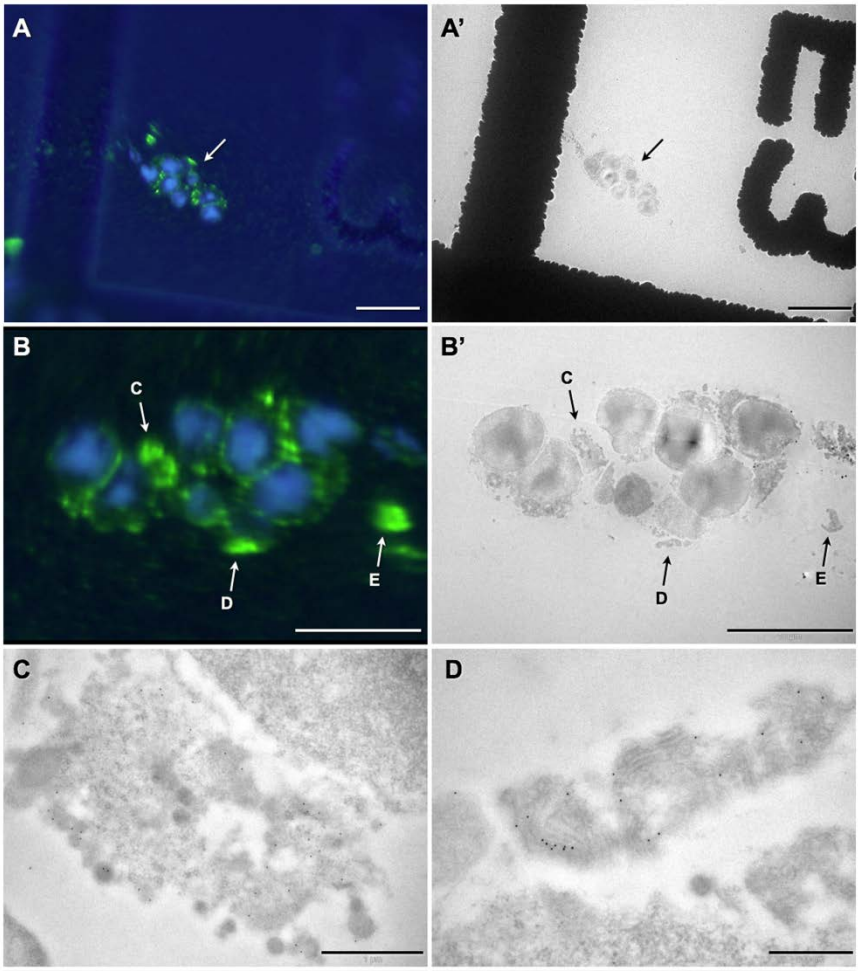

Figure 2. CLEM analysis of Vitreal-located transplanted photoreceptor precursor cells. Adapted from ref.[16]

A limitation of this type of protocol is the use of typical EM sample preparation protocols, such as this, is typically incompatible with fluorophores like fluorescent proteins, as the fixation conditions often lead to loss of fluorescent and the heavy metals often reduce fluorescence too. Methods have emerged to try and retain fluorescence but these typically use more gentle fixation conditions which can compromise the ultrastructural preservation.[9] However, due to the nature of the transition metal

complexes, the use of fixatives should not affect these complexes and therefore ideal fixation conditions can be utilized.

6.2.1 Results

Utilizing a similar preparation method for samples as the paper mentioned above,[16] it was decided that HeLa cells would be stained live as normal with complex **3.1** at 100 μM for 20 mins, which was the conditions found to give the best results in the previous studies. These HeLa cells were then fixed in glutaraldehyde (2 % in Na cacodylate buffer) over night at 4 °C, fixed and stained with OsO_4 and uranyl acetate, dehydrated and sectioned identical to the protocol used in previous chapters but instead of the sections being mounted on a normal grid, finder grids were used to aid in refinding areas of interest. Once the sections were mounted on finder grids the grids were then mount in between microscope slides and immersed in glycerol as a mounting agent to be viewed under a LM.

This section was then imaged in a widefield microscope in brigthfield mode to find the finder grid and note the exact location before imaging the cells. However, no luminescence was found in the initial imaging and no cells were observed on the grid under brightfield. As this created more questions than answers, it was decided to image one of the grids that had been imaged to inspect the integrity of the section and search for cells that could be seen under TEM. It was also decided to image a grid and note the location of cells for future light microscopy so we would have a region of interest predecided. Finally, it was decided to image a single grid and then immerse the grid in glycerol before cleaning it and reimaging it to see if the glycerol has adverse effects to the grid.

Upon imaging under TEM it was observed that the grid that had been imaged did not have any section left on it, which explained the lack of cells in brightfield and emission. Upon imaging a grid which had not been used in LM, it was found that some of the sections were very fragile and even disintegrated while being imaged in TEM, corroborating that the section may have been damaged before imaging on the LM. However, once a strong grid was carefully imaged under TEM it was then immersed in glycerol for 15 mins to simulate the imaging for LM and was then cleaned with DI water before being reimaged under TEM. Using the finder grid it was possible to locate the same areas and reimage the same cells in the section without any noticeable damage across two different areas.

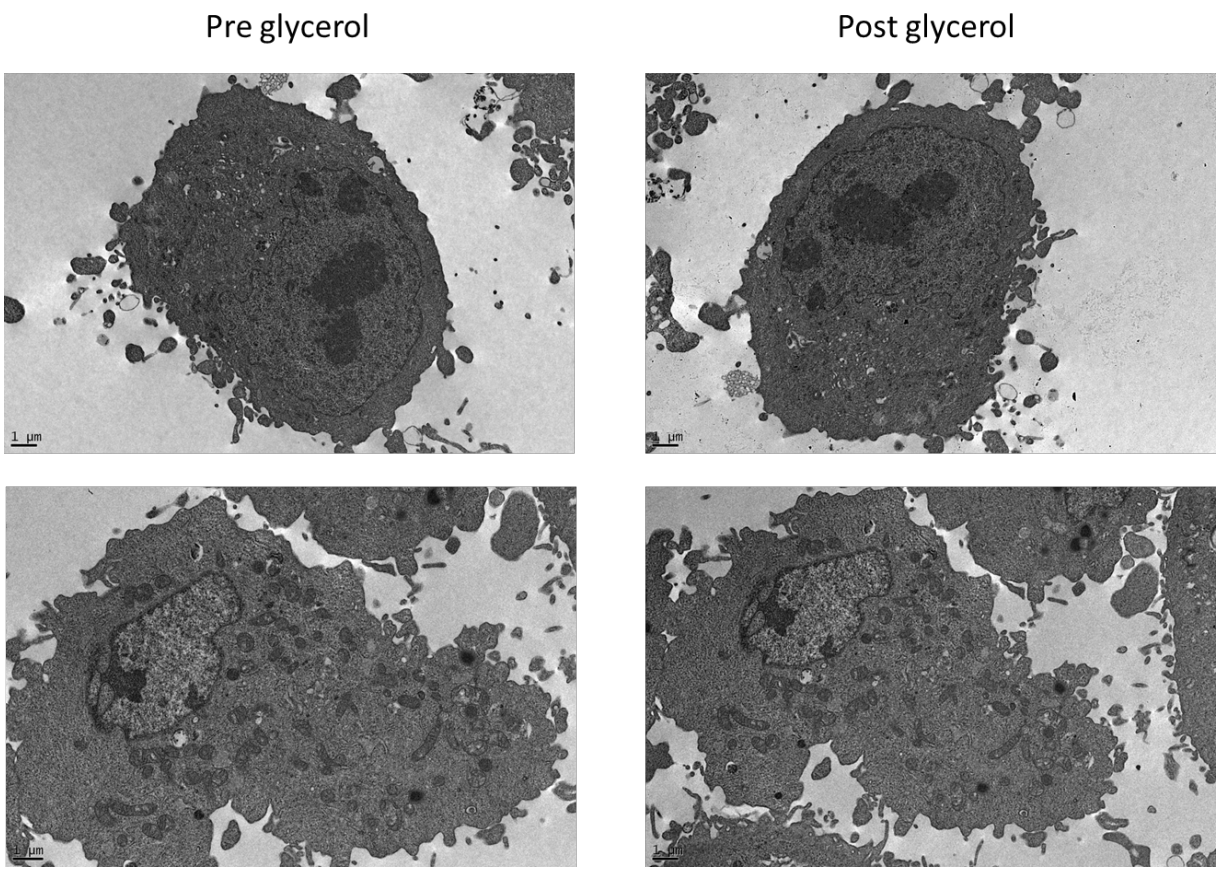

Figure 3. TEM micrographs of HeLa cells which had been stained with complex 3.1, then prepared for TEM and then immersed in glycerol to simulate the imaging on the light microscope.

It was noted that the grids had to be handled very carefully to ensure no damage to the section occurred and this was the suspected reason for the section not being present in the initial imaging attempts. Some of the fragile sections which were imaged on the TEM still has parts of the section present after being damaged but these were so damaged that no useful images could be obtained using them as seen in Figure 4.

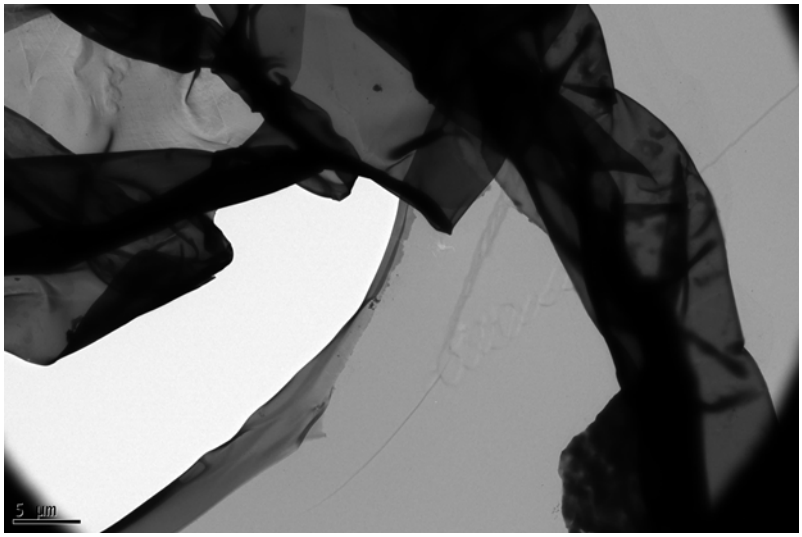

Figure 4. TEM micrograph of a piece of section which had ruptured and folded in on itself.

As the localisation of complex **3.1** (which accumulates in the nucleus, but also throughout the cytoplasm) was not easily correlated between LM and EM it was decided to use complex **4.6** instead as the lysosomal and mitochondrial localisations (typical for **4.6**) was much clearer in both modalities. Upon imaging of cells treated with complex **4.6** (50 µM, 2 h) only some cells were found in the section and only one was found to have any appreciable amount of luminescence signal but it was too weak and SIM reconstruction and deconvolution were affected by the weak signal. It is difficult to ascertain if the presence of the other heavy metal ions affected the luminescence of the Ir complex or if there simply wasn't enough compound in the thin section to be easily visible.

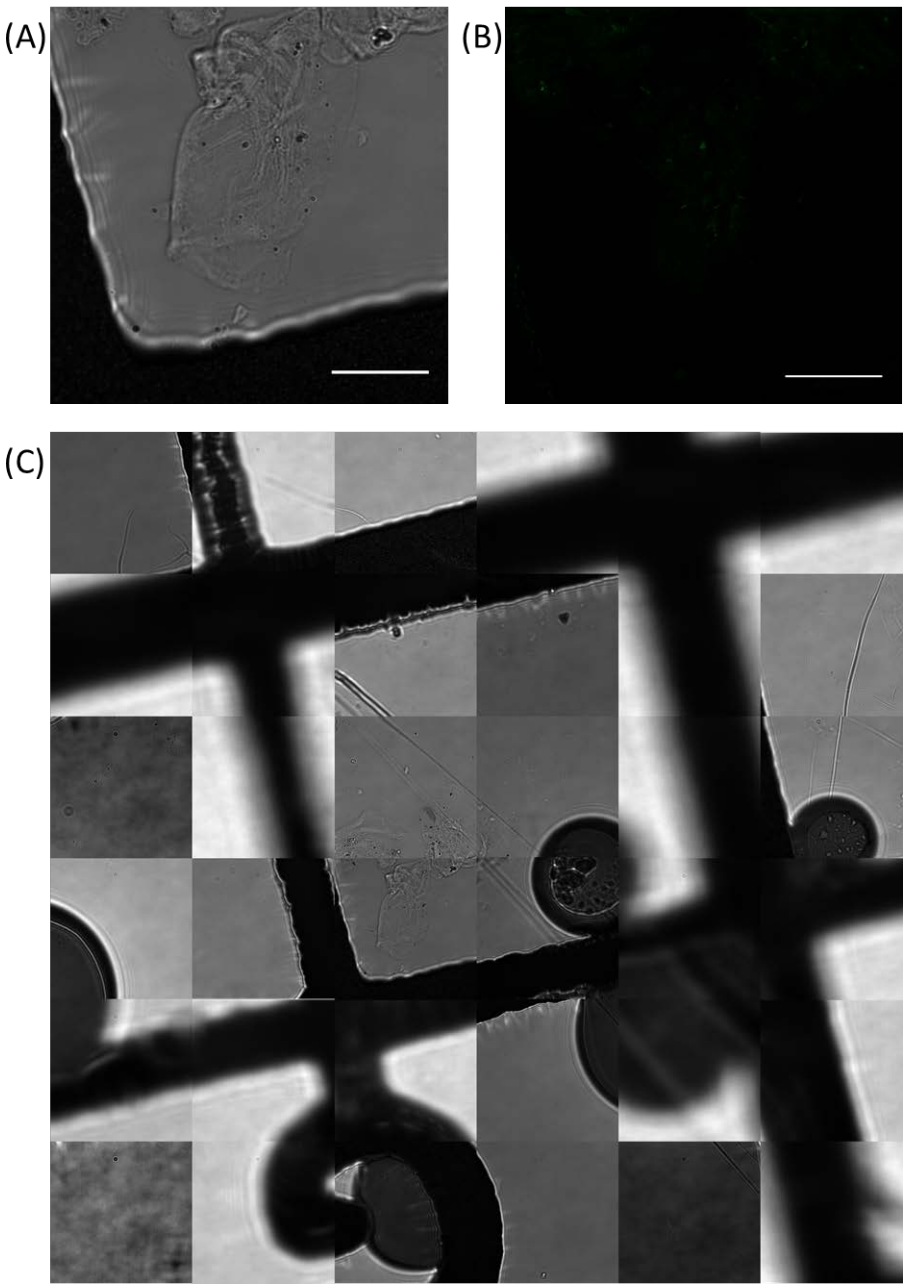

Figure 5. Widefield microscopy images of HeLa cells prepared for TEM and mounted on a TEM finder grid (A) Brightfield, (B) excitation (λ = 405 nm) (C) mosaic brightfield map of area. Scale bar = 10 µm.

Since these cells had a very weak signal it was decided that another approach would be tried. While more complex could be used to stain the cells, it would appear that that would make little difference due to how weak the signal is in this sample.

6.3 CLEM Using Gridded Culture Dishes

Due to the difficulties of the previous approach a different CLEM protocol was considered. A common type of CLEM protocol is the use of small culturing compatible dishes or coverslips, such as

35 mm culturing dishes with embossed grids on the bottom, which allow the recording of the location of the cells imaged. Once cells are stained and imaged they are fixed if not already done so and then dehydrated, stained and embedded in the dish. Once embedded the resin is removed from the dish and the grid is transferred by virtue of the resin being set in the dish, thus allowing the block to then be trimmed and sectioned to relocate the cells imaged. This method has been described in the literature[17,18] but is still a skilled niche that is steadily being disseminated by the groups who have pioneered its development.

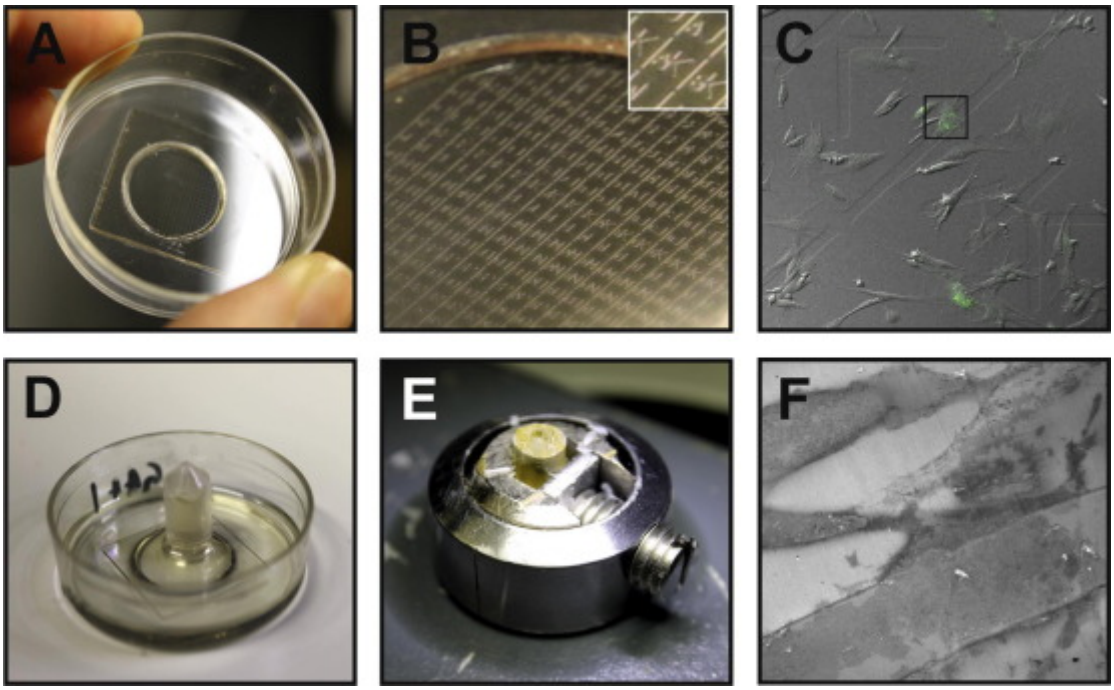

Figure 6. CLEM workflow (A) MatTek dish with grid for CLEM applications, (B) etched grid coordinated visible on coverslip, (C) Cells of interest identified by LM, (D) sample processed and embedded with beem capsule on area of interest, (E) block prepared for trimming and sectioning, (F) Cells imaged in TEM where specific cells were localised. Reproduced from ref.[18]

6.3.1 Protocol Refinement

This method is known to be complex and intrinsically low throughput due to rigor and precision required to take a single sample from the LM preparation, LM imaging and then prepare the sample for EM in such a way that the exact same cells can be located. As such, careful refinement of the sample preparation was required to be able to take samples through the whole protocol intact. One of the first considerations was the choice of 35 mm culturing dish as both MatTek and Ibidi offered slightly different dishes with high precision glass bottoms for LM imaging and a finder grid for recovering regions of interest (fig. 6).

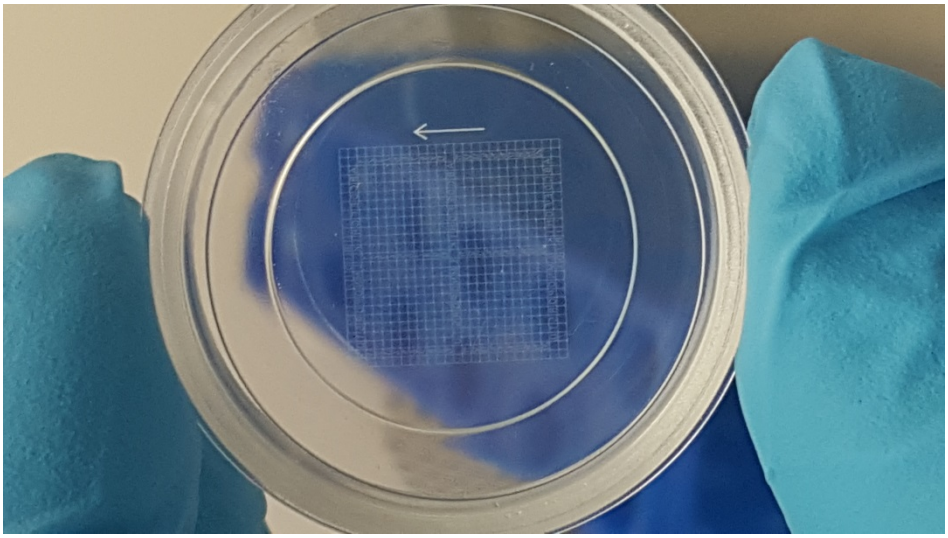

Figure 7. Ibidi 35 mm cell culture plate with a grid embossed on the glass to aid in relocation of areas of interest.

Initially, both dishes were used in the protocol to look for advantages and disadvantages of either. Typically, samples are fixed using a mixture of glutaraldehyde and paraformaldehyde or just glutaraldehyde, so both methods were used with no obvious differences in cell ultrastructure observed under TEM and as such fixation with only glutaraldehyde was the preferred method for simplicity.

While both dishes seem to work well with the light microscope that was intended for use in the CLEM protocol, the MatTek dishes had grids with very large lettering but also had large spaces between the lettering designed to allow precision localisation. This large space required a large finder region imaged on the LM to be able to discern precisely where on the dish the cells of interest were actually located, which required one to generate large stitched images (Fig. 7). Furthermore, these large stitched images obscured the grid below requiring laborious manual marking to be able to distinguish the grid (Fig. 7). In contrast, the Ibidi plates had grids with smaller sized lettering and grid size and while not having lettering all over the grid it only require the locating of some lettering to be able to precisely correlate where the region of interest was for post EM preparation recovering of the region of interest(Fig. 7).

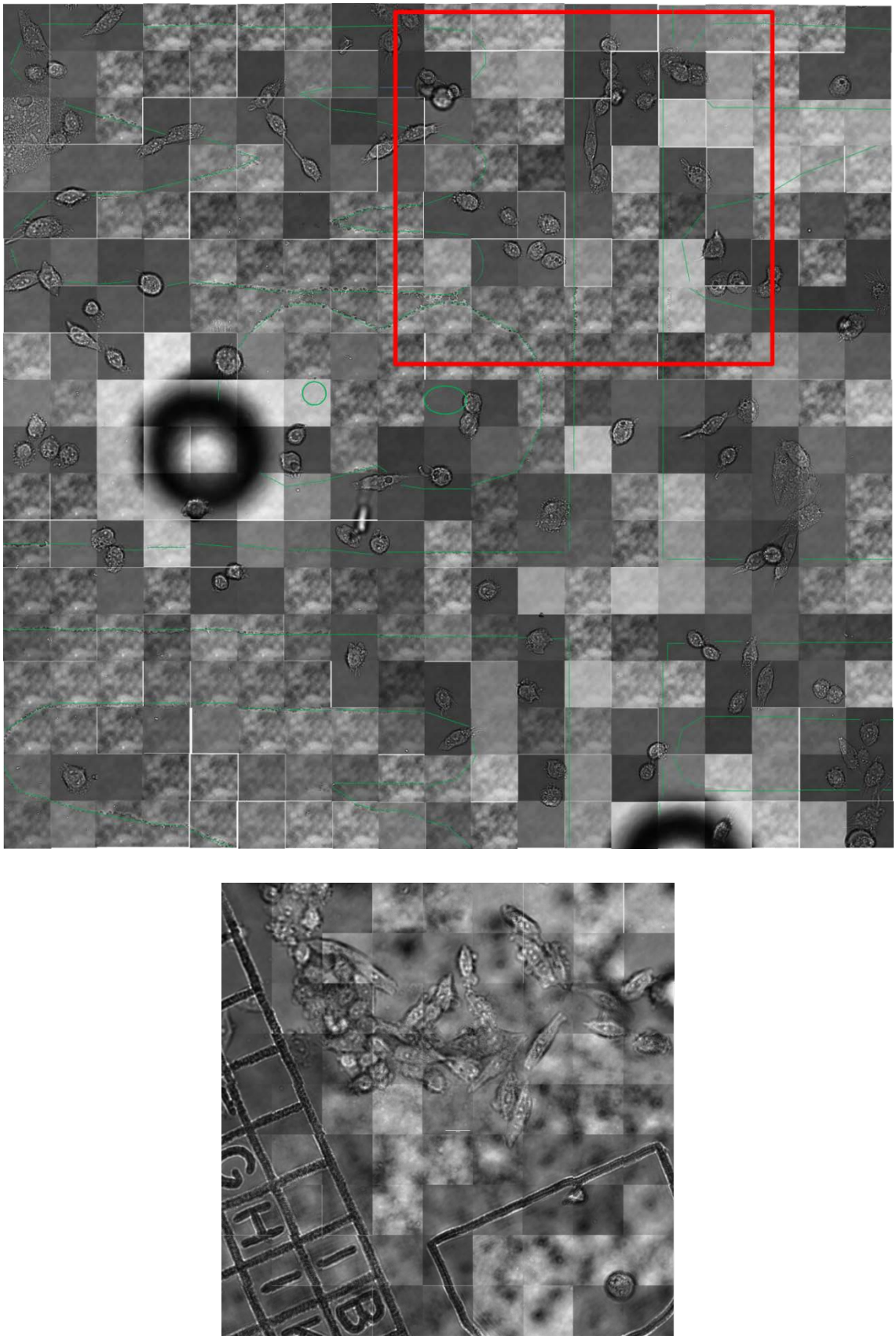

Figure 8. Mosaic of brightfield images of HeLa cells on a MatTek dish with the grid highlighted in green as it is difficult to distinguish (top) and an Ibidi plate (bottom)

The next step in the protocol was secondary fixation using osmium tetroxide, at this point it was suggested that we reduce the normal amount of osmium used to highlight the staining of the metal complex and as such the lower concentration of 0.5 % OsO_4 for 15 minutes was used. The cells were then washed in cacodylate buffer and staining using uranyl acetate (3 %, 20 mins) using typical conditions. The sample was then washed again with sodium cacodylate buffer and dehydrated in the dish using an ethanol gradient from 70 %, 80%, 90%, 96 % and 100 % ethanol for 5 – 10 minutes in each concentration. Here some typical TEM protocols use propylene oxide as an intermediate solvent before been infiltrated with resin, however it was observed that the propylene oxide eroded the tops of the dishes, as seen in Figure 9, and so this step was omitted from the protocol with no ill effects observed in samples processed in this way.

Figure 9. Lid of the Ibidi plate displaying erosion from the intermediate solvent, propylene oxide.

Once the dehydration was finished, the sample was covered in 100 % epon resin to allow the resin to infiltrate the cells for 2 hours. While there are a number of different resins for EM protocols, with various ways of curing and other differing properties, epon was chosen as it has excellent cutting properties, thus allowing careful and precise trimming of blocks. After 2 hours, the epon was removed and fresh epon was added and either a pre cured cylinder of resin or a beem capsule full of uncured resin was placed over the region of interest before the sample was placed in an oven at ~60 °C for 24-48 hours to cure the resin.

Once the samples were fully cured, the resin blocks then needed to be removed from the glass bottoms of the dishes. This was generally achieved by heat shocking the sample by plunging the sample in liquid nitrogen until the rapid bubbling of N_2 had stopped and then plunging the sample into boiling water to utilize the differing expansions rates of the materials to release the coverslip. It was also noted, while heat shocking the plates to remove the coverslip from the resin block, that the Ibidi plates when plunged into the boiling water generally easily release the coverslip and this was

thought to be possibly due to the glue being soluble in boiling water. On the other hand, the MatTek dishes would typically require the application of a razor blade in between the dish bottom and the coverslip to achieve the removal of the coverslip. For this reason, and that of the better grids of the Ibidi dishes, the Ibidi dishes were favoured over the MatTek dishes.

Figure 10. Ibidi 35 mm plates with the resin blocks heat shocked to remove the coverslip with the excess resin visible in the further samples (top) and a close up of the resin block after trimming showing the transferred grid pattern (bottom).

Differences were noted in the application of the resin block on top of the gridded area, when a pre cured cylinder of resin was placed on top of the area of interest before curing the resin, the trimming of the resin after heat shocking was always disordered as the resin would break in no particular fashion as can been seen in Figure 10, with potential to cross the region of interest. However, if some of the uncured resin mixture is place in a beem embedding capsule and then placed over the gridded area resin side down, when the resin is cured and the trimming begins, the excess resin filling the rest of the 35 mm plate is then easily separated from the gridded region as the rim of the beem capsule provides a natural boundary and the resin factures around it as seen in the samples of Figure 11.

With the resin block trimmed to the grid area (or in the case off the Ibidi plates easily cut to the shape of the beem capsule) it was then important to identify the exact region that was imaged in LM using the mosaic images and the imprinted grid to find the exact cells. Once found the area was marked with two sets of parallel lines perpendicular to one another, forming a square where the cells are located using a razor blade as seen in Figure 11 (black arrow) it was possible to start trimming the block to prepare it for sectioning.

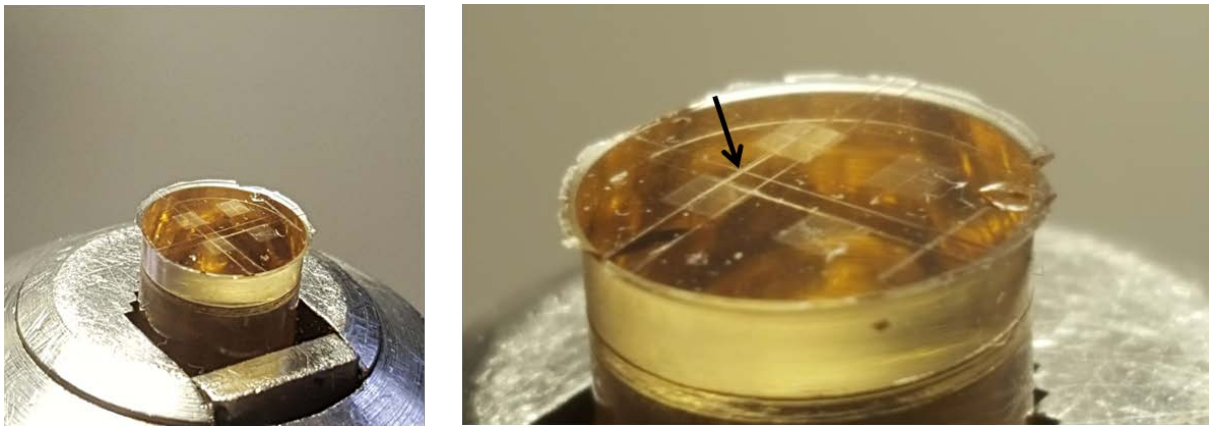

Figure 11. Roughly trimmed resin block with the region imaged in LM marked using a razor blade (black arrow) before more precision trimming is performed.

First of all, the block was trimmed using normal single blade razor blades to carefully cut the majority of the resin away from the area of interest, while being careful not to damage the area where the cells of interest are present. This is very important as the cells are on the very edge of the resin block and any external damage from the razor blade will cause damage all the way through the cells of interest. Once the majority of the unwanted resin is removed, as seen in Figure 12 (top image), an extremely sharp double headed razor blade is used to precisely removed the final pieces of resin and to shape the block ready for sectioning as seen in Figure 12 (bottom image). While in normal TEM preparation, the face of the block will need to be cut in to a flat face so that sectioning can be done, this is not required for this preparation as, by virtue of the protocol, the face should already be flat from the bottom of the dish.

Sectioning on the block was performed to provide a ribbon of the same sample area to give multiple serial sections of the cells of interest. This approach allows multiple sections passing through the Z axis of the sample to be collected ready for imaging so that the correct image from the Z stack of the LM imaging and the EM can be overlaid and correlated.

Figure 12. Resin block roughly trimmed to the area of interest with a razor blade (top) and the final trimming and shaping of the resin block ready for sectioning (bottom).

6.4 CLEM of Complex 4.6

Initial experiments with complex **4.6** were undertaken in the University of Bristol in collaboration with Dr Paul Verkade, adapting their protocol as discussed above. Live HeLa cells grown on gridded 35 mm plates were incubated with 100 μM for 2 hours as this concentration was known to give the best contrast in EM. Following incubation, cells were covered with fresh CO_2 independent media for live imaging. Cells of interest were found and their location noted for later reference and z-stacks taken. These cells were then fixed in glutaraldehyde (3%) for an hour before following the protocol detailed above in section **6.3.1**. The cells that were imaged in confocal microscopy were retraced in TEM using the grid and were images. As is shown in Figure 13, the punctate staining of the lysosomes can be seen both in the confocal images and the TEM images, with good agreement in the emission and contrast in both (white arrows). There are however a number of lysosomes which are

slightly misaligned from the confocal microscopy and we ascribe this to the small delay in fixation of the cells, giving time for natural cell processes to continue long enough to slightly displace the lysosomes. This confirms what had been conferred in chapters 3, 4 and 5 where luminescent metal complexes were shown to provide emission and EM contrast but only in separate samples. Furthermore, no special changes where required for the sample preparation for light or electron microscopy to yield CLEM images.

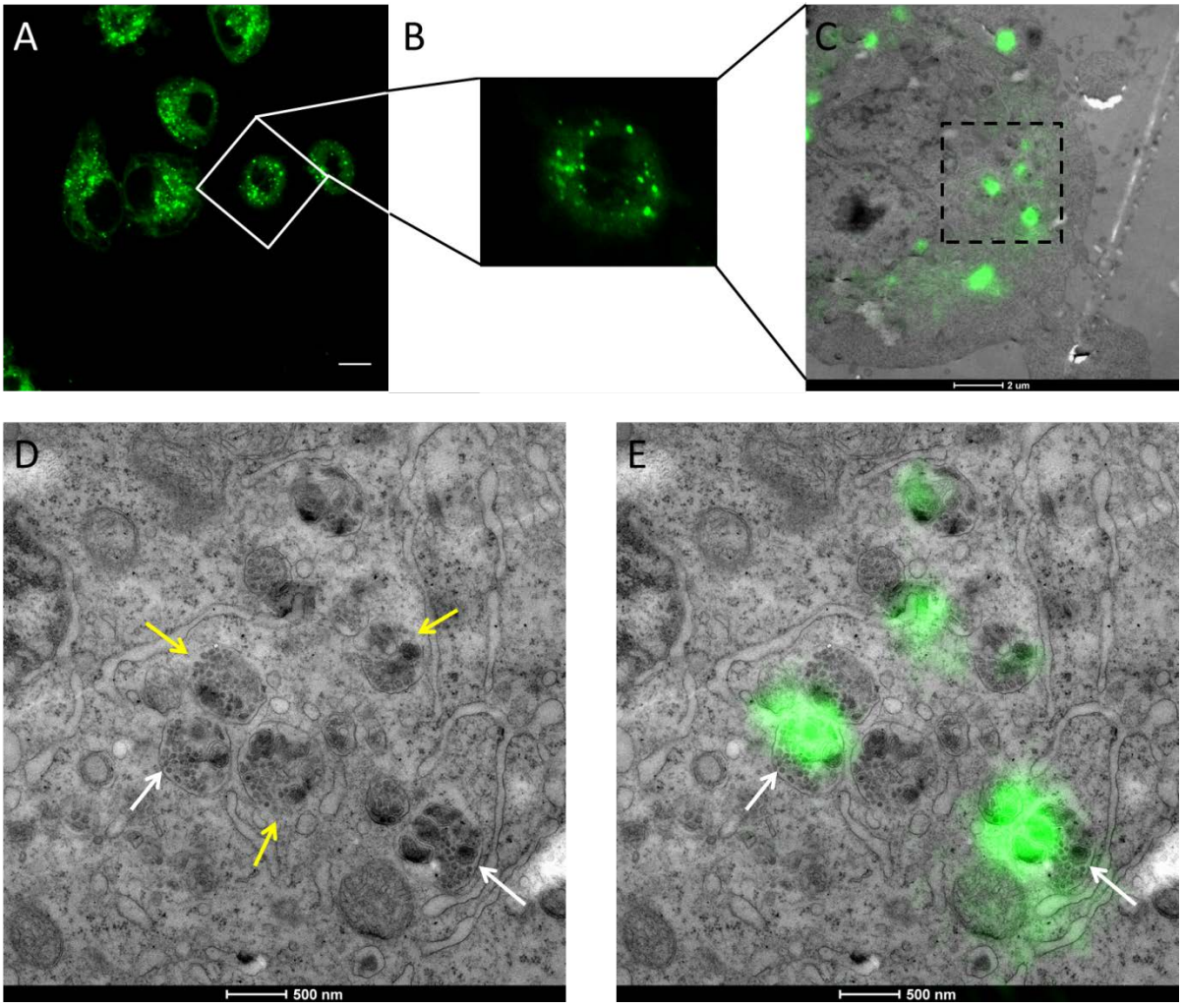

Figure 13. CLEM images HeLa cells incubated with complex 4.6 (100 µM, 2 h, λ_{ex} = 405 nm). (A) LSCM micrograph of cells, (B) zoomed in image of single cell, (C) CLEM micrograph of cell, (D) zoomed in TEM micrograph of lysosomal staining, (E) CLEM micrograph of lysosomal staining. White arrows highlighting co-occurring emission and contrast in CLEM, yellow arrows highlighting groups of vesicles and membrane ruptures of lysosomes. Scale bar = 10 µm.

Interestingly, it was also noted that the lysosomes, when imaged in TEM, were found to be broken up into what appeared like small grouping of vesicles, with obvious breaks where the membrane of the lysosome was present (yellow arrows). This damage is likely due to complex **4.6** generating $^1O_2$ while being irradiated. Curiously, although the complex also accumulates in the mitochondria, there are no obvious signs of mitochondrial damage in the TEM micrographs. Despite the lack of damage observed, it is possible that mitochondrial function is affected by the singlet oxygen generation but

less catastrophic damage is caused. This phenomenon has been already harnessed by McKenzie and co-workers to demonstrate the potential of this complex as a photosensitizer for photodynamic therapy (PDT) in cancer cell lines.[19] It was shown that complex **4.6** causes cell death through apoptosis (a type of programmed cell death) but the exact mechanism of how this comes about was not known. Evidenced in these CLEM images it's clear that the lysosomes of cells are ruptured while being irradiated, releasing an acidic cocktail of lytic enzymes into the cytoplasm, and is likely a key factor in the initiation of apoptosis. This illustrates how metal complexes can act as CLEM probes to yield information not available from either imaging technique alone.

As a comparison, HeLa cells were prepared in the University of Sheffield using the same method but the cells were fixed using glutaraldehyde (3%) after incubation and then imaged on an OMX blaze in widefield mode. A mosaic of the area of interest was taken with the imaged cells location noted as shown by the red box in Figure 14.

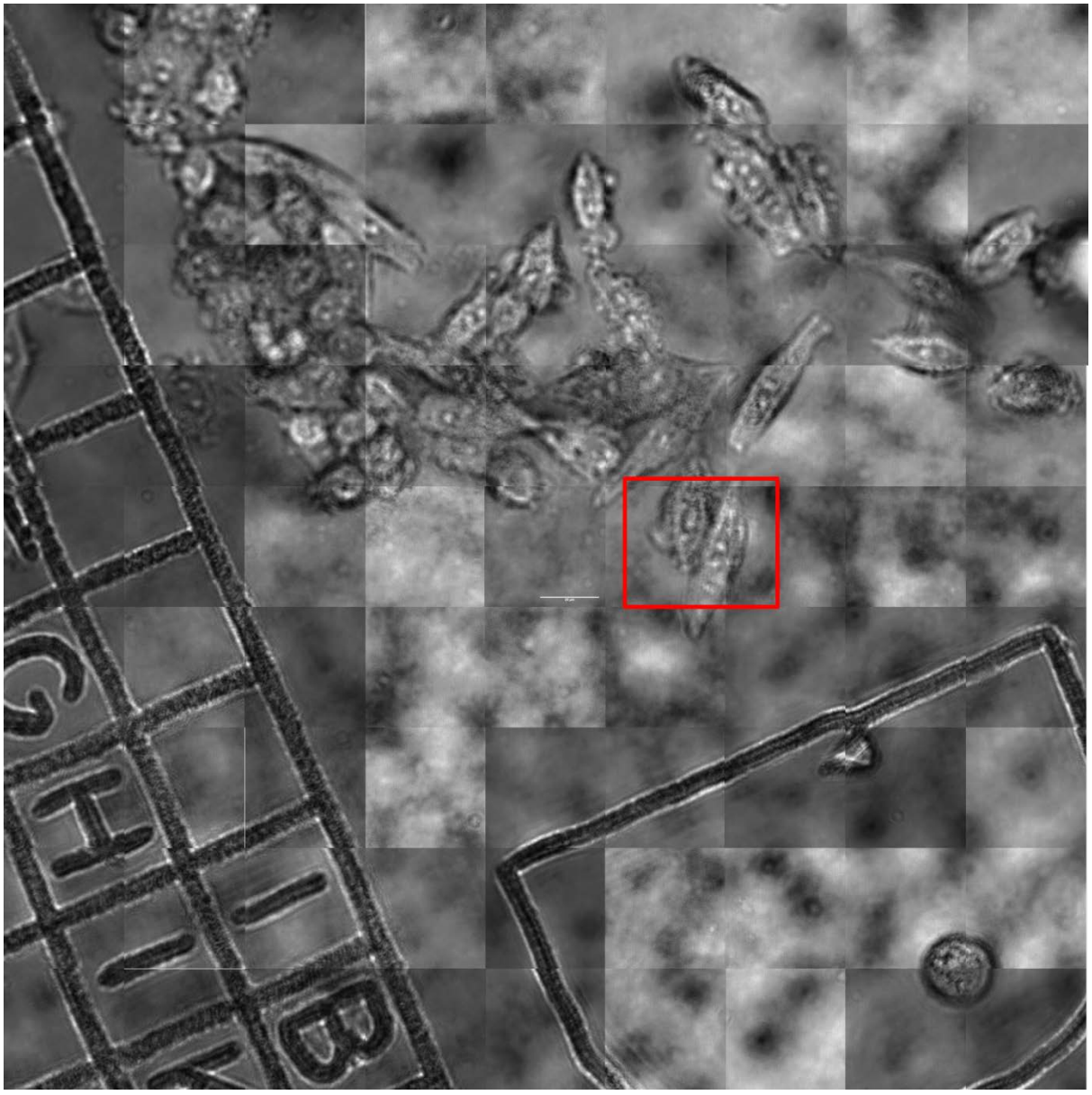

Figure 14. Brightfield mosaic of the region of interest with the cells imaged highlighted by a red box. Scales bar = 20 µM.

Fully correlative images of the cells was found to be difficult to obtain due to the inability to find a TEM section that aligned with one of the images from the Z-stack of the light microscopy. However, it is clear from the light and electron microscopy images that these are the same cells. In contrast to the live imaging of HeLa cells, these cells do not exhibit any destruction of their lysosomes and this is due to the structural preservation imparted by fixation of the membranes within the cells.

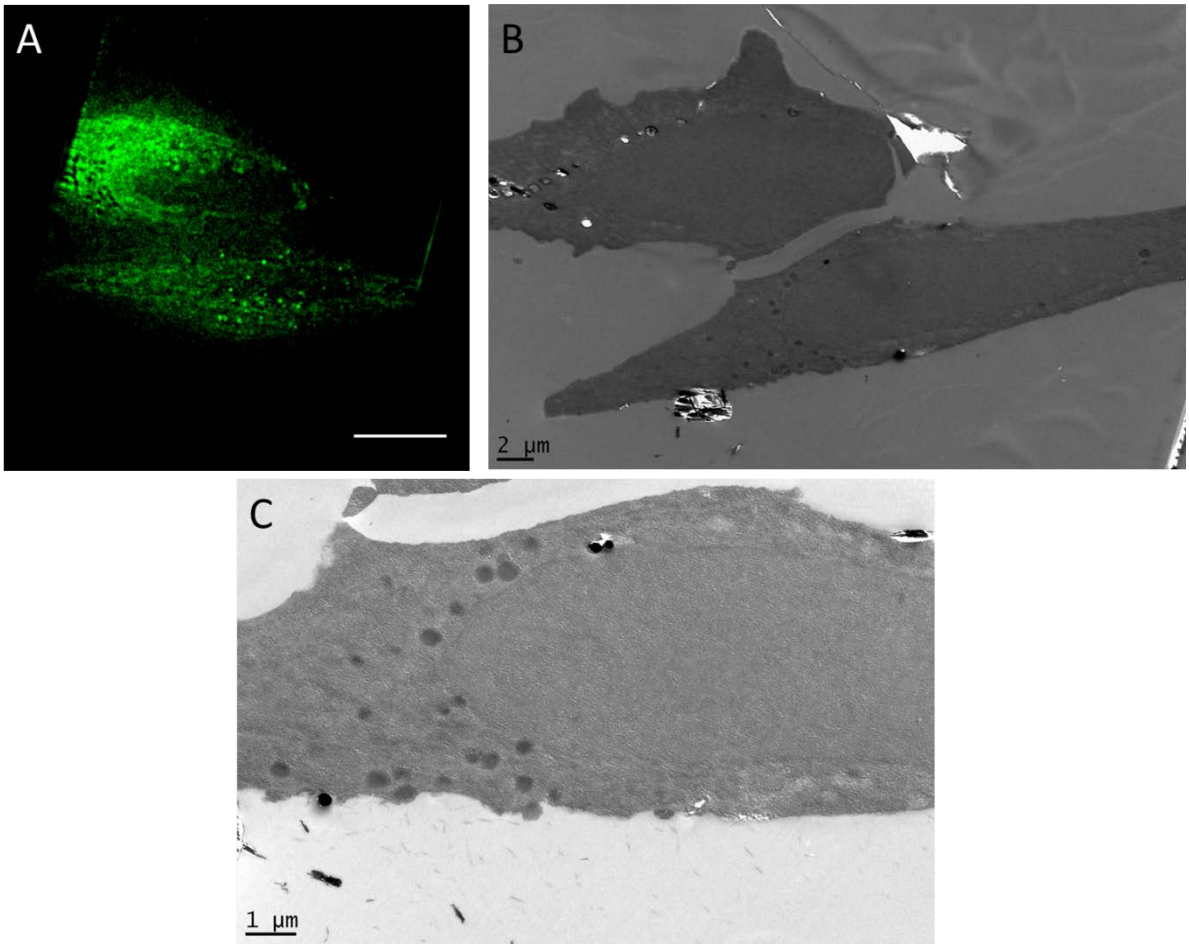

Figure 15. Fixed HeLa cells incubated with complex 4.6 (100 µM, 2 h, , λ_{ex} = 405 nm), (A) widefield micrograph of cells, (B) TEM micrograph of the same cells, (C) zoomed in image of lysosomal staining showing intact lysosomes.

6.5 CLEM Using High Pressure Freezing

High pressure freezing offers a method of preservation that maintains near native structure due to the speed at which the sample is frozen into a glass under high pressure and extremely low temperature. Once a sample is frozen it can be dehydrated using acetone and embedded in resin without melting the ice and losing the preservation. While HPF provided almost unparalleled preservation, the samples typically only get stained with small amounts contrast agents, thus only the low contrast is observed. This is further compounded by the fragility of the samples; due to the lack of fixatives present the samples are easily damaged by high electron beam power. Thus luminescent metal complexes could prove to be invaluable tools for this technique by providing contrast in cells that have been preserved by HPF by incubating the live cells before HPF. The method outlined below was adapted from a method reported in the literature.[11]

6.5.1 Preliminary HPF Studies

HeLa cells were seeded on sapphire discs which had been carbon coated with a finder grid, as shown in Figure 16. Sapphire discs are requires as they are small but strong enough to withstand being subjected to the high pressure and sudden decrease in temperature that required for the cells to be properly preserved. Cells were placed in BSA solution to act as a cryoprotectant and were then HPF by placing the sapphire disc in a gold sample holder before using a Leica EMPACT 2 High Pressure Freezer, subsequently being stored in liquid nitrogen. From here the sample was placed in a Leica AFS 2 Freeze Substitution Equipment at -180 °C. The sample was then slowly warmed to -90 °C and freeze substituted using acetone to dehydrate the sample and stained with 0.5 % uranyl acetate in acetone. The sample was then slowly warmed up to -40 °C and immersed in Lowicryl® and cured using UV irradiation. The sample was then allowed to warm to room temperature and removed from the embedding capsule. The bloc was the trimmed to expose the gold sample holder and sapphire disc. The sample holder and sapphire disc were carefully removed using a razor blade, with extra care taken to not damage the resin beneath. From here cells of interest could be identified by the superimposed carbon grid and the resin trimmed and sectioned for imaging.

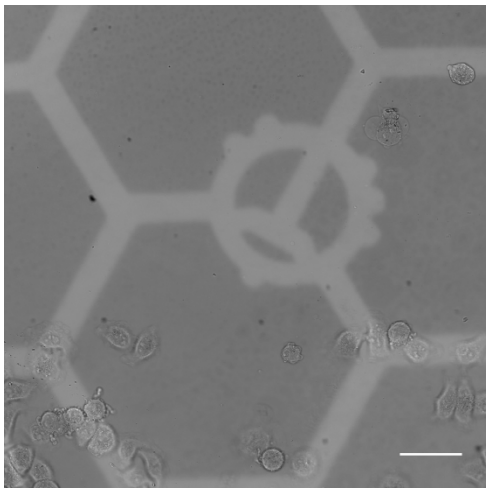

Figure 16. Brightfield image of a sapphire disc with a carbon coated grid visible. Scale bar = 50 µm.

HeLa cells treated with complex **4.6** (100 µM, 2 h) were taken through the method described above, however once the sapphire disc was removed from the cured resin it was observed that no cells were present. While the BSA layer could be discerned by the characteristic brown colour in the resin, no cells or cellular material was found. This was initially puzzling as cells had been imaged by confocal microscopy before the HPF and freeze substitution. However, after repeating the process a number of times to ensure practical errors were unlikely to be the cause, it was realised that complex **4.6** would be producing singlet oxygen while the resin is being cured. This prolonged UV exposure must have caused the complex to obliterate the cells within the resin leaving no sign of cells. This is unfortunate

as the curing of the resin by UV allows the sample to keep at sub-zero temperatures until it's in resin is cured, maintaining a high level of cellular preservation.

While further experiments were not undertaken, it is possible to get around this problem by using fixative like glutaraldehyde while the sample is still frozen at -20 °C to maintain the near native preservation after the sample is allowed to warm to room temperature and the resin is cured in an oven. This would potentially allow the excellent preservation to be maintained, while avoiding the problem of damage to the cells caused by singlet oxygen generation in the sample.

6.6 Summary

Following the success of chapter 3, 4 and 5 to show that luminescent transition metal complexes can potentially act as CLEM probes, here complex **4.6** was accessed over 3 different CLEM methods. The first of these methods focused on the preparation of samples using standard TEM sample preparations and then relying on the luminescence being maintained in the resin for light microscopy. Once samples were prepared it was found that these were very fragile and were easily lost completely or damaged. Samples that were imaged were found to only exhibit very low levels of luminescence and no subcellular information could be discerned. It appeared that there might not be enough complex present to be easily detected and future attempts at this method should consider using thicker ultrathin sections, such that more complex would be present in the resin and likely give more signal. However, it is also a possibility that the presence of uranyl or osmium ions in the section could also adversely effected the luminescence properties of the complex, reducing (quenching) the luminescence.

The second technique used cell culture dishes with a grid on the bottom to allow for live cell imaging with the location of the cells of interest recorded so that it could be retraced afterwards. Once the light microscopy was performed the sample would be prepared for TEM in the dish, transposing the grid on to the resin once the cells were prepared and allowing the cells of interest to be sectioned for TEM. During the refinement of the method, it was noted that the Ibidi culture dished had much more clear grids which aided in retracing the area of interest. Live HeLa cells incubated with complex **4.6** were imaged in light microscopy and prepared for TEM following the correlative method. The lysosomal staining of the complex was very clear in both light and electron microscopy, allowing alignment of the images in ec-CLEM, a plugin for icy designed for correlative image processing. It was observed in TEM that the HeLa cells which has been imaged live displayed damage to their lysosomes, where the lysosomes appeared to have broken up in to small vesicle like bodies. This was in contrast to the images of cells which had been fixed before luminescence imaging, which exhibited fully intact lysosomes. This finding has brought to light some of the physical details of how the complex damages

cells when used for PDT, while it was known to cause apoptosis the exact details of how were not known. This finding highlights how CLEM with luminescent transition metal complexes can offer information previously unavailable. While only complex **4.6** was used in this technique, it is highly likely that both complexes **3.1** and **5.1** would also be able to function as probes for this method.

The third technique that was explored was high pressure freezing. This technique aims to achieve unparalleled sample preservation by high pressure freezing samples rapidly in to vitreous ice, giving near native state preservation. While live HeLa cells incubated with **4.6** were successfully frozen and the freeze substitution preformed, it was discovered that the UV exposure required to cure the resin without raising the temperature caused the complex to generate large amounts of singlet oxygen and destroyed the samples. Further studies were not undertaken but this problem could potentially be circumvented by using fixatives, such as glutaraldehyde, while the sample is still frozen to stabilise and maintain the preservation of the sample before warming the sample and curing the resin by temperature. This would avoid the UV exposure and thus the singlet oxygen generation, while maintaining preservation.

In this chapter complex **4.6** has illustrated that luminescent metal complexes have the potential to be new probes for CLEM with less stringent sample preparation required to function, improving the accessibility for users. However, most CLEM is concerned with single proteins within cells and while metal complexes utilised in cells have only been able to staining specific organelles it is possible that metal complexes could be conjugated to proteins through systems such as Halo[20] or SNAP[21] tags. This could yield metal complexes specific to single proteins of interest and further improve the utility of metal complexes as CLEM probes.

6.7 References

1 J. Caplan, M. Niethammer, R. M. Taylor and K. J. Czymmek, *Curr. Opin. Struct. Biol.*, 2011, **21**, 686–693.

2 E. Brown and P. Verkade, *Protoplasma*, 2010, **244**, 91–7.

3 G. M. Gaietta, B. N. G. Giepmans, T. J. Deerinck, W. B. Smith, L. Ngan, J. Llopis, S. R. Adams, R. Y. Tsien and M. H. Ellisman, *Proc. Natl. Acad. Sci. U. S. A.*, 2006, **103**, 17777–82.

4 V. Krieger, D. Liebl, Y. Zhang, R. Rajashekar, P. Chlanda, K. Giesker, D. Chikkaballi and M. Hensel, *PLoS Pathog.*, 2014, **10**, e1004374.

5 O. Yolanda, L. Hodgson, J. Mantell, P. Verkade and J. G. Carlton, *Nature*, 2015, **522**, 236–239.

6 S. M. Markert, S. Britz, S. Proppert, M. Lang, D. Witvliet, B. Mulcahy, M. Sauer, M. Zhen, J.-L. Bessereau and C. Stigloher, *Neurophotonics*, 2016, **3**, 41802.

7 C. Loussert Fonta and B. M. Humbel, *Arch. Biochem. Biophys.*, 2015, **581**, 98–110.

8 U. Schnell, F. Dijk, K. A. Sjollema and B. N. G. Giepmans, *Nat. Methods*, 2012, **9**, 152–158.

9 P. De Boer, J. P. Hoogenboom and B. N. G. Giepmans, *Nat. Methods*, 2015, **12**, 503–513.

10 M. H. Ellisman, T. J. Deerinck, K. Y. Kim, E. A. Bushong, S. Phan, A. Y. Ting and D. Boassa, *J. Chem. Biol.*, 2015, **8**, 143–151.

11 P. Verkade, *J. Microsc.*, 2008, **230**, 317–28.

12 X. Shu, V. Lev-Ram, T. J. Deerinck, Y. Qi, E. B. Ramko, M. W. Davidson, Y. Jin, M. H. Ellisman and R. Y. Tsien, *PLoS Biol.*, 2011, **9**, e1001041.

13 B. A. Griffin, S. R. Adams and R. Y. Tsien, *Science*, 1998, **281**, 269–272.

14 M. J. Saxton and K. Jacobson, *Annu. Rev. Biophys. Biomol. Struct.*, 2003, **26**, 373–399.

15 T. Q. Vu, W. Y. Lam, E. W. Hatch and D. S. Lidke, *Cell Tissue Res.*, 2015, 71–86.

16 D. Eberle, T. Kurth, T. Santos-Ferreira, J. Wilson, D. Corbeil and M. Ader, *PLoS One*, 2012, **7**, 1–11.

17 H. Asakawa, Y. Hiraoka and T. Haraguchi, *Micron*, 2014, **61**, 53–61.

18 K. Hellström, H. Vihinen, K. Kallio, E. Jokitalo and T. Ahola, *Methods*, 2015, **90**, 49–56.

19 L. K. Mckenzie, I. V Sazanovich, E. Baggaley, M. Monneau, V. Guerchais, J. A. G. Williams,, J. A. Weinstein and H. E. Bryant, *Chem. Eur. J.*, 2017, **23**, 234–238.

20 G. V Los, L. P. Encell, M. G. McDougall, D. D. Hartzell, N. Karassina, C. Zimprich, M. G. Wood, R. Learish, R. F. Ohana, M. Urh, D. Simpson, J. Mendez, K. Zimmerman, P. Otto, G. Vidugiris, J. Zhu, A. Darzins, D. H. Klaubert, R. F. Bulleit and K. V Wood, *ACS Chem. Biol.*, 2008, **3**, 373–82.

21 A. Keppler, S. Gendreizig, T. Gronemeyer, H. Pick, H. Vogel and K. Johnsson, *Nat. Biotechnol.*, 2003, **21**, 86–9.

Chapter 7. Experimental methods

Complexes **3.1** was synthesised and characterised by Elizabeth Baggaley and the synthetic route has been published.[1] Complexes **4.1**-**7** were synthesised in Gareth Williams lab in Durham University, UK and only complex **4.6** has been reported in the literature previously,[2] all others are unpublished work. Complexes **5.1** and **5.2** were synthesised and characterised by AJ Cankut and the synthetic routes have been reported.[3]

7.1 Cell Culture

HeLa cells were cultured in Dulbecco's modified Eagle's medium (DMEM), purchased from Aldrich (500 mL), supplemented with 5 mL L-glutamine (200 mM solution), 50 mL fetal calf serum(10%). Cultures were grown as monolayers in T-75flasks at 37 °C in an atmosphere of 5% CO_2 / 95% air. Once cells had reached ~90% confluency, cells were subcultured using Trypsin EDTA (2 mL). Sub-cultures for live imaging and TREM were cultured in 35 mm glass bottomed culture dishes.

7.1.1 Live Cell Staining

Cells were cultured in glass bottomed culture dishes in DMEM (with supplements as described above) until ~60% confluent. Metal complexes were dissolved in DMSO to form stock solutions of typically 5-10 x 10^{-3} M, which were then diluted in DMEM to form working solutions (<1% DMSO). Media was removed and the cells washed with sterile PBS (3 x 1 mL per well), then covered with working solutions of metal complex(2 mL) and incubated at 37 °C for the desired length of time. Any co-staining was added into the working solution to form the desired concentration when the correct amount incubation time was left for both the complex and co-stain. The working solution was then removed and the cells washed with sterile PBS (3 x 1 mL) and then phenol red free DMEM was place on top of the cells and then imaged.

7.1.2 Fixed Cell Staining for 3D Structure Illumination Microscopy

Cover glasses were sterilised (IMS) and placed in 6 well plates. Cells were seeded at a density of ~1 x 10^5 cells per well and incubated overnight in DMEM (with supplements). . Metal complexes were dissolved in DMSO to form stock solutions of typically 5-10 x 10^{-3} M, which were then diluted in DMEM to form working solutions (<1% DMSO). Media was removed and the cells washed with sterile PBS (3 x 1 mL per well), then covered with working solutions of metal complex(2 mL) and incubated at 37 °C for the desired length of time. The working solution was then removed and the

cells washed with sterile PBS (3 x 1 mL) and fixed in 4% paraformaldehyde solution for 20 minutes at room temperature. Cell were then washed again with PBS (2 x 1 mL) and quickly with deionised water (1 x1 mL) and mounted on microscope slides (ProLong® Gold antifade, ThermoFisher).

7.1.3 Transmission electron microscopy Staining

Cells were cultured in T-25 flasks as above until ~90% confluency is achieved. Media was then removed and the cells washed with sterile PBS (5 mL) and then covered with working solution of the metal complex (3 mL) and incubated for the desired amount of time. The working solution was the removed and the cells washed with sterile PBS (2 x 5 mL) before having Trypsin EDTA (1mL) added for 5 mins. Once the cells were detached media (6 mL) was added to the solution and the cells transferred and centrifuged down(1200 rpm, 3mins). These cells were the resuspended in media(1 mL) and transferred to a 1.5 mL Eppendorf and centrifuged(2000 rpm, 3 mins), the media removed and glutaraldehyde (2.5% in cacodylate buffer) was added to fix the cells overnight at ~4 °C. Cells were then dehydrated, embedded in Araldite and sectioned in to 85 nm sections and mounted on copper grids before imaging under TEM.

7.1.4 MTT Assay

96-well plates were seeded with cells at 1000/well and left overnight. Wells were treated with concentrations of complex specified or DMSO control and incubated for the standard incubation period of the complex in question before replacing the treatment with 25 µL of 3 mg/ml thiazoyl blue (MTT) solution in each well. Following incubation for 3 hours the solution was removed from each well and 250 µL / well DMSO added ensuring mixing of crystals. Optical density of wells at 540 nm was recorded on a plate reader (Multiskan fc, Thermo Fisher Scientific, Warrington, UK).

7.1.5 Correlative Light and Electron Microscopy

This method was adapted from the following references.[4,5] HeLa cells were cultured in 35 mm dishes with gridded embossed on the glass bottoms (n = 1.5) either from MatTek (P35G-2-14-C-GRID) or Ibidi (µ-dish 35 mm, high grid 50 glass bottom), seeded at 150000 cells per dish overnight. These cells were then prepared as describes above for live cell imaging, stained with complex at the desired concentration (75-100 µM, 2 h for complex **3.6**). Samples were then fixed using Glutaraldehyde (1 mL/well, 3 %) for ~1 hour. Cells were then washed in Cacodylate buffer (1 x 1 mL) before being fixed in osmium tetroxide (0.5-2 % aq) for 20 minutes. Cells were again washed with Cacodylate buffer (1 x 1 mL) before being stained with uranyl acetate (3 %) for 15 minutes. Cells were washed with Cacodylate buffer (1 x 1 mL) and then dyhydrated using an ethanol gradient(1 x 1 mL) from 70 %, 80%, 90%, 96 % and 100 % ethanol for 5 – 10 minutes in each concentration. Cells were then immersed in Epon for 2 hours, the Epon was then removed and fresh placed on the sample(~1 mL)

with a Beem capsule filled with resin placed over the grid area. The resin was then cured in an oven at 56 °C for 24 hours. Once the resin was fully cured the glass bottom of the dish was heat shocked off by first placing the dish in liquid nitrogen for approximately 5-10 seconds before placing the sample into boiling water. If this step did not allow the removal of the glass bottom with a set of forceps the heat shock could be repeated until it was achieved. The resin was the pushed out of the rest of the dish from the bottom and the excess resin was removed using wire cutters. Cells of interest were retraced and the resin trimmed to allow sectioning of the cells of interest (typically ~400 x 400 µm). Serial sections were then taken and the sections imaged on a FEI Tecnai20 or a FEI tecnai 120Kv G2 Biotwin TEM. Image analysis was performed using imageJ and icy using the ec-CLEM (v 1.0.0.6) plugin to perform image registration and alignment of the light and electron micrographs.

7.1.6 High Pressure Freezing

HeLa cells were seeded at 100000 cells per dish overnight in 35 mm culture dishes with two or three sapphire discs (Leica) placed on the bottom of the dish. These Cells were then incubated with complex **4.6** (75 µM, 2 h) and then imaged live. The sapphire discs were then submersed in BSA fo 2-4 mins before being mounted into gold carries for HPF. The samples were then placed into an EMPACT 2 High Pressure Freezer (Leica) and HFP. The samples were then stored under liquid nitrogen until loading in to a AFS 2 Freeze Substitution equipment (Leica) in a solution of water (5 %), uranyl actate (0.1 %) in acetone at – 132 °C. The temperature was then slowly dropped over 24 hours to - 40 °C before being embedded in Lowicryl and the resin being cured by UV light. The sample was the brought slowly up to room temperature once the resin is cured. The samples were then removed and the resin carefully removed the top of the sample where the gold holder and sapphire disc is placed. Once the gold holder is reach the resin is trimmed around the holder until it can be carefully removed and the disc is exposed. The disc is then carefully removed to expose where the embedded cells should be.

7.2 Imaging

7.2.1 Confocal Microscopy

All confocal imaging was performed on live cells on an inverted Nikon confocal microscope (TE2000-U) using a 60x water immersion objective with a NA of 1.2. All complexes were excited at 405 nm and emission filter sets of 480-550 and 650-710 nm were used. All images were processed using imageJ.

7.2.2 Two-Photon Time-Resolved Mircoscopy

All time resolved imaging was done in collaboration with Dr Stanley Botchway at the OCTOPUS facility, CLF, Rutheford Appleton laboratory, Didcot, UK. The imaging was performed on bespoke experimental system, build on site and used in the imaging mode described by Baggaley *et al.*[6] All processing and image generation was performed using Becker-Hickl SPCImage v5.3 analysis software.

7.2.3 Emission Spectra

Spectra were collected under two-photon excitation were recorded by sending the emission signal from a given pixel position through a spectrometer to a CCD Andor iDUS at another microscope port.

7.2.4 Two-Photon Microscopy

All imaging of fixed mammalian cells was done using a Carl Ziess LSM 510 NLO upright using a Chameleon for excitation source (760 nm excitation). All images were processed using imageJ.

7.2.5 3D Structure Illumination Microscopy

3D SIM imaging was performed in the Wolfson light microscopy facility on a GE Deltavision OMX blaze in structured illumination mode, live cells were incubated with complex and then fixed using paraformaldehyde (3 %). Complexes were imaged under 405 nm excitation with a filter set for detection of 528/20; whilst Mitotracker orange and Lysotracker red were imaged using 561 nm excitation with a filter set of 600/37 nm. Imaging was done using DV immersion oil (GE healthcare) with a refractive index of 5.14 for all 3D SIM imaging. Imaging was performed sequentially and channels were corrected using the implemented software tool. All SIM reconstructions were performed on Softworx version 6.5.2 (GE healthcare) using OTFs optimised for the specific wavelength and oil used. Images were analysised using the ImageJ plugin SIMcheck.[7] Further image analysis was performed on Imaris 7.1(Bitplane AG, Switzerland).

7.2.6 Transmission Electron Microscopy

All TEM imaged was carried out using a FEI tecnai 120Kv G2 Biotwin TEM with an Orius SC100 bottom mounted camera using Gatan Digital Micrograph software. Image analysis was performed using imageJ.

7.3 References

1 J. A. G. Williams, A. Beeby, E. S. Davies, J. A. Weinstein and C. Wilson, *Inorg. Chem.*, 2003, **42**, 8609–11.

2 L. K. Mckenzie, I. V Sazanovich, E. Baggaley, M. Bonneau, V. Guerchais, J. A. G. Williams, J. A. Weinstein and H. E. Bryant, *Chem. - A Eur. J.*, 2017, **23**, 234–238.

3 Shewring, Jonathan R., A. J. Cankut, L. K. Mckenzie, B. J. Crowston, S. W. Botchway, J. A. Weinstein, E. Edwards and M. D. Ward, *Inorg. Chem.*, 2017, **56**, 15259–15270.

4 K. Hellström, H. Vihinen, K. Kallio, E. Jokitalo and T. Ahola, *Methods*, 2015, **90**, 49–56.

5 Y. Olmos, L. Hodgson, J. Mantell, P. Verkade and J. G. Carlton, *Nature*, 2015, **522**, 236–239.

6 E. Baggaley, S. W. Botchway, J. W. Haycock, H. Morris, I. V. Sazanovich, J. A. G. Williams and J. A. Weinstein, *Chem. Sci.*, 2014, **5**, 879–886.

7 G. Ball, J. Demmerle, R. Kaufmann, I. Davis, I. M. Dobbie and L. Schermelleh, *Sci. Rep.*, 2015, **5**, 15915.

Summary and Future work

The work presented here documents the development and characterisation of luminescent transition metal complexes as probes for super resolution microscopy and correlative light and electron microscopy. The first application of metal complexes in the super resolution technique 3D SIM is reported. The first use of metal complexes in correlative light and electron microscopy to give signal in both techniques is shown.

Initial work was preformed using the well-studied by emission microscopy "Pt N^C^N" (Pt(2,6-dipyrido-benzene)Cl) complex in order to assess the potential of such complexes to give contrast in electron microscopy. It was observed that the complex did not provide any notable contrast in EM at the concentrations and incubation times normally used for emission based microscopy techniques. However, when incubation times were increased, some higher contrast areas where observed that were consistent with the staining expected. This result highlighted the need for a complex to accumulate in sufficient amounts to give any noticeable contrast enhancement, and Pt N^C^N was found to stain too diffusely to give contrast at its emission microscopy staining concentration and incubation time. Thus more specific localisation was required for potential probes to operate at a similar concentration in both techniques. While Pt N^C^N did not fulfil the correlative criteria perfectly, it was found to be well suited to use as a 3D SIM probe. The complex displayed excellent photostability, with estimated intensity decays of $\leq$ 5% over ~1000 images, whilst Syto 82, a commercial stain of the same localisation pattern, displayed a 10-fold increase in intensity under the same conditions.

Informed by the initial work, a number of platinum and iridium based complexes were screened as potential CLEM and super resolution probes. Of these, only 3 were taken on for further study and an iridium di(phenylpyridine) bisbenzimidazole complex, ($[Ir(ppy)_2(bbim)]^+$) was found to have a pH-dependent emission lifetime *in vitro,* allowing mapping of pH across live HeLa and CHO cells. The complex was observed to accumulate in the lysosomes and mitochondria of cells, confirmed by co-staining with lysoTracker and MitoTracker in confocal microscopy and 3D SIM. The complex functioned well as a 3D SIM probe, illustrated by its excellent photostability, with only 4.5 % estimated intensity decay observed over ~700 images. In TEM studies the complex was not found to provide contrast at the (relatively low) concentrations used for emission microscopy. However, upon gradual increase of the concentration of the incubating solution, it was found that contrast enhancement could be observed at 50 µM, with much clearer enhancement at 75 µM and 100 µM (2 h incubation time). This work illustrates how metal complexes can feature properties that are desirable

for both CLEM and 3D SIM probes, but also highlights the need for specific accumulation of the complex in cells.

Striving to find more selective complexes that might operate at the same concentration in emission based and electron microscopy, we have investigated two iridium di(phenylpyridine) complexes with triazole-pyridine ligands present and either a tolyl or pyridyl moiety attached through the triazole (a collaboration with Professor Mike Ward, compounds made by Dr Ahmed Cancut). These complexes where found to localise specifically in the mitochondria of live HeLa cells by confocal microscopy and displayed extremely low cell toxicity as shown by MTT assay. TEM studies using these complexes at the same concentration as used in confocal microscopy found that contrast enhancement could be observed in the mitochondria. Solubility of the tolyl complex was found to be an issue and as such it was not studied in 3D SIM. The pyridyl complex was found to be a reasonable 3D SIM probe (2.63 % versus 32.1 % intensity decay of the commercial stain); although while the photostability of the complex compared to that of MitoTracker™ was found to be far superior, the complex exhibited much lower brightness. This meant that the contrast-to-noise ratio of cell incubated with the pyridyl complex was such that the strength of SIM reconstruction was only just adequate. These complexes are another step forward in producing CLEM probes but the photophysical properties make them a less than ideal 3D SIM probe.

As the iridium di(phenylpyridine) bisbenzimidazole complex had proven to be a good candidate for CLEM the complex was used in 3 different correlative light and electron microscopy methodologies. The first of these aimed to prepare the sample for TEM as normal but with cell incubated with complex before beginning sample preparation. This leads to ultrathin sections which potentially display luminescence and allow correlative microscopy of the same sample. These samples were found to be very fragile and easily damaged while handling. The luminescence of the samples was found to be very low, likely due to the section being so thin that a very small amount of complex was present. The second technique used cell culture dishes with grids embossed on the bottom to aid retracing the cells of interest and cells were imaged and then prepared for TEM in these dishes. This approach proved to be successful for this complex, with fully correlative images being obtained. Interestingly, during the CLEM it was noted that the cells displayed damage to their lysosomes in TEM after being imaged live in confocal microscopy but not mitochondrial damage was observed, shedding some light on the mechanism of cell death cause by this complex in photodynamic therapy. The final technique focused on the preservation of cells by high pressure freezing to give near native state preservation of samples in vitreous ice by rapidly freezing samples under extreme pressure. Unfortunately, during the freeze substitution method the resin is normally cured using UV to avoid heating the sample and lose preservation. However, this causes the complex to generate large amounts of singlet oxygen, destroying the cells.

Future work in the field should in part, focus on the development of new complexes as the ones presented here have gone some way to proving the ability of complexes to act as CLEM probes but none have displayed perfect characteristics. Specific localisation will continue to be paramount and ideally complexes could also be conjugated to SNAP or HALO tags to facilitate single protein level specificity. Furthermore, the photophysical properties are also key for super resolution microscopy applications, while photostability has been show across the range of complexes tested; the complexes are still required to be bright for these applications. With the conjugation to SNAP or HALO tags the complexes with the best photophysical properties could be utilised, with less focus given to the localisation of the complexes as this would be redundant. The second part should focus on further development of the complexes in CLEM methodologies. While the TEM preparation method did not produce samples with sufficient luminescence for imaging purposes, it could be possible to use thicker sections, such as those used in tomography (~300 nm), which would mean far greater amounts of complex would be present, thus raising the overall luminescence. The gridded culture dishes work well for one complex but further work should look to expand this with other complexes. The high pressure freezing method was found to be incompatible with complexes as it stands, however modification to the procedure by utilising fixatives, such as glutaraldehyde at low temperatures could potentially allow the samples to be heated after the freeze substitution to allow resin to be cured by heat while maintaining the preservation of the sample.

With the progress as it stands, the applications of metal complexes could now be explored using the gridded culture dish method to scrutinise samples from the dynamics of live cells to the ultrastructure in electron microscopy. This could lead to further breakthroughs in our understanding of the mechanisms by which cells are damaged in photodynamic therapy, leading to breakthroughs in the clinical applications of these. Furthermore, luminescent metal complexes can now be further developed to be used as easy CLEM probes, which with further work could be applicable to multiple preservation techniques.